TOR VERGATA
UNIVERSITÀ DEGLI STUDI DI ROMA

Dottorato di ricerca in Fisica - XVI Ciclo

Energetic Neutral Atom Imaging of Planetary Environments

Alessandro Mura

Relatore:

Dott. Stefano Orsini

Contents

Included papers

Paper **I**

A. Milillo, S. Orsini, and A. Mura. Empirical model of H^+ fluxes in the equatorial inner magnetosphere, *Conference Proceedings Vol 75,* "Sun-Earth Connection and Space Weather", SIF, Bologna, 2001

Paper **II**

Milillo, A., S. Orsini, D. C. Delcourt, A. Mura, S. Massetti, E. De Angelis, and Y. Ebihara, Empirical model of proton fluxes in the equatorial inner magnetosphere: 2. Properties and applications, *J. Geophys. Res*., 108 (A5), **1165**, 2003

Paper **III**

A. Mura, A. Milillo, S. Orsini, E. Kallio, and S. Barabash Energetic neutral atoms at Mars: 2. Imaging of the solar wind-Phobos interaction, *J. Geophys. Res*., 107(A10), **1278**, 2002

Paper **IV**

S. Massetti, S. Orsini, A. Milillo, A. Mura, E. De Angelis, H. Lammer, and P. Wurz. Mapping of the cusp plasma precipitation on the surface of Mercury. *Icarus,* 166, p. 229-237, 2003

Paper **V**

A. Mura, S. Orsini, A. Milillo, D. Delcourt, and S. Massetti. Dayside H^+ circulation at Mercury and neutral particle emission. To be submitted to *J. Geophys. Res*.

1. Introduction

1.1 Purpose and structure of this thesis

The aim of this work is to investigate the applications of the neutral atom imaging to the environments of the Earth, Mars and Mercury. This innovative technique permits the study of energetic plasma by means of analysing the result of the interaction of this plasma with a neutral thermal population or with a surface. The main advantage, when compared to the direct ion detection, is that it is possible to have an instantaneous survey of the whole magnetosphere of a planet. An example could help. Before the first ENA data, most of the knowledge about the Earth magnetospheric plasma came from *in situ* measurements of ions, electrons and electromagnetic fields. Those measurements, of course, could not represent any real instantaneous situation, but only an averaged picture of it, since the temporal and spatial variation cannot be easily be distinguished. Some short time scale phenomena, such as substorms, have been found difficult to comprehend without a global and continuous imaging. Even if some information about the plasma may be extracted from other sources, such as UV imaging [like aurorae, e.g. *Horwitz*, 1987], some populations (for example, the ring current) remained invisible.
Furthermore, neutral atom imaging gives information not only about the energetic plasma, but also about the thermal neutral population (in the case of charge-exchange) or about the surface composition (in the case of sputtering). Conversely, it is necessary to set up some dedicated unfolding techniques to recover the 3D plasma distributions from the 2D ENA images. In chapter **2** I will discuss the details of ENA and LENA imaging and how to extract information by using this technique.
Chapters **3**, **4** and **5** are focused on the environments of the Earth, Mars and Mercury; each chapter is followed by a section dedicated to ENA instrumental concepts. In some way, this structure reflects the chronology of my thesis work. In fact, as far as it concerns the Earth and Mars, some papers have been already accepted and published. Here I present a summary of my work, and most of the information is also contained in the included publications. The studies about Mercury, conversely, are in progress. For this reason I include here not only a submitted paper about Mercury, but also other unpublished results of my research in this last year.
The Earth. In chapter **3** I will present an empirical model of H^+ equatorial distribution in

the inner magnetosphere. I will use this model to reconstruct the global magnetospheric configuration during the geomagnetic storm of July 1991. The study could be a preliminary tool for ENA deconvolution techniques; moreover, it investigates the charge-exchange process, as a main loss of the magnetospheric plasma. In this frame, a new concept for a MH-ENA sensor is presented in section **3.4**, as a first example of neutral atom space instrumentation.

Mars and Mercury. While the Earth is, in principle, our main scientific objects, it is worth noting that Mars and Mercury represent some complementary "subsets" of the Earth. Mars has a faint atmosphere, but no large-scale magnetic field; Mercury has a magnetic field but only a tenuous exosphere. The complexity of the Earth magnetospheric environment, in addition to the ENA unfolding difficulties, makes it interesting to study those "laboratory planets".

Even if no ENA/LENA actual measurements have been done either for Mars or for Mercury until now, the scientific community is already focusing on these planets. As far as it regards Mars, ESA mission Mars Express (MEX) has reached Mars in December 2003. The ASPERA-3 instrument, on board MEX, is about to collect the first ENA data about Mars; it is hence extremely important to focus our attention on the unfolding methods. Moreover, ENA imaging may also be applied to Phobos, a natural satellite of Mars. In this case, surface properties can be studied, and this will give information about the origin and history of this satellite. In section **4.2** I will present a new model for the exosphere of Phobos, which may also be applied to many other outgassing natural satellites. In sections **4.3** and **4.4** I will introduce an investigation technique for Phobos' outgassing rate, and in sections **4.5** and **4.6** I will briefly resume main ASPERA-3 facts as well as my participation to the instrument development. Last but not least, I will show the first ENA data from ASPERA-3, collected while it was travelling to Mars.

Concerning Mercury, both ESA (with Bepi Colombo) and NASA (with Messenger) space agencies are planning to explore this inner planet of the solar system. In this case, the lack of available data is proportional to the effort in studying this planet. The chance to have a Neutral Analyser (SERENA: Search for Exospheric Refilling and Emitted Neutral Abundances) on board Bepi Colombo has focused the attention of most of the ENA community, and of SERENA team too, on the study of this planet. In fact, before proposing such an instrument, it is crucial to know as many details as possible about the expected ENA/LENA signal. It is also important to point out what information may be obtained, which instrument sensitivity is necessary and which satellite attitude is

optimal. My effort here consists in the feasibility study of this kind of remote-sensing applied to Mercury's environment. More particularly, a new model of magnetospheric ion and neutral circulation, which is one of the major goals of this thesis, has been developed and presented here.

Furthermore, ENA/LENA imaging study merges here with the instrument design activity. In section **5.10** I will report designs for some proposed ENA/LENA sensors. Incidentally, just some days before the presentation of this thesis (December 2003), BC mission was definitely approved and SERENA experiment is selected to be part of the Italian payload, which will be proposed to ESA by the Italian Space Agency.

Finally, in chapter **6** I will summarize my thesis work, I will stress the main scientific results, and I will propose future developments.

This thesis includes, as a fundamental part, four published papers and a submitted one. However, I intend this thesis to be readable also without those papers. For this reason, some parts and main results presented in the papers are resumed, expanded or simply reported here, and some figures have been shared.

2. The Energetic Neutral Atoms

2.1 Energetic and Low Energy Neutral Atoms: A brief history

The existence of Energetic Neutral Atoms (ENAs), arising from charge-exchange of ionospheric plasma with the local exospheric gas, was discovered in the early 50's. During an aurora, *Meinel* [1951] detected a blue-shifted H_α line, indicating that some precipitating Hydrogen ions were being neutralized. Some years later, *Moritz* [1972] reported the detection of protons of about two hundred keV at equatorial low altitudes. He suggested that they could have come from the outer radiation belt, turned into ENA by exchanging their charge with some neutral thermal population, then reached low altitudes without being affected by the magnetic field, and finally been re-ionised just before detection. In the 70's, the ion detectors on board IMP 7, IMP 8 and ISEE-1, while the satellites were orbiting out of the magnetospheric environment, detected some

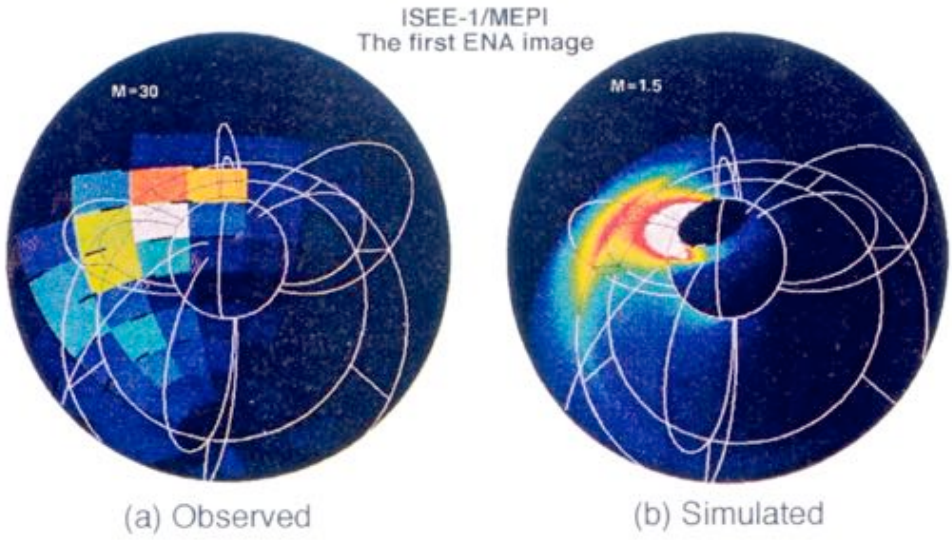

Figure 1.1 Panel a) First ENA image reconstructed by Roelof and Williams from ISEE-1/MEPI data. Sun is to the right; the smaller circle represents Earth, with a terminator line crossing it. Other lines are examples of magnetic field lines for L values of 3 and 5. **Panel b**) Same image as **a)**, simulated using a ring current model. From *Roelof,* [1987].

energetic particle flux coming from the Earth. The existence of ENA was again invoked, since no ion flux is expected in these regions. Since ENA fly almost unperturbed after their emission, more or less like photons, the scientific community started talking of "ENA imaging". Roelof [*Roelof et al.,* 1985; *Roelof and Williams,* 1988] reconstructed the first ENA image of the geomagnetosphere (Figure **1.1**) by using an ion detector on ISEE-1 and thus opening the way to an ENA remote-sensing of both planetary magnetosphere and neutral population.

Nowadays, after several other ENA detections by means of ion sensors, new instruments specifically designed for ENA imaging of the Earth magnetosphere are collecting useful data (such as IMAGE/M-H-LENA and CASSINI/INCA) or are about to be launched (such as those on board TWINS and DOUBLE STAR). Moreover, the potential of ENA imaging has become so clear that ENA sensors are also on board extra-terrestrial space exploration missions such as Mars Express (ASPERA-3) or Venus Express (ASPERA-4). A new concept ENA sensor has also been proposed for the future ESA exploration mission to Mercury, Bepi Colombo (BC).

Neutral atom imaging may be applied not only to charge-exchange, but also to all processes producing directional neutral atoms. For example, if plasma interacts directly with a planetary surface, sputtering processes may occur and neutral atoms may be extracted. The detection of those neutrals may give information about both plasma and surface properties. Such a technique can be applied, for example, to the exploration of Mercury's environment and a dedicated instrument package (SERENA) has been proposed on board BC.

While ENAs coming from charge-exchange have energies between some hundreds of eV to some hundreds of keV, the typical energy of the sputtered neutrals is, generally, between fractions of eV to some hundreds of eV. For this reason, and also following a consolidated nomenclature, I will call ENAs only the formers, and I will introduce the term LENAs (low energy neutral atoms) for the latters. In the following, I will discuss those processes separately, but it is worth noting that this separation is made only to better explain the different features of the processes themselves. In fact, a neutral sensor is able to discriminate between emission processes only if the energy ranges are completely separated, and, in principle, this is not always true.

2.1 Charge exchange process: imaging plasma-exosphere interaction

When an energetic ion collides with a neutral and non-energetic target particle, it may charge-exchange and be neutralized, becoming ENA. An electron and a small amount of kinetic energy are exchanged between the neutral and the ion. Some examples of this kind of process, active on the Earth and involving energetic ring current ions and cold atmospheric neutrals, are the following:

$$H^+ + H \rightarrow H + H^+$$

$$O^+ + H \rightarrow O + H^+$$

$$H^+ + O \rightarrow H + O^+$$

$$O^+ + O \rightarrow O + O^+$$

In principle, the energy defect of the process is equal to the difference of the two atomic ionisation potentials [*Hasted*, 1964]. Charge-exchange is a resonance process; symmetrical when the species of the ion and the neutral are the same, and accidental otherwise [*Stebbings et al.*, 1964; *Hasted*, 1964]. While the target is scattered at an approximately perpendicular angle with respect to the projectile path, the newly created ENA retains approximately both the energy and the direction of the colliding energetic ion. No longer affected by magnetic or electric fields, the ENA travels along ballistic trajectories (straight lines at these energies), and can be detected outside the interaction region. Figure **2.1** shows a scheme of this process.

Let us consider a vantage point S_0 and a unit vector $\hat{v}$. The differential ENA flux of direction $\hat{v}$ observed at S_0 is generated by the interaction of the energetic ion fluxes with one or more ambient neutral populations in a generic point S along the line (S_0, $\hat{v}$). At S, the infinitesimal ion flux dJ_+ directed toward S_0 is:

$$dJ_+ = n_+(l)\, v\, f(l, \mathbf{v})\, d\mathbf{v}, \qquad (\mathbf{2.1})$$

where $n_+(l)$ is the ion density, v is the velocity, $f(l, \mathbf{v})$ is the ion velocity distribution function and l is the distance $\overline{S_0 S}$. If f is expressed by means of the kinetic energy E, the direction $\hat{v}$ and the infinitesimal solid angle $d\Omega$, as usual, the above formula could be changed by using the following one:

$$f(l, \mathbf{v})\, d\mathbf{v} = f'(l, E, \hat{v})\, dE\, d\Omega. \qquad (\mathbf{2.2})$$

At point S the mean free path of ions of energy E relative to charge exchange process is:

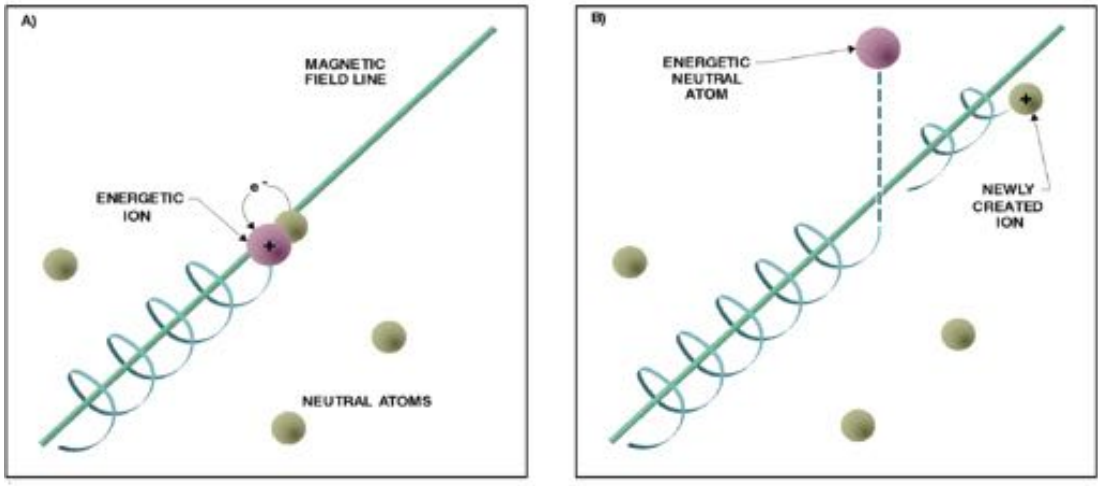

Figure 2.1 Scheme of the charge-exchange process. Energetic ion hits a neutral target (panel **A**) and gets an electron from it. After collision, it may proceed with a straight-line trajectory (panel **B**).

$$\lambda_+(l,E)=\frac{1}{\sum_k \sigma_k(E)n_k(l)}, \qquad (\mathbf{2.3})$$

where n_k is the density of the k^{th} neutral species at point S, σ_k is the charge-exchange cross-section between ions and the k^{th} neutral species. We can now estimate the ENA infinitesimal flux $dJ_E(E, \hat{v})$:

$$dJ_{ENA}(E,\hat{v})=\int_{l=0}^{l=\infty} dJ_{H^+}\frac{1}{\lambda_+(l,E)}\,dr=\int_{l=0}^{l=\infty}\sqrt{\frac{2E}{m_+}}f'(l,E,\hat{v})\frac{1}{\lambda_+(l,E)}n_+(l)\,dl\,dE\,d\Omega; \qquad (\mathbf{2.4})$$

and the ENA differential flux integrated along a certain line of sight $\Phi_{ENA}(E, \hat{v})$:

$$\Phi_{ENA}(E,\hat{v})=\frac{dJ_{ENA}(E,\hat{v})}{dE\,d\Omega}=\int_{l=0}^{l=\infty}\sqrt{\frac{2E}{m_{H^+}}}f'(l,E,\hat{v})\frac{1}{\lambda_{ION}(l,E)}n_{H^+}(l)\,dl\,. \qquad (\mathbf{2.5})$$

Charge exchange (CE) cross sections are obviously function of energy (see figure **2.2**) and have significant values only between 1 keV and some hundreds of keV. Typical value for the CE cross section is 10^{-16} cm^{-2}; even if this value is not very high, in magnetospheric physics cases the integration path may be long enough to cause relevant ENA fluxes at S_0.

The ENA flux moving towards S_0 may be removed by other processes, such as photon ionisation or stripping [*C:son Brandt*, 1999]. In this case, it is easy to include a destruction function by means of the mean free path λ_{ENA} in equation (**2.5**) [*Orsini et al.*, 1994]:

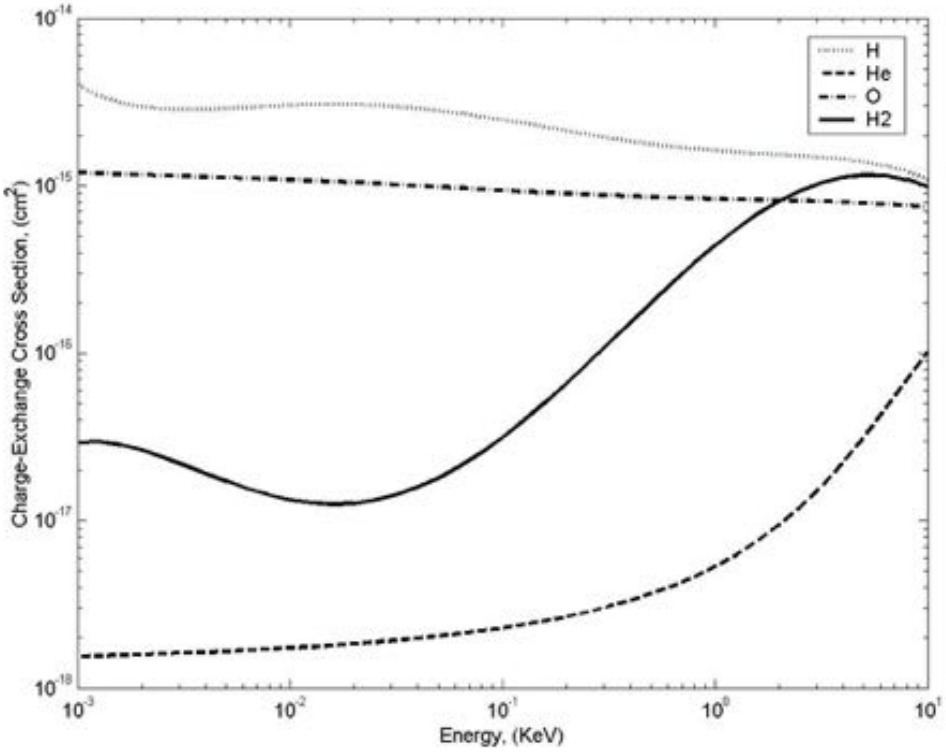

Figure 2.2 Charge exchange cross sections for H^+ with some typical neutral exospheric species. Data from *Barnett et al.* [1977], *Stebbings et al.* [1977], and *Barnett* [1990].

$$\Phi_{ENA}(S_0,E,\hat{v}) = \int_{l=0}^{l=\infty}\left[\sqrt{\frac{2E}{m_{H^+}}}f'(l,E,\hat{v})\frac{1}{\lambda_{ION}(l,E)}n_{H^+}(l) - \frac{\Phi_{ENA}(S,E,\hat{v})}{\lambda_{ENA}(S,E,\hat{v})}\right]dl \ . \quad (\mathbf{2.6})$$

In all cases discussed here, the medium can be considered "optically thin" to ENA, i.e. the mean free path is long enough, and ENA can transport information out of the generation region, thus allowing remote-sensing of the interaction process [*Roelof et al.*, 1985; *Roelof*, 1987; *Henderson et al*., 1997; *Orsini and Milillo*, 1999; *Milillo and Orsini*, 2001].

At the time CE creates new ENA, it removes ion from plasma flux. The ion destruction rate may be expressed as:

$$\frac{d\Phi_+}{dt} = \frac{\Phi_+}{\lambda_+}v. \quad (\mathbf{2.7})$$

The integration in equation **2.5** is, almost always, solved numerically over a large number of directions to obtain a simulated ENA image. Moreover, as I will discuss better later in this section, while trying to unfold some ENA data a large number of

simulated ENA image may be needed. In many cases, the plasma and exospheric properties are not defined by analytical functions, but by discrete grids. Hence, the integration step Δs and the angular resolution $\Delta\alpha$ and $\Delta\beta$ must be small enough to have a very large number of integration points inside the same cell. In the end, this procedure may take a lot of time.

Here I introduce a different kind of ENA simulation, which may be called "weighted-grid integration". It can be applied only if the plasma is defined over a 3D grid, and this happens, for example, if plasma distribution has been simulated numerically. The principle is to consider each plasma cell in the space as if it were a light source, and to treat ENA flux as light. Hence, to obtain the light as seen at vantage point S_0, I will sum over all plasma cells, giving them a weight that is inversely proportional to the square of the distance between the cell (point S_{ijk}) and S_0. The ENA production rate $\frac{d\Phi_{ENA}}{ds}$ for any point of the grid may be calculated as:

$$\frac{d\Phi_{ENA}}{ds} = \frac{|v| n_H}{\lambda_+}, \tag{2.8}$$

and the total flux escaping from a cell located in S_{ijk} and detected in S_0 is:

$$\Phi_{ENA}(S_0, S_{ijk}) = \frac{d\Phi_{ENA}(S_{ijk})}{ds} \Delta V \, f_\alpha(\hat{v}) \frac{1}{|\overline{S_0 S}|^2}, \tag{2.9}$$

where ΔV is the volume of the ijk^{th} cell; $f_\alpha(\hat{v})$ is the 3D angular distribution function, $\hat{v}$ is the direction from S to S_0.

This procedure may be faster than the previous one, especially if the plasma and neutral properties are defined over a discrete grid. In the following, for historical reasons, I will use the former for Mars' ENA imaging, and the latter for Mercury's case.

ENA deconvolution. I have already remarked that neutral atoms are good messengers of information. However, this information should be unfolded, because a 2D image, intrinsically, cannot have the amount of information stored in a 3D volume. The first and simplest kind of unfolding method for ENA data is simulating the corresponding ENA image by using theoretical or empirical models of plasma and neutrals, and then comparing the simulated image with the experimental one. A second step is to introduce some free parameters in the models and tune them until a good fit between real and simulated data is found. In section **5.7** I will show an example of the parameter tuning in the case of ENA generation in Mercury's cusps.

Even if the easiest way to obtain information from ENA imaging is the method described above, it has been demonstrated [*Roelof*, 2003] that ENA imaging can produce interesting results even without models, if some intrinsic symmetry or property of the plasma can add enough additional information to remove the ENA ambiguity. In the case of the Earth, for example, the plasma distribution could not have the degrees of freedom of an arbitrary C°($\mathbf{R^3 \rightarrow R}$) function, if we want it to satisfy the adiabatic expansion law. This consideration, plus the assumption that the pitch angle (PA) distribution is flat at the equator, is able to remove the "ENA ambiguity". In the case of Mars, additional information may be obtained, for example, by considering that the plasma distribution must have, approximately, cylindrical symmetry around the Mars-Sun axis.

Finally, it must be noted that even in the cases where ENA images don't need any magnetospheric model to be unfolded, they do need some to be understood. In fact, a sequence of ENA images, alone, is able to technically reconstruct a sequence of magnetospheric plasma distribution, but only a model is able to provide them with an interpretation, forecast their future development, and distinguish the physical processes involved.

2.2 Sputtering process: imaging a planetary surface

ENA image is as useful as the charge-exchange process is effective in removing ions from the magnetospheric plasma. This is the case of the Earth and Mars; elsewhere, such as at Mercury, plasma may interact directly with a planetary surface, and sputtering may be the dominant process (see sections **5.5** and **5.6**). This latter process is the result of the impinging of a particle on a surface; if the impact energy (E_i) of this particle is sufficient, another particle (sputtered particle) may be extracted. The energy distribution of the sputtered particles, $f(E_e)$, can be expressed as:

$$f(E_e) = \begin{cases} k \dfrac{E_e}{(E_e + E_b)^3} \left[1 - \left(\dfrac{E_e + E_b}{E_i} \right)^{\frac{1}{2}} \right] & E_e \le E_i - E_b \\ 0 & E_e > E_i - E_b \end{cases}, \qquad (\mathbf{2.10})$$

[*Siegmund,* 1969, *Sieveka and Johnson*, 1984], where E_e is the ejection energy and k is a normalization constant. The energy E_b is the surface binding energy and depends on the atomic species. Typical values for E_b are few eV, while E_i may reach values of some

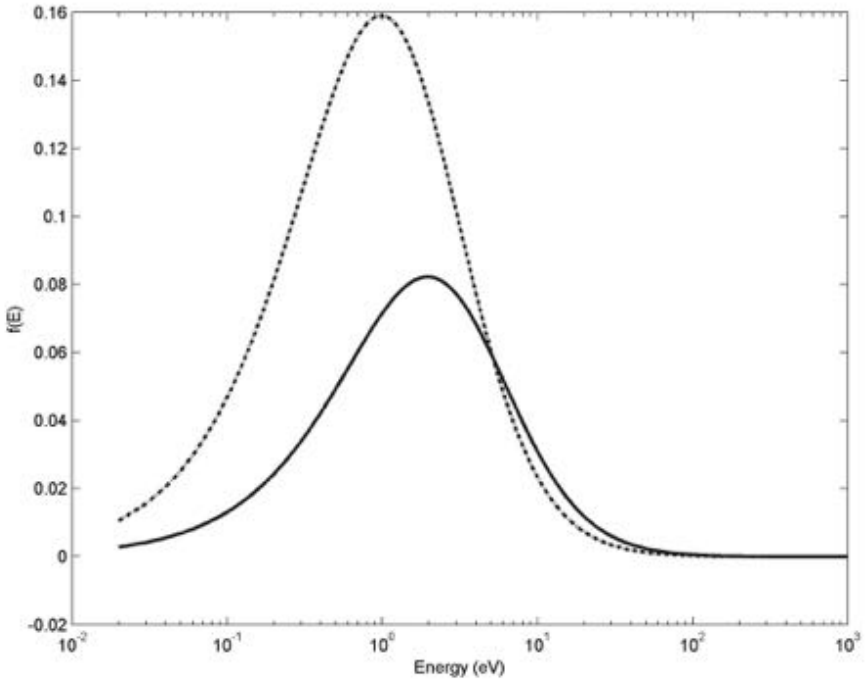

Figure 2.3 Energy distribution function for sputtered particles, $F(E_e)$, as a function of ejected Na (continuous line) and O particle (dashed line) energy E_e in the case of E_i = 1 keV (solar wind protons). Binding energies here are 2 eV for Oxygen [*McGrath et al*., 1986; *Cheng et al*., 1987] and 4 eV for Sodium [*Lammer and Bauer,* 1997].

keV. In this case, it may be shown that the shape of $f(E_e)$, except for the highest energies, depends mostly upon the binding energy E_b, which corresponds approximately to the peak energy of the spectrum. Figure **2.3** shows two examples of this function in the cases of Oxygen and Sodium.

The resulting LENA flux is hence:

$$\frac{d\Phi}{dE} = Y\,R \int_{E\min}^{E\max} \frac{d\Phi_{H+}}{dE_i} f_S\left(E_e, E_i\right) dE_i \ , \qquad (\mathbf{2.11})$$

where R is the fraction of the considered species in the soil composition, and Y is the yield for sputtering production. As for the ENAs coming from charge-exchange, the LENA flux may be simulated once the soil composition and the binding energy (depending on the atomic composition) have been assumed.

The charge of the products arising from this particle bombardment depends both on the composition and the chemical structure of the planetary surface, but generally most of the sputtered particles are neutral. A more oxidized surface produces higher ion content, which is typically between 0.1% and 10% of the total.

The LENA signal coming from the surface of the planet carries information about the precipitating energetic particles (neutrals and ions) and the surface properties. Even if there is no line-of-sight integration, the deconvolution may be difficult as well, and the LENA source is still not univocally determined. In fact, the low energies of LENAs make their trajectories not rectilinear. In the case of energies close to or below the gravitational escape energy (typically some eV or fraction of eV), the trajectories must be treated taking into account the ballistic laws. In the case of Mercury, a hypothetic LENA sensor on board an orbiting spacecraft may detect particles coming from the other side of the planet. For lower energies, the situation merges with that of an exosphere, and LENA sensor will work as an exospheric neutral detector. In section **5.8** I will show examples of LENA trajectories for medium and low energies.

3. The Earth: where all has started.

This chapter is dedicated to my first work as a PhD student: storm-time monitoring of the Earth equatorial magnetosphere. The complexity of the terrestrial magnetosphere makes it extremely difficult to develop time-evolving theoretical models of plasma circulation. Here I will present an original approach, which uses an empirical model of the 90° pitch angle proton distribution in the equatorial plane [*Milillo et al.* 2001]. This model depicts a "virtual magnetospheric configuration", statistically including all possible processes [*Paper* **I**, *Paper* **II**], and in the following is also referred to as *reference model* (section **3.1**).

In section **3.2** I will demonstrate that it is possible to reconstruct different magnetospheric configurations, i.e. to obtain *modified* models from the *reference* one, just tuning some of its numerical constant.

Finally, I will show how to use *in situ* data to guide the model parameters. Their modulation during a geomagnetic storm leads to a time-series of different *modified* models, and hence a sequence of pictures of the magnetosphere during the storm. In other terms, the observed energy spectra collected in a single position are able, via the empirical model, to give information about global plasma properties such as ring current and partial ring current development, L-shell compression/stretching and cross-tail potential drop. In section **3.3** this method will be applied to CRRES/MICS/LOMICS data collected during July 1991 storm.

This study does not directly involve ENA imaging; nevertheless, magnetospheric modelling is the basis for ENA simulation and unfolding. Moreover, the method described here can still be referred to as a "magnetospheric imaging", obtained by applying the model to *in situ* data. Last but not least, this model is able to show how important the losses due to charge-exchange are, and, in turn, how useful ENA imaging is to monitor the magnetospheric configuration.

In section **3.4** I will present the instrumental concepts and some preliminary simulations of a medium-high energy neutral analyser (MH-ENA NAOMI) proposed to ESA for the ISS (International Space Station).

3.1 Reference model.

The present analysis is based on an empirical model of the 90° pitch angle proton fluxes

in the equatorial plane of the Earth [*Milillo et al.,* 2001]. The model is based on the AMPTE/CCE/CHEM experiment data, and it is a superposition of different functions representing different equatorial populations and/or physical processes; a complete description of the model is given in *papers* **I** and **II**.

The model has been developed using a filtered data set, which represents a statistical configuration (AE < 100 nT) averaged during solar minimum. All large-scale spatial and temporal processes coexist in the model, which does not depict any specific and instantaneous configuration. However, in section **3.2** I will show that the model is able to reconstruct *any* magnetospheric configuration, provided that its numerical constants are opportunely tuned.

The goal of this study is to reconstruct, via the model, the different configurations of the geomagnetosphere during a storm. Hence, among different segments/populations of the model, I am focusing on the ones that describe the injection and the diffusion of protons

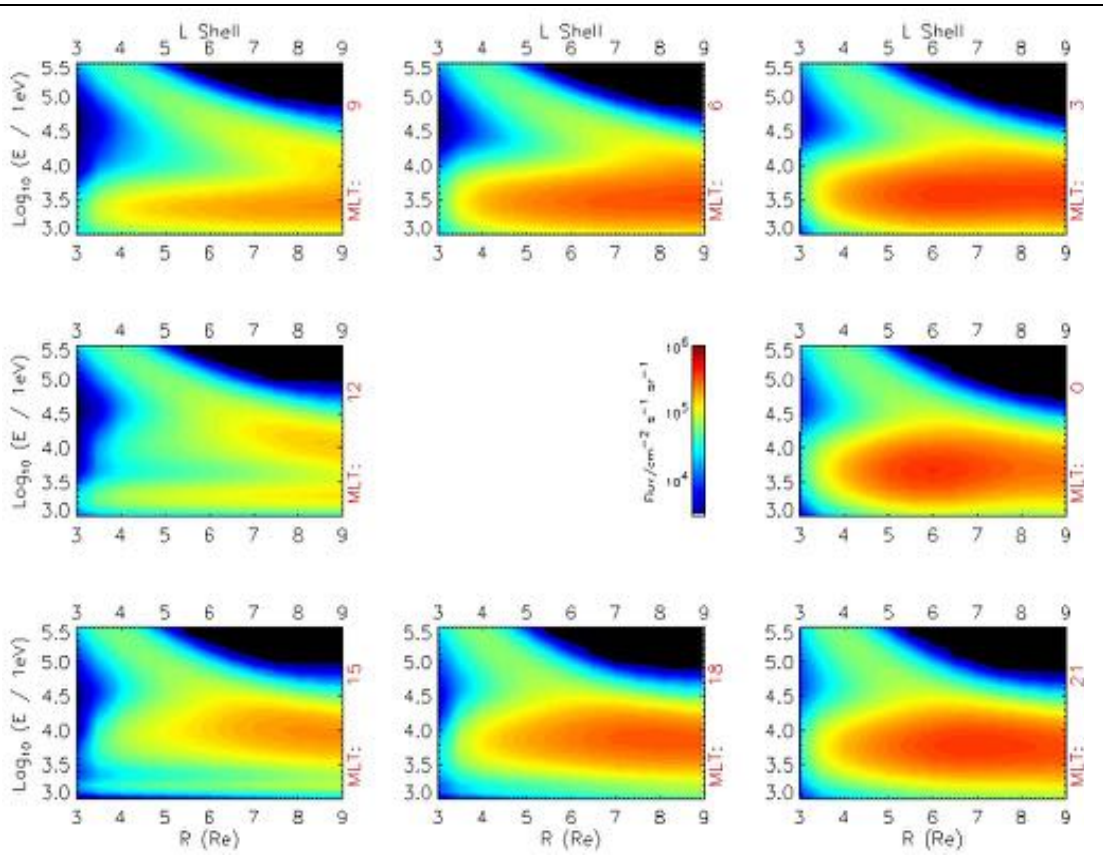

Figure 3.1 Colour-coded picture of the modelled 90° pitch angle differential proton fluxes as a function of *LS* and *E* at different *MLT*

in the equatorial magnetosphere. These functions, expressed in terms of H^+ flux (Φ_{H+}) versus *L-Shell* (*LS*), are summed to obtain the total H^+ differential flux:

$$\frac{\Phi_{H+}(LS)}{dE\,d\Omega} = \left[A_{G2} \exp\left(-\frac{(LS - P_{G2})^2}{2W_{G2}^{\ 2}} \right) + CO \right] \exp\left(-\frac{I_S^{\ 2}}{(LS - P_S)^2} \right) + A_{G3} \exp\left(-\frac{(LS - P_{G3})}{2W_{G3}^{\ 2}} \right) \qquad \textbf{(3.1)}$$

where *A, P* and *W* simply stand for amplitude, peak positions and widths of the *G2* and *G3* gaussian functions. The first addendum in equation **3.1** describes the injected population, in the following simply referred to as *CO+G2*. The second addendum represents the diffused population, or simply *G3* in the following (this nomenclature has been adopted for consistency with the model description in *papers* **I** and **II**).

The Φ_{H+} versus energy (*E*) and Magnetic Local Time (*MLT*) dependency is not explicit in equation **3.1,** but it is obtained by other gaussian and trigonometric functions for a total of 37 physical coefficients (see *Paper* **II**)**.** The model is represented in figure **3.1;** each panel is a colour-coded intensity map of the Φ_{H+} in the *E* vs. *LS* plane, and different panels refer to different *MLT*.

The *CO+G2* (injection-related) population is represented by the intense peak of Φ_{H+} at low energy. The energy corresponding to the peak of this population is function of the *MLT*. In fact, this population is more energetic at dusk than at dawn. This effect, also known as *dawn-dusk* asymmetry, will be discussed below.

The *G3* (diffusion-related) population is distinguishable by its high-energy peak at low *LS*; its shape is almost *MLT*-independent and its peak (P_{G3}) has a strong *LS* vs. *E* inverse dependency. This effect follows theoretical predictions and has a strong implication in the monitoring of a geomagnetic storm, as it will be better explained in section **3.2**. The *G3* populations cannot be discriminated from the *CO+G2* one at high *LS*, since there the former is generated by the latter.

The model is able to reconstruct some of the magnetospheric quantities. The velocity distribution function $f(v)$ can be obtained from Φ_{H+} (equation **B.1** in appendix **B**); then, it is possible to obtain the particle density n_{H+} and the energy density ε as the momentum of order two and four of the $f(v)$ distribution (equations **B.2** and **B.3**).

If the pitch angle (*PA*) distribution is isotropic, the parallel and perpendicular pressures are both equal to $\frac{2}{3}\varepsilon$ (equation **B.4**), and the current density J_{H+} is derived from pressure *P* applying equation **B.5**.

The electric field can be obtained from the mean kinetic energy $\overline{K} = \varepsilon / n_{H+}$ if we also

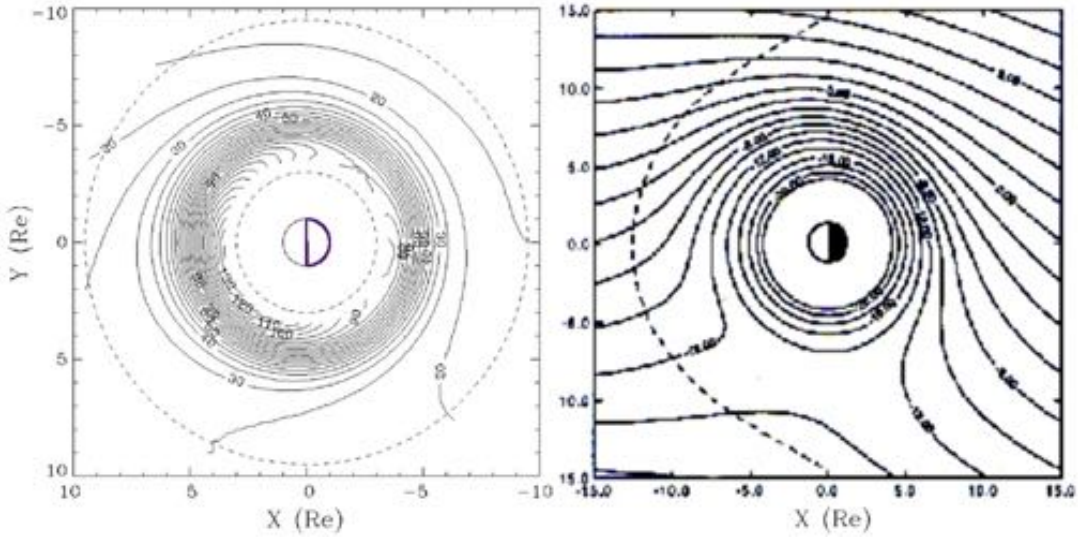

Figure 3.2 Quiet time electric potential contours, as calculated using the model (left panel) and as predicted by McIlwain [1986].

hypothesize that: i) protons motion is adiabatic; ii) **E**×**B** = 0; iii) **E** and **B** are time-independent; iv) all the protons are injected in a small region with similar energy.

Under hypotheses i), ii), and iii), and if all protons were injected at one point r_0 with *exactly* the same energy E_0, they all should follow the same trajectory, ruled by the guiding centre (GC) approximation (see appendix **B**). For the conservation of energy, at any point **r** reached by the protons, the energy spectrum should result in a sharp peak at energy $K(\mathbf{r})$:

$$K(\mathbf{r}) = K_0 + qV(\mathbf{r_0}) - qV(\mathbf{r}) \qquad (\mathbf{3.3})$$

where V is the electric potential and q is the charge. Under the more realistic hypothesis iv), the energy spectrum at point **r** extends to more than one energy $K(\mathbf{r})$, and equation **3.3** should be applied, as an approximation, to the *mean* kinetic energy $\overline{K}$. Under these assumptions, the map of lines of equal mean kinetic energy corresponds to the map of the equipotential lines.

Figure **3.2** shows a comparison between the electric potential estimated by using equation **3.3** and the McIlwain [*McIlwain,* 1986] electric field model associated to quiet conditions. It is evident the good agreement between these models for $LS > 5$; at lower LS, however, this model is not able to reconstruct the electric field. In fact, since protons

are supposed to be injected with approximately same energy, they should always have an energy spectrum that depicts a single population. Hence, this approximation is less valid when it is possible to recognize two different populations ($LS < 5$), because the diffused one (*G2*) is driven by non-adiabatic processes.

3.2 Modified model.

As mentioned before, it is necessary to tune the model coefficients to make the model fit a given, real magnetospheric configuration. As an example, we may imagine to detect a certain proton energy spectrum, at a given location P_0 (LS_0, MLT_0) and at a given time t_0. The situation is described by figure **3.3**; the energy spectrum is a vertical segment at $LS=LS_0$ in the panel corresponding to MLT_0. In principle, it is not necessary to modify all the 37 model coefficients to obtain a good agreement between the experimental spectrum and the one predicted by the model. In fact, any spectrum is the sum of two populations (injected and diffused) and it is sufficient to introduce 6 parameters that are able to modulate the peak position, intensity and width of these two populations. For simplicity, these parameters are normalized so that a value of 1 represents the *reference* condition for each parameter. These parameters are summarised in table **3.1**.

The intrinsic correlation between these pure numbers and the model coefficients is discussed in *paper* **II**; however, it is more important to understand how the modification of these parameters reflects different physical configurations of the magnetosphere.

The intensities *B* and *D* at some time t_0 represent the relative importance of the two different processes versus time, until t_0. The modulation of the cross-tail electric field

Table 3.1

Name	Meaning	Population
A	Related to energy of peak position (vs. L-Shell)	G3 Diffused
D	Intensity	
F	Temperature or width	
C	Related to energy peak position (vs. MLT)	CO+G2 Injected
B	Intensity	
E	Temperature or width	

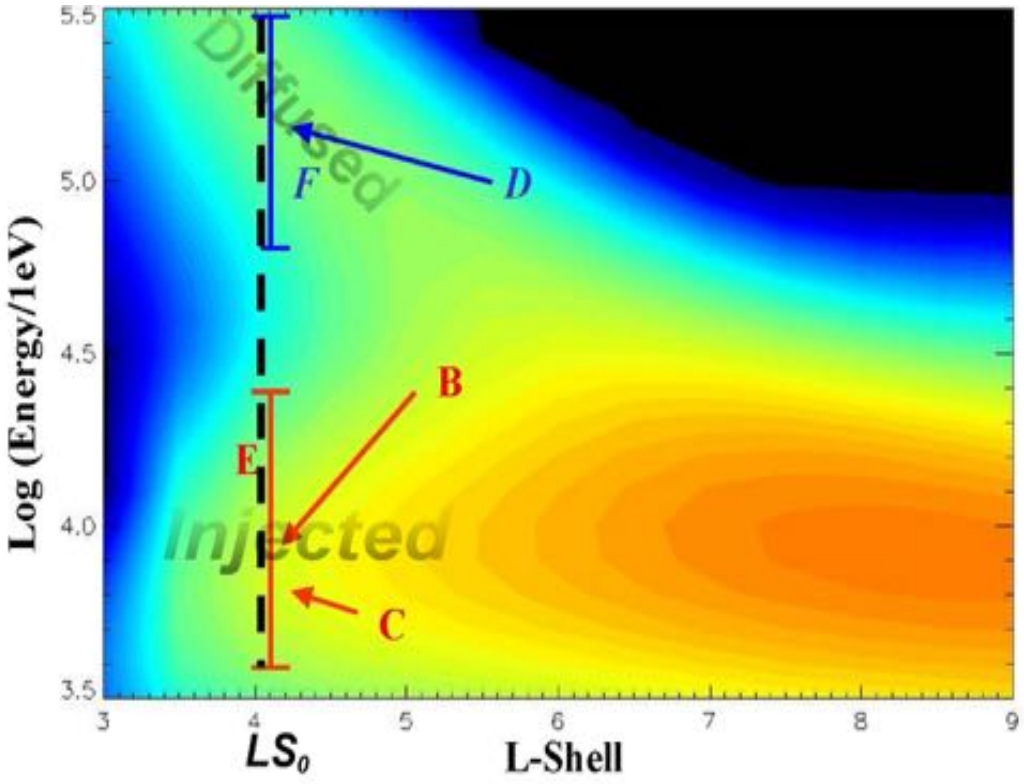

Figure 3.3 Colour-coded H^+ differential flux in a *LS* vs. *E* plane, for a generic *MLT*. The dashed vertical line represents an energy spectrum at a single L-Shell (LS_0). The coloured segments explain the meanings of the parameters *B* (intensity of *CO+G2*), *C* (related to position of *CO+G2*), *E* (temperature of *CO+G2*), *D* (intensity of *G3*), *F* (temperature of *G3*).

and of the potential drop is related to the *dawn-dusk asymmetry*, which is in turn related to the difference of the energy of the (*CO+G2*) peak (factor *C*). An increase of *C* can be imagined as a translation of the whole (*CO+G2*) population towards higher energy in all panels in figure **3.1**. Since the energy scale is logarithmic, the energy shift in the dusk sector will be higher than the one in the dawn sector. In the end, the difference in mean energy between these sectors will increase.

In principle, there is no way to modify the peak position of the diffused population *G3*. This value, actually, follows the theoretical and empirical equation [*Ejiri,* 1978]:

$$\begin{cases} E = \dfrac{1}{LS^3} & PA = 90° \\ E = \dfrac{1}{LS^2} & PA = 0° \end{cases} . \qquad (\mathbf{3.4})$$

Hence, an increase (decrease) of the *G3* peak energy can be obtained only if we move

our point P_0 to lower (higher) *LS.* Alternatively, we may imagine to be at a fixed point P_0 and to observe an expanding (compressing) magnetosphere. Hence, I introduce a parameter A, which is defined as:

$$A = \frac{LS_1}{LS_0} \qquad (\mathbf{3.5})$$

where LS_1 is the *L-Shell* for which the spectrum is calculated. Hence, $A>1$ ($A<1$) means that we have to move our point outward (inward) in order to find the proper energy spectrum, or that the whole magnetosphere has been compressed (stretched).
In summary, the model is able to reconstruct any given magnetospheric configuration, provided that the six chosen parameters are opportunely tuned.

3.3 Imaging the equatorial magnetosphere during a substorm

I have shown that, given an experimental energy spectrum at a certain point P_0, it is possible to find a set of parameters for which the model fits the experimental data. Once the *best-fit* parameters have been found, the global image of the magnetosphere can be obtained by using the model (this procedure may be performed iteratively if we have several spectra at different times and different positions). Now, the tasks I want to address myself to are the following:
1) to validate the H^+ model with experimental data, by verifying that it is possible to reconstruct any real magnetospheric spectrum;
2) to reconstruct the time-development of the 6 chosen parameters, and discuss it in the frame of the interpretation given in section **3.2**;
3) to use the 6 parameters to obtain the whole equatorial magnetosphere configuration (ring current, electric field, plasma density and spectra).
This method has been applied to proton energy spectra, collected by CRRES MICS/LOMICS experiment along the spacecraft orbit in the midnight-dusk quadrant between L ~4 and ~9, energies between 4 and 400 keV. Figure **3.4** shows the best-fitted parameters, function of time, during July 1991 storm. The coloured lines are the running-window time-averages of the parameters; the running-window covers one orbit (10 hours). In addition, AE, KP and Dst indexes are plotted to help the discussion. In the development of these indexes it is possible to recognize two main storm phases (approximately between DOY 190-191 and between DOY 194-195).
Panel **3.4-B** shows the development of parameter B. The good correlation between the

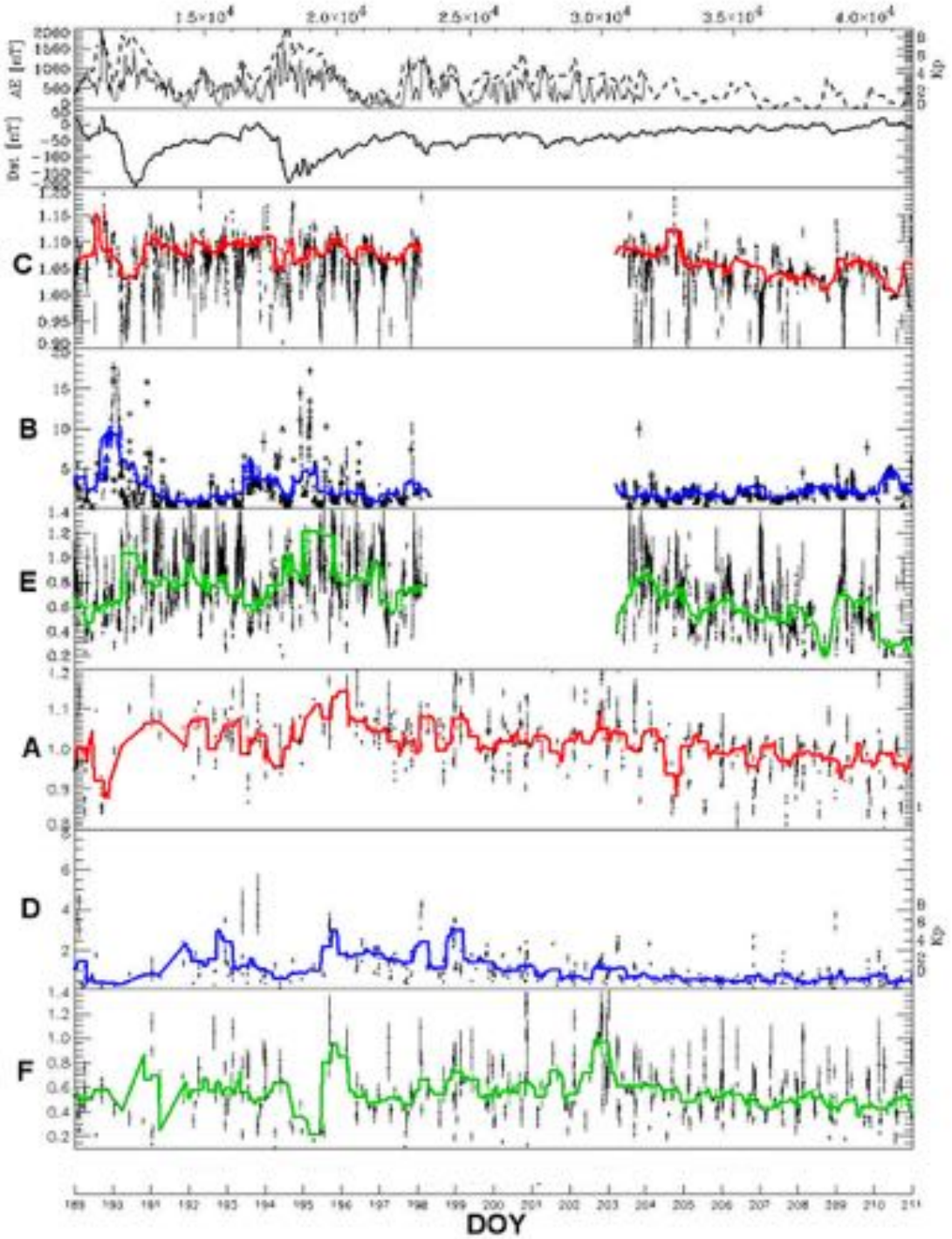

Figure 3.4 Parameters *C, B, E* (position, intensity and temperature of *CO+G2*) and *A, D, F* (position, intensity and temperature of *G3*) vs. time during July, 1991 storm. Blank interval in first three parameter curves is due to instrumental failure. Dst, AE and *Kp* are shown in the first two panels.

Dst depletions and *B* increases indicates that the model is able to reconstruct the injection and convection of new, fresh particles in the magnetosphere. A similar effect can be recognized in the width of the injected population (parameter *E*). After these processes decrease, loss processes such as charge-exchange rapidly erode the H^+ signal

at low energy.

Parameter *A* is shown in panel **3.4-A**. During the evolution of a storm, the magnetosphere stretches (A <1) before main phase development, then depolarises (A>1) just some time after injection of fresh particles [e.g. *Lui*, 2000], and finally slowly gets back to quiet time configuration (A=1) during the recovery phase. Actually, two major increases of *A* can be noted just after the two main storm phases, indicating that *A* is a good tracer of the magnetospheric instantaneous geometry.

Parameter *D* is shown in panel **4.3-D**. The intensity of the diffused population is expected to decrease during the main phase of the storm, when this population is removed from the magnetosphere due to the opening of the electric field and of the closed drift paths [*Ebihara and Ejiri*, 1998; *Liemohn et al.*, 1999]. After the main phase, the new protons start to diffuse and *G3* intensity reaches its maximum. As protons get closer to the Earth, however, they reach regions where exospheric densities are higher, and generally several loss processes affect the particle distributions. There, the charge-exchange, as well as other loss processes, starts removing particles, and parameter *D* reacts to that by exhibiting a slow decrease. The reconstructed development follows exactly this theoretical prediction. Moreover, this interpretation explains a little difference between the two analysed recovery phases. In the first one, the *G3* has enough time to reach its maximum, but not enough to decay back to the *reference* model; the second recovery phase is longer, and *D* decreases in an approximately exponential way.

Once the six functions $A(t)$, $B(t)$ … $F(t)$ have been reconstructed, it is possible to use them as an input for the model and obtain all the magnetospheric quantities at any time during the storm. Before attempting such a data-analysis, however, it is necessary to stress two considerations: i) experimental data set has been time-averaged, and since the satellite spends the most of its time in the outer part of the magnetosphere, the spectra collected in this region give a higher contribution to the fitting process; ii) during the injection phase, *CO+G2* vs. *LS* deviate from the model, because electric field shielding decreases and particles penetrate deeper into the inner magnetosphere. For these reasons, during storm time, the inner part of the magnetosphere cannot be properly reconstructed until model improvements are done.

In figure **3.5** I show the global reconstruction of mean kinetic energy (electric potential, panels **A, B, C**), energy density (panels **D, E, F**) and perpendicular current density (panels **G, H, I**) at three different stages of the storm.

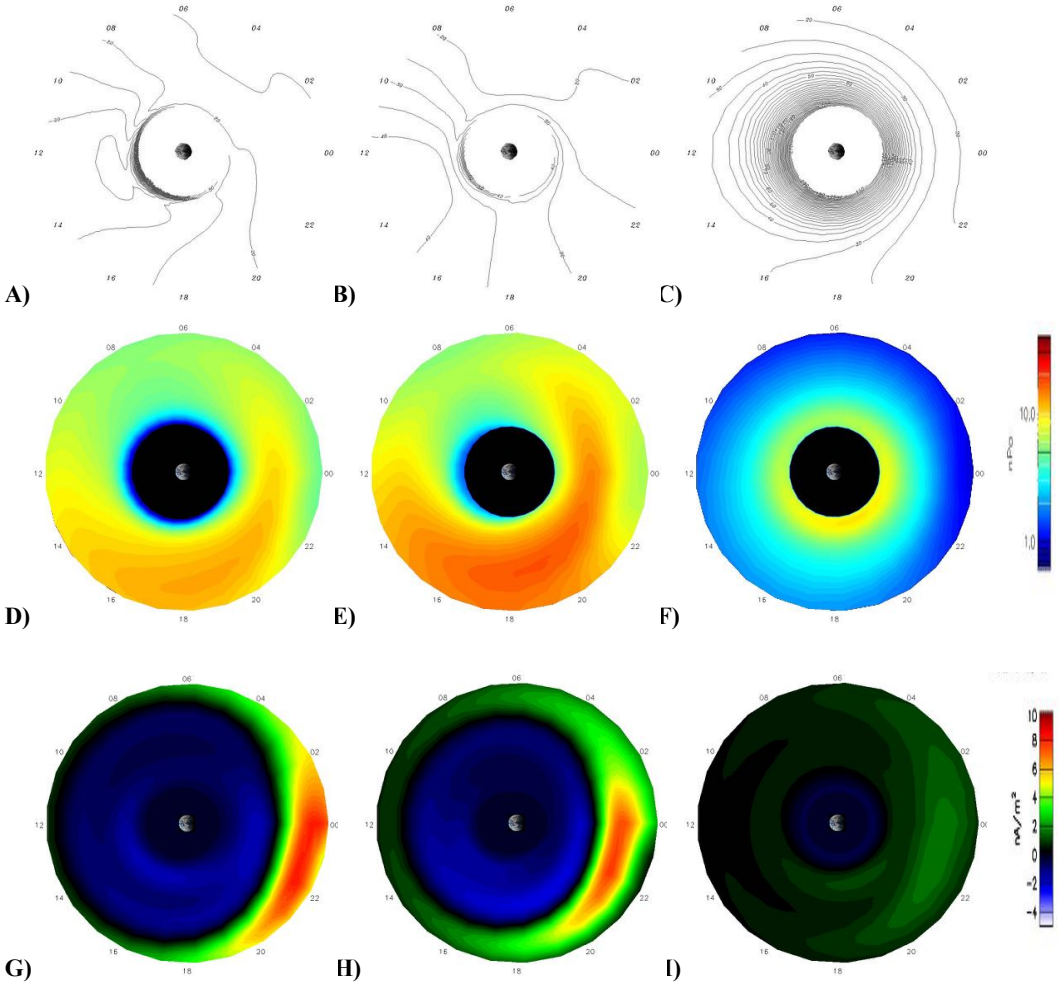

Figure 3.5 Global reconstruction of electric potential (panels **A, B, C**), energy density (panels **D, E, F**) and perpendicular current density (panels **G, H, I**) at three different stages of the storm. Panels **A, D, G:** initial phase of the storm; panels **B, E, H:** main phase; panels **C, F, I**: recovery phase.

Panels **A, D, G** refer to the initial phase of the storm (*sudden commencement*), just before the *main phase*. The cross-tail electric field penetrates into the inner part of the magnetosphere; the energy density intensifies at dusk because protons flush in that region and escape through the afternoon magnetopause [*Ebihara and Ejiri*, 2000]; at the same time the tail current intensifies and is directed towards dusk.

During the *main phase* (panels **B, E, H**) the electric field is still *dawn-dusk*; the energy density is even higher because particles are being populating the inner-dusk regions; the current density shows the depolarisation of the magnetosphere, as it is localized at lower *LS*.

During the *recovery phase* (panels **C, F, I**) the co-rotating electric field shields the inner regions, the energy density becomes symmetric and the ring current closes around the Earth.

In conclusion, this approach provides a unique tool to understand the dynamics of the inner magnetosphere, by taking into account that any given situation is driven by previous effects which are recorded and must be considered for a correct interpretation. I've already stressed that ENA images are in principle able to depict such real conditions, and a comparison with this model could be able to give the dynamical time profile that has led to the configuration photographed by ENA images (see also final comment in section **2.1**).

3.4 A new design for a Medium-High Energy Neutral Detector

In this chapter I have discussed main magnetospheric features, and I have introduced an investigation method that could be considered as alternative or complementary to ENA remote-sensing.

Before leaving this chapter, I will briefly discuss about ENA instrumentation applicable to the Earth's magnetosphere. At present, several neutral particle detectors are part of the payload of spacecrafts actually orbiting around the Earth (IMAGE) or travelling to other planets (Cassini). Different detection techniques have been applied, depending on the energy of the detected particles. A summary of ENA flying detectors can be found, for example, in [*C:son Brandt* 1999] and [*Wurz,* 2000]. Here, as an example, I will introduce a new design of a medium-high energy neutral atom (MH-ENA) detector to be possibly located onboard the International Space Station (ISS): NAOMI (Neutral Atom Observer and Magnetospheric Imager).

The scheme of this sensor is shown in figure **3.6.** The instrument has energy, mass and direction resolutions, and is suited for ENA particles in the 1 keV-300 keV energy range.

The detector consists of a pinhole-focusing ENA camera. First, high-voltage deflection plates remove the ion component of the entering flux and collimate the ENA flux. Then, the collimated neutrals pass through a thin carbon foil (CF). There, secondary electrons are emitted and the neutrals are ionised with a certain efficiency, depending on their energy.

The carbon foil is placed just above a double grid, which is charged at some electric potential ΔV. The electric field that is generated between grids causes the electrons to be accelerated upward; they are detected by a start-MCP (micro channel plate). At the same time, the positive-ionised fraction of the incoming neutrals is post-accelerated and deflected downward; depending on their energy, these ions impact onto a stop-MPC or onto a solid-state detector (SSD).

For each event, it is possible to reconstruct the direction of the incoming neutral by analysing the position of the electron signal on the start-MCP. Moreover, the detector is able to resolve the time-of-flight (ToF) between CF and stop-MCP/SSD.

The particles with energy less than or equal to $q\Delta V$ (some keV) are deflected and impact onto the stop-MCP. The impact position depends on the particle energy before the post-acceleration (E); the particle energy after post-acceleration is simply $E+q\Delta V$. This information, in addition to ToF, provides energy and mass resolution. The particles with energy well above $q\Delta V$, as well as the non-ionised particles, travel more or less along

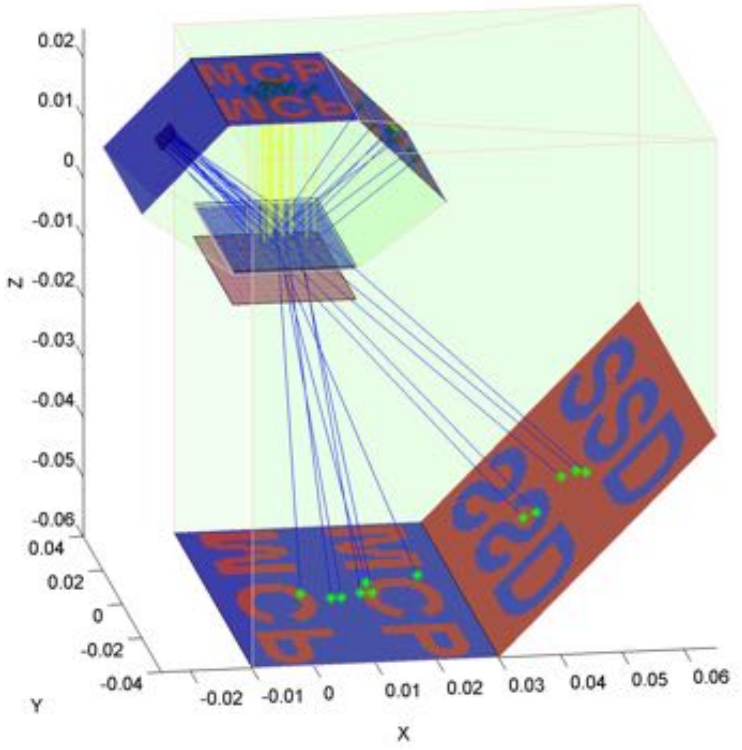

Figure 3.6 NAOMI scheme and simulated trajectories. Red and blue surfaces are respectively stop-SSDs and start-MCPs. Grid and carbon foil are in the middle of the figure; blue lines are protons' trajectories; yellow lines are electrons' trajectories.

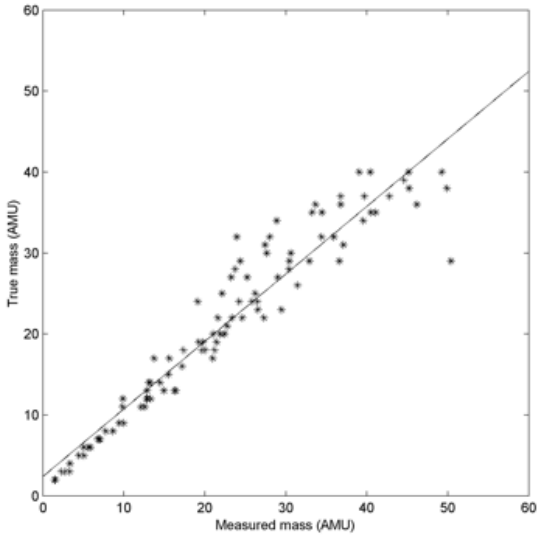

Figure 3.7 Scatter plot of true mass versus measured mass in a simulated detector. The error on the mass is calculated taking into account only the ToF.

straight lines and are collected onto the SSD. In this case, it is possible to roughly determine the particle energy in the ToF chamber by means of the pulse-height analysis on the SSD, and hence the mass of the particle. However, the initial particle energy (before CF) is not known, since is it not possible to determine the charge of the particle, and whether it has been post-accelerated or not.

As an example, figure **3.7** shows a scatter plot of measured vs. true mass in a simulation of the instrument, for particles of about 1 keV, and with ΔV=20 kV. The error on the mass resolution has been computed taking into account only that on the ToF.

4. Mars and Phobos: waiting for Mars Express

This part of the thesis is dedicated to Mars/Phobos environment in the frame of the forthcoming ESA mission Mars Express (MEX). More particularly, I will present here an application of ENA imaging at Mars: the investigation of the Oxygen population generated from natural satellite Phobos. In fact, the existence and the magnitude of this population could give precious information about the evolution of this moon [*Fanale and Salvail*, 1989]. This study has been already published, and the details can be found in *paper* **III**; here I will summarise the principal topics and the results.

First, I will introduce some empirical models for proton plasma and neutral population at Mars, and a dedicated model for Phobos-originated Oxygen population. These neutral atoms are supposed to outgas from Phobos and fill a torus all along its orbit, but the existence of such a torus is still debated. So far, only indirect evidences of it have been found [*Paper* **III**]. The ENA imaging technique would be a useful investigation tool, since in next few months new data from ASPERA-3 sensor on board MEX will be available. While waiting for these data, the feasibility of such an investigation is

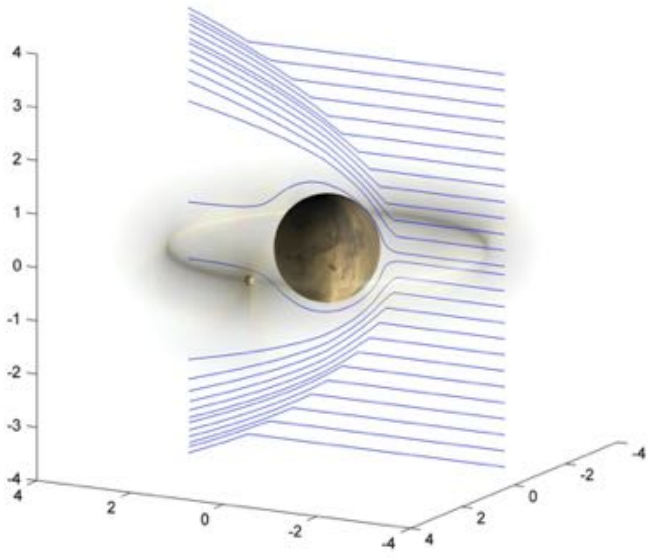

Figure 4.1 Interaction of solar wind with Mars. Blue lines represent the proton trajectories as calculated by Kallio [1997]. The ring around the planet is a reconstruction of the Phobos Oxygen torus as it has been simulated in *paper* **III**. Dimensions of Phobos are not on scale.

discussed here.

Last but not least, I will present here some fundamental concepts of ASPERA-3 instrument as well as the first ENA data from ASPERA-3.

4.1 Mars environment

Introduction. The environment of Mars, the last of the terrestrial solar system planets, could have been for many aspects similar to the Earth's one, because of comparable planetary dimensions and distances from the Sun. The main difference is probably the absence of a global magnetic field at Mars: this single lack leads to an enormous amount of consequences in the present and in the past of Mars' environment.

Since the solar wind interacts with Mars mainly through direct impact with the ambient atmospheric/exospheric gas [*Kallio et al.,* 1997], charge-exchange is expected to be very effective. ENA imaging is hence a potentially useful tool to understand the geometry, the physics, and the dynamics of the plasma around Mars.

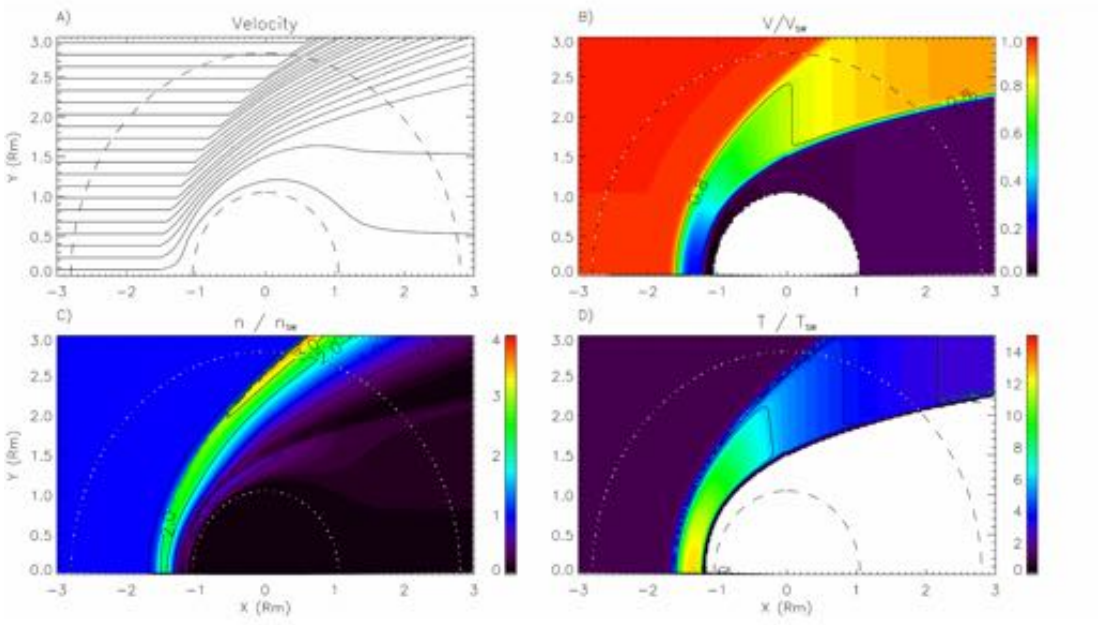

Figure 4.2 Empirical model of the proton flow, based on ASPERA three-dimensional proton velocity measurements [*Kallio*, 1996]. Panel A) and B): proton streamlines and velocity, panel B) proton density; panel D) proton temperature. An axial symmetry around Sun-Mars axis has been postulated. The inner circumference shows the position of the planetary obstacle boundary; the outer one shows the position of Phobos' orbit.

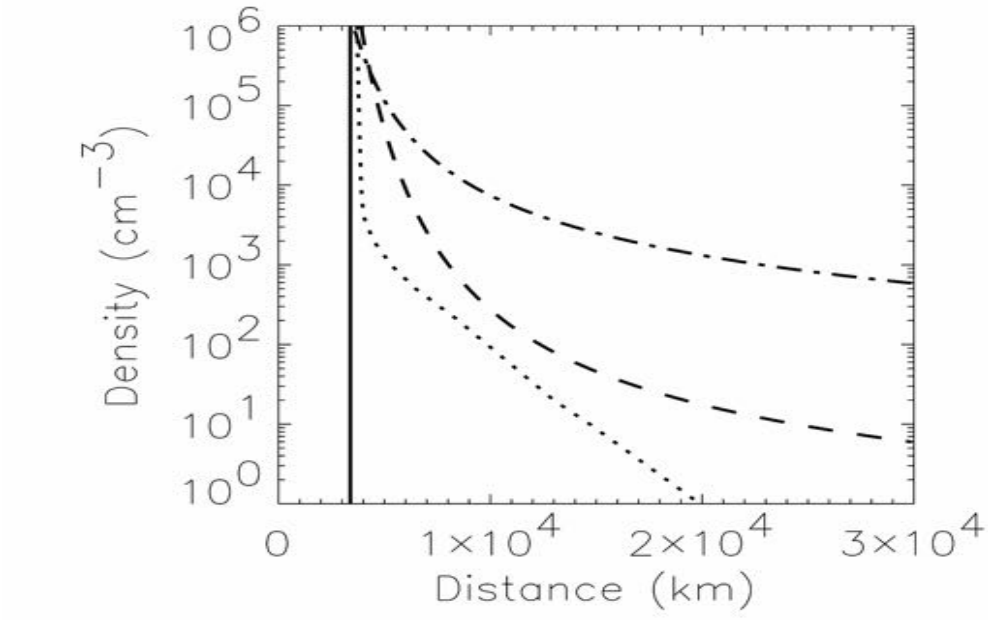

Figure 4.3 Neutral particle density profiles in the Martian exosphere versus altitude: Oxygen (dotted), Hydrogen (dash-dotted), and molecular Hydrogen (dashed), from *Krasnopolsky and Gladstone*, 1996. The solid line indicates the Mars surface.

Mars "Magnetosphere" and neutral population. A schematic of Mars "magnetosphere" is shown in figure **4.1.** Some examples of proton trajectories (blue lines), as well as Phobos' torus, are shown. It could be useful to define specific regions of interaction [e.g. *Vaisberg et al.*, 1990]. Going from the outside towards the planet, we find:

1) a bow shock, where the solar wind starts to be deflected;

2) a "magnetosheath", a region between the bow shock and the magnetopause, where the solar wind particles are effectively deflected and mixed to planetary particles;

3) a "magnetopause", where the plasma speed decreases;

4) a "magnetosphere", the region inside the magnetopause;

5) an obstacle boundary, no plasma or field penetrates it.

The term "Magnetosphere", as well as "Magnetopause" and "Magnetosheath", doesn't seem to be appropriate in Mars context, since there is no magnetic field. Nevertheless, this nomenclature is widely used for consistence with the Earth topology, and for simplicity.

The plasma model used in this study [*Kallio*, 1996] considers the solar wind origin plasma as composed by protons only. Figure **4.2** shows maps of the streamlines, the velocity, the density, and the temperature of the proton flow around Mars. This

empirical model, based on PHOBOS-2/ASPERA data (1989), is able to reconstruct all regions mentioned above. More particularly, if we refer to panel **b**), the red region is the unperturbed solar wind; the blue/green/orange region is the magnetosheath; the dark blue region is the magnetosphere. Bow shock and magnetopause are the boundaries between these regions; obstacle boundary corresponds more or less to planetary surface. According to this model, half of Phobos' orbit is inside the bow shock, but its presence does not modify the model. In fact, due to its very small dimensions, Phobos is not able to deflect the proton flux on large scales.

Our simplified model of neutral population considers Mars' atmosphere and exosphere as composed only of Oxygen, Hydrogen and molecular Hydrogen. In fact, other neutral species are present (such as Helium, for example), but they have a lower charge-exchange cross-section. The neutral profiles for those populations are approximated by exponential functions of the distance from Mars and are shown in figure **4.3;** more details can be found in *paper* **III**.

4.2 A model for Phobos' torus

Phobos, the inner of the natural satellites of Mars, is an irregular object with dimensions of 13.5 x 10.8 x 9.4 km and a mass of 1.08×10^{16} Kg. Its orbit is located on the ecliptic plane and is approximately circular. The orbital radius (R_{MP}) is 9500 km ($\cong 2.7\ R_M$) and the revolution period is about 7 hours.

The suggestive hypothesis that a dust/gas torus may surround Phobos' orbit has been suggested since 1971 [*Soter*, 1971]. Lately, after PHOBOS-2 observation of Mars in 1989, its presence has been invoked to explain some strange effects on IMF and electron density measurements [*Ip and Banaszkiewicz*, 1990; *Horanyi et al*., 1990; *Dubinin et al*., 1990; 1991].

More particularly, one of the hypotheses is that Phobos may contain water [e.g.: *Fanale and Salvail*, 1989], and that surface outgassing of Oxygen may occur. The escaping particles should have enough energy to escape the attraction of Phobos, but not that of Mars. They are supposed to travel in ballistic orbits around Mars, thus leading to the formation of the neutral component of the above-mentioned torus. In any case, the presence of such a population is still an open question: if this Oxygen population is really present, which outgassing rate is responsible for it? A possible value, which could explain the PHOBOS-2 disturbances, is 10^{23} s^{-1} [*Sauer et al.,* 1995; *Paper* **III**]; so far,

no direct observation of this population has been successful. The other hypothesis (a dust ring), however, seems to be less probable since a direct observation of a possible dust ring around Mars [*Duxbury and Ocampo*, 1988] didn't evidence any significant signals.

It is worth noting that Phobos' orbit is partially embedded both in the Martian magnetosheath (in the dusk and dawn sectors) and in the magnetosphere (in the night side). Hence, the outgassing material around the orbit may interact not only with the undisturbed solar wind, but also with the plasma flowing around Mars [e.g.: *Barabash and Lundin*, 1994]. In my analysis, I will focus on the charge-exchange interaction between the Oxygen component of this torus and the energetic protons, and I will discuss on the feasibility of a detection of this population via ENA imaging.

Theoretical studies [*Krimskii*, 1992] suggest that the torus cross section is approximately circular, and that the mean O density $<n_o>$ inside is ~10^4 cm^{-3}. Nevertheless, this value should necessary be higher close to Phobos. In this case, values up to n_o=10^6 cm^{-3} could be found [*Paper* **III**]. In fact, under the hypothesis of a free expansion from Phobos, the oxygen density near the satellite is:

$$n_o = \frac{dN}{dV} = \frac{dN}{4\pi r_P^2 \, dr_P} = \frac{1}{4\pi r_P^2} \frac{dN}{dt} \frac{dt}{dr_P} = \frac{Q}{4\pi r_P^2 \, v_n}; \qquad \textbf{(4.1)}$$

where r_P is the distance from Phobos and $v_n = dr_P / dt$ is the mean particle velocity while escaping from Phobos. This latter value can be obtained by using $v_n = (2\ k\ T_P / m_O)^{1/2} = 500\ m\ s^{-1}$, where T_P = 250 K is the surface temperature of Phobos, and m_O is the oxygen mass [*Ip and Banaszkiewicz*, 1990; *Krymskii et al*, 1992].

Some preliminary ENA simulations were done using this value, and the result was promising: ENA imaging should be able to investigate the outgassing rate from Phobos. Then I've decided to improve the accuracy on the estimation of the O density function inside the torus, by means of an *ad hoc* numerical, Monte-Carlo model. More than 10^7 test particles trajectories have been tracked, taking into account gravitational and Coriolis force in the non-inertial frame of Phobos. The test-particle trajectories have been reconstructed with a special mix of analytic and numerical treatment, since full-analytical trajectory solution in a non-inertial frame is not easy (more details can be found in *paper* **III**; used equations are in appendix **B)**. The model includes a random source for Oxygen particles, and all possible loss processes.

The result, in terms of neutral distribution n_o, is shown in figure **4.4**. Here I adopt cylindrical coordinates: r is the distance from Mars, ϕ is the angle from Phobos

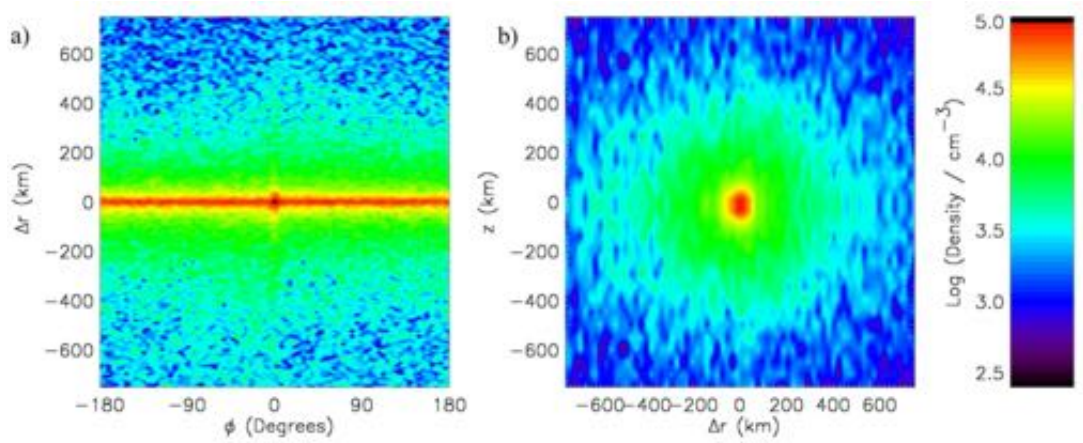

Figure 4.4 Simulated neutral Oxygen density near the orbit of Phobos for different bi-dimensional sections: ϕ versus Δr, z=0 (Panel A); Δr versus z, ϕ=0 (Panel B); $Q = 10^{23}$ s^{-1}. Phobos position is at Δr=0, ϕ=0°, z=0; its velocity is directed toward the increasing ϕ.

direction, $\Delta r = r - R_{MP}$. The two panels refer to two distinct bi-dimensional sections: [ϕ, Δr, z = 0] (Panel A), and [z, Δr, ϕ = 0] (Panel B). The O density n_o in a small region surrounding Phobos reaches values up to $2 \cdot 10^5$ cm^{-3}. In the remainder of the torus n_o is almost ϕ-independent, with a peak of $\approx 3 \cdot 10^4$ cm^{-3} located at Δr=0.

An important parameter for the Oxygen distribution simulation is lifetime τ. There are three important causes of O-atom losses in Phobos' torus: charge-exchange, photo-ionisation and electron impact ionisation, and all of them cause relevant losses. A zero-order estimation, using solar wind plasma parameters, leads to a charge-exchange loss frequency $f_{CE} = 10^{-7}$ s^{-1} [*Paper* **III**]. This value is comparable to other loss frequencies. In fact, at Mars' orbit and during solar minimum, the photoionisation loss frequency is $f_\gamma = 10^{-7}$ s^{-1}, and the electron impact ionisation frequency is $f_e = 2 \cdot 10^{-7}$ s^{-1} [*Zhang et al.,* 1993]. The total loss frequency f is the sum of all these frequencies ($f = 4 \cdot 10^{-7}$ s^{-1}), and I have hence considered an oxygen gas lifetime $\tau = f^{-1} = 2\ 10^6$ s.

4.3 Mars ENA imaging

If we want to study the outgassing rate of Phobos by means of ENA imaging, the ENA flux coming from Mars environment should be considered as "background", even if it is, actually, the major objects of ASPERA-3 investigation. The estimation of such a

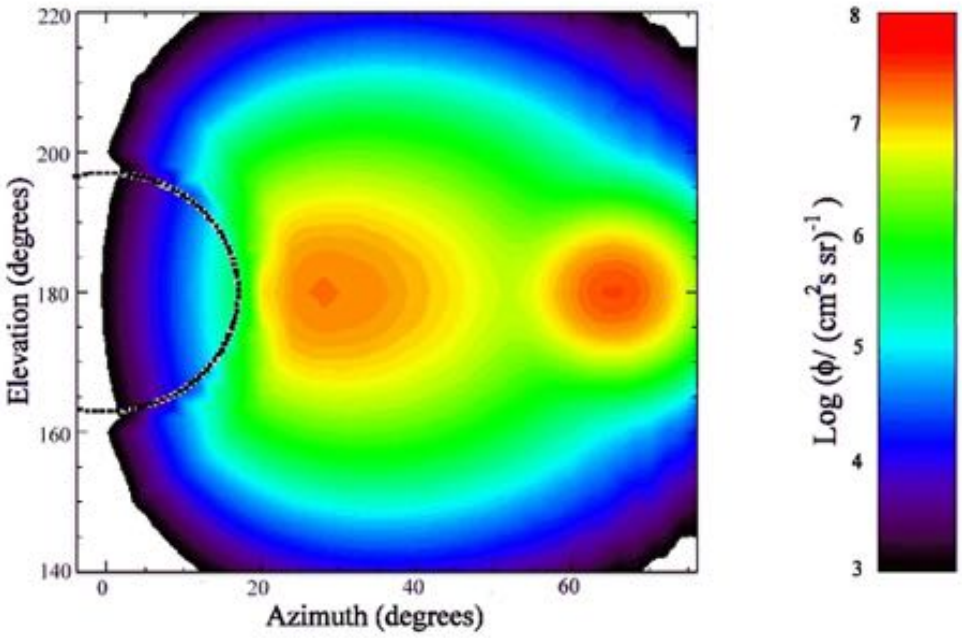

Figure 4.5 Pseudo-color map of the ENA differential flux, function of the elevation and azimuth angle, if only Mars exosphere was present. The dashed line represents Mars' obstacle boundary. Azimuth angle is measured on the equatorial plane, beginning from Mars' centre; elevation angle is measured perpendicular to the equatorial plane, Mars' centre is at 180°.

background is a preliminary step for this investigation.

The ASPERA-3 package on board MEX includes a Neutral Particle Imager (NPI), with good angular resolution but no energy resolution, and a Neutral Particle Detector (NPD), with low angular resolution (more details in section **4.5**). Hence, for some realistic vantage point configurations, I have simulated some ENA images and the related ENA energy spectra.

An example of Mars' ENA image is shown in figure **4.5**. The vantage point, in this case, is at (-1.3 R_M, 2.9 R_M, 0) in Mars-Solar-Ecliptic (MSE) coordinates, and it is schematised as a grey point in figure **4.6**. The dotted line represents Mars' obstacle boundary. The ENA differential flux has been calculated by using line of sight integration (equation **2.5**), and then it has been integrated over all energies (from 10 eV to 2 keV). Two peaks can be recognized in the image: a narrow and circular one centred on the sunward direction, and a more extended one closer to the planet. The first is related the ENA flux generated outside the bow shock by the unperturbed solar wind; the second is related to the ENA flux generated in the magnetosheath, by the

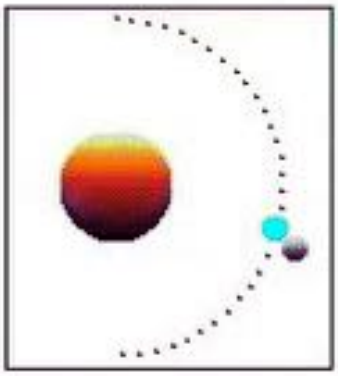

Figure 4.6 Scheme of the relative Mars-Phobos-ASPERA position, as used for ENA images simulation of figures **4.5, 4.8, 4.9.**

thermalised solar wind. Figure **4.7 (**solid line**)** shows the ENA spectra relative to Figure **4.5**. The spectrum related to Mars' ENA flux (solid line) is the envelope of the fluxes from all regions. The low energy flux (below 400 eV) is generated very close to Mars' surface (see figure **4.2**); the high energy flux (0.4-2 keV) results both from unperturbed solar wind outside the bow shock, and from deflected solar wind in the magnetosheath.

4.4 A simple deconvolution: Phobos' outgassing rate

The hydrogen ENA flux generated at Mars can be considered as the sum of two: the one coming from Mars' exosphere and the one coming from Phobos' torus. The first is almost always detectable; the latter, due to the small dimensions of Phobos' torus (see figure **4.4**), is not. In fact, the integration path is, in most cases, too small to produce a noticeable ENA flux. The most favourable configuration for this latter signal occurs when the vantage point is located on Mars' equatorial plane and close to Phobos. During MEX mission, three useful Phobos' close approaches are planned [*Barabash, private communication*].

Figure **4.8** shows the ENA flux generated by Phobos' neutral population, with the exclusion of the background signal reported in figure **4.5**, assuming hypothetically that $Q = 10^{23}$ s^{-1} (see previous comments in section **4.2**).

The ENA image is of course concentrated on the equatorial plane. Here, the peak

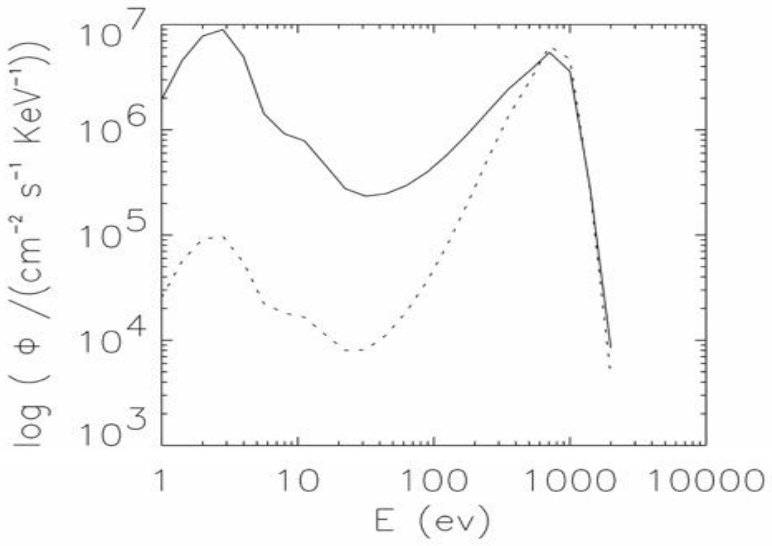

Figure 4.7 Spectra of the ENA fluxes coming from Mars (solid line) and Phobos (dotted line), integrated over all directions in the sky. Vantage point and Phobos position are the same as in figure **4.5.**

intensity is higher than the "background" in the same location. However, if we look at the ENA spectrum (figure **4.7**, dashed line), we note that it is well below the background at any energy. Hence, such a measurement is possible only via NPI. I have also simulated ENA images and spectra for other different Mars-Phobos-vantage point configurations, but if the vantage point is placed outside the equatorial plane the ENA flux from Phobos is not detectable. This latter fact suggests a way to make the measurement of Q.

The polar orbit of MEX crosses the equatorial plane at approximately right angles. While approaching Phobos, its period is roughly the same as Phobos' one (7 hours). Even if the torus virtually extends to infinity, the region where O density is noticeable is very thin, i.e. less than 200 km. Hence, ASPERA-3 will be at a "good" vantage point position only for one or two minutes. During this time, the ENA image detected from NPI should be similar to the superposition of figures **4.5** and **4.8**. The result is shown in figure **4.9**. Just before (or just after) this crossing, the ENA image should be the one of figure **4.5**. The difference between those images is the ENA flux coming from Phobos' torus. Since this flux is simply proportional to the O neutral density n_o, a rough estimation of Q is possible.

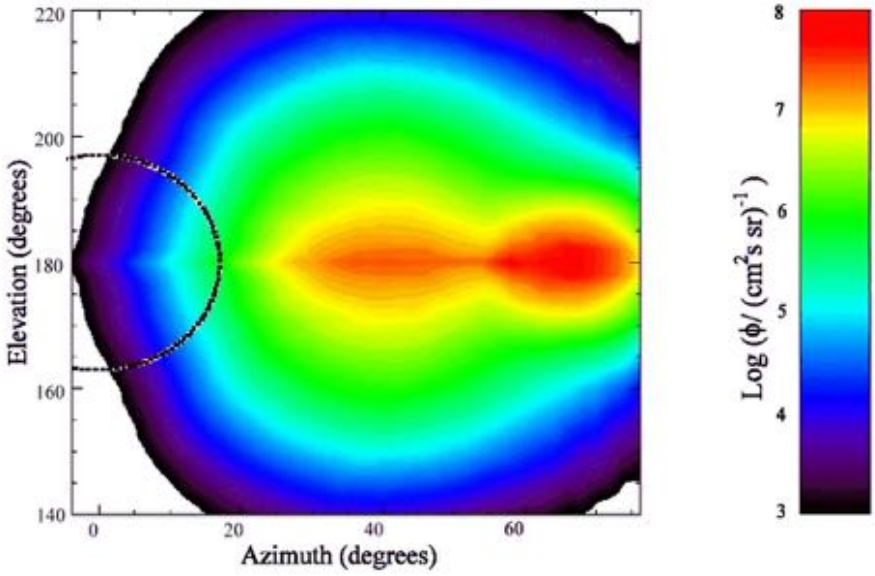

Figure 4.8 ENA image simulation: same as **4.5**, if only Phobos torus-halo was present.

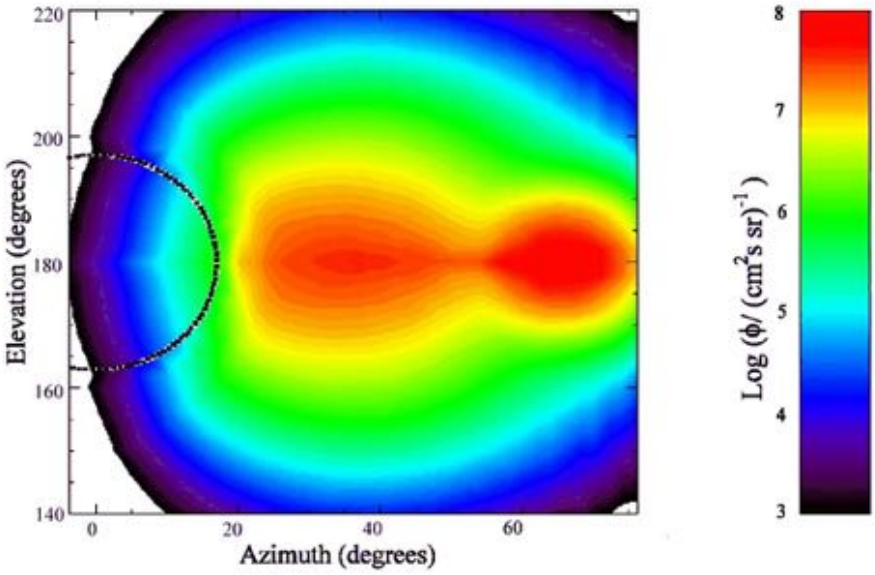

Figure 4.9 ENA image simulation: overall ENA image resulting from the superposition of ENA images in figures **4.5** and **4.8.**

The very short time scale should guarantee that the external conditions do not change. In any case, this can be verified by comparing the ENA image just before with the one just after the encounter. According to my simulation, the angular resolution of NPI (4.6° × 11.5°) should be good enough to resolve the thin signal in the equatorial plane.

In conclusion, the presence of a neutral population originated from Phobos induces an

extra ENA signal that should be detectable. In the considered configuration, this allows the estimation of the outgassing rate Q, but only if Q is equal or greater than 10^{23} s^{-1}. Since I have used the most favourable conditions (vantage point/Phobos configuration), it is not realistic to imagine the detection of a smaller rate. Anyhow, this consideration does not affect the feasibility of this measure. In fact, disturbances on PHOBOS-2 data can be explained by outgassing only if $Q \geq 10^{23}$ s^{-1}. If this last hypothesis is right, NPI sensor will detect some extra signal/disturbance during MEX-Phobos approach, and Q will be estimated in detail.

4.5 ASPERA-3 Instruments

During my thesis, I actively participated to the development of the ASPERA-3 experiment (Analyser of Space Plasmas and EneRgetic Atoms). More particularly, I was responsible for the development of both data display and real-time analysis software (DDU, Data Display Unit). The scientific instrumentation (figure **4.10**), part of the MEX payload, includes both ion and electron sensors, and two different neutral analysers: NPI (Neutral Particle Imager) and NPD (Neutral Particle Detector). Here I

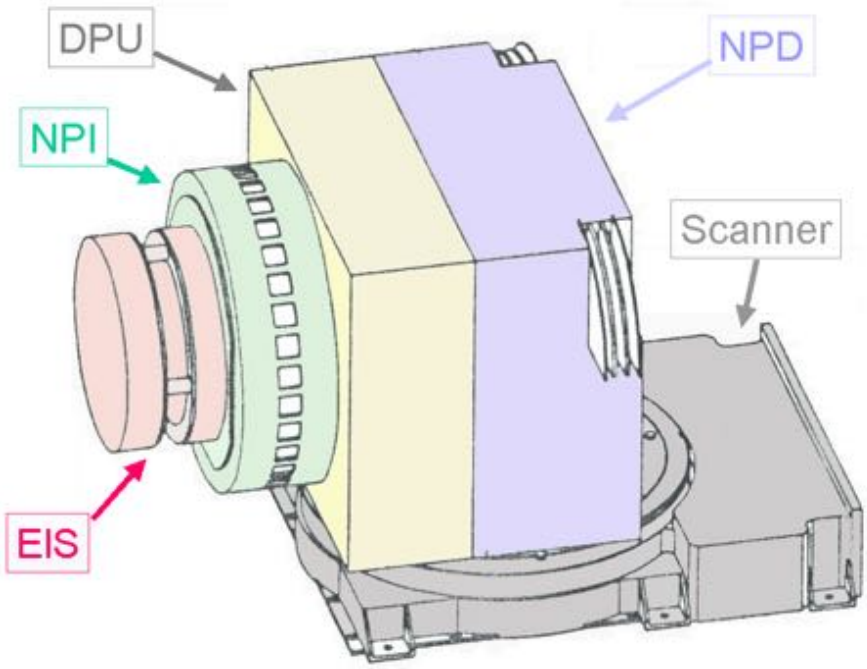

Figure 4.10 ASPERA-3 Layout.

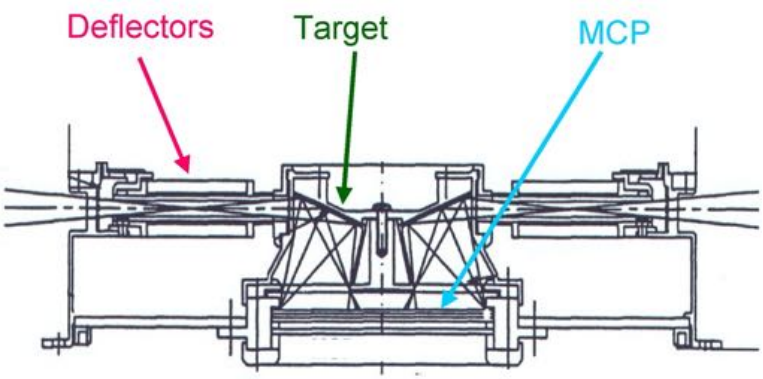

Figure 4.11 NPI scheme.

will briefly resume some concepts about these two last instruments.

NPI is substantially an imager. It has neither energy nor mass resolution, but good angular resolution. It is placed over a rotating platform, in order to perform a 3D full exploration. It has a cylindrical shape, with symmetry axis at right angles to the rotation axis. Figure **4.11** is a section of the instrument in a plane containing the symmetry axis, showing two of the 32 sectors of the instrument.

The sensor head is provided with electrostatic deflection plates, which remove the incoming ions. The neutrals are allowed to hit a 32-faced target. The sputtered particles produced by the collision, and/or the reflected neutral, can hit the micro channel plate (MCP) below. The MCP, with 32 anodes revealing which sector has been crossed, operates in negative-bias mode, and hence can accept all projectiles except electrons. The UV entering the instrument are suppressed by using a resin-based graphite-dispersion target. A summary of the instrument characteristics is given in table **4.1**.

Table 4.1

Energy Range	0.1 – 60 KeV
Angular Resolution	4.6° x 11.5°
Azimuthal sectors	32
Geometrical factor	2.5 10^2 cm^2 sr
Efficiency	~1%
Power	0.8 W
Mass	0.7 kg

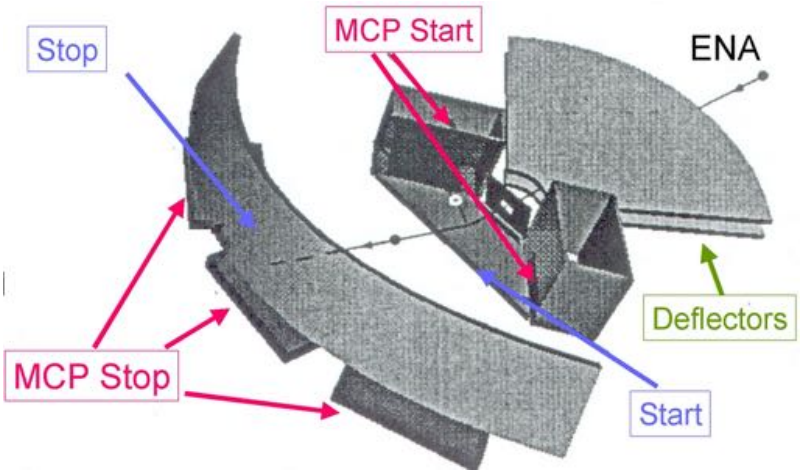

Figure 4.12 NPD scheme.

NPD is substantially a mass and energy spectrometer, with poor angular resolution (~30°). Two NPD units are included in ASPERA-3, and placed over the rotating platform looking at opposite directions. Detecting the energy or the mass of a neutral implies that this neutral must be perturbed somehow (this consideration has a very important exception: see section **5.10**). In general, this happens either forcing it to cross a very thin carbon foil (as for MH-ENA, section **3.4**), or deflecting it by an ionising surface at very low grazing angles. The ionisation through a carbon foil is not suitable for low energy neutrals; hence, NPD uses the surface-scattering technique. Particles are not necessary ionised; upon their scattering on the surface some electrons are released and the detection of the latters makes the start of a ToF measurement. Figure **4.12** shows a 3D view of the instrument.

After the deflection plates, similar to those of NPI, the neutrals hit a graphite surface.

Table 4.2

Energy Range	100ev – 10 KeV
Energy Resolution	16 step
Azimuthal sectors	3
Efficiency	~1%-50%
Power	1.5 W
Mass	1.8 kg

The result of this collision is the ejections of some electrons, which are collected on two start-MCPs using appropriate electric field. The electrons detection gives the start time. After the collision, the particle (sometimes ionised) is scattered and proceed until it reaches a stop target. The electrons ejected are collected over stop-MCP to give the stop time. The time-of-flight measurement gives the particle velocity, while the number of collected stop-electrons roughly gives the particle energy, and then the masses. Table **4.2** gives a summary of NPD characteristics.

4.6 ASPERA-3 First image

During ASPERA-3 development, I have been responsible of the Data Display Unit (DDU), under the direction of Dr. Stefano Orsini. After MEX launch (June 2, 2003) the instrument has been switched-on to perform some on-flight calibrations and tests. I have actively participated to these operations, and DDU s/w has been used extensively. In particular, some data have been collected during a changing in the satellite attitude. Figure **4.13** shows the DDU control panel and the NPI data collected between 18:00 and 21:20 July 9, 2003. The deflection voltage was off, i.e. most of the detected particles

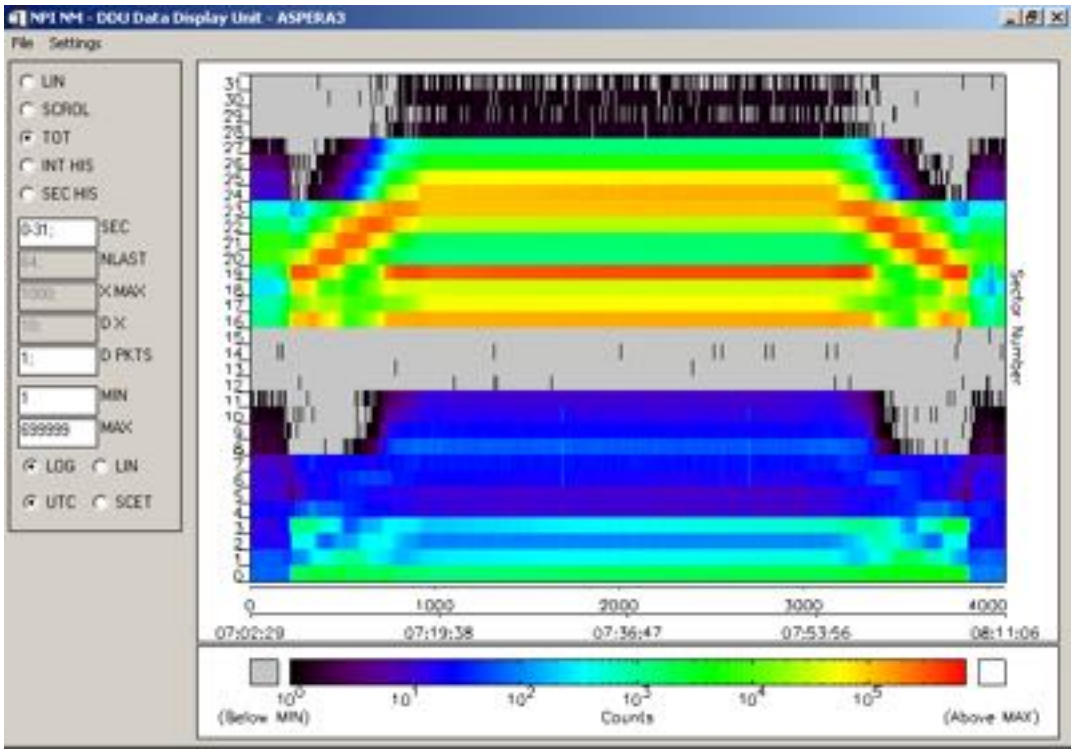

Figure 4.13 DDU monitor with first ENA data. On *y* axis: sectors. On *x* axis: time. Colours are coded according to count rate.

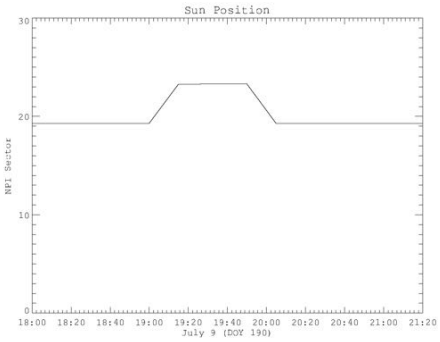

Figure 4.14 Position of the Sun direction respect to sectors of NPI, function of time, in the same period as in figure **4.12** (from ***K.*** *Jonsson,* private communication).

were solar wind ions. Figure **4.14** shows, for the same time interval, the Sun's position within the NPI sectors. The movement of the Sun's signal across sectors from 19 to 26 clearly shows that all those sectors are working fine. Conversely, is it not clear why sector 16 is counting particles, since it should be artificially blocked.

After a six months' flight, Mars Express is going to be inserted into an orbit around Mars. The ASPERA instrument is about to collect and send us the first ENA data of Mars' environment.

5. Mercury and the ESA mission Bepi Colombo.

In this part of the thesis, I will discuss about general features of ENA imaging at Mercury. I will first consider the present knowledge of Mercury's environment (**5.1**); then I will introduce the models of Mercury's magnetosphere, exosphere and surface composition adopted for further calculations (**5.2**). In section **5.3** I will present a preliminary simulation of Mercury's equatorial proton circulation, and discuss about the existence of a ring current at Mercury. In sections **5.4** and **5.5**, a general model of proton circulation in all Hermean magnetosphere will be developed, and its results will be applied to ion-sputtering and exospheric profile simulations (**5.6**), and ENA emission simulations (**5.7**). The feasibility of neutral atom imaging will be also discussed (**5.8**), as well as the related instrument requirements (**5.9**). This study includes also a published paper (*Paper* **IV**) and a submitted one (*Paper* **V**).

The importance of this study will been enhanced, however, if we consider that the future Bepi Colombo mission to Mercury will probably include a Neutral Particle Analyser (NPA-SERENA), led by Dr. Orsini and his SERENA group at IFSI. The ESA planning of this mission has induced a big effort by the international community to produce

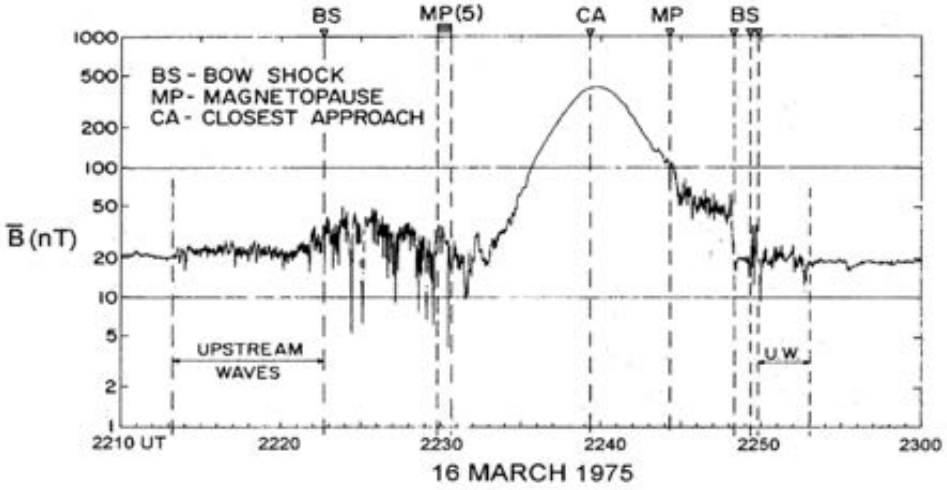

Figure 5.1 Magnetic field profile inside Mercury's magnetosphere as measured by Mariner 10 in March 1975.

simulations and feasibility studies. This chapter resumes my personal contribution to such an effort. Actually, it may be assumed as one of the main results of my thesis, especially because it provided a major support to the selection of SERENA.

5.1 Mercury's Environment

Prelude. Why looking at Mercury? The Hermean environment is from almost all angles very different to the Earth's one. Its small distance from the Sun makes surface temperature and daily excursion extremely high; the eccentricity of its orbit causes a high variability in the solar wind conditions at Mercury; the absence of an atmosphere and the weakness of the intrinsic magnetic field result in a peculiar magnetospheric behaviour. These extreme conditions make Mercury a unique case in the solar system: Mercury can be referred to as a "laboratory planet", and all scientific results obtained at Mercury can be applied, even if not transferred, to the Earth.

Mercury's magnetosphere. The Hermean magnetosphere was an almost complete mystery until 1974, when the first spacecraft to approach Mercury, Mariner 10, revealed the existence of an intrinsic magnetic field (see figure **5.1)**. The magnetic field

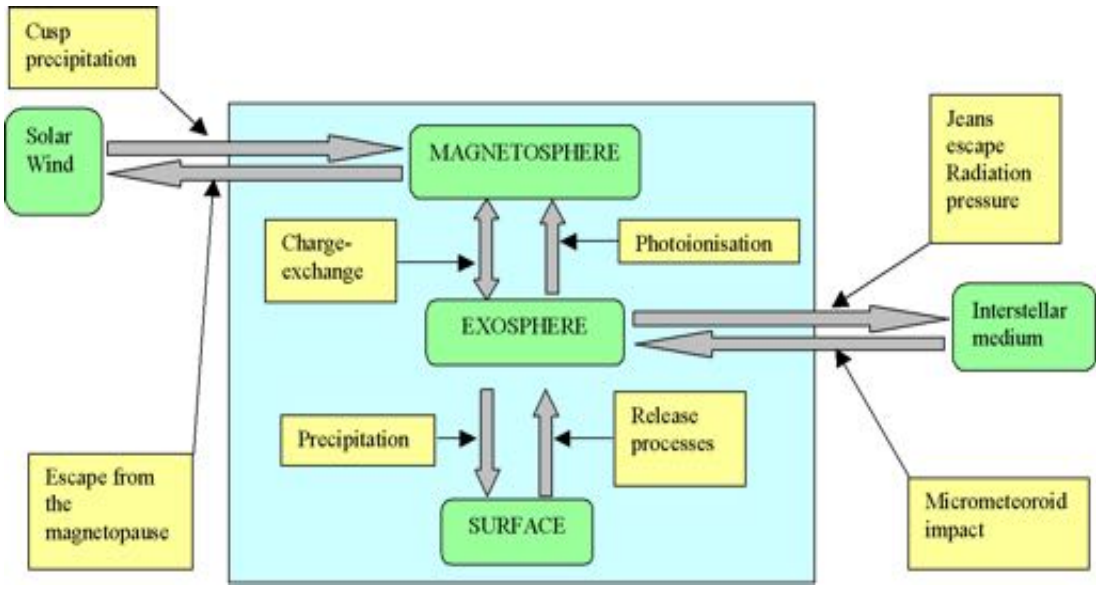

Figure 5.2 Block diagram showing main exchange processes in Mercury's environment. [*A. Milillo,* private communication, *2003*].

estimation has large uncertainty, because it is difficulty to separate the internal and external magnetic field components [*Connerney and Ness*, 1988]. Nevertheless, the dipole moment is probably between 284 and 358 nT R_M^3 [*Ness et al*., 1975], pointing approximately 10° from the South Pole. For reference, the Earth's dipole is approximately 3×10^4 nT R_E^3.

Peculiarities in Mercury's magnetosphere arise also from the extreme conditions of the solar wind at Mercury's orbit (0.3÷0.44 AU), which differs substantially from the average conditions present at 1 AU. Parker spiral forms an angle of about 20° with the solar wind radial direction, while it is approximately 45° at the Earth. This implies a change of the relative ratio of the IMF components with respect to the near Earth conditions, and a modified solar wind-magnetosphere relationship. The average solar wind density is about ten times higher than at the Earth, and this value varies considerably due to the high eccentricity of the orbit of the planet, going from 34 cm^{-3} at the aphelion (0.44 AU), to 83 cm^{-3} at the perihelion (0.29 AU). Solar wind speed is approximately 430 km/s, and the dynamic pressure is, on average, 16 nPa.

Applying all above parameters, it has been estimated that the sub-solar point, where the internal and external pressures balance together, is at the distance of 1.5÷1.7 R_M from Mercury's centre [*Siscoe and Cristofer*, 1975; *Goldstein et al*., 1981], while at the Earth this point is located at 11 R_E. This latter consideration may be applied while trying to simulate the Hermean magnetosphere with a scaled model of the Earth's one (see section **5.2**): with respect to magnetospheric dimensions, Mercury appears to be seven times bigger than the Earth. This scale factor has many important implications, for example, in the development of a ring current around the planet. In fact, at the Earth, this current develops at ~ 5 R_E, which corresponds to ~ .7 R_M at Mercury, i.e. below the planetary surface. Hence, the injecting ions from the tail fall down to the planet before a complete revolution. This feature will be better discussed in section **5.3.**

Last but not least, a smaller spatial scale implies a smaller time scale at Mercury. Magnetospheric processes are ten times shorter than at the Earth (few minutes instead of approximately 1 hour) [*Siscoe et al*., 1975], and they are highly conditioned by the solar wind parameters [*Luhmann et al*., 1998].

Plasma sources. The origin of a hermean magnetospheric ion can be essentially either interplanetary (solar wind) or planetary (exospheric thermal ions). Both these sources are located in the dayside.

Solar wind plasma can enter the magnetosphere when magnetic reconnection occurs between IMF and Mercury's intrinsic **B** field [*Luhmann et al.,* 1998; *Killen et al.,* 2001]. Massetti *et al*. [*Paper* **IV**] have estimated that about one half of the magnetosheath ions that lie on reconnected field lines actually crosses the magnetopause, while the remaining part is reflected by the boundary. The ions entering the magnetosphere may either reach the planet surface, causing ion sputtering; or be diffused toward closed field lines and start circulating; or exchange their charge with the thermal exospheric atoms (see section **2.1**), thus producing a H-ENA signal in the keV range. The small inclination of Parker's spiral causes the contribution of the IMF B_y component to be less relevant than at the Earth, and the magnetic reconnection at the dayside magnetopause is essentially driven by the IMF B_z component. Moreover, the increasing weight of the IMF B_x component might play a role in the way Mercury's magnetosphere links with the solar wind [e.g. *Sarantos et al.,* 2001, *Killen et al.*, 2001, *Kallio and Janhunen*, 2003]. The three panels of figure **5,** *Paper* **IV,** show position, extension of the open field lines area, and energy distribution mapped on the northern dayside surface of Mercury in response to different solar wind conditions.

The ions of planetary origin at Mercury may come both from the photo-ionised exospheric gas and from the ionised component of ion-sputtering product. The ion-sputtering is the dominant source in the area where solar wind precipitates. Those ions have generally an initial energy up to some eV, depending both on the process involved in the generation of the exosphere and on the photo-ionisation efficiency. Once extracted, they are trapped by the magnetic field and start to circulate within the magnetosphere.

Mercury's Exosphere. The UV spectroscopic observations on Mariner-10 and ground based observations of the gaseous envelope of Mercury established the presence of H, He, O, Na, K and Ca [*Killen and Ip*, 1999; *Morgan and Killen,* 1997; *Bida et al*., 2000]. Moreover, other volatile constituents such as H_2, N_2, O_2, H_2 and CO_2 are expected [*Wurz and Lammer,* 2003]. All those species, together, do not establish an atmosphere, having too small a column density. The gaseous envelope of Mercury is hence uncollisional, and gas atoms interact mainly with the surface and with magnetospheric plasma. A schematic summary of the refill and loss processes is shown in figure **5.2**.

The main exospheric sources are due to release processes of atoms from the surface. The released particle energy depends on the process involved. Photon stimulated desorption (PSD), thermal evaporation and micrometeoroid impact produce low energy

(few eV) particles. Ion-sputtered neutrals reach higher energies (see equation **2.10**). Among the emitted atoms, some are gravitationally bound, and fall back onto the surface; the others (especially the sputtered ones) have enough energy to escape from the exosphere. The major exospheric losses are photo-ionisation, especially in the dayside hemisphere, recombination with the soil and Jeans escape.

Another process involving exospheric neutrals is charge-exchange. This process, however, is numerically less important; it produces high-energy neutrals that escape from the exosphere very fast, and replaces them with thermal ions.

Final considerations. Given previous argumentations, Mercury's magnetosphere has sometimes been referred to as a "pocket magnetosphere". The occurring processes are simpler than at the Earth. The whole Mercury environment/system, from the point of view of a space scientist, may be schematised as magnetosphere + exosphere + surface. The lack of knowledge about Mercury, hence, is due mostly to the lack of data, more than to the complexity of the related physics. If we look at the future, we expect to have much more data after the NASA and ESA missions Messenger and Bepi Colombo.

5.2 Adopted models

Magnetic field model. Since most of the magnetic field features are uncertain, with the exception of the mean dipole moment (see section **5.1**), in this study I have tried to reconstruct the magnetic field around Mercury using two different approaches. First, I started with a pure dipole (M=300 nT R_M^3), limited by a parabolic magnetopause in the dayside hemisphere (an ellipsoid: subsolar point at x=1.7 R_M).

This model has been used in the preliminary study of the equatorial circulation (see section **5.3**), but since it cannot reconstruct most of the magnetospheric features (such as open field lines, for example) it has been discarded in the following of the study (sections **5.4-5.7**). Subsequently, in order to model the dayside proton circulation (section **5.4**), I have modified a T96 Tsyganenko model, according to the study of *Massetti et al.* [*Tsyganenko*, 1996; *Paper* **IV**]. The use of such a complex model introduces the difficulty of having several parameters to guess. Its main features are: i) defined realistic magnetopause; ii) large-scale Region 1 and 2 Birkeland current systems; iii) IMF penetration across the magnetospheric boundary [*Tsyganenko,* 1996]. It accepts both IMF B_y and B_z as independent input parameters.

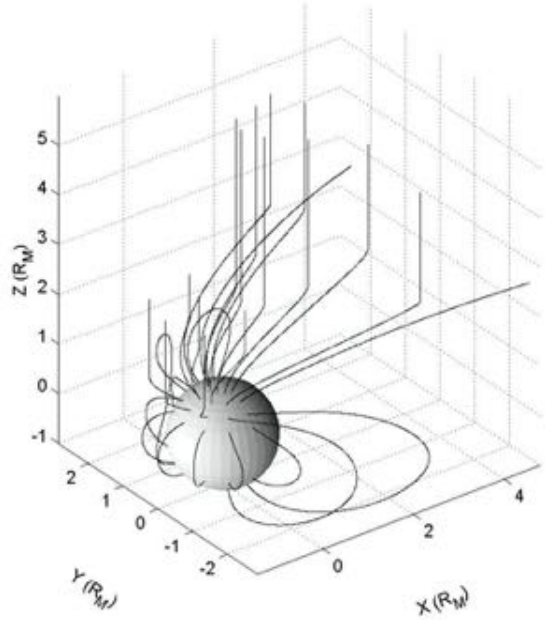

Figure 5.3 Magnetic field as simulated by the model in the *reference* conditions (see section **5.2**).

First of all, to take into account the differences between both the intensities of the magnetic fields and the radii of Mercury and the Earth, I have divided every space constants in the T96 model by a factor 6.9, like in previous analyses based on the Mariner 10 data [e.g., *Siscoe et al.* 1975, *Luhmann et al*. 1998]. Then, I have removed from the model the contribution of the ring current, because the presence of this structure in the magnetosphere of Mercury is uncertain; a more detailed discussion of this feature will be reported in section **5.3**. I have also assumed a 50% contribution of Birkeland's currents in the T96 model, which is a halfway position between the Earth's case and a null contribution. In fact, due to the expected lack of a conducting ionosphere on Mercury, there is still a wide debate regarding the existence of field-aligned currents [*Slavin et al*., 1997].

Finally, it must be noted that: i) this model does not describe the field depression caused by the diamagnetic effect of the plasma engulfing the magnetospheric cusps; ii) it is not possible to introduce a non-zero x component of IMF magnetic field; iii) the model is stationary, and hence it cannot take into account particle acceleration due to magnetic field line drag.

As a *reference* configuration, here I assume $\mathbf{B_{IMF}}$**= (**0, 0, -20) nT, which can be considered as reasonable values [*Paper* **IV**], if we discard the B_x component. Other

configurations of the magnetosphere have been considered by changing some of the IMF components (B_y= ±5 nT and B_z= -10 nT), in order to study the plasma circulation dependence on the above-mentioned parameters. Figure **5.3** shows the magnetic field lines in the *reference* conditions.

Electric field model. At very early stages of this study (section **5.3**), I have approximated the electric field with a simple stationary and uniform one, in the dawn to dusk direction (*y* axis), and with different absolute values in the range 0.1-10 mV/m, which seems to be a reasonable range for |**E**| in the hermean magnetosphere (see below). Then, this field has been modified by supposing the surface of Mercury to be, alternatively, both conductive and non-conductive, as there is still some controversy about this feature. This model of electric field has been used in the preliminary study of the equatorial circulation (see section **5.3**), but since it was not consistent with the magnetic field one it has been discarded in the following of the study (sections **5.4-5.7**).

It is possible to develop a model for the electric field taking into account the magnetic field one. In fact, with the assumption:

$$\mathbf{E} \times \mathbf{B} = 0, \qquad (\mathbf{5.1})$$

$V(\mathbf{r})$ in an arbitrary point of space can be calculated following the **B** field line as far as it reaches any region where $V(\mathbf{r})$ is well known, and **E** is calculated from V. Following the study of *Delcourt et al*, [2003] here I have assumed, as a zero order hypothesis, that the potential at the surface of Mercury is similar to the Volland [*Volland,* 1978] potential at the ionosphere of the Earth. Using appropriate solar wind parameters, and taking into account the smaller size of Mercury's magnetospheric cavity with respect to the Earth's one, we can estimate a cross-polar cap potential drop (*PD*) between 10 and 100 kV [*Delcourt et al.,* 2003]. Willing to test the particle trajectories under different conditions, here I use *PD* = 10 kV as "*reference*" condition [*Ogilvie et al.* 1977], *PD* = 100 kV as "*high PD*" condition and the less realistic value of 1 KV as "*extremely low PD*" condition. This last value intentionally reduces the influence of **E**, and can be also used to evaluate the importance of **E** in the reconstruction of the proton circulation.

The mean electric field in the central magnetotail is, in these three cases, equal to 1, 10 and 0.1 mV/m respectively.

Exosphere model. As mentioned before, the exospheric components may come from several sources. My model includes only those species that have a significant CE cross-section in the case of proton projectiles, i.e. H, H_2, He and O. According to *Wurz and Lammer* [2003], H, H_2 and He may come from thermal emission as well as from

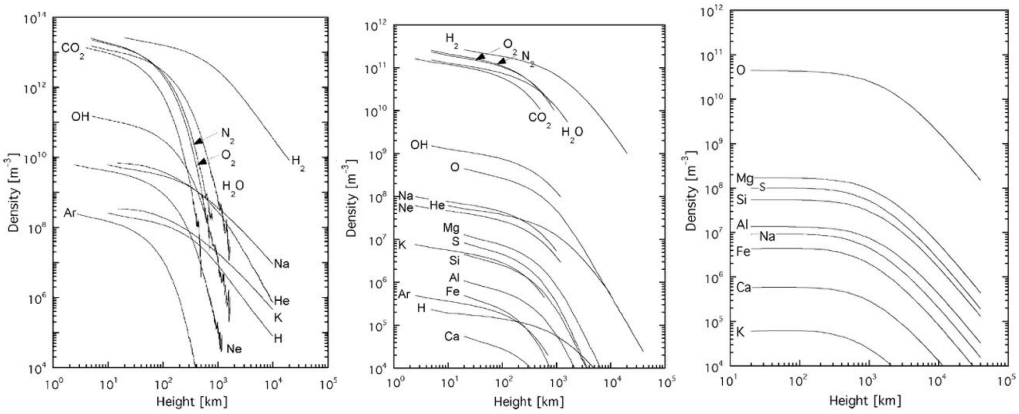

Figure 5.4 Exospheric density vertical profiles at Mercury (dayside) for different components. From *Wurz and Lammer* [2003].

micrometeorite impacts; their density vertical profiles are shown in figure **5.4.** It is worth noting that H_2 density has been depleted as indicated by authors. Oxygen is supposed to be produced substantially from ion-sputtering [*Wurz and Lammer,* 2003]. In this latter case, the process is included in the dayside proton circulation model (section **5.4**). Hence, I have estimated the O vertical profile, and compared the result with experimental estimations. The vertical profile for O is discussed in section **5.6** and shown in figure **5.4**. Exceptionally, also ion-sputtered Sodium has been considered as an exospheric constituent, and its vertical profile has been simulated (section **5.6**). Even if it has no implications with CE, due to its low cross-section, this element may be considered as an important tracer of Mercury exospheric behaviour [*Killen et al*., 1990] since it can be observed from the Earth.

Surface Model. The surface model includes only Oxygen and Sodium. Even if there are some discrepancies among authors on the binding energies of these two species, theoretical computations suggest that the binding energies of Oxygen and Sodium are respectively 2 eV [*McGrath et al*., 1986; *Cheng et al*., 1987] and 3-4 eV [*Lammer and Bauer,* 1997], and these values have been used in the following of my study. Other authors [*Weins et al*., 1997], after having measured that the empirical distribution of Na particles sputtered from a Na_2SO_4 surface (pressed powder sample) peaks at 1.5 km/s, have deduced lower values (.54 eV) for the related binding energy. If those empirical measures were found correct, and considering that the lower is E_b the less is the function F at energies well above E_b, the sputtering flux calculated in the following should be reduced of a factor 10 approximately. In section **5.6** I will discuss the implications of the sputtering process for the exospheric abundance of Na and O.

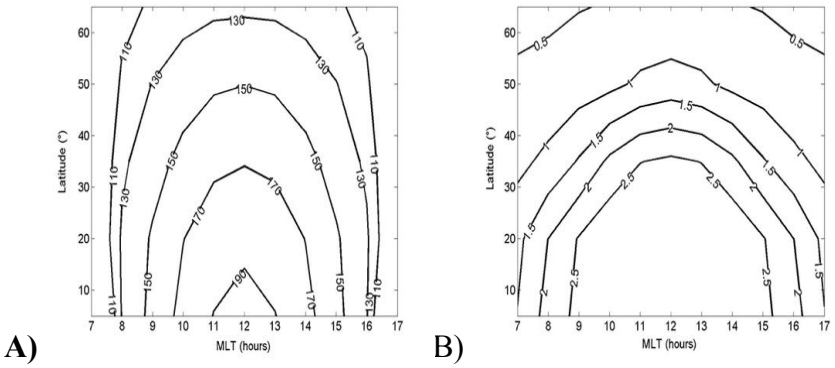

Figure 5.5 Panel **A):** Lines of equal H^+ density at the magnetopause, in the MLT versus Latitude plane. Panel **B):** same as **A**), with lines of equal H^+ mean energy at the magnetopause.

Proton source. In my simulation I start tracking the protons as they cross the magnetopause (MP), entering the magnetosphere from the magnetosheath. In this latter region the protons of solar wind origin are decelerated, compressed and heated. The H^+ density exhibits a bulk in the subsolar region; as the protons move tailward along the flanks of the magnetosphere, their velocity grows and their temperature and density decrease.

In agreement with the T96 model, I have approximated the dayside magnetopause with an ellipsoid, and all test particle trajectories start from this surface. According to this model, the distance between the surface of Mercury and the magnetopause at the subsolar point is approximately 0.5 R_M.

Proton mean energy and density functions over this surface have been derived from the work of *Spreiter et al.* [1966], and adapted to the case of Mercury [*Paper* **IV**]. Figure **5.5** shows contours of H^+ density and mean energy on the MP surface, in a MLT vs. geographic latitude reference system.

It should be noted that the mean proton energy peaks near the subsolar point, whereas the proton group velocity increases while they move away from it, as they are dragged together with the frozen-in IMF. Here we consider the energy of those protons in the reference system of the magnetic field lines, since the magnetic field is steady in our model. Hence, the energy we use as initial condition for our test particle reaches its maximum near the subsolar point, where the proton acceleration due to magnetic reconnection is higher [*Paper* **IV**].

It may be useful to estimate the total H^+ flux impacting the MP of Mercury, as predicted

by the model, in order to have a reference value when discussing the proton precipitation on the planetary surface. Integrating the data shown in figure **5.5** over all the MP, a total flux between 2 and 3×10^{27} s^{-1} is found. It is worth noting that this value, as well as the distribution of protons over MP and the shape of the MP itself, depend on the external conditions, such as the SW velocity and density. However, in this model I use a fixed source. A change in the unperturbed SW density reflects linearly upon the estimated magnetospheric H^+ density, and can be included by applying a simple proportion; the change of the MP shape has been neglected for simplicity.

5.3 Equatorial proton circulation at Mercury: a partial ring current?

The main purpose of this study is modelling the proton precipitation in the cusp regions, and the subsequent dayside circulation. Before doing this, one question must be answered: is the tail sunward convection capable to feed the equatorial plasma circulation? Most of the authors [O*rsini et al*., 2001; *Lukyanov et al.,* 2001] suggest that this process, if present, cannot turn-on a steady ring current or even a partial ring current. In fact, as mentioned before, the dimension of the planet, if compared to its magnetosphere, is too big to let room enough for a ring current. To better validate this hypothesis I have run an extremely simple model, based on the guiding centre approximation and on the continuity equation. The simulation considers only the protons circulating in the night-side equatorial plane (r,φ) of Mercury and with a 90° pitch angle. To demonstrate the absence of a stable ring current there is no need of a whole 3-dimensional simulation. In fact, the particles that have 90° PA and populate the equator experience, in general, fewer losses with respect to those particles that have different PA. These latter particles, actually, get closer to the planet at their mirroring points, where CE is more efficient and planetary impacts are more probable.

The guiding centre (GC) approximation supposes that the proton trajectories come from the superimposition of two motions: a circular motion around the guiding centre, due to Lorenz force, and the drift of the guiding centre itself. Hence, on the average, a particle moves only if its GC does, and this may happen either if there is an electric field ("**E**×**B** drift") or if the magnetic field is non-homogeneous ("**B**-gradient drift" and "**B**-curvature drift"). In principle, this approximation is valid if the GC drift velocity may be neglected if compared to the velocity of the particle itself. As I will discuss in detail later, this assumption is not valid in the whole space around Mercury. However, in the

equatorial plane this assumption is generally reasonable: a preliminary estimation of the error indicates that the discrepancy between the GC path and the real path is less than 10% of the path length. For the purpose of this preliminary study, this approximation is hence acceptable.

Since protons are treated as a fluid, we have the continuity law:

$$\frac{dn_{H+}}{dt} + \nabla\left(n_{H+}\,\mathbf{u}\right) = F - S, \qquad \textbf{(5.2)}$$

where n_{H+} and **u** are respectively the proton density and velocity, while F and S are two functions for the proton sources and sinks. Here, this equation must be applied to a 3 dimensional space: r and φ are the polar coordinates of the GC of the protons in the equatorial plane; K is the kinetic energy of the protons themselves. The first two components (u_r and u_φ) of the velocity **u** are given by the **E**×**B** plus the **B**-gradient drift, using electric and magnetic models described in section **5.2**. The third component of the velocity (u_k) can be estimated considering that, as a zero order hypothesis, only the electric field is able to change the kinetic energy of the particle. Hence, we have:

$$u_k = \frac{dK}{dt} = \frac{dK}{dx}\frac{dx}{dt} + \frac{dK}{dy}\frac{dy}{dt} = E_x u_x + E_y u_y. \qquad \textbf{(5.3)}$$

In our case, the function F for the sources is assumed to be zero everywhere except at instant $t=0$, when an arbitrary source has been considered. In fact, since we want to demonstrate the impossibility of a stable circulation in the equatorial regions of Mercury, it is sufficient to suppose some a-priori extended distribution in the tail. If this source leads to a rapid disappearing of protons, then all possible sources do the same. The $n_{H+}(0)$ function used here is a simple gaussian function in the three dimensions r, φ, K.

The function S for the sinks is calculated taking into account charge exchange and collisions with the planet. Charge-exchange losses have been estimated using neutral density of H, He and O given by *Wurz and Lammer* [2003], and relative cross-sections (figure **5.4**). As far as it concerns the planetary collisions, I have adopted an *ad hoc* function *dp* representing the probability for a proton to hit the surface after each integration step *dt*. In fact, GC method approximates the trajectory of a particle with a drifting circle or radius equal to Larmor radius (R_L). Hence, a particle close to the planetary surface may have part of this circle inside the planet. Function *dp* is proportional to the particle velocity v and inversely proportional to R_L:

$$dp = \begin{cases} 0 & r > (R_M + R_L) \\ \dfrac{v\,dt}{2\pi R_L} & R_M < r < (R_M + R_L) \\ 1 & r < R_M \end{cases} \qquad \textbf{(5.4)}$$

Equation **5.2** has been solved numerically. To have a good accuracy, the integration step *dt* and the grid sizes (Δr, $\Delta\varphi$, ΔK) must satisfy the relation:

$$dt << \min\left(\frac{v_r}{\Delta r}; \frac{v_\varphi}{\Delta\varphi}; \frac{v_K}{\Delta K}\right) \qquad \textbf{(5.5)}$$

in every point of the grid. A good compromise between machine-time consumption and accuracy has been found using a grid of 50×50×50 bins and dt=10^{-2} s.

Figure **5.6** shows an example of the evolution of the H^+ population, in the case of Tsyganenko modified **B** model and with a "conductive" planetary surface. The mean **E** field in this case is 1 mV/m. Protons move sunward under the **E×B** drift and then clockwise around the planet under the **B**-grad drift, depending on their energy. In fact, this latter drift is energy-dependent, and after a while the higher energy protons will

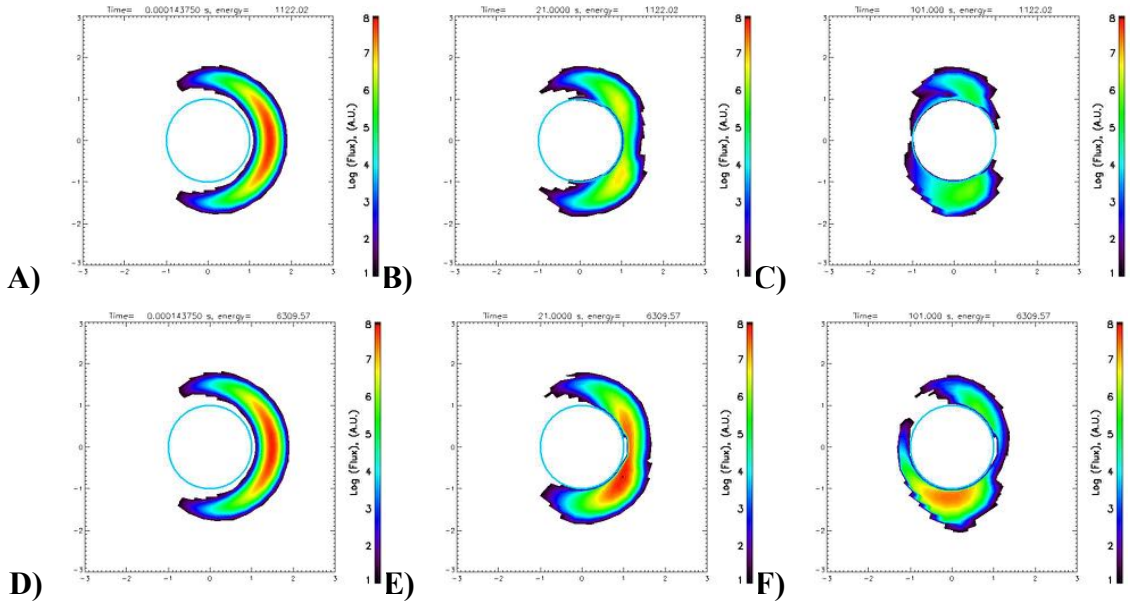

Figure 5.6 Equatorial H^+ flux as simulated using the continuity equation and guiding centre approximation and an arbitrary source. Panels **A, B, C**: H^+ Flux @ 1 keV, respectively after 0, 20, 100 s. from the injection; panels **D, E, F**: H^+ Flux @ 5 keV, after 0, 20, 100 s from injection. Colour is coded according to H^+ flux using an arbitrary scale.

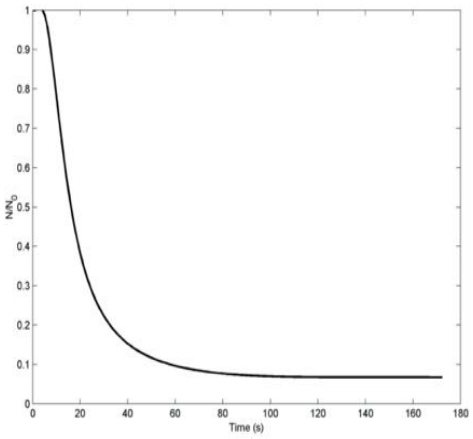

Figure 5.7 Relative abundance of protons in the equatorial plane of Mercury, as a function of time elapsed since injection, respect to proton abundance at t=0. The H^+ distribution at is arbitrary.

concentrate in the dusk side. This feature is similar to what happens at the Earth, and has been already discussed. It is worth noting that, for all other possible external configurations, the time evolutions of protons are very similar to this one.

I have run similar simulations with different external configurations, starting with the "dipole **B** + uniform **E**" configuration described in section **5.2** and then using the "Tsyganenko **B** + Volland **E** " one. In all cases, no ring current or partial ring current has ever been able to form. The CE and the planetary collisions rapidly remove the protons from the magnetosphere. In figure **5.7** I show the relative intensity of the proton flux (@ 90° PA) versus the elapsed time, in the same case as figure **5.6**.

As a matter of fact, even if some short-time proton circulation is possible in the night side, it will hardly extend to the dayside. A stable circulation of protons around Mercury is extremely difficult, and a complete and stable ring current is not able to form. This latter consideration is important also while reconstructing the **B** field by means of a Tsyganenko model (see section **5.2**).

5.4 Dayside proton circulation at Mercury: model description

Simulation of H^+. To obtain a full spatial, pitch angle and energy distribution of the protons in the magnetosphere of Mercury I have used a Monte-Carlo (MC) single-particle model. I have simulated the trajectories of a large number of protons (hereafter

called "test particles") by solving the full equation of motion (including electromagnetic and gravitational forces). In fact, Larmor's radius of protons in the energy range I am analysing (approx. 0.1÷10 keV) is generally not small when compared with the dimension of Mercury magnetosphere. Hence, non-adiabatic effects may become of crucial importance for most of the ion magnetospheric transport [*Delcourt et al.*, 2003], and the use of an adiabatic treatment based on the guiding centre approximation will lead to non-negligible errors when reconstructing H^+ paths in full 3D space around Mercury.

Each test particle trajectory begins at the bow shock of Mercury (see section **2.4**) and finishes if either:

1) the test particle hits the surface of the planet; or

2) the test particle reaches a non-connected IMF field line; or

3) the test particle gets too far from Mercury in the nightside (r>10 R_m).

The H^+ distribution function in space, energy (E) and pitch angle (α) has been reconstructed over a 5-dimensional grid, and it is represented by a matrix N_{ijklm}. The grid extends from 1 to 2 Mercury radii (R_M), 0 to 24 h (MLT), –90° to 90° (latitude), 0° to 180° (pitch angle) and 100 eV to 10 keV (energy); the number of bins for each dimension is respectively 8×48×24×4×4.

In this simulation, each test particle represents a certain number of real protons. If we assume that all those protons were "born" (i.e. they enter the simulation region) from the same point Q on the MP within an infinitesimal surface ΔS_Q, then they all have the same trajectory. We can also imagine that those protons were "born" from ΔS_Q with a fixed frequency $1/\Delta T$. If the H^+ flux at Q is Φ_Q, the time interval between protons is:

$$\Delta T = \frac{1}{\Phi_Q \, \Delta S_Q} \tag{5.6}$$

Since they are equally spaced in time along the trajectory (forming a sort of "train"), the total number of protons N within an arbitrary cell $ijklm$ is simply $T/\Delta T$, where T is the time a proton stays within that cell. This time is the same for both protons and the associated test particle:

$$T = N \, \Delta T = n \, dt \tag{5.7}$$

where dt is the time integration step for the test particle and n is the number of times that, during its trajectory, the associated test particle is inside that cell. It follows that:

$$N = \frac{n\,dt}{\Delta T} = n\left(dt\ \Phi_Q\,\Delta S_Q\right) \qquad \textbf{(5.8)}$$

Hence, after every integration step *dt*, I just have to increase the value of the bin corresponding to its position (N_{ijklm}) of a value w_{H+}:

$$w_{H+} = dt\ \Phi_Q\ \Delta S_Q\ f_{CE}(t)\,. \qquad \textbf{(5.9)}$$

The function f_{CE} takes into account the losses due to charge-exchange with the neutral exosphere of Mercury. This function has been calculated solving numerically the following differential equation:

$$\begin{cases} f_{CE}(0) = 1 \\ \dfrac{df_{CE}}{dt} = |\mathbf{v}|\sum_i \sigma_i\, n_i \end{cases}, \qquad \textbf{(5.10)}$$

where σ_i and n_i are the charge-exchange cross section and the local number density of the i^{th} neutral species (see figure**s 2.2** and **5.4**). The 5-D number density ($\frac{dn_{H+}}{dE\,d\alpha}$) of H^+ in any point of the grid is obtained by dividing the bin value N_{ijklm} by its 5D-volume, while the proton flux Φ_H is simply n_{H+} times $v(E)$. The surface ΔS_Q may be estimated just dividing the total surface where the generation of test particles occurs, by the number of test particles that have been run.

In principle, to perform an accurate numerical integration of the motion, it should be necessary to calculate the electric field for a very large number of points along each trajectory. This procedure, in general, is very expensive in terms of machine-time, because at each point it is necessary to trace the magnetic field line up to the planetary surface (see section **5.2**). To permit the simulation of a large number of test particles, I have preliminarily estimated the electric potential *V* on the vertexes of a three-dimensional cubic grid. The potential in any other point can be calculated via 3-linear interpolation using the eight nearest vertexes. The bin size is 500 km, which leads to an error on the potential, which has been empirically found to be less than 5 ‰. This error may be neglected if compared to other uncertainties in the model.

Simulation of neutral particles. In this model, neutral particle emission is related to ion circulation through two processes: ion-sputtering and charge exchange. In fact, such processes are included in the model as proton losses, and both of them may produce neutral particles. In section **6** and **7** I will present simulated neutral signal coming from both processes.

Sputtering. This process has been discussed in section **2.2**. Here I solved the integral in equation **2.11** in a numerical way. Every time a test-particle hits the surface, it is converted to a test-neutral or a test-ion, with random initial direction. The energy is chosen randomly according to energy distribution in equation **2.10** (see figure **2.2**); the species of the sputtered particle is chosen randomly according to different relative abundances R_k; the weight w in equation **2.11** is multiplied by a factor Y_k. This new test-particle may, of course, hit the surface again: the procedure exposed here is then performed again, as far as its weight is greater than one and its energy is able to produce sputtering ($E_i > E_b$).

In this study I have concentrated my attention to Oxygen and Sodium only. In fact, both O and Na have been observed in the exosphere of Mercury [*Broadfoot at al.,* 1976; *Potter and Morgan,* 1985*,* 1997]. The overall fraction of Oxygen (R_O), if we consider all molecules containing O, may be up to 50% [*Wurz and Lammer*, 2003]. The sodium content of the surface (R_{Na}) has been estimated to be within 0 and 1.4 % [*Goettel*, 1988]; here I have chosen a halfway value, i.e. 0.5%. Yields for those species strongly depend on the molecular structure of the surface; here I have adopted a rough value of 0.1 for both O and Na, since the uncertainty on the surface abundance probably overcomes the error on the yield. It is worth noting that a bad estimation of either Y or R does not affect the estimated vertical profile of the neutral emitted population, but it can be considered as a scale factor for the whole density distribution function of neutrals. More particularly, an overestimation of the O sputtering flux may come from considering the same yield for all surface constituents containing Oxygen.

The surface binding energy, conversely, has a deep impact on the energy spectrum of the particles emitted towards the exosphere. For any $E_i >> E_b$, in fact, it may be shown that $f_S(E_e, E_i)$ peaks approximately at $E_b/2$. Surface binding energies are, generally, of the order of some eV; here I have adopted, respectively, 3.5 eV and 2 eV for O and Na. Some recent studies [e.g. *Weins et al*., 1997] indicate lower values (~.5 eV) for the Na binding energy. Considering that the lower is E_b the less is the function F at energies well above E_b, if this estimation is found correct, the Na flux from ion-sputtering calculated in the following should be reduced of a factor of 10 approximately.

Charge-Exchange. This process has been discussed in section **2.1**. The ENA flux and images have been obtained by using equation **2.9**; cross-sections for H^+ colliding various neutral species (H, H_2, He and O) are shown in figure **2.2**; estimated exospheric densities (from *Wurz and Lammer* [2003]) are shown in figure **5.4**; all processes have

been considered. It is worth noting that the H_2 density has been depleted as suggested by authors. The depletion coefficient here is 0.01, in order to be conservative with the estimation of ENA fluxes.

5.5 Dayside proton circulation at Mercury: results

Here I present the simulation results in terms of H^+ circulation. Six different sets of boundary conditions have been used, and about 3×10^5 test-particles have been tracked for each set. A particular set of boundary conditions, called "*reference*" conditions, is: $\mathbf{B_{IMF}}$=(0, 0, 20) nT, *PD* = 10 kV. Then I have changed PD (1 kV and 100 V), B_y (± 5 nT) and B_z (-10 nT). To reduce the amount of runs, I have not explored all combinations of these values, but just all variations of a single parameter from the "*reference*" one. This must be taken into account in general, since variations of potential drop and $\mathbf{B_{IMF}}$ often occur simultaneously.

To obtain the H^+ number density n_{H+}, the differential number density ($\frac{dn_{H+}}{dE\,d\alpha}$) has been integrated over all pitch angles and over two different energy ranges: 0.1-1 keV and 1-10 keV. Particles outside these two ranges have been discarded.

To help the discussion, I present an overall summary of results (table **5.1)**, sections of H^+ density (figure **5.8**) and maps of H^+ flux on the surface (figure **5.9**). Table **5.1** shows three parameters that synthesize some features of the H^+ flux impacting the surface, i.e. the total flux (F_T), the mean MLT ($\overline{MLT_S}$) and the mean latitude ($\overline{\varphi}_S$). Those parameters have been calculated for different boundary conditions and energy ranges. In particular, the mean position of the H^+ spot on the surface corresponds roughly to the bulk of the emission of the sputtered neutrals, which will be monitored by the NPA-SERENA orbiting sensor; the total flux of H^+ impacting the surface has important implications on the exospheric refilling.

Panels in figure **5.8** show colour-coded sections of the H^+ density distribution. Each panel shows n_{H+} over the superposition of two different surfaces: the one outside the red circle is the *x-z* plane; the one inside the red circle is a hemisphere just above Mercury's surface, in the dawn side. The Sun is on the right. Different panels refer to different external conditions and energy ranges. It is worth noting that panels in figure **5.8** do not show the protons that cross the magnetopause (thus becoming elements of the simulation) in the south hemisphere. In this way, the protons that are found in the

southern hemisphere can be immediately identified as "bouncing protons". To obtain the complete distribution it is sufficient to superimpose this H^+ distribution to another one, which is symmetric to the first with respect to the equatorial plane.

Panels in figure **5.9** show polar-stereographic projections of the H^+ flux on the northern surface of Mercury, colour-coded according to the $\log_{10}$ of the intensity. This flux has been obtained by using the H^+ density distribution function (position, energy and PA), in the cells just above the surface. However, a small error will arise from this procedure because those cells have a height of about 300 km, and even if the **B** field lines can be considered more or less parallel over this short scale, some protons may bounce inside

Table 5.1

Energy Range (keV)	B_y (nT)	B_Z (nT)	P. Drop (V)	Total Flux (10^{25} s^{-1})	Mean MLT (*hh:mm*)	Mean Lat (°)
Total: .1÷10	-5	-20	10^4	18	11:36	44
	0	-10	10^4	16	11:40	48
	0	-20	10^3	27	10:40	37
	0	-20	10^4	19	11:39	44
	0	-20	10^5	5.6	11:38	63
	5	-20	10^4	21	11:28	44
Low Energy: .1÷1	-5	-20	10^4	3.6	11:54	57
	0	-10	10^4	3.3	12:04	60
	0	-20	10^3	4.8	11:53	53
	0	-20	10^4	3.7	11:54	57
	0	-20	10^5	0.94	11:51	67
	5	-20	10^4	3.8	11:50	57
High Energy: 1÷10	-5	-20	10^4	16	11:28	38
	0	-10	10^4	13	11:27	42
	0	-20	10^3	22	10:24	31
	0	-20	10^4	16	11:32	39
	0	-20	10^5	4.7	11:32	60
	5	-20	10^4	17	11:19	38

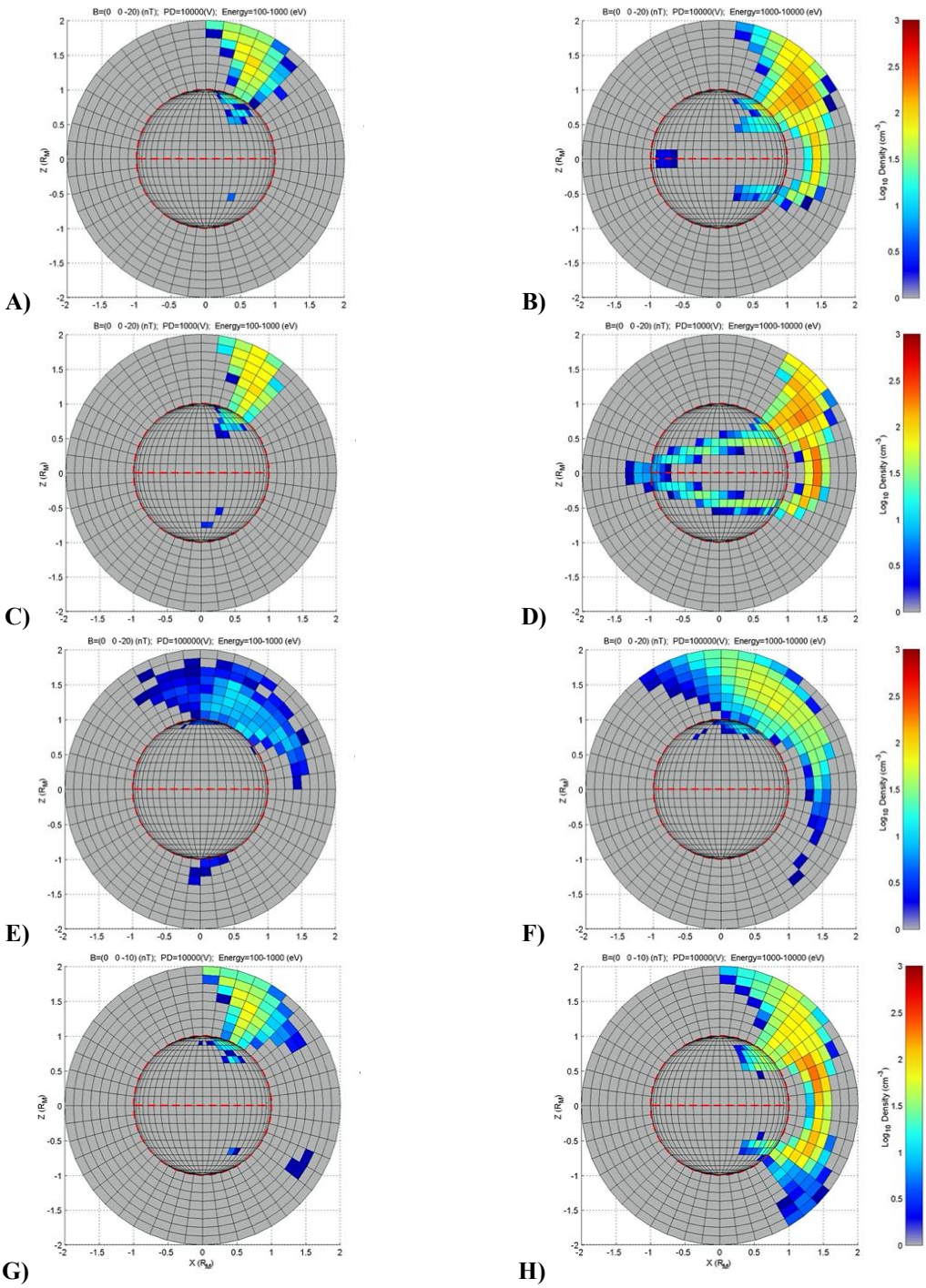

Figure 5.8 Colour-coded maps of H^+ density over two different surfaces: *x-z* plane (outside the red circle) and Mercury surface (inside red circle). Panels **A, C, E, G**: low proton energy (100 eV – 1 keV); Panels **B, D, F, H**: high proton energy (1-10 keV). Panels **A, B**: *reference* condition. Panels **C, D**: same as **A, B**, but low potential drop (*PD*=1 kV). Panels **E, F**: same as **A, B**, but high potential drop (*PD*=100 kV). Panels **G, H**: same as **A, B**, but low IMF (B_z = -10 nT).

this cell. The flux obtained in this way is hence an upper limit for the real flux at the surface. Different panels refer to different external conditions and energy ranges.

General features. In a typical H^+ simulated distribution it is possible to recognize three different and peculiar populations, whose relative intensity is a matter of interest of the

present study. The first one (α), present in all external conditions, is the population precipitating towards the planet along the magnetic field lines. Some of them are bounced by the increasing magnetic field; the others reach the planetary surface. During this motion, particles are drifted northward by the **E×B** drift and westward by the grad-**B** drift. The former is energy-independent; the latter is more efficient for the highest energies. The proton source is symmetric around noon, and any longitudinal shift in the surface precipitation (evidenced by the parameter $\overline{MLT_S}$) is due to **B**-grad drift.

The second population (β) is made by protons that are bouncing in the dayside, and is concentrated between the subsolar point and the surface. The third population (γ) is made by protons that move westward and eventually hit the surface in the nightside. Both these two last populations are generated from the first, because of the diffusion through field lines. Diffusion occurs if the temporal or spatial scale of the **B** field variations is shorter, respectively, than the Larmor period or radius. In the present study, however, only the second case is of interest, because the **B** field is static.

Reference **conditions.** Panels **5.8A** and **5.8B** show the precipitating H^+ in the "*reference* conditions" for different energy ranges. In both cases the α population extends down to the surface, but high energy protons (1-10 keV, panel **5.8B**) impact Mercury at lower latitudes with respect to low energy ones (100 eV – 1 keV, panel **5.8A**). In fact, the mean energy of the H^+ at the magnetopause is higher when close to the sub-solar point (see figure **5.4)**. The population close to the Low Latitude Boundary Layer [*Paper* **IV**] is able to diffuse towards lower latitudes and start bouncing, raising the β population. Low energy protons are injected at higher latitude and cannot experience any bouncing. No β population is, in fact, recognizable in panel **5.8A**.

The H^+ flux impacting the surface (see panels **5.9A, 5.9B**) is up to 10^9 cm^{-2} s^{-1} for low-energy protons and up to 5×10^9 cm^{-2} s^{-1} in the case of high-energy protons. The mean flux intensity in the open field line area is approximately $10^8 \div 10^9$ cm^{-2} s^{-1} for both energy ranges, which is in agreement with previous studies [*McGrath at al.* 1986]. The difference of the distribution for the two energy ranges is more evident if we consider the position of the precipitating protons (see table **5.1** and panels **5.9A, 5.9B**), which is (11:32 MLT, 39°) for protons above 1 keV, and (11:54 MLT, 57°) for protons below 1 keV. The $\overline{MLT_S}$ shift between these two populations is due to the energy-dependence of the **B**-grad drift.

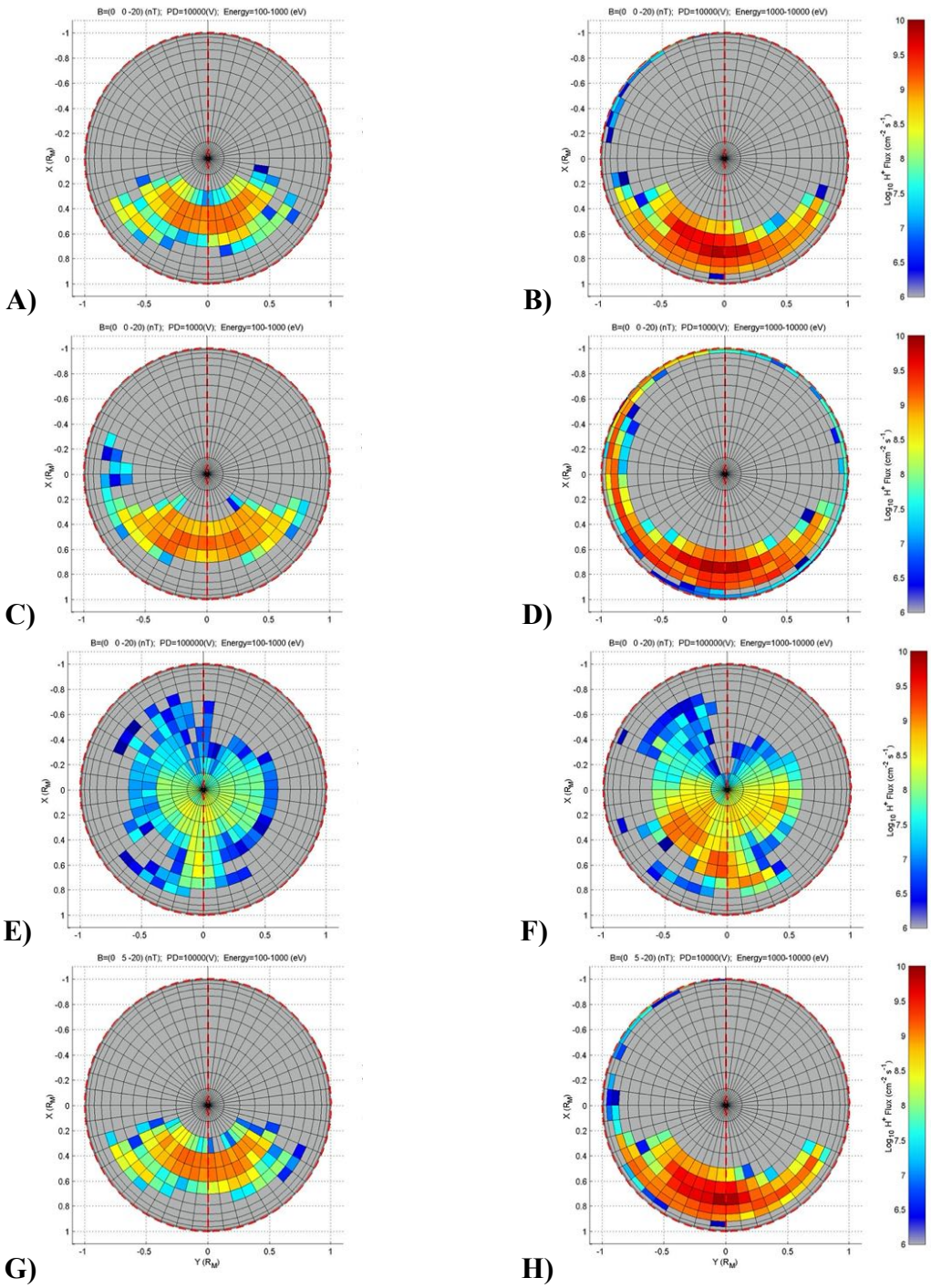

Figure 5.9 Colour-coded maps of H^+ flux over Mercury's surface. Panels **A, C, E, G**: low proton energy (100 eV – 1 keV); Panels **B, D, F, H**: high proton energy (1-10 keV). Panels **A, B**: *reference* condition. Panels **C, D**: same as **A, B**, but low potential drop (*PD*=1 kV). Panels **E, F**: same as **A, B**, but high potential drop (*PD*=100 kV). Panels **G, H**: same as **A, B**, but different IMF (B_y = -5 nT).

Electric field variation. In this analysis I have used two extreme values for the potential drop (1 kV and 100 kV) in order to have two extreme conditions for the electric field. The mean |**E**| in each case is respectively .1 mV/m and 10 mV/m (see section **2.3**). The first, clear effect of the increasing/decreasing **E** is the

increasing/decreasing of the northward shift of the surface footprint due to the **E×B** drift. This effect is energy-independent, and actually is clearly recognizable by comparing figures **5.8C** with **5.8E** (low energy), and **5.8D** with **5.8F** (high energy). The same comparison may be done, with identical results, on figure **5.9** (panels **C, E, D,** and **F**), using the H^+ flux at the surface instead of the density.

Another evident effect, originated from the same cause, is the modulation of β and γ population magnitude. With the increasing of the **E** field, in fact, protons are drifted northward, and no β population is able to form. Conversely, if the potential drop is low, the **B-**grad drift becomes predominant for high and low energy protons, and the γ population is drifted more westward, while β population does not change significantly. In this case, high-energy particles may reach the nightside. Panel **5.8D** clearly indicates that γ particles are bouncing during their drift, and they are gradually getting closer to the planet. Hence, a sort of small "partial ring current" is able to form; an important consequence of this drift is the possibility of proton precipitation in the nightside and the subsequent emission of sputtered particles from that region (panel **5.9D**). As far as it concerns low energy protons (panels **5.8C** and **7C**), some of them are drifted westward, but the bulk precipitates directly onto the surface with a small spread.

According to table **5.1**, intense electric fields cause less surface precipitation. The protons are supposed to be deflected northward and to be lost in the nightside.

In order to evaluate the effect of the **E×B** drift on the H^+ precipitation in the *reference* conditions, we may assume that *PD* = 1 kV reduces the influence of the electric field, so that it roughly corresponds to a "*zero electric field*" condition. By comparing total precipitating flux as reported in table **5.1**, in the cases of *PD*=10 kV (19×10^{25} s^{-1}) and *PD*=1 kV (26×10^{25} s^{-1}), we can conclude that at least one third of the protons that could precipitate onto the planetary surface are removed by **E×B** drift.

Magnetic field variation. The efficiency of the reconnection process is roughly proportional to the negative *z* component of the $\mathbf{B_{IMF}}$ field. This phenomenon has been studied here by comparing the "*reference*" case with the case of $\mathbf{B_{IMF}}$=(0, 0, -10) nT. The total precipitating flux, in this latter case, is lower ($4.2\ 10^{26}$ cm^{-2} instead of $5\ 10^{26}$ cm^{-2}). Moreover, protons impact at higher latitudes on the average (see table **5.1**). There is no other evident modulation on the density distribution shape (see figures **5.8G** and **5.8H**); the β population is slightly more evident, and there is less nightside precipitation.

In conclusion, the influence of B_z parameter is more on the intensity rather than on the shape of the n_{H+} distribution function.

The influence of the B_y component, as one may aspect, is mainly on the footprint longitude, with a westward shift of about 3° for each 10 nT. There is no other evidence of an influence of the B_y component on the general shape of the H^+ distribution, probably because IMF drives the input of the plasma more than the circulation after injection (see figures **5.9G** and **5.9H** for example).

It is worth noting that, in terms of influence, the $\mathbf{B_{IMF}}$ variation seems to be less relevant than *PD* also because in the first case I have chosen a more conservative position. Actually, more extreme conditions can be expected at Mercury; the B_z component, for example, may range between –30 and 30 nT, to say nothing of the B_x component absence.

5.6 Sputtering at Mercury

In this study I concentrate on the sputtering of Oxygen and Sodium. Both of them have been proved to exist in Mercury's exosphere: the first has been observed by Mariner 10 UVS [*Broadfoot at al.,* 1976]; the second has been detected by ground-based observations [*Potter and Morgan,* 1985]. I will first discuss the simulated vertical profiles for these species, as they are a general matter of interest; then I will concentrate on the feasibility of monitoring the cusp proton precipitation by means of a neutral particle imager (ELENA).

Figure **5.10** shows the estimated mean vertical profile for these species in the dayside exosphere (solid lines). These densities have been calculated considering sputtering as the only source; since other source processes (i.e. photo-stimulated disorption and thermal emission) are possible, such densities may be considered as lower limits. Moreover, I don't take into account the "ambient atoms" [*Killen and Ip,* 1999], i.e. atoms that are not at their first ballistic orbit. Dashed lines represent the vertical profiles over the point of maximum proton precipitation, and can be considered as an upper limit for sputtering-generated exosphere. These values have been obtained using the "*reference*" conditions, and the vertical profile density in other cases can be estimated just applying a simple proportion, using total flux in table **5.1**. Sputtering emission, in fact, is roughly proportional to precipitating flux (E_i does not modify much the emission spectrum, except for very high E_i). Hence, densities may be up to 50% higher (for

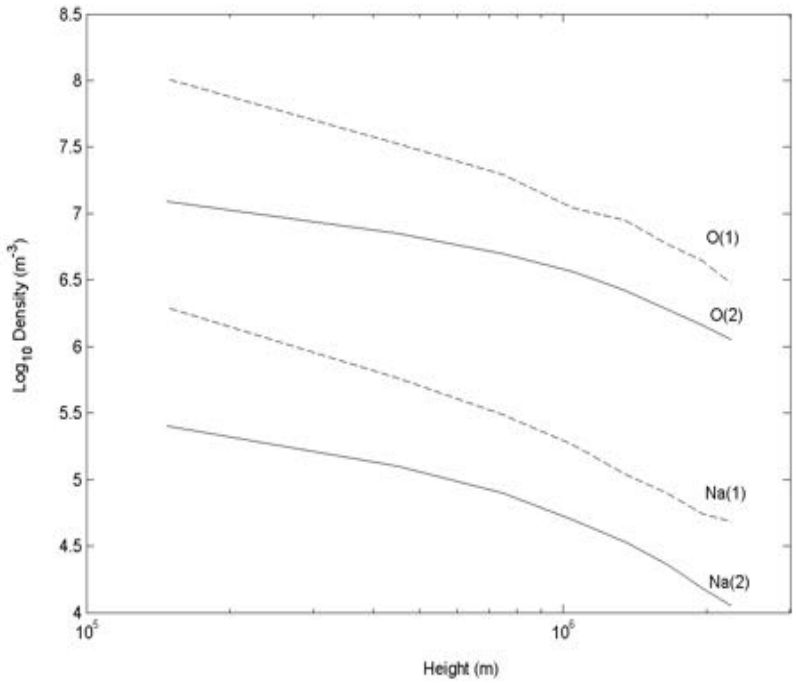

Figure 5.10 Exospheric density for O and Na, function of altitude from planetary surface, calculated considering sputtering as the only release process (solid lines, **2**). Dashed lines (**1**) still consider only sputtering, but refer to the vertical profile in the region of maximum ion precipitation.

example in the minimum potential drop conditions), or down to 80% lower (in maximum potential drop conditions).

As far as it concerns Oxygen, the estimated total column density is between 5×10^8 and 5×10^9 cm^{-2}, the surface density is between 20 cm^{-3} and 200 cm^{-3} and the scale-height is between 500 and 1000 km. Once again, it is worth noting that the thermal part of this population is underestimated: the first measure of the Oxygen exospheric content made by Mariner UV camera indicates 7×10^3 cm^{-3} as an upper limit, even if the scale-eight estimation was doubtful.

As far as it concerns Na, it has been noted [*Killen et al.*, 2001] that its temporal variability was found to be compatible with solar activity, which is in turn related to sputtering. The estimated total column density is up to 10^8 cm^{-2}, whereas the measured value is considerably higher (between 1 and 3 x10^{11} cm^{-2} [*Killen et al.*, 1990]). This may be explained if sputtering were not the first source for exospheric sodium. Another reason, which must be taken into account while discussing the results, is that I have intentionally discarded the ambient atom (i.e. neutral scattering on the surface plus accommodation/release), which have lower energy and reside in the lower part of the exosphere. Their inclusion in the model will be a further step, and will lead to a

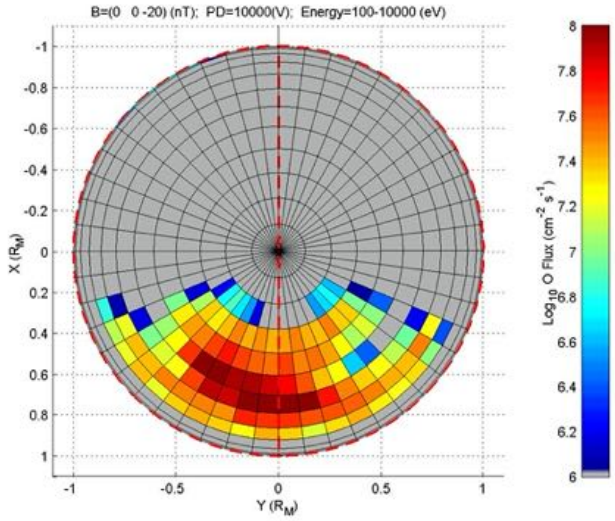

Figure 5.11 Colour-coded O-ENA flux generated by ion-sputtering on the northern surface of Mercury. Flux is integrated over all energies above escape energy (1.4 eV).

modelled sodium exosphere more concentrated in the lower altitudes. Scale-height analysis seems to confirm this last hypothesis. For example, simulated scale-height for Na is about 500 km, and a factor 10 greater than that observed (50 km) [*Killen et al.* 1990, *Wurz and Lammer,* 2003].

We now want to speculate on the possibility of remote-sensing the plasma-surface interaction. The estimated total proton flux on Mercury surface is between 10^{26} s^{-1} and 7×10^{26} s^{-1}, depending on external conditions. For comparison, we can obtain the amount of protons removed in one second by the charge-exchange process by integrating the charge-exchange loss function (equations **2.3** and **2.7**) in all the 5D space. This value is between 10^{22} s^{-1} and 10^{24} s^{-1}, depending on the boundary conditions and exospheric models. We can conclude that surface impact is the first cause of loss, in terms of magnitude, for proton plasma circulation. Consequently, sputtering process is an important source for the refilling of the exosphere, and since both sputtering and CE result in neutral atoms production, neutral atom imaging of the sputtering process is probably the best way to make remote-sensing of the plasma circulation. The Bepi Colombo/planetary orbiter (BC-MPO) is expected to have a neutral particle analyser on board. The proposed package (SERENA) includes a neutral particle imager (ELENA) with angular (~2°) and energy (~5%) resolution. Such an instrument would be able to detect the high-energy tail of the neutral sputtering emission, approximately above 10

eV. These particles travel more or less along straight lines (escape energy is 1.4 eV for O and 2 eV for Na) and their detection at MPO orbit (height: 1500 km at apocentre, 400 km at pericentre) would give an image of the sputtering release at the surface. Figure **5.11** shows the simulated intensity of sputtered O flux at the surface, integrated over all energies above 10 eV and over all directions, in the "*reference conditions*"; in the same configuration, the Na flux is similar in shape and approximately 1% of the O flux. In both cases, the intensity is high enough to be detected by ELENA; the angular resolution of the instrument results in a surface resolution down to tens of km. It is hence possible to monitor the variations in shape and intensity of the H^+ precipitation on the surface by the ELENA sensor on board BC. Since ELENA sensor can discriminate masses, the high surface resolution would permit the observation of differences in the surface local composition. Last but not least, the global analysis of the sputtering erosion of the surface would give unique information about the present and the past of Mercury's surface, revealing if (and how) the solar wind/surface interaction, in the past millions of years, has influenced the present surface composition.

5.7 ENA production at Mercury

Even if charge-exchange is not the main loss mechanism for magnetospheric protons, monitoring the product of such an interaction allows having important information about the magnetospheric and exospheric properties [*Barabash,* 2001]. In this frame, I will first discuss the general feasibility of ENA imaging and then its implications for neutral particle sensors on board MMO and MPO.

ENA images have been simulated, for different vantage points, by applying the procedure described in section **2.1** (*weighted cell integral*) to the simulated H^+ density shown in figure **5.8**. After a preliminary study, I have focused on two different positions for the vantage point. The first one is in the tail region, outside the equatorial plane but still in the shadow of the planet; as an example, I have chosen the point P_1: (-1.8, 0, 0.8) R_M. From this point, by looking sunward, it is possible to monitor simultaneously the plasma precipitating into the cusp, and that escaping in the dawn region. The second point P_2, which can be located in the dawn hemisphere, approximately on the y axis and with $r < 2$, is a good point to look at the γ population that drifts from dayside to nightside. In my study I have located P_2 at (0, -2, 0) R_M.

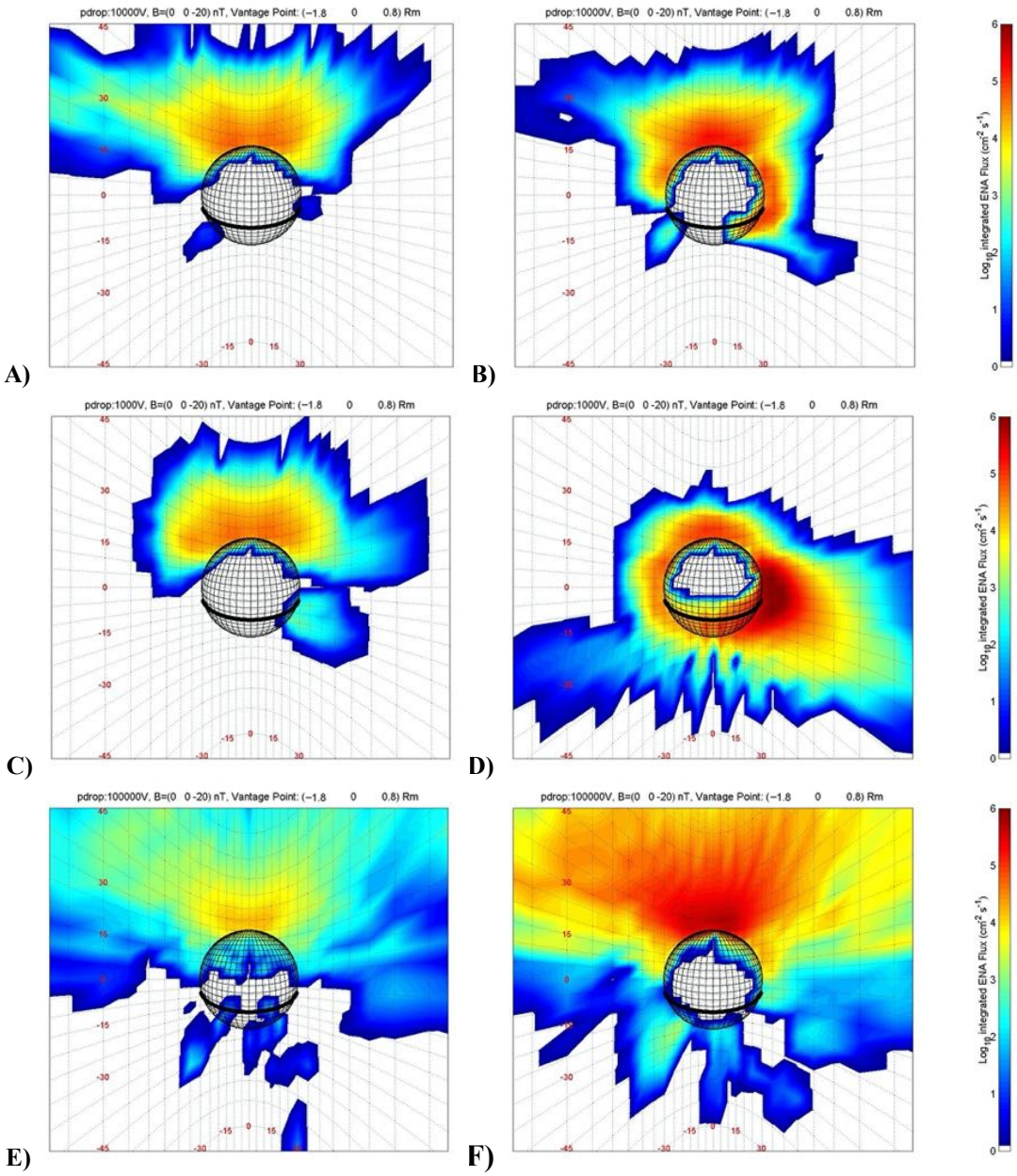

Figure 5.12 Simulated ENA images, from a vantage point in the nightside (P_1=[-1.8, 0, 0.8] R_M). Colour is coded according to ENA flux, integrated over two energy ranges: 100 eV - 1 keV (panels **A, C** and **E**) and 1-10 keV (panels **B, D** and **F)**. The boundary conditions are: $\mathbf{B_{IMF}}$ = (0, 0, -20) nT; *PD* = 10 kV (panels **A** and **B**), *PD* = 1 kV (panels **C** and **D**), *PD* = 100 kV (panels **E** and **F**).

Figure **5.12** shows simulated ENA images, as seen from P_1 in a "fish-eye" projection, for different *PD* values and integrated over two different energy ranges: 100 eV-1 keV, and 1 keV-10 keV. As for figure **5.8**, protons that enter the simulation area in the southern hemisphere are not shown. Generally, in these images, it is possible to observe ENA coming from two different H^+ populations. The first one is **α**, made by protons

that are precipitating into the cusp regions or that are passing above the North Pole before escaping in the nightside, and that get close enough to experience charge-exchange with the hermean exosphere. This process results in an intense signal in the upper part of the ENA image. The second population (γ), which is clearly evident especially for low *PD* and in the higher energy range, is made of protons that are drifting westward and are bouncing during their motion. These protons reach low altitude at their mirroring points, and even if their flux is generally lower than the flux of the precipitating ones, they may produce an intense ENA signal, distinguishable in the right side of ENA images.

The westward proton circulation is generated by **B**-grad drift, the intensity of which is proportional to proton energy. Hence, the second ENA signal is present only at energies above 1 keV; moreover, the **B**-grad drift dominates the **E×B** drift if the *PD* is low. Hence, the second ENA peak is more evident for low values of *PD*.

Similar considerations apply to ENA images simulated from point P_2 (Figure **5.13)**. In this case the ENA signal has been integrated over all energies. In addition to α and γ populations, which are clearly distinguishable, those protons that are mirroring in the dayside (β) generate a clear ENA signal as well. The ENA signal in the centre of the image comes from the γ population, and hence increases as the *PD* decreases.

Generally, the information carried by ENA images need to be unfolded, applying models of plasma and exosphere. However, the simulations suggest that ENA imaging at Mercury, alone, is able to give some useful information. This happens, for example, if the vantage point is in P_1. There, the proton precipitation into the cusp can be directly

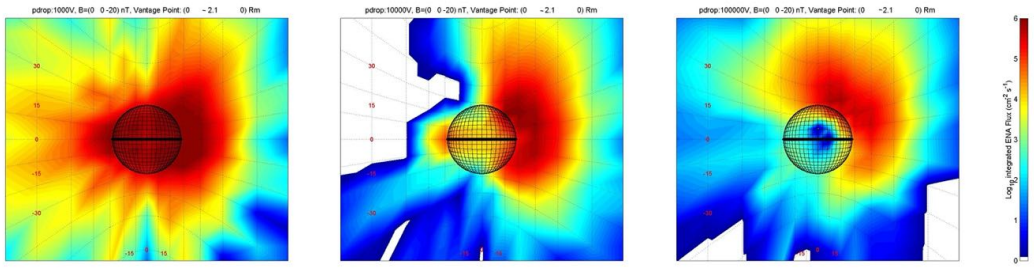

A) **B)** **C)**

Figure 5.13 Simulated ENA images, from a vantage point in the dawn sector (P_2=[0, -2.1, 0] R_M). Colour is coded according to ENA flux, integrated over all energies (100 eV-10 keV). The boundary conditions are: $\mathbf{B_{IMF}}$=(0, 0, -20) nT; *PD* = 10 kV (panel **A**), *PD* = 1 kV (panel **B**), *PD* = 100 kV (panel **C**).

monitored: any increase is immediately reflected in an increase of the ENA flux, since no other sources contribute. The ENA sensor on board MMO could address itself to such investigations. Moreover, in the case of a vantage point located in position similar to P_2, it is also possible to instantaneously monitor the open field line area on the surface. The chosen position for the vantage point is suitable for the MPO, and hence for NPA-SERENA. The SERENA/ELENA sensor will cover a field of view of about 2°×60°. Providing a proper spacecraft attitude, the detection of the α and β populations in the dayside will be possible by means of ENA imaging. At the same time, it will be possible to detect the γ population that is drifting in the space between the sensor and the surface (through ENA imaging), as well as the γ population that is precipitating onto the surface of Mercury (through the imaging of the directional neutral atoms coming from ion-sputtering).

5.8 Neutral atom detection at Mercury. Instrumentation and feasibility

Instrumentation. The ENA sensors discussed so far, such as NAOMI (section **3.5**) and NPD (section **4.5)** need to make a two-step measurement for each incoming ENA in order to resolve simultaneously mass and energy. To do this, it is necessary, in principle, to interact with the ENA; such an interaction (with a carbon foil or surface) perturbs the neutral and affects the precision of the measurement.

An innovative technique is presented here: the sensor ELENA (Emitted Low-Energy Neutral Atoms) is a Time-of-Flight Detector, based on the state-of-the art of ultra-sonic oscillating choppers (>100 kHz) and mechanical gratings.

The incoming neutral particles are separated from ions by HV plates. Then the micro-valve choppers let neutrals enter the chamber with a definite timing. Particles are then flown into a TOF chamber, and finally detected by a 2-dimesional stop array (based on MCPs and discrete anode sets). The mechanical layout of the instrument is shown in figure **5.14**: the stop surface is on the top; the particle entrance, with shutters, is on the bottom.

The MCP "sees" a sequence of pulses generated by the oscillation of the random mask with respect to a fixed collimator (see figure **5.15**); the random intervals are multiples of Δt. We can imagine this "opening/closing" as a sequence of ones and zeros, i.e. an array s_i of length N. Each element of array s_i represents a fixed time interval Δt. Let $F(t)$ be the time of flight distribution of neutral particles; F_i is the discrete representation of it,

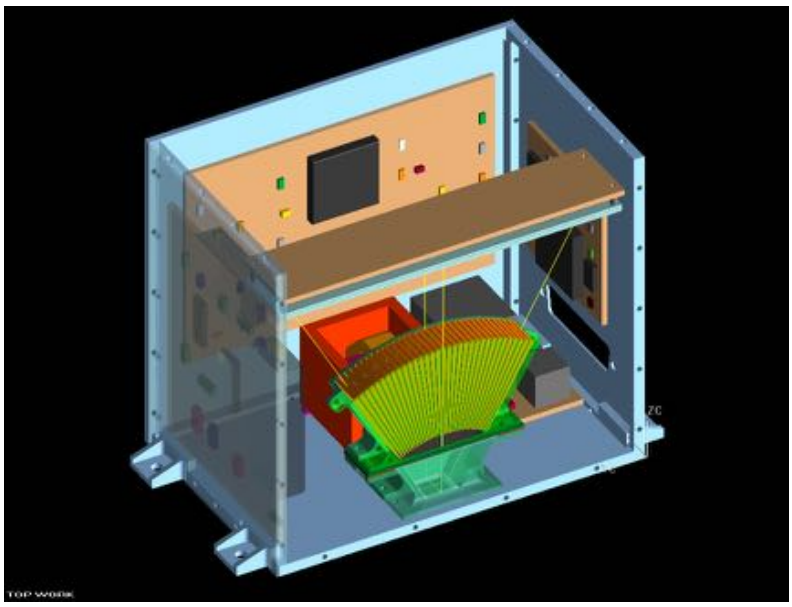

Figure 5.14 ELENA mechanical layout.

with i=1,N. The signal on the MCP in the interval j (Z_j) is hence equal to [*Wilhelmi and Gompf*, 1969]:

$$Z_j = C\,\Delta t \sum_{i=1}^{N} s_{j-i} F_i + U_j \qquad (\mathbf{5.11})$$

where C is a normalisation constant and U_j is introduced to take into account the noise. The array s_i should be a random array, i.e. its autocorrelation function should be zero. Let S_{jk} be a *circulant* matrix, obtained from s_i:

$$S_{ij} = s_{j-i} = \begin{pmatrix} s_N & s_{N-1} & \cdots & s_1 \\ s_1 & s_N & \cdots & s_2 \\ \vdots & \vdots & & \vdots \\ s_{N-1} & s_{N-2} & \cdots & s_N \end{pmatrix}; \qquad (\mathbf{5.12})$$

in this case, equation **5.11** can be written in a more compact notation:

$$Z_j = S_{ij} F_i + U_j \qquad (\mathbf{5.13})$$

and, in principle, the ToF distribution F can be obtained from the MCP signal Z by inverting matrix S.

Figure **5.16** shows the transform simulator for ELENA. Red line is the energy spectrum of an input, mono-energetic signal. Blue line is the energy spectrum of the reconstructed signal, as simulated by using a Monte-Carlo model and equation **5.13**. If the signal/noise ratio were too small, an alternative solution is to use non-random

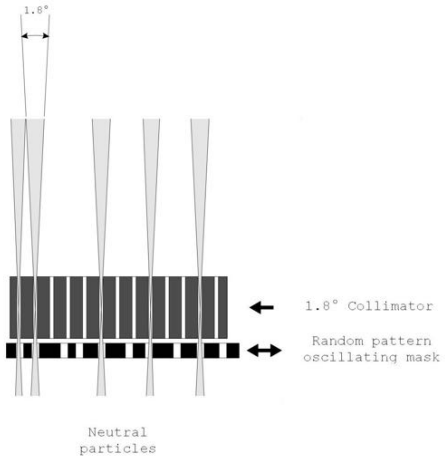

Figure 5.15 ELENA shuttering concept.

sequences, with s_1=1 and $s_{j>1}$=0. We can measure the ToF of each single particle by assuming that it has entered the chamber in the middle of the first "opening". In this case, it is necessary to find a compromise between the ToF resolution (Δt), the number of ToF channels (N-1) and the duty cycle ($N \cdot \Delta t$). The particle energy is measured in the same way as NPD (see section **4.5**); the particle mass is known once having measured its energy and velocity. The main characteristics of ELENA sensor are shown in table **5.2**.

Feasibility. One of the main scientific purposes of this study is to investigate the feasibility of neutral atom imaging at Mercury. In doing this, we must take into account that different production processes need different treatment. Neutral atoms coming from charge-exchange have been simulated by using a Monte-Carlo model (in sections **5.4** and **5.5**), and their detection has been discussed**.** Neutral atoms coming from the surface

Table 5.2

Intrinsic field-of-view (IFOV)	1.8° x 1.8°
Total field-of-view (FOV)	60° x 1.8°
swath width (cross track, 8 pixels)	102.96 km @t 400 km altitude 386.40 km @ 1500 km altitude
swath length (along track, 1 pixel)	12.87 km @ 400 km altitude > 48.30 km @ 1500 km altitude
dwell time	5 s

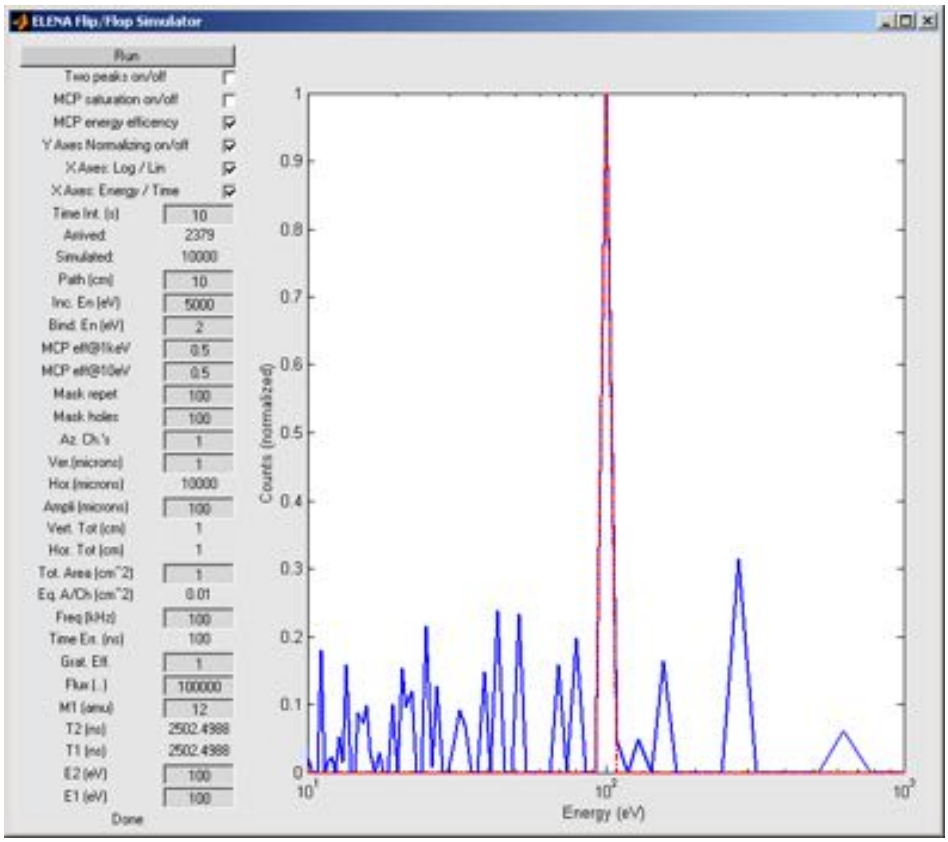

Figure 5.16 Sample transform simulator for ELENA. Red line is the energy spectrum of an input, mono-energetic signal, simulated using a Monte-Carlo model. Blue line is the energy spectrum of the measured signal, as reconstructed by using equation **5.13**.

---

could be generated by using the same model, but in this case the resolution of the numerical grid is probably too rough. Those latter neutrals, in fact, do not travel in straight lines (because of their lower energy), hence a little variation in energy and direction at the surface may completely change their trajectory. Moreover, since this study may also give some advice about suitable ELENA allocation on board BC, several tests must be done in a short time. The study of the trajectory from source to detector, hence, needs a separate, analytical treatment.

To achieve this goal, I have developed a dedicated *tool of analysis*. The philosophy of this tool is in the questions: "for a given instrument allocation, field of view and energy range, which signal is detectable?" and "can a strong surface composition anisotropy be resolved by the neutral flux entering the instrument?". To give the answers, the model just backtracks the particle trajectories from the sensor to the surface. This can be done analytically by solving the gravitational equation of motion. The mathematical procedure is very simple and is not reported here; the used equations are in Appendix **B**.

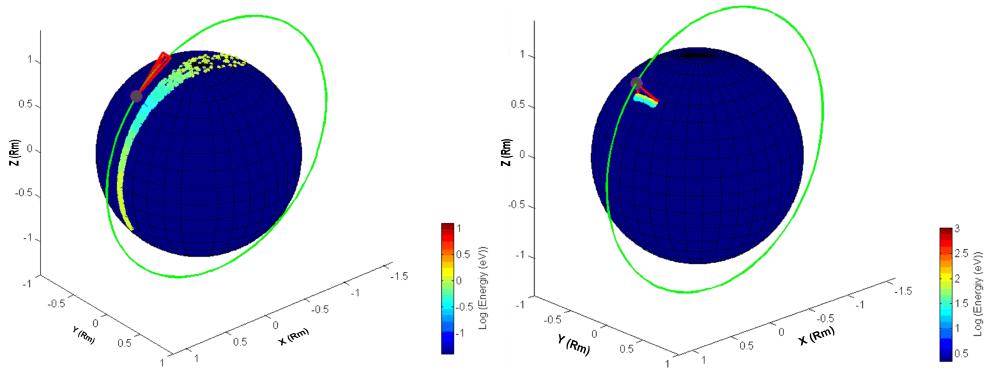

Figure 5.17 Footprints of LENA trajectories that can be detected from BEPI COLOMBO spacecraft. Coloured points on the surface of Mercury are colour-coded according to the sputtering energy. Green curve is the spacecraft orbit, red lines represent the sensor viewing angle for two different proposed sensors: STROFIO, a low energy exospheric sensor (left panel), and ELENA, a mid energy directional sensor (right panel).

As an example, I show the simulations of the source that may produce a signal in the range 10-1000 eV. The results are shown in figure **5.17**. The simulation shows that neutral mass spectrometer, detecting particles below 50 eV (namely: STROFIO, part of the SERENA package) detects a signal that is generated in a narrow region. If STROFIO is pointing towards RAM (as in figure **5.17A**) this region lies around the surface projection of the satellite's orbit. Within this region, however, it is not possible to determine the location where sputtering has occurred. As far as it concerns ELENA (figure **5.17B**), some uncertainty arises from the energy detection. In fact, an error on the detected energy results in an error on the estimation of the source position. This error is due to the combination of the satellite velocity (2÷3 km/s) and the detected particle velocity, which depends on the energy. Hence, this error can be neglected for energies above hundreds of eV. For low energy particles, however, this additional error should be considered. As an example, a 50% error on the energy of detected sodium @ 20 eV results in a 25 km error on the position of the source, which must be added to the intrinsic error due to IFOV (see table **5.2**); this error decreases to less than 10 km for sodium @ 200 eV and is negligible above 500 eV.

6. Summary and Conclusions

Here I'm presenting a summary of the scientific results of this work. Among them, I'm focusing on the three most important ones, i.e. the global reconstruction of the ring current during a geomagnetic storm, the feasibility of the ENA investigation applied to Phobos and a global modelling of the Solar Wind/Mercury interaction.

6.1 Earth equatorial proton distribution during storm time

Nowadays, the importance of ENA imaging among the instruments of investigation of the magnetosphere of the Earth has been widely accepted. Actually, several orbiting spacecrafts include ENA sensor as part of their payload. Nevertheless, ENA imaging needs to be used in addition to accurate plasma circulation models to produce the best results.

It is important to understand how plasma modelling and ENA imaging are complementary. As an example, we may consider an arbitrary configuration of the model presented in chapter **3** and a given ENA image of the same plasma circulation. ENA imaging gives 2D information about a 3D volume; the model gives information and interpretation about the H^+ distribution over a 2D equatorial plane. Even if ENA imaging alone is able to give an accurate reconstruction of the plasma circulation, only a model is able to focus and distinguish the physical processes occurring, to provide a correct interpretation of the present and, eventually, a forecast of the future.

The main scientific steps/results of this study are:

1) the model is able to reconstruct any instantaneous real magnetospheric configuration;

2) it is possible to monitor the storm-time development of proton distribution by using this model tuned by best-fitting some selected parameters with experimental data,

3) details on partial/global ring current evolution, energetic particle flow patterns and electric potential can be obtained through model analysis.

At present, the model has been tested using CRRES/MICS/LOMICS data collected during July 1991; in the future, the use of more experimental data (if possible, observed by two or more spacecrafts simultaneously) is recommended. Moreover, the future inclusion of a pitch angle analysis in the model will allow to reconstruct the full 3D magnetospheric circulation. In this way, the comparison between ENA images as predicted by the model and as actually observed by, for example, IMAGE/MENA-

HENA will be possible.

6.2 ENA and Mars-Phobos environment

One of the main open questions about Phobos' exosphere composition and outgassing rate is related to the presence of a gas/dust torus along its orbit. Its presence has been suggested, but never observed, after PHOBOS-2 observations in 1989; a definite clarification of such an intriguing issue would be of fundamental interest to determine the time evolution of Phobos.

In chapter **4**, I have presented a method able to investigate Phobos' exosphere properties. I have simulated the ENA signal/disturbance generated by the interaction between the solar wind and the outgassed Oxygen, as expected according to an original O-torus model. The simulations show that this ENA signal may be discriminated from the background for particular positions of the vantage point. This technique can give relevant information, and determine the major characteristics of neutral outgassing, whose rate has not been directly measured. The importance of such a study is clear, if we consider that the simulated ENA images will be compared with *in situ* measurements. In fact, ESA mission Mars Express (MEX), launched in June 2003, will have at least three close approaches to the natural satellite Phobos. The data collected by the ASPERA-3 instrument on board MEX will probably give the scientific community an ultimate answer to the Phobos-torus dilemma.

More generally, many issues related to the effects of the interaction between solar wind and Martian environment will be addressed by ASPERA-3. In fact, the ENA imaging technique is a powerful tool to understand the fundamental role played by the solar wind for the planetary evolution.

6.3 Neutral Atom imaging of Mercury's Environment

In this study I have presented a Monte-Carlo model of the magnetosphere of Mercury, and I have used it as an input for the simulation of neutral particle emission from both the surface (via ion-sputtering) and the exosphere (via charge-exchange).

The main purposes of this study are: an investigation of the dayside H^+ circulation, and a feasibility analysis of the neutral particle imaging technique while applied to it.

Major steps. The development of the magnetospheric model involves:

1) modifying a T96 magnetic field model;

2) reconstructing the electric potential by using a Volland model of ionospheric potential;

3) reconstructing the H^+ distribution on the magnetopause;

4) estimating the error caused by the actual neglecting of the H^+ convection from the tail, by using a very simple model of Hermean "ring-current". Incidentally, this last estimation has given another proof of the non-existence of such a current in the equatorial plane of Mercury.

Model limits. Among the limits of the model, I have to mention the absence of a B_x component in the modelled $\mathbf{B_{IMF}}$, and the fact that the magnetopause surface has not been modified while tuning the external conditions. In any case, it is important to remember that the high uncertainties about Mercury's environment may cause the highest errors.

The accommodation/release of particles on the surface has not been taken into account; this process will be included in a future study. Here, it causes an underestimation of the exospheric Na and O, but this fact does not affect the estimation of the neutral atom fluxes as detected by ELENA. In fact (see figure **5.11**), this estimation has been done by considering only "directional" particles (i.e. above escape energy), which by definition cannot be "re-accommodated".

As a matter of fact, one of the exospheric species that give a higher contribution to ENA generation in our model is H_2. The exospheric density of H_2, as given by *Wurz and Lammer* [2003], has been intentionally depleted as suggested by authors. The factor adopted here (0.01) is intentionally low, and leads to a conservative estimation of ENA fluxes.

Main results. This model has reconstructed the general circulation of protons in the dayside hemisphere of Mercury; so far, this model does not foresee any intense H^+ circulation in the nightside. Three main H^+ populations have been identified, and their behaviour under different external conditions has been discussed.

The model is able to estimate the total flux on the surface in different external conditions. This value has important implications in modelling the ion-sputtered-originated exosphere of Mercury (see section **5.6**). If we compare it to the total H^+ crossing the MP ($\sim 2\times10^{27}$ s^{-1}, see section **5.2**), we can conclude that about one tenth of it is able to precipitate onto the planetary surface, depending on the external condition. The remaining part is mostly bounced back; actually, the **E×B** drift prevents a considerable amount of protons from falling down to Mercury's surface. According to

this estimation, and taking into account that we have used extreme potential drop conditions, the modulation of the surface precipitation made by the potential drop seems to be comparable to the one made by the IMF magnetic field.

After the H^+ circulation has been reconstructed for different external conditions, I have focused my attention on plasma loss processes, more particularly on surface collisions and charge-exchange. Both these processes open the way to a remote-sensing of the plasma circulation via neutral atom imaging; in fact, both of them produce neutral atoms. Moreover, sputtering process resulting from surface collisions is expected to be a powerful tool of investigation, since: i) proton fluxes on the planetary surface may be extremely high; ii) surface composition may be analysed as well as plasma circulation.

In this frame, I have studied the feasibility of neutral atom remote-sensing made by the SERENA/ELENA instrument on board Bepi Colombo/MPO. As a matter of fact, such an instrument should be able to address itself to all the scientific issues discussed in this study.

References

Barabash, S., and R. Lundin, On a possible dust-plasma interaction at Mars, *IEEE Transactions on Plasma Science, 22,* 2, 173, 1994.

Barabash, S., A.V. Lukyanov, P. C:son Brandt, and R. Lundin, Energetic neutral atom imaging of Mercury's magnetosphere 3. Simulated images and instrument requirements*, Planet. Space Sci.*, **49**, 1685, 2001.

Barnett, C. F., J. A. Ray, E. Ricci, M. I. Wilker, E. W. McDaniel, E. W. Thomas and H. B. Gilbody, Physics Division: Atomic Data for Controlled Fusion, Oak Ridge Natìonal Laboratory, Oak Ridge, Tennessee, February 1977.

Barnett, C. F., Collisions of H, H_2, He and Li atoms and ions with atoms and molecules, *Atomic Data for Fusion Ser.*, vol. 1, Rep. ORNL-6086, edited by H. T. Hunter et al., Oak Ridge Nat. Lab., Oak Ridge, Tenn., 1990.

Bida, T. A., R. M. Killen and T. H. Morgan, Discovery of calcium in Mercury's atmosphere, *Nature***, 404**(9): 159–161, 2000.

Broadfoot A.L., D.E. Shemanky, and S. Kumar, Mariner 10: Mercury atmosphere, *Geophys. Res. Lett.*, **3**, 577, 1976.

C:son Brandt, P., Ena Imaging of Planetary Magnetospheres, *IRF Scientific Report* 259, 1999.

Cheng, A.F., R.E Johnson, S.M. Krimigis and L.J. Lanzerotti, Magnetosphere, exosphere and surface of Mercury, *Icarus*, **71**, 430.440, 1987.

Connerney, J. E. P., and N. F. Ness, The magnetosphere of Mercury, in *Mercury* (Eds. F. Vilas, C.R. Chapman, and M.S. Matthews) Tucson, The University of Arizona Press: 494, 1988.

Delcourt, D. C., S. Grimald, F. Leblanc, J.-J. Berthelier, A. Millilo, A. Mura, and S. Orsini, A quantitative model of planetary Na^+ contribution to Mercury's magnetosphere, *Annales Geophys*, **21**, 1723 - 1736, 2003.

Dubinin, E. M., R. Lundin, N. F. Pissarenko, S. V. Barabash, A. Z. Zakharov, H. Koskinen, K. Schwingenschuh, and Ye. G. Yeroshenko, Indirect evidences for a gas/dust torus along the Phobos orbit, *Geophys. Res. Lett.,* 17, 861, 1990.

Dubinin, E. M., N. F. Pissarenko, S. V. Barabash, A. Z. Zakharov, R. Lundin, H. Koskinen, K. Schwingenschuh, and Ye. G. Yeroshenko, Tails of Phobos and

Deimos in the Solar Wind and in the Martian Magnetosphere, *Planet. Space Sci., 39*, 1, 123, 1991.

Duxbury , T. C. and A. Ocampo, Mars: satellite and ring search from Viking, *Icarus* 76, 160-162, 1988.

Ebihara, Y., and M. Ejiri, Modeling of solar wind control of the ring current buildup: A case study of magnetic storms in April 1997, 25, 3751-3754, *Geophys. Res. Lett.*, 1998.

Ebihara, Y., and M Ejiri, Simulation study on fundamental properties of the storm-time ring current, *J. Geophys. Res.,* 105, 15843-15859, 2000.

Ejiri, M., Trajectory traces of charged particles in the magnetosphere, *J. Geophys. Res.,* 83, 4798-4810, 1978.

Fanale, F. P. and J. R. Salvail, Loss of water from Phobos, *Geophys. Res. Lett. 16*, 4, 287, 1989.

Goettel K.A., Present bounds on the bulk composition of Mercury: Implications for planetary formation processes. In *Mercury*, pp. 613-621, (F. Vilas, C.R. Chapman and M.S. Matthews, Eds.) Univ. Arizona Press, Tucson, 1988.

Goldstein, B.E., S.T. Suess, and R.J. Walker, Mercury: Magnetospheric processes and the atmospheric supply and loss rates, *J. Geophys Res*., **86**, 5485-5499, 1981.

Hasted, G. B., *Physics of atomic collisions*, 416, Butterworths, London, 1964.

Henderson, M. G., G. D. Reeves, H. E Spence, R. B. Sheldon, A. M. Jorgensen, J. B. Blake and J. F. Fennel, First energetic neutral atom images from polar, *Geophys. Res. Lett., 24,* 1167-1170, 1997.

Horanyi, M., M. Tatrallyay and J. G. Luhmann, Simulations of dust particles in the Martian environment, *Geophys. Res. Lett.*, *17,* 857, 1990.

Horwitz, J. L., Core plasma in the magnetosphere, *Rev. Geophys.,* 25, 579, 1987.

Ip, W.-H. and M. Banaszkiewicz, On the dust/gas tori of Phobos and Deimos. *Geophys. Res. Lett., 17,* 857, 1990.Kallio, E., H. Koskinen, S. Barabash, C. M. C. Nairn, and K. Schwingenschuh, Oxygen outflow in the Martian magnetotail, *Geophys. Res. Lett., 22*, 2449, 1995.

Kallio, E., An empirical model of the solar wind flow around Mars, *J. Geophys. Res., 101*, 11133, 1996.

Kallio, E., and P. Janhunen, Modelling the solar wind interaction with Mercury by a quasineutral hybrid model, *Annales Geophysicae*, in press, 2003.

Kallio, E., J.G. Luhmann, and S. Barabash, Charge exchange near Mars, The solar wind absorption and energetic neutral atom production, *J. Geophys. Res., 102*, 22183, 1997.

Killen, R.M., A.E. Potter, and T.H. Morgan, Spatial Distribution of sodium vapor in the atmosphere of Mercury. *Icarus* **85**, 145-167, 1990.

Killen, R.M., and W-H Ip, The surface-bounded atmosphere of Mercury and the Moon, *Reviews of Geophysics*, **361**, 1999.

Killen, R.M., A.E. Potter, P. Reiff, M. Sarantos, B.V. Jackson, P. Hick, and B. Giles. Evidence for Space Weather at Mercury. *Journ. Geophys Res. (Planets)*, **106**, 20,509-20,525, 2001.

Krymskii, A. M., T. K. Breus, M. K. Dougherty, D. J. Southwood, W. I. Axford, The electromagnetic effects of the solar wind interaction with the Phobos neutral gas halo and dust torus, *Planet. Space Sci., 40*, 8, 1033, 1992

Lammer, H., and J. Bauer, Mercury's exosphere: origin of surface sputtering and implications, *Planet. Space. Sci*., **45**, 73-79, 1997

Liemohn, M.W., J.U. Kozyra, V.K. Jordanova, G.V. Khazanov, M.F. Thomsen, and T.E. Cayton, Analysis of early phase ring current recovery mechanisms during geomagnetic storms, *Geophys. Res. Lett.*, 26, 2845–2848, 1999.

Lindslay, B.G., D. R. Sieglaff, D. A. Schafer, C. L. Hakes, K. A. Smith, and R. F.Stebbings, Charge transfer of 0.5-, 1.5-, and 5-keV protons with atomicoxygen: Absolute differential and integral cross sections, *Phys. Rev. A*, *53*, 212, 1996.

Luhmann, J.G., C.T. Russell, and N.A. Tsyganenko, Disturbances in Mercury's Magnetosphere: Are the Mariner 10 'Substorms' Simply Driven?, *J. Geophys. Res*. **103**, 9113-9119, 1998.

Lui, A. T Y., Tutorial on geomagnetic storm and substorms, *IEEE Transactions on Plasma Science, 28,* 6, 2000.

Lukyanov, A. V., S. Barabash, R. Lundin, and P. C:son Brandt, Energetic neutral atom imaging of Mercury's magnetosphere, 2. Distribution of energetic charged particles in a compact magnetosphere, *Planet. Space Sci.,* **49**, 1677, 2001.

McGrath, M. A., Johnson, R. E., and Lanzerotti, L. J.: Sputtering of sodium on the planet Mercury, Nature, 323, 694–696, 1986.

McIlwain, C.E., A Kp dependent equatorial electric field model, *Adv. Space Res*., 6(3), 187, 1986.

Meinel, A. B., Doppler-shifted auroral hydrogen emission, *Astrophys. J., 113*, 50, 1951.

Milillo A., S. Orsini, I.A. Daglis, Empirical model of proton fluxes in the equatorial inner magnetosphere. 1. Development, *J. Geoph. Res*., 106**,** 25713-25730, 2001.

Milillo, A., and S. Orsini, Energetic Neutral Atoms: Potential Merits and First Observations, *Recent Research Developments in Geophysical Research*, *Research Signpost*, Trivandrum-India, **3**, 153, 2001.

Morgan, T.H. and R.M. Killen, A non-stoichiometric model of the composition of the atmospheres of Mercury and the Moon. *Planet Space. Sci*. **45**, 81-94, 1997.

Moritz, J., Energetic protons at low equatorial altitudes: A newly discovered radiation belt phenomenon and explanation, *J. Geophys., 38*, 701, 1972.

Ness N.F., K.W. Behannon, R.P. Lepping, and Y.C. Whang, The magnetic field of Mercury confirmed, *Nature*, **255**, 204, 1975.

Ogilvie, K. W., J. D. Scudder, V. M. Vasyliunas, R. E. Hartle, and G. L. Siscoe, Observation at the planet Mercury by the plasma electron experiment: Mariner 10, *J. Geophys. Res., 82*, 1807-1824, 1977.

Orsini, S., I. A. Daglis, M. Candidi, K. C. Hsieh, S. Livi, and B. Wilken, Model calculation of energetic neutral atoms precipitating at low altitudes, *J. Geophys. Res., 99*, 13489, 1994.

Orsini, S., and A. Milillo, Magnetospheric Plasma Loss Processes and Energetic Neutral Atoms, *Il Nuovo Cimento*, **22 C**, N 5, 633, 1999.

Orsini, S., A. Milillo, E. De Angelis, A.M. Di Lellis, V. Zanza, and S. Livi, Remote sensing of Mercury's magnetospheric plasma via energetic neutral atoms imaging, *Planet. Space Sci.*, **49**, 1659, 2001.

Potter, A.E., and T.H. Morgan, Discovery of Na in the atmosphere of Mercury, *Science* **229**, 651-653, 1985.

Potter, A.E. and T.H. Morgan Sodium and Potassium Atmospheres of Mercury, *Planet. Space. Sci.,* **45**, 95-100, 1997.

Roelof, E. C., D. G. Mitchell, and D. J. Williams, Energetic neutral atoms (E ~ 50 keV) from the ring current, IMP 7/8 and ISEE 1, *J. Geophys. Res., 90*, 10991, 1985.

Roelof, E. C., Energetic Neutral Atom image of a storm-time ring current. *Geophys. Res. Lett., 14*, 652-655, 1987.

Roelof, E. C., and D. J. Williams, The terrestrial ring current: from *in situ* measurement to global images using energetic neutral atoms, *John Hopkins APL Techn. Dig., 9*, 144, 1988.

Roelof, E. C., A new approach to extracting energetic ion distribution from ENA images, *J. Geophys. Res.,* 2003 in press.

Sarantos, M., P.H. Reiff, T.W. Hill, R.M. Killen, A.L. Urquhart, A Bx-interconnected magnetosphere model for Mercury, *Planetary and Space Science,* 49, 1629-1635, 2001.

Sauer, K., E. Dubinin, K. Baumgartel, A. BogdanOv; Deimos: An Obstacle to the Solar Wind; *Science*, Vol. 269, 1995.

Sigmund, P., Theory of Sputtering. I. Sputtering Yield of Amorphous and Polycrystalline Targets Phys. Rev. 184, 383–416, 1969.

Sieveka, E.M., and R.E. Johnson, Ejection of atoms and molecules from Io by plasma-ion impact. *Astrophys. J.* **287**, 418-426, 1984.

Siscoe, G.L., and L. Christofer, Variations in the solar wind standoff distance at Mercury, *Geophys. Res. Lett*., **2**, 158, 1975.

Siscoe, G.L., N.F. Ness, and C.M. Yeates, Substorms on Mercury?, *J. Geophys Res*., **80**, 4359-4363, 1975.

Slavin, J.A., J.C.J. Owen, J.E.P. Connerney, and S.P. Christon, Mariner 10 observations of field-aligned currents at Mercury, *Planet. Space Sci*., **45**, 133-141, 1997.

Soter, S. The dust belts of Mars, Center for Radio-physics and Space Research, *Cornell University, CRSR* 462. 1971

Spreiter, J.R., A.L. Summers, and A.Y. Alksne, Hydromagnetic flow around the magnetosphere. *Planet. Space Sci.* **14**, 223-253, 1966.

Stebbings, R. F., C. H. Smith, and H. Ehrahardt, Charge transfer between Oxygen atoms and O^+ and H^+ ions, *J. Geophys. Res., 69*, 2349, 1964.

Tsyganenko, N.A., Effects of the solar wind conditions on the global magnetospheric configuration as deduced from data-based field models, in *Proc.of 3rd International Conference on Substorms* (ICS-3). *ESA* ***SP-389***, 181-185, 1996.

Vaisberg, O. L., Luhmann, J. G., Russell, C. T., Plasma observations of the solar wind interaction with Mars, *J. Geophys. Res., 95*, 14841, 1990.

Volland, H.: A model of the magnetospheric convection electric field, *J. Geophys. Res*., 83, 2695–2699, 1978.

Weins, R.C., D.S. Burnett, W.F. Calaway, C.S. Hansen, K.R., Lykkem and M.L. Pellin, Sputtering products of sodium sulphate: Implications for Io's surface and for sodium bearing molecules in the Io's torus, *Icarus*, **128**, 386-397,1997.

Wilhelmi, G. and F. Gompf, Binary sequences and error analysis for pseudo-statistical neutron modulators with different cycles, *Nuclear Instr. And Meth.* 81, 36-44, 1970.

Wurz, P., Detection of energetic neutral atoms, *The outer heliosphere & Beyond the Planets,* Eds. K. Scherer, H. Fichtner, and E. Marsch, Copernicus-Gesellschaft, Katlenburg-Lindau*,* 251-288 (2000)

Wurz, P., and H. Lammer, Monte-Carlo Simulation of Mercury's Exosphere, *Icarus*, **164**(1), 1-13, 2003.

Zhang, M. H. G., J. G. Luhmann, A. F. Nagy, J. R. Spreiter and S. S. Stahara, oxygen ionisation rates at Mars and Venus: Relative contribution of impact ionisation and charge exchange, *J. Geophys. Res., 98*, 3311, 1993.

Acknowledgements

I would like to express my deep gratitude to Dr. Stefano Orsini and Dr. Anna Milillo, my advisors at the Interplanetary Space Physics Institute. Their support during these last three years has been fundamental for me as a person and as a scientist. I am very happy to look back and see what a long way we have gone together. Thank you.

Appendix A: Acronyms

AE	Auroral Electrojet Index
AU	Astronomical Unit (1.469×10^{11} m)
CE	Charge exchange
CF	Carbon Foil
Dst	Disturbance Storm index
ENA	Energetic Neutral Atom
FOV	Field of View
GC	Guiding Centre
Kp	Planetary K index
LENA	Low Energy Neutral Atom
LS	L-Shell
MC	Monte-Carlo
MCP	Micro Channel Plate
MLT	Magnetic Local Time
PD	(Cross-tail) Potential Drop
R_E	Earth Radius
R_M	Mars/Mercury Radius
SSD	Solid State Detector
SW	Solar Wind
TOF	Time Of Flight

Appendix B: Symbols, useful equations and laws

B.1 *Electro-magnetism and plasma properties*

$f(v)$	Velocity distribution function
m	Particle mass
$\Phi(v)$	Particle flux
n	Particle density
v	Particle velocity
ε	Energy density
$\mathbf{v}_E$	**(**Guiding centre) **E×B** drift velocity
$\mathbf{v}_{\nabla \mathbf{B}}$	**(**Guiding centre) Grad-**B** drift velocity
$\mathbf{E}$	Electric field vector
$\mathbf{B}$	Magnetic field vector
B_r, B_θ, B_ϕ	Magnetic field components in spherical coordinates
M_B	Magnetic moment
r_L	Larmor radius
$P_\perp$	Perpendicular plasma pressure
$P_{//}$	Parallel plasma pressure

$$f(v) = \Phi(v)\, m\, v^{-2}; \qquad \textbf{(B.1)}$$

$$n_{H+} = 4\Pi \int_0^\infty f(v) v^2\, dv; \qquad \textbf{(B.2)}$$

$$\varepsilon = 2\Pi m \int_0^\infty f(v) v^4\, dv \qquad \textbf{(B.3)}$$

$$P_\perp = P_{//} \frac{2}{3} \varepsilon \qquad \textbf{(B.4)}$$

$$J_\perp = \frac{\mathbf{B}}{B^2}\left[\nabla P_\perp + (P_{//} - P_\perp)\frac{\mathbf{B}\times\nabla\mathbf{B}}{B^2}\right] \qquad \textbf{(B.5)}$$

$$\mathbf{v}_E = \frac{\mathbf{E}\times\mathbf{B}}{B^2} \qquad \textbf{(B.6)}$$

$$\mathbf{v}_{\nabla B} = \frac{1}{2} v_\perp r_L \frac{\mathbf{B}\times\nabla\mathbf{B}}{B^2} \qquad \textbf{(B.6)}$$

$$r_L = \frac{m v_\perp}{q|\mathbf{B}|} \qquad \textbf{(B.7)}$$

$$\begin{cases} B_r = -\dfrac{2M_B}{r^3}\sin\theta \\ B_\theta = \dfrac{M_B}{r^3}\cos\theta \\ B_\phi = 0 \end{cases} \quad \textbf{(B.8)}$$

B.2 *Ballistic orbits equations*

G	Gravitational constant
M	Planetary mass
$\mathbf{r}$	particle position
$\mathbf{v}$	particle velocity
a	Apocentre
b	Pericentre
L	Momentum
E	Energy

$$E/m = \frac{1}{2}v^2 - \frac{GM}{r} \quad \textbf{(B.9)}$$

$$L/m = \mathbf{r} \times \mathbf{v} \quad \textbf{(B.10)}$$

$$\begin{cases} b = \dfrac{\left(\dfrac{L}{m}\right)^2}{GM + \sqrt{(GM)^2 + 2\left(\dfrac{E}{m}\right)\left(\dfrac{L}{m}\right)^2}} \\ a = \dfrac{\left(\dfrac{L}{m}\right)^2}{GM - \sqrt{(GM)^2 + 2\left(\dfrac{E}{m}\right)\left(\dfrac{L}{m}\right)^2}} \end{cases} \quad \textbf{(B.11)}$$

Appendix C: Planetary fact sheet

Table C.1

	Mars	The Earth	Mercury
Mass (10^{24} kg)	0.64185	5.9736	0.3302
Volume (10^{10} km^3)	16.318	108.321	6.083
Equatorial radius (km)	3397	6378.1	2439.7
Polar radius (km)	3375	6356.8	2439.7
Mean density (kg/m^3)	3933	5515	5427
Surface gravity (m/s^2)	3.71	9.80	3.70
Escape velocity (km/s)	5.03	11.19	4.3
Bond albedo	0.250	0.306	0.119
Solar irradiance (W/m^2)	589.2	1367.6	9126.6
Black-body temperature (K)	210.1	254.3	442.5
Maximum surface Temperature (K)	-	-	700
Minimum surface Temperature (K)	-	-	90
Semi-major axis (10^6 km)	227.92	149.60	57.91
Sidereal orbit period (days)	686.980	365.256	87.969
Orbit eccentricity	0.0935	0.0167	0.2056
Length of day (hrs)	24.6597	24.0000	4222.6

Mars Atmosphere

Surface pressure: 6.36 mb at mean radius (variable from 4.0 to 8.7 mb depending on season) [6.9 mb to 9 mb (Viking 1 Lander site)]

Surface density: ~0.020 kg/m^3

Scale height: 11.1 km

Total mass of atmosphere: ~2.5 x 10^{16} kg

Average temperature: ~210 K (-63 C)

Diurnal temperature range: 184 K to 242 K (-89 to -31 C) (Viking 1 Lander site)

Wind speeds: 2-7 m/s (summer), 5-10 m/s (fall), 17-30 m/s (dust storm) (Viking Lander sites)

Mean molecular weight: 43.34 g/mole

Atmospheric composition (by volume):

Major: Carbon Dioxide (CO_2) - 95.32%; Nitrogen (N_2) - 2.7% Argon (Ar) - 1.6%; Oxygen (O_2) - 0.13%; Carbon Monoxide (CO) - 0.08%

Minor (ppm): Water (H_2O) - 210; Nitrogen Oxide (NO) - 100; Neon (Ne) - 2.5; Hydrogen-Deuterium-Oxygen (HDO) - 0.85; Krypton (Kr) - 0.3; Xenon (Xe) - 0.08

Mercury Atmosphere

Surface pressure: ~10^{-15} bar

Average temperature: 440 K (167 C) (590-725 K, sunward side)

Total mass of atmosphere: <~1000 kg

Atmospheric composition: 42% Oxygen (O_2), 29% Sodium (Na), 22% Hydrogen (H_2), 6% Helium (He), 0.5% Potassium (K), possible trace amounts of Argon (Ar), Carbon Dioxide (CO_2), Water (H_2O), Nitrogen (N_2), Xenon (Xe), Krypton (Kr), Neon (Ne)

[From http://nssdc.gsfc.nasa.gov/planetary/factsheet]

Table C.2 . Atmospheric abundances and loss rates at Mercury

Species	Surface abundance (cm^{-3})	Total Zenith Column (cm^{-2})	JeansFlux (cm^{-2} s^{-1}) T=550	Photo-ionisation lifetime (sec) R=0.386 AU	Photoionisation rate (cm^{-2} s^{-1}) R=0.386 AU
H	23; 230 [a]	$3x10^{9}$ [h]	2.7 [l]	$2.0x10^{6}$ [l]	$1.5x10^{3}$ [l]
He	$6.0\ x10^{3}$ [a]	$<3x10^{11}$ [h]	5.3 [l]	$2.8x10^{6}$ [l]	$1.1x10^{5}$ [l]
O	$4.4x10^{4}$ [a]	$<3x10^{11}$ [h]	$6.3x10^{-9}$ [l]	$7.4x10^{5}$ [l]	$4.0x10^{5}$ [l]
Na	$1.7\text{-}3.8x10^{4}$ [a]	$2x10^{11}$ [i]	$6.9x10^{-15}$ [l]	5500-14000 [m-e] 14000-38000 [m-t] 25000 [n]	$2.1x10^{7}$ [m-e] $7.4x10^{6}$ [m-t]
K	$3.3x10^{2}$ [b]	$1x10^{9}$ [b]		$9.0x10^{4}$ [l] 6700 [n]	$1.5x10^{5}$ [l]
Ar	$< 6.6x10^{6}$ [a]	$<2x10^{13}$ [h] $1.3x10^{9}$ [k]		$4.8x10^{5}$ [l]	$4.2x10^{7}$ [l]
^{20}Ne	$6x10^{3}$ day [c] $7x10^{5}$ night [c]	$3.7x10^{10}$ [h]			
H_2	$< 2.6x10^{7}$ [a]	$<8.7x10^{14}$ [h]		$2.3x10^{6}$ [l]	$8.8x10^{8}$ [l]
O_2	$< 2.5x10^{7}$ [a]	$<9.6x10^{13}$ [h]		$2.6x10^{5}$ [l]	$2.7x10^{9}$ [l]
N_2	$< 2.3x10^{7}$ [a]	$<1x10^{10}$ [h]		$4.1x10^{5}$ [l]	$4.5x10^{4}$ [l]
CO_2	$<1.6x10^{7}$ [a]	$<4.5x10^{13}$ [h]		$1.9x10^{5}$ [l]	$2.0x10^{8}$ [l]
H_2O	$< 1.5x10^{7}$ [a]	$<1x10^{12}$ [e] $<1x10^{14}$ [h]		$3.7x10^{5}$ [l]	$2.0x10^{8}$ [l]
OH	$1.4x10^{3}$ [d,e]	$>1x10^{10}$ [d,e]		$6.2x10^{5}$ [l]	$2.7x10^{6}$ [l]
Mg	$7.5x10^{3}$ [d]	$3.9x10^{10}$ [d]			
Ca	387 [d] <239 [f]	$<1.2x10^{9}$ [d] $< 7.4x10^{8}$ [e] $1.1x10^{8}$ [j]			
Fe	340 [d]	$7.5x10^{8}$ [d]			
Si	$2.7x10^{3}$ [d]	$1.2x10^{10}$ [d]			
S	$5x10^{3}$ [d] $6x10^{5}$ [g]	$2.0x10^{10}$ [d] $2.0x10^{13}$ [g]		$1.3x10^{5}$ [l]	$1.5x10^{5}$ [l] $1.5x10^{8}$ [l]
Al	654 [c]	$3.0x10^{9}$ [d]			

a *Hunten et al*. [1988]: measurements or upper limits

b *Potter and Morgan* [1988]

c *Hodges* [1974]: model abundance

d *Morgan & Killen* [1997]: model abundances

e *Killen et al*. [1997]: model abundances

f *Sprague et al.* [1993]: measured upper limit

g *Sprague et al*. [1995]: prediction

h *Shemansky* [1988]: Mariner 10 measurements

i *Killen et al.* [1990]: measured abundance

k *Killen et al*. [2002]: model abundance

j *Bida et al.* [2000]

l *Killen and Ip* [1999]

m *Huebner et al*. [1992] ionisation rates: experimental (e), theoretical (t) for quiet and active Sun

n *Cremonese et al*. [1997]

[*A. Milillo*, private communication]

Empirical model of proton fluxes in the equatorial inner magnetosphere: 2. Properties and applications

A. Milillo,[1] S. Orsini,[1] D. C. Delcourt,[2] A. Mura,[1] S. Massetti,[1] E. De Angelis,[1] and Y. Ebihara[3]

Received 12 July 2002; revised 31 October 2002; accepted 4 February 2003; published 2 May 2003.

[1] The most probable magnetospheric condition during solar minimum is investigated by using the empirical model of the equatorial proton fluxes presented by *Milillo et al.* [2001]. The model consists of several segments that reproduce the effects of different physical processes. Those segments describing particle injection and diffusion in the equatorial magnetosphere are considered. The model provides an overall picture of the magnetosphere plasma distributions, thus allowing estimates of the major physical parameters. From this statistical distribution we reconstruct the pattern of the electric field equipotential lines on the equatorial plane. We compute drift paths of test particles at different initial energies and positions, and we focus on both open and closed trajectories and examine through energy-time spectrograms typical features, like dawn-dusk asymmetries of particle transport or flux depletions at specific energies (ion spectral gaps). Some selected parameters of the model are properly varied in order to investigate its possible capability to reproduce different magnetospheric conditions. *INDEX TERMS:* 2740 Magnetospheric Physics: Magnetospheric configuration and dynamics; 2730 Magnetospheric Physics: Magnetosphere—inner; 2778 Magnetospheric Physics: Ring current; 2708 Magnetospheric Physics: Current systems (2409); 2760 Magnetospheric Physics: Plasma convection; *KEYWORDS:* ring current, empirical model, proton fluxes, proton distribution, electric potential model

Citation: Milillo, A., S. Orsini, D. C. Delacourt, A. Mura, S. Massetti, E. De Angelis, and Y. Ebihara, Empirical model of proton fluxes in the equatorial inner magnetosphere: 2. Properties and applications, *J. Geophys. Res.*, *108*(A5), 1165, doi:10.1029/2002JA009581, 2003.

1. Introduction

[2] *Milillo et al.* [2001] (hereafter referred as Paper 1) presented a new empirical model, based on measurements performed by the AMPTE/CCE/CHEM experiment; this model is able to reproduce an average global distribution of the proton fluxes at 90° pitch angle in the equatorial inner magnetosphere. The used dataset represented the most probable configuration (characterized by AE < 100 nT) during solar minimum. The model consisted of the sum of five distinct segments as a function of *L*-shell, energy, and MLT, dependent on 43 numerical factors.

[3] In principle the given factor values are able to simultaneously represent all the possible processes. More specifically, due to the data selection criteria, all of the large-scale spatial and temporal processes occurring during magnetic storms coexist into the model. It follows that this model should be unable to match any specific storm phase, unless the factor values are properly tuned. This has been already stated in Paper 1, where it is also explained that any ion population or plasma regime may be described by specific parts of the resulting function, thus allowing separate studies of specific processes. Basically, the analysis of the factors allows speculating on those physical quantities that play an important role in the magnetospheric dynamics.

[4] In this paper we will speculate on those segments (identified in section 2) describing the proton fluxes convected under the combined action of dawn-dusk electric field and magnetic field gradient, as well as those describing the proton fluxes diffused and accelerated by betatron processes due to the action of magnetic and electric field fluctuations [e.g., *Blanc et al.*, 1999].

[5] According to the storm picture of *Ebihara and Ejiri* [1998] and *Liemohn et al.* [1999] and to the IMAGE observations [*C:son Brandt et al.*, 2002], during the very first phases of a storm the particles are injected from the tail in open drift paths and are lost in the dayside magnetopause. Later, during the recovery phase, convection electric field weakens, the open trajectories become closed, and the ions are trapped in a symmetric ring current. Hence the diffused preexisting populations are swept out during the storm main phase and are recreated when the newly injected particles fall down into closed paths and have time to diffuse [*Kozyra et al.*, 2002]. Moreover, *Chen et al.* [1993] show that the

[1]Istituto di Fisica dello Spazio Interplanetario, CNR, Roma, Italy.
[2]Centre d'étude des Environnements Terrestre et Planétaires, CNRS, France.
[3]National Institute of Polar Research, Tokyo, Japan.

0148-0227/03/2002JA009581$09.00

trapped population at high energy increases during a storm. This population is due to diffused particles as well as to convected particles, and contribution of diffusion is more important when the storm main phase is longer [*Chen et al.*, 1994]. Hence it is possible that during the latest phases of a storm the injected and diffused populations are simultaneously present in the ring current region, where they slowly decay mainly through charge-exchange processes [*Daglis et al.*, 1999]. This picture fits with the model characteristics; hence it is reasonable to consider that the model described in Paper 1 is basically depicting a quiet magnetosphere, just refilled by storm injection.

[6] In order to test the model capability to represent local and instantaneous proton distributions, a comparison between the modeled flux and an example of proton spectra, collected by the CRRES/MICS instrument during a quiet time period will be shown in section 2.

[7] In section 3 an estimation of the major physical parameters associated to the model will be carried out. The quantitative analysis of these physical parameters (density, mean kinetic energy, magnetic moment, magnetic pressure, ring current intensity) can provide an overall picture of a late recovery phase magnetosphere and, more generally, of the most probable magnetospheric configuration where the disturbances may develop.

[8] The uncertainty of the equatorial electric field estimates is one of the most crucial difficulties when attempting to model the ring current region. Theoretical estimations of the various components of the total electric field [e.g., *Volland*, 1978] are only a first-order approximation for describing the real processes in the inner magnetosphere. On the other hand, empirically derived models [e.g., *McIlwain*, 1972] have been shown to be more appropriate to depict the magnetospheric conditions [*Liemohn et al.*, 2001]. In section 4 we will examine the equatorial electric field pattern as derived by the average kinetic energy equipotential lines.

[9] In section 5, by using these electric potential contours, we will compute the single particle drift paths at different initial energies and positions. We will focus on both open and closed drift paths and examine, through energy-time spectrograms, well-established observational features such as dawn-dusk asymmetries of particle transport [*Sheldon and Hamilton*, 1993; *Milillo et al.*, 1996] or flux depletions at specific energies (ion gaps) [*Kovrazhkin et al.*, 1999; *McIlwain*, 1972].

[10] In section 6 we will analyze the effect induced in a made-up magnetosphere obtained by varying the model according to three factors, sensitive to magnetospheric parameters and/or processes.

[11] We will conclude by summarizing the main results in section 7.

2. Modeled Proton Distribution

[12] As stated in Paper 1, the plasma population that originates from the action of convection is described by a wide gaussian function versus L-shell at energies of tens of keV that exhibits a cut-off close to the Earth ($L \sim 3$) (that is, the CO + G2 functions weighted by a step function), while the diffused population is described by another gaussian function at higher energies that has an energy versus L dependence (that is, the G3 function). Hence in the following we will use a subset of the model that includes only the mentioned functions. Since the L-shell (l) used in the original AMPTE/CCE/CHEM dataset has been derived by applying a simple dipolar magnetic field, we make the assumption that it corresponds to the geocentric distance (r) when mapped onto the equatorial plane (that is, $l = r$). Hence the proton differential flux per energy and steradiant, f, that we will consider in the following is

$$f(l) = \left[\mathrm{AG2}\cdot\exp\left(-\frac{(l-\mathrm{PG2})^2}{2\cdot\mathrm{WG2}^2}\right)+\mathrm{CO}\right]\cdot\exp\left(-\frac{\mathrm{IS}^2}{(l-\mathrm{PS})^2}\right) + \mathrm{AG3}\cdot\exp\left(-\frac{(l-\mathrm{PG3})^2}{2\cdot\mathrm{WG3}^2}\right) \quad (1)$$

The log-energy (e) and MLT (h) dependences of the factors are shown in Figures 4 and 9 of Paper 1.

[13] The proton fluxes at eight selected MLT are shown in a color-coded picture (Figure 1) as a function of l (between 3 and 9.5) and e (ranging from 3 to 5.5 log(eV)). The diffused population (G3), characterized by increasing energy versus geodistance decreasing, is clearly distinguishable; the more intense injected population (CO + G2) is observed at lower energies and is characterized by nearly constant energy versus geodistance. While the diffused population is almost symmetric in MLT, the second one is affected by the dawn-dusk asymmetry. The two populations mix up in the outer regions ($l > 5$), while they are clearly separated in the inner regions. For this reason we prefer to analyze the two populations together, by keeping in mind that the diffused population originates from the other one and that it is well defined only within $l < 5$.

[14] Generally, the particles move in the inner magnetosphere accordingly to the conservation of the first adiabatic invariant; hence it could be interesting to map the energy differential fluxes at different magnetic moments $\mu = \frac{K_\perp}{B} = \frac{K}{B}$, where K is the kinetic energy of the 90° pitch-angle particles. In this way, by analyzing the energy differential flux intensities, which are proportional to the absolute velocity distribution function, the phase-space regions occupied by any specific population convected or diffused in the magnetosphere may be studied. Since the modeled proton fluxes refer to magnetospheric activities with AE < 100 nT, we have decided to use the *McIlwain* [1972] magnetic field model associated to quiet conditions. In Figure 2 the differential flux at MLT 0000 as a function of l and μ (Figure 2a), and four equatorial maps of the proton differential fluxes, each at a fixed μ value (Figures 2b, 2c, 2d, and 2e), are shown.

[15] From this analysis it is not possible to trace the particle trajectories or to investigate the process able to produce the observed distributions, anyway some considerations on the possibility of populating each magnetospheric region with particles at specific μ are possible. Moreover, the relative intensification of different regions could provide information on the source location. The particle paths will be analyzed with more detail in section 5, by using the equation of motion.

[16] In Figure 2a, the two CO + G2 and G3 populations exhibit distinct μ versus l trends at $l < 5$. The former decreases versus lower l, generally implying a nonconservation of the first adiabatic invariant. While the latter slowly increases versus lower l, although it is nearly constant at μ

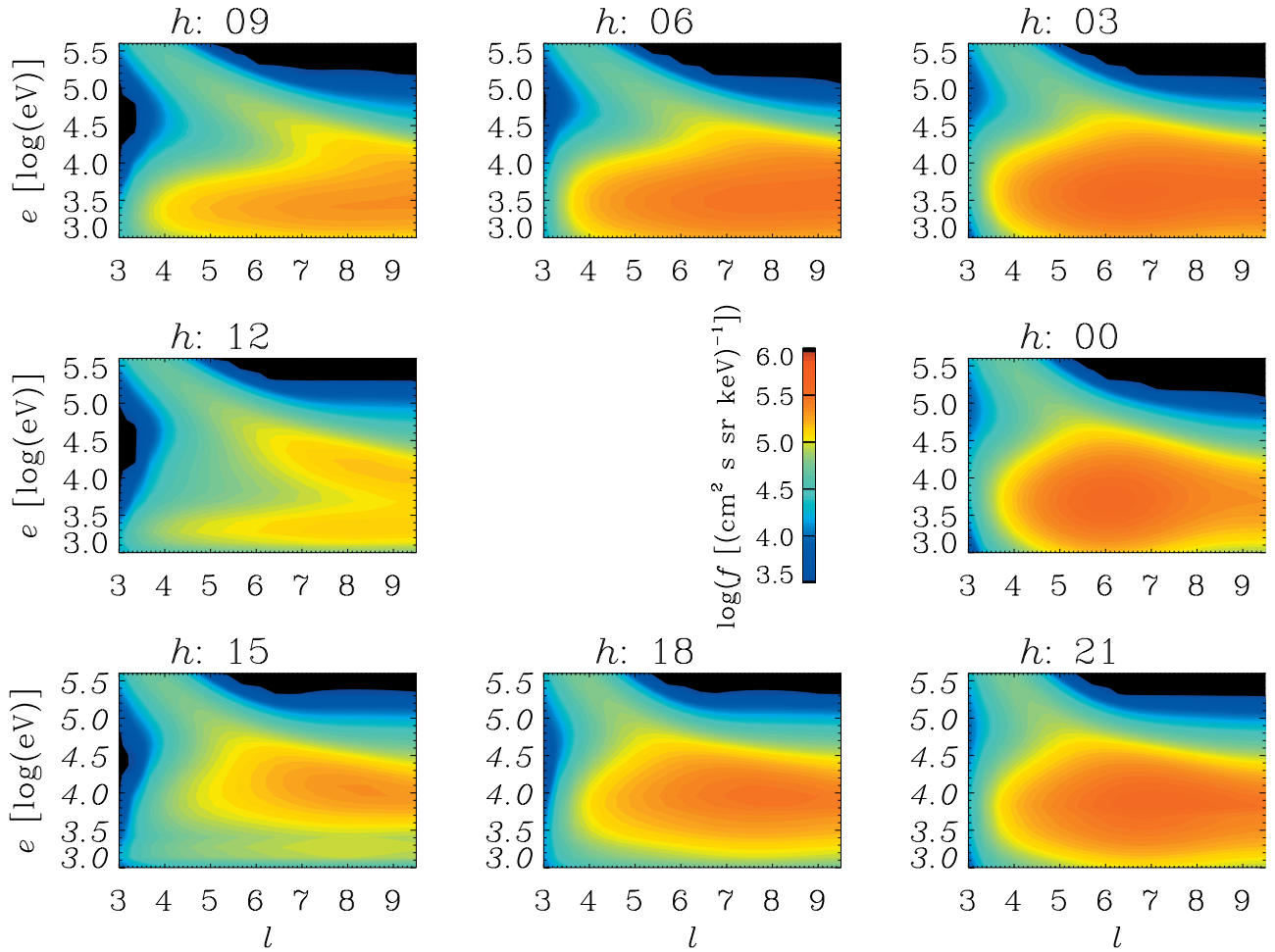

Figure 1. Color-coded picture of the modeled 90° pitch angle differential proton fluxes as a function of *l* and *e* at different *h*.

~0.4 keV/nT. This essentially implies the μ conservation; nevertheless the diffusion coefficient does not seem to follow exactly the standard diffusion law.

[17] Possible different interpretations could be given for the apparently contradictory behavior of the G3 function. *Sheldon* [1994] analyzed a quiet time dataset derived by the same AMTE/CCE/CHEM data used to obtain our averaged dataset. His analysis of the high-energy distribution evinced that below *L*-shell = 6, internal (probably ionospheric) electric field fluctuations cause most of the cross-*L* transport and that the radial trend of these ionospheric fields suggests that they are shielded from the magnetosphere.

[18] It could be noticed that at higher μ (~1.077 keV/nT, Figure 2b) the protons do not enter into the inner magnetosphere. On the contrary, the μ ~ 0.4 keV/nT proton population shown in Figure 2c is distributed inside the whole inner magnetosphere, thus implying that it is probably trapped into closed trajectories so that it has time to diffuse across the magnetic field lines. This population reflects the G3 distribution identified at high energies in Figure 1. Since the magnetic energy is dominant with respect to the electric energy, the flux isocontours of the high-energy particles follow the *B*-field equipotential lines. The observed noon-midnight asymmetry reflexes the stretched magnetic filed configuration.

[19] In Figure 2d (μ ~ 0.18 keV/nT) we can clearly see a dawn-dusk asymmetry so that the flux is stronger in the dusk side. Furthermore, we can see that particles characterized by this magnetic moment populate the *L*-region between 5 and 10. At lower μ (~0.04 keV/nT, see Figure 2e) the fluxes are again MLT dependent, like the case shown in Figure 2d. Actually, in opposition to previous case, the flux is more intense in the dawnside; in fact, these populations are sensitive more to electric field convection than to gradient/curvature drifts. They populate the inner regions; nevertheless, the source of these particles is not clearly distinguishable, since the fluxes peak inside the simulation region. It is possible that these particles have been transported inside the magnetosphere during more disturbed magnetospheric conditions (not included in the AMPTE/CCE/CHEM data set) and subsequently that they have been trapped when the magnetospheric activity has relaxed. Alternatively, they could be the result of processes that cause the violation of μ conservation, for instance Coulomb collisions.

[20] A comparison between the modeled flux and the proton spectra collected by the CRRES/MICS instrument, in the energy range 20–300 keV, at three different MLT and *L*-shells, during a quiet time period (18 April 1991), is shown in Figure 3. Within the energy range of the instru-

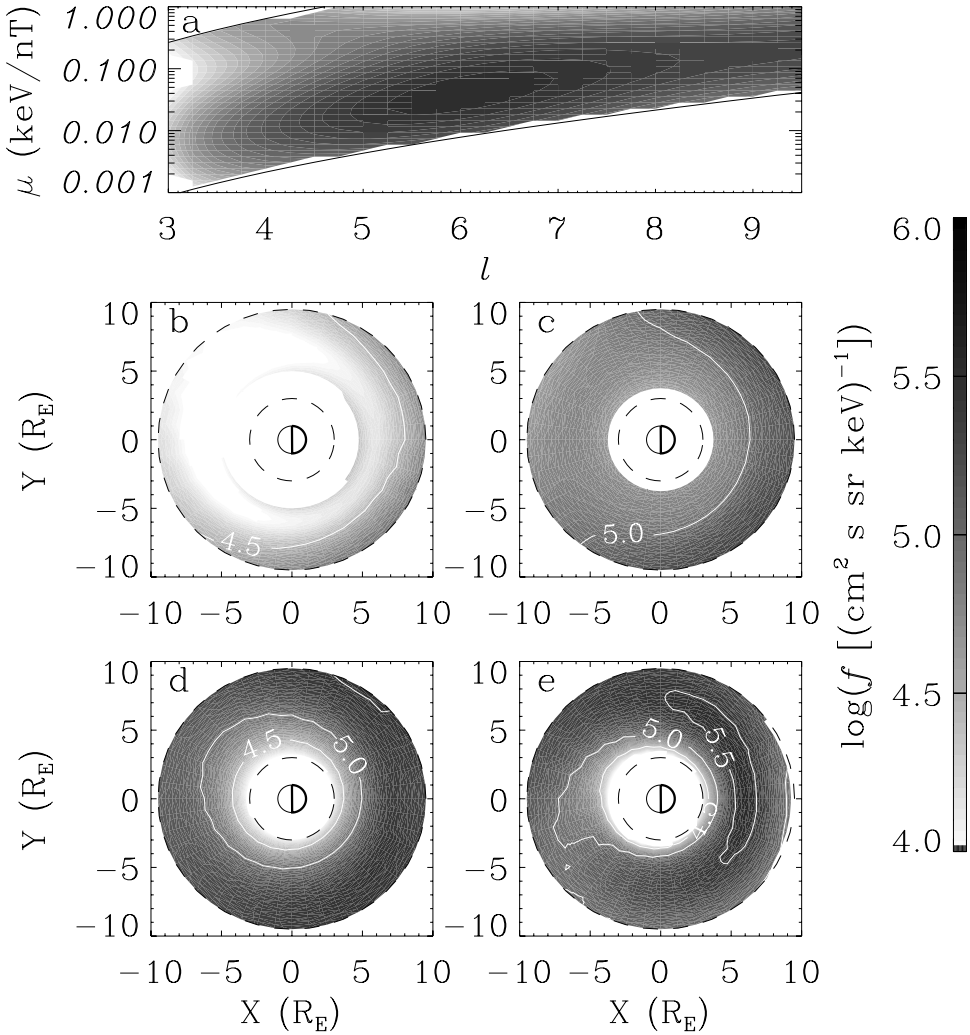

Figure 2. (a) Grey-scaled contours of the differential proton fluxes at MLT 0000 as a function of l and μ. The solid lines delimit the energy range 1–300 keV of our model. Lower panels: grey-scaled maps of the equatorial differential proton fluxes at fixed μ value: (b) μ = 1.077 keV/nT, the energy corresponding to the maximum flux (in the outer regions of the night side) is 29 keV; (c) μ = 0.442 keV/nT, the energy corresponding to the maximum flux (in the outer regions of the night side) is 12 keV; (d) μ = 0.181 keV/nT, the energy corresponding to the maximum flux (close to the outer regions of the midnight-dusk side) is ~6 keV; (e) μ = 0.038 keV/nT, the energy corresponding to the maximum flux (inside the night side magnetosphere) is ~5 keV. The radial distances 3 and 9.5 R_E are evidenced with dashed circles. The Earth is schematically shown at the center of each panel, the bold hemisphere indicating the night side.

ment the main portion of the CO + G2 population is hardly discernable because the peak of the distribution is located below the low energy limit. However, the most energetic G3 distribution as well as the high-energy portion of the CO + G2 is identifiable in the observed profiles. We may notice that generally the modeled spectra are hotter than the observations. This is probably due to the effect of the averaging process. Nevertheless, we notice that the spectra are generally well reproduced, especially considering that we are comparing local and instantaneous spectra with spectra averaged over more than 2 years.

3. Magnetospheric Parameters

[21] Aiming to reconstruct the major magnetospheric parameters in order to obtain an average global view of the inner equatorial magnetosphere, we first need to compute the velocity distribution function f(v). This function is related to the differential flux f, shown in equation (1), through the following expression:

$$\mathrm{f}(v,r) = f\, m\, v^{-2} \tag{2}$$

where m and v are particle mass and flow velocity, respectively.

[22] To compute the particle density and other physical parameters we need to know the angular distribution of the flux, that is, the pitch angle distribution. Presently, the model is not yet able to reproduce the pitch angle dependence; hence we must do some guessing. Here, for simplicity we assume an isotropic flux, that is, a flat pitch angle profile. This assumption is more appropriate during per-

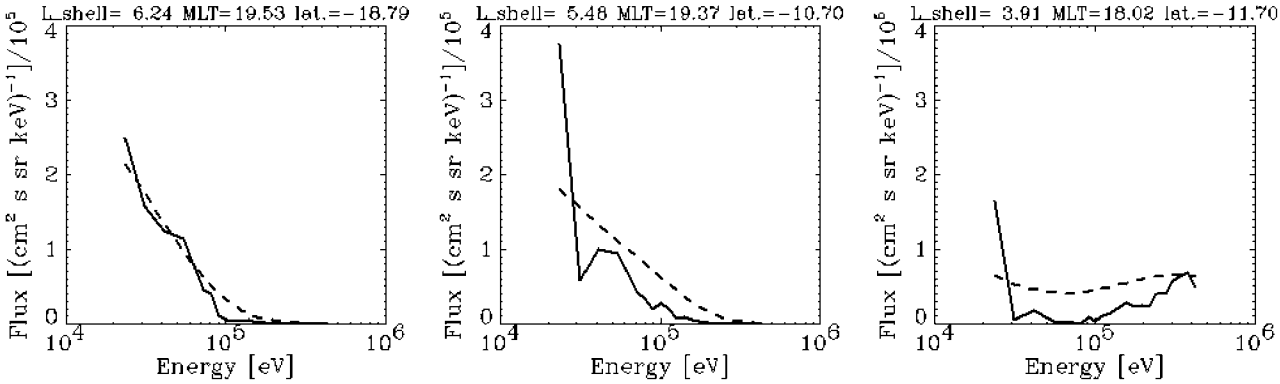

Figure 3. Comparison between modeled (dashed lines) and observed (solid lines) proton spectra at three different MLT and L_shells. The data were collected by the CRRES/MICS instrument in the energy range 20–300 keV, during a quiet time period (18 April 1991).

turbed periods at l above 4 [*Lui et al.*, 1987]; anyway, as a first-order analysis, we can neglect such anisotropies.

[23] Under the previous assumption, we can derive the particle density N:

$$N = 4\pi \int \mathrm{f}(v,r)v^2 dv \tag{3}$$

[24] The global equatorial particle density contours are shown in Figure 4. The particles are denser in the night sector, close to midnight at $r = 5\ R_E$. In fact, this is the region where the bulk of the particles are injected from the tail.

[25] The energy density ε can be easily computed by the following expression:

$$\varepsilon = 2\pi m \int \mathrm{f}(v,r)v^4 dv \tag{4}$$

[26] If the pitch angle distribution is isotropic, the normal magnetic pressure $P_\perp$ is equal to the parallel pressure $P_\parallel$, and it can be expressed:

$$P_\perp = P_\parallel = \frac{2}{3}\varepsilon \tag{5}$$

[27] In Figure 5a the normal pressure is represented in a color-coded picture. The pressure values range between 2 and 7 nPa. In previous literature the value of the modeled ring current pressure [e.g., *Ebihara and Ejiri*, 2000] as well as the empirical estimates of the quiet time plasma pressure [*Lui and Hamilton*, 1992], are of the same order of magnitude, even if during a storm the estimations can exhibit values up to 10 nPa. The pressure shown in Figure 5a increases with distance between $r = 3$ and 4 R_E, where it reaches its maximum value, and then it starts decreasing. These results are in good agreement with other estimates recently shown in the literature [e.g., *Lui and Hamilton*, 1992; *De Michelis et al.*, 1999; *Ebihara and Ejiri*, 2000; *Liemohn et al.*, 2001]. The pressure profile versus MLT is mainly symmetric, although it shows a little asymmetry; in fact, in the dusk-midnight sector it is a little bit more intense. This pressure profile is comparable to the modeled pressure during the late recovery phase [*Ebihara and Ejiri*, 2000; *Liemohn et al.*, 2001], giving confidence that the current model, in its present configuration, roughly depicts a late recovery phase magnetosphere.

[28] The normal current $J_\perp$ is

$$\mathbf{J}_\perp = \frac{\mathbf{B}}{B^2} \times \left[\nabla P_\perp + \left(P_\parallel - P_\perp\right)\frac{(\mathbf{B}\cdot\nabla)\mathbf{B}}{B^2}\right] \tag{6}$$

being positive for westward currents. By assuming isotropic pitch angle distributions, the last term in equation (6) can be neglected; hence the normal current can be simply written as

$$J_\perp = -\frac{1}{B}\frac{\partial P_\perp}{\partial l}. \tag{7}$$

[29] In the present computations the magnetic field modeled by *McIlwain* [1972] that refers to quiet time conditions

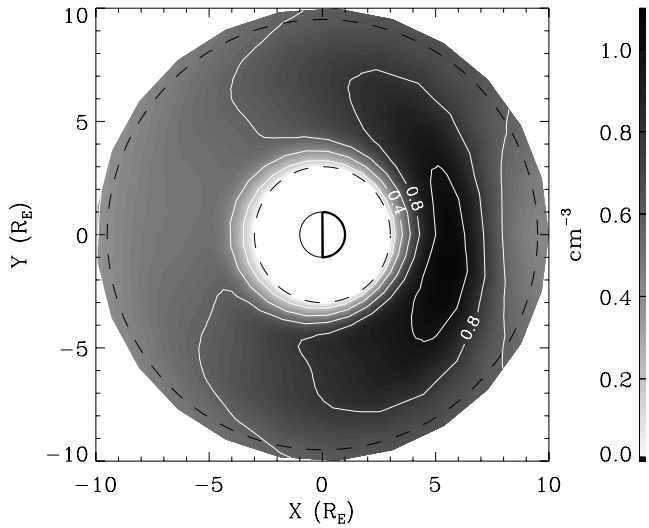

Figure 4. Gray-scaled picture of the modeled proton density in the equatorial plane. As in Figure 2, the r = 1, 3, and 9.5 R_E shells are shown.

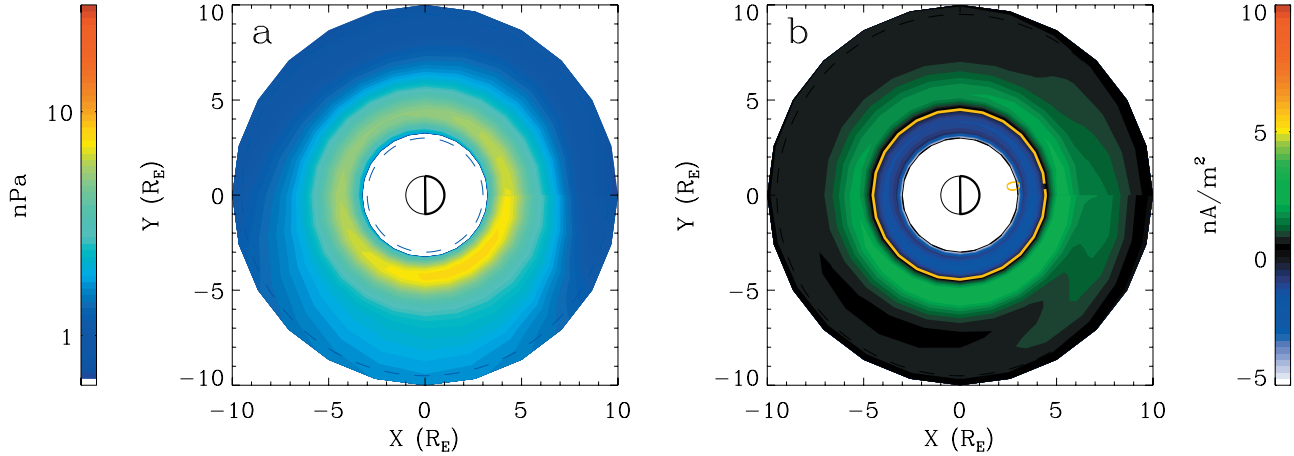

Figure 5. Color-coded pictures of (a) normal pressure and (b) normal current density computed by using the empirical model. Westward currents are positive. As in Figure 2, the r = 1, 3, and 9.5 R_E shells are shown.

is adopted. Such a quiet time configuration is the most probable one, as shown in Paper 1.

[30] Figure 5b shows the normal current derived from our model. It is clear that a weak eastward current is present inside $r = 4\ R_E$, while a weak westward current is present at higher r. The westward current exhibits MLT asymmetry; in fact, it reaches 4 nA/m^2 in the midnight-dusk sector, while it takes lower values in the noon-dawn sector. Eastward and westward currents up to 10 nA/m^2 are predicted in a similar configuration during late recovery phase periods by the simulations of *Ebihara and Ejiri* [2000] and of *Kozyra et al.* [2002]. Probably, the magnitude of the current in our computations is less intense due to the model average architecture. Our calculations obtained by this empirical model validate the hypothesis of a not negligible presence of a partial ring current that resides in the dusk-midnight region, even during recovery phases.

[31] In Figure 6 the mean kinetic energy

$$\overline{K} = \frac{\varepsilon}{N} \tag{8}$$

is mapped. The equipotential lines show that the kinetic energy is higher in the inner region and decreases with distance. Even for these parameters, a clear MLT asymmetry can be outlined. At dusk, the mean kinetic energy does not extend below 20 keV, while at dawn it reaches lower values. This is a clear evidence of the heating/cooling effect due to the adiabatic motion of the plasma when a dawn-dusk electric field is present [*Sheldon and Hamilton*, 1993; *Milillo et al.*, 1996]. This argumentation will be more stressed in the next section.

[32] Figure 7 maps the mean first adiabatic invariant at 90° pitch angle:

$$\bar{\mu} = \frac{\overline{K}}{B} \tag{9}$$

[33] The mean μ values are almost constant around 0.2 keV/nT. This value increases only in the dusk outer region, where it reaches 0.6 keV/nT. The small variation of the mean magnetic moment in the inner regions indicates, on average, that plasma originating from similar sources (characterized by a certain mean magnetic moment) fills these regions. A simple interpretation of the mentioned uniformity is that the particles are mostly trapped. As a matter of fact, the contribution of the high-energy diffused population dominates in equations (8) and (9). The magnetic moment variation in the dusk side, at higher distances, shows that particles with higher μ populate these regions, probably through open trajectories.

4. Electric Potential Model

[34] In this Section a simple electric potential derivation, by using a few assumptions on the magnetospheric conditions, is presented. If we consider an almost quiet time

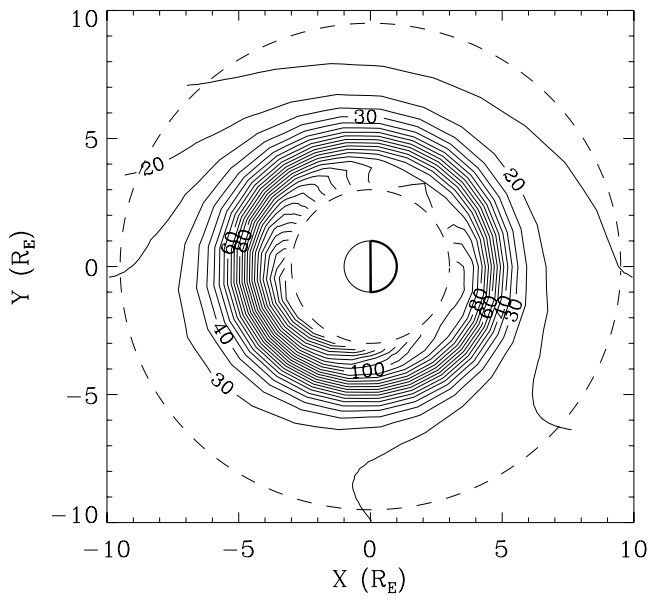

Figure 6. Contour plot of the mean kinetic energy (keV) as derived by using the empirical model. As in Figure 2, the r = 1, 3, and 9.5 R_E shells are shown.

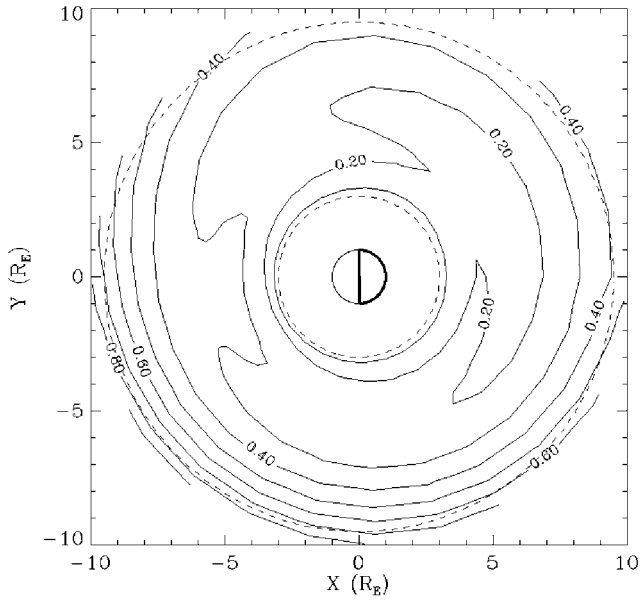

Figure 7. Contour plot of the mean first adiabatic invariant (keV/nT) at 90° pitch angle as derived by using the empirical model. As in Figure 2, the r = 1, 3, and 9.5 R_E shells are shown.

magnetosphere, we can assume that (1) there is no electric field parallel to B; (2) the electric and magnetic fields are time independent; (3) the particle motion is adiabatic, particles not involved in loss processes maintain constant the first magnetic moment (μ) and the total energy; and (4) the protons originate from a localized region in the tail with a gaussian-like energy distribution.

[35] Given the previous assumptions, the whole inner magnetosphere is populated by protons exhibiting distributions with the same average total energy. Hence we can argue that particles with similar kinetic energies and similar pitch angles (e.g., 90° at equator) originating from neighboring regions are transported toward similarly localized regions in the inner magnetosphere. It follows that we may establish a more or less direct relationship between initial and final kinetic energies as well as regions of space. However, since in this empirical model the injected and the diffused populations that are transported under different magnetospheric conditions coexist and since the diffused population originates by processes that do not conserve the total energy, we assume that where these two populations are decoupled (i.e., the distribution is no more single, at $l < 5$), our approach is no more valid.

[36] The total energy (W) is given by the sum of the kinetic energy (K) and the electric potential (U) energy:

$$W = K + qU \tag{10}$$

where q is the particle charge.

[37] If the particles move in the magnetosphere with total energy conservation, then a variation of the electric potential corresponds to variation of the kinetic energy:

$$\Delta K = -q\Delta U \tag{11}$$

Hence the equipotential lines of the mean kinetic energy, shown in Figure 6, have the same shape of the electric equipotential lines. A kinetic energy difference of 1 keV corresponds to an electric potential drop of −1 kV. We may estimate that the total dawn-dusk potential drop is ∼15 kV, corresponding to a mean electric field of ∼0.1 mV/m. This estimation matches with a weak electric field characterizing the end of a storm [e.g., *Wygant et al.*, 1998; *Ejiri et al.*, 1978].

[38] However, the particle distributions do not conserve the average total energy in the whole magnetosphere, also due to loss processes. If we consider the major loss processes in the magnetosphere, we can see that charge-exchange acts at low energies and at low distances [e.g., *Daglis et al.*, 1999]. Coulomb collisions act in a similar way but with a minor contribution [*Ebihara et al.*, 1998]. The wave-particle interactions act at higher energy and higher latitudes but with a minor contribution during quiet time [e.g., *Daglis et al.*, 1999, *Jordanova et al.*, 1999, 2001].

[39] Hence if the previous assumptions are verified, the electric field equipotential pattern can be reconstructed in this straightforward manner in the outer regions of the inner magnetosphere ($5\ R_E < r < 9.5\ R_E$). As a matter of fact, there is a very good agreement between the modeled mean kinetic energy equipotential lines and the empirically derived electric potential lines as mapped by *McIlwain* [1972]. The model can be a useful tool to reproduce the global evolution of the electric potential pattern during storm development (our next future goal). Actually, the electric field could be underestimated, due to the fact that the assumptions listed in section 4 may be partially violated in real conditions. Anyway, these limitations of the proposed electric field model do not affect the intrinsic validity of this approach.

5. Particle Drift Path

[40] In this section, by using the single-particle code of *Delcourt et al.* [1992], we compute the trajectories of equatorially trapped protons in the quiet configuration of *Tsyganenko* [1989] magnetic field model. We consider that their magnetic moment remains constant and we use the guiding center approximation. In order to test the applicability of the electric potential model proposed in previous section, we check if the typical features observed in the magnetospheric plasma distributions are reproduced as obtained by other authors by using different electric potential models. Since the electric potential model derived in the previous section is valid only in the outer regions, in the inner regions we match this model with the *McIlwain* [1986] electric potential model for Kp = 2 (U_{MI}) by adding a potential drop offset $\Delta U = -17.5$. More specifically, we use the following expression.

$$U = \begin{cases} -K & -K \geq U_{MI} + \Delta U \\ U_{MI} + \Delta U & -K < U_{MI} + \Delta U \end{cases} \tag{12}$$

[41] We traced the forward trajectories of the outer night-side particles at energies between 1 keV and 10 keV (ΔK = 1 keV). In Figure 8 sample trajectories are traced from MLT 2200, 2300, 0000, 0100, 0200 and three initial

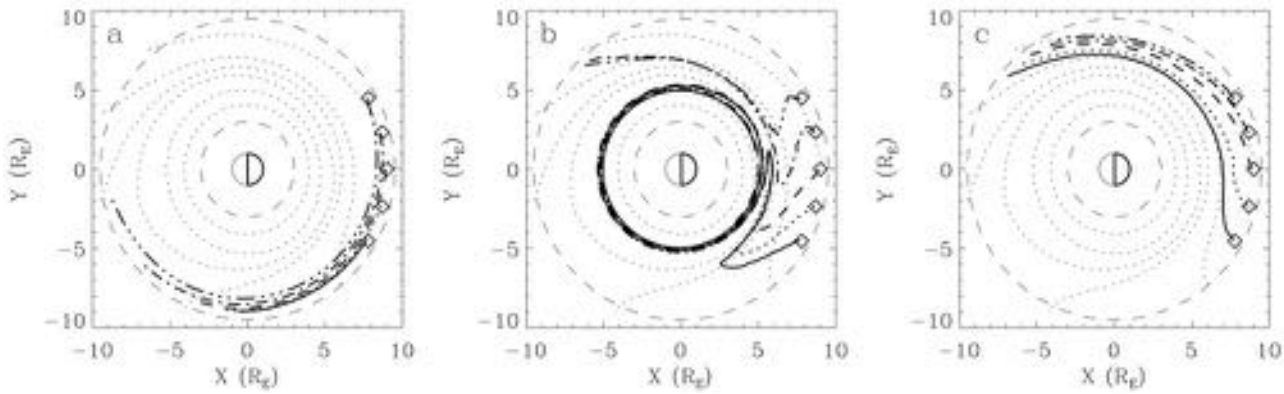

Figure 8. Samples of forward trajectories of the outer night-side particles traced from $r = 8.9$ R_E, MLT 2200, 2300, 0000, 0100, 0200 and initial energies (a) 10 keV, (b) 3 keV, and (c) 1 keV. The starting positions are labeled by diamonds. In the background the electric field equipotential lines derived from equation (12) are mapped by dotted lines. As in Figure 2, the $r = 1$, 3, and 9.5 R_E shells are shown.

energies 1, 3, 10 keV. The higher energy test particles (Figure 8a) exhibit open trajectories drifting toward the dusk magnetopause, in accordance with the simulations performed by *Takahashi and Iyemori* [1989]. This last behavior implies a sharp decrease of the 90° pitch angle particle flux (see Figure 2b and 2c), in agreement with the observed butterfly-shaped pitch angle distributions of the night-side particles at $l > 7$ [*Fritz et al.*, 2000]. We have found out that the threshold energy value between closed and open trajectories toward dusk is 5 keV. More generally, this study shows that, during quiet times, the particles at energy $\geq$10 keV, injected from the tail can reach the inner regions only through diffusion processes, in accordance with what we argued form Figure 2c, while the $\sim$3–4 keV particles are able to fill through adiabatic motion the outer part of the nightside magnetosphere (L-shell between 5 and 9), increasing their energy up to 20 keV (Figure 8b), as seen also in Figure 2d. On the contrary, the test particles with lower energy (<1–2 keV particles) cannot enter nor populate the inner regions during quiet times, since they are lost in the dawn side of the equatorial plane (Figure 8c), as proved by the maps of Figure 2e. It must be noticed that some of the traced trajectories seem to intersect the trajectory of themselves; this is due to the rough gridding steps that we have used in the electric potential computation in the code, anyway this does not modify the results of our qualitative analysis.

[42] In the dayside magnetosphere the modeled fluxes are significantly attenuated in the low energy range, within a MLT-dependent interval (see Figure 1). Actually, these flux decreases or gaps occur at higher/lower energies in the dawn/dusk sectors, respectively. Such features are in good agreement with in situ measurements both at high latitudes [*Kovrazhkin et al.*, 1999] and near the equator [*McIlwain*, 1972]. In the dayside sector, such spectral gaps are likely due to enhanced residence times (larger than the ion lifetime) in the magnetosphere [*Kovrazhkin et al.*, 1999] rather than to an inward limit of penetration from the magnetotail or transition from open to closed orbits [*Shirai et al.*, 1997]. Recently, *Buzulukova et al.* [2002] have analyzed accurately the ion gaps during quiet time, and they have found that the reproduction of this kind of gap is greatly sensitive to the convection model and to the assumed particle source. Aiming to verify the effectiveness of such an interpretation in the frame of our electric field derived configuration, in Figure 9 the backward trajectories of particles at energies between 1 and 19 keV ($\Delta K = 2$ keV) are traced from $r = 7.5$ R_E and MLT = 1000 (Figure 9a), 1200 (Figure 9b), and 1400 (Figure 9c). The trajectories are traced up to $r = 7.7$, since the ion loss rate is almost negligible out of this shell. We would like to notice that not only the particle residence time is important to determine the flux depletion but also the radial profile of the backward trajectory as well as the particle energy history play a role. In fact, the more the trajectory penetrates into the magnetosphere, the more the particle impacts on geocoronal neutrals. Actually, the geocoronal density decreases with Earth's distance as well as the rate of charge-exchange processes. On the other hand, particles with higher energy have lower charge-exchange cross sections and hence longer lifetimes. As a result, by comparing panels 2 and 3 of Figure 9 in the three (a, b, and c) configurations, it is clear that the residence times (within $r = 7.7$) always maximize at the energy of the flux minima. As stated by *Buzulukova et al.* [2002], the ion spectral gap observations verify the average convection pattern during quiet time. The identification of such gaps in our model based on average magnetospheric plasma data indicates that they frequently occur in the dayside magnetosphere.

Figure 9. (opposite) Backward trajectories of the dayside particles from $r = 7.5$ R_E, up to maximum 7.7 R_E for different energies, between 1 and 20 keV, for (a1) MLT 1000, (b1) MLT 1200, (c1) MLT 1400. The starting positions (i.e., final in time) are labeled by diamonds. As in Figure 8, the electric field equipotential lines are mapped by dotted lines, and the $r = 1$, 3, and 9.5 R_E shells are shown. Spectra of the modeled proton fluxes at the final position for MLT 1000, MLT 1200, and MLT 1400 are shown in (a2), (b2), and (c2) panels, respectively. Residence times versus energies are plotted in panels (a3) for MLT 1000, (b3) for MLT 1200, and (c3) for MLT 1300.

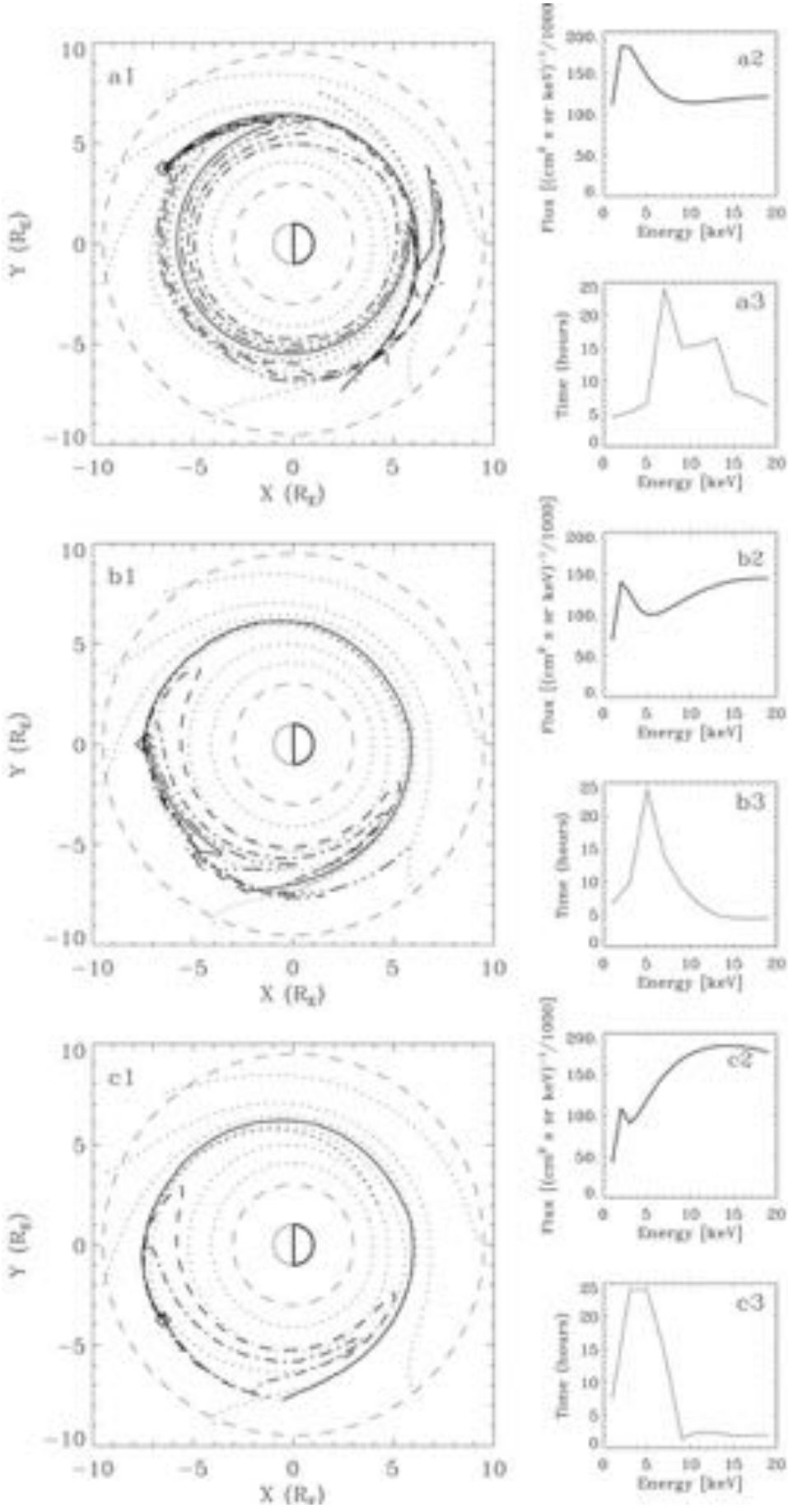
a1
b1
c1
Y (R_E)
X (R_E)
a2
b2
c2
Flux [(cm² x sr keV)⁻¹/1000]
Energy [keV]
a3
b3
c3
Time (hours)

6. Effects on the Model Induced by Variation of Selected Factors

[43] In Paper 1 the model consisted of the sum of five distinct segments as a function of *L*-shell, energy, and MLT, dependent on several numerical factors. In the present paper we have studied a subset of the model, consisting of those segments describing both the convected and the diffused proton populations. In the introduction section we noticed that this model should be unable to perfectly match any specific storm phase, unless the factor values are properly tuned. As a matter of fact, the analysis of the most sensible factors should allow speculating on the dominant physical regimes in any specific geomagnetic condition. For this purpose we will analyze the profiles of the mean kinetic energy, of the plasma pressure and of the ring current density as a function of these factors, selected as in the following.

6.1. Factors Identification

[44] Since the increase of the convection electric field produces new plasma entry, it is reasonable that, during perturbed periods the CO + AG2 intensity (factor CO_A + $AG2_A$, see Paper 1) could increase as well. Hence we introduce a new parameter:

$$B = (CO_A + AG2_A)^*/(CO_A + AG2_A)$$

where the asterisk indicates the modified factor. As an example, we will modify this factor by imposing B = 5.

[45] Figure 8 of Paper 1 shows the CO + AG2 contour plot as a function of MLT and *e*. Let us now consider the factor $COAG2_B$, i.e., the CO + AG2 maximum-flux energy. A direct consequence of the observed profile is that the two-dimensional semilog plot of $COAG2_B$ versus MLT exhibits a linear trend (see Figure 10). Since this MLT asymmetry is clearly due to the convection electric field intensity, we note that the intercept H of the semilog linear function $COAG2_B$ is strongly related to the asymmetry rate. Hence H is assumed to be a potential-drop sensitive factor. As an example, we will recompute the model by increasing the selected factor of 20%, that is:

$$C = H^*/H = 1.2.$$

[46] As soon as fresh injected plasma populates the magnetospheric equatorial plane, particle-trapping mechanisms should cause a significant increase of the G3 population. For this reason we consider factor AG3 described in Paper 1 as a useful quantity to estimate such an effect. For example we may assume:

$$D = AG3^*/AG3 = 3.$$

6.2. Magnetospheric Parameters Variation

[47] Figure 11 shows the modified configuration of mean kinetic energy (top), perpendicular pressure (middle), and ring current (bottom). The three columns (from the left) relate to B = 5, C = 1.2, and D = 3, respectively.

[48] The mean kinetic energy computed by applying B = 5, is shown in Figure 11a. With respect to the unmodified model (see Figure 6) we may notice that the enhanced population at low energy becomes dominant also in the inner regions so that the G3 high-energy population does not prevail any more. Anyway, the global dawn-dusk energy drop does not change significantly. Hence by increasing B the consequent dawn-dusk potential drop remains unmodified, whereas the plasma circulation in the inner region seems to be less effective in shielding the convection electric field. This could prove that the inner proton distributions are convected there by an electric potential profile different from the quiet time configuration. Figure 11b shows the mean kinetic energy contours, computed by assuming C = 1.2. The equipotential lines assume a more x-aligned configuration so that if we refer them to the electric potential, we can argue that this parameter is able to control the convection electric field intensity. This intensity deduced by this figure ranges between 0.3 mV/m in the night-side and 0.8 mV/m in the dayside out of distances of 6 R_E. These values are a little bit lower than the ones estimated during major storms (up to 1 mV/m at geosyncronous distances around midnight). The reason of this could consist in different argument. First of all, the inner configuration, where major electric field are foreseen, could not be correctly reconstructed; furthermore, as stated before, probably the absolute value of the electric field is a little bit underestimated, moreover other parameters in the empirical model related to the two populations described could play a role. If the model is modified in order to intensify the G3 population, specifically D = 3, the kinetic equipotential lines assume a more circular symmetry, also in the outer regions as shown in Figure 11c. This configuration could be referred to a recovery time magnetosphere, thus evidencing that the convection electric field gives a minor contribution during this phase.

[49] The pressure profile, computed by applying B = 5, as shown in Figure 11d, exhibits a MLT asymmetry. It reaches its maximum value (around 12 nPa) at $r \cong 4.5$ R_E and MLT $\cong$ 2000. The intensity is comparable to the pressure modeled by *Ebihara and Ejiri* [2000] during the main phase of the 10–11 April 1997 storm; the intensification at dusk is in accordance with the recent ring current models and the geodistance of the maximum intensity is comparable to the maximum energy density modeled by *Liemohn et al.* [2001]. The pressure slowly decreases with distance; at

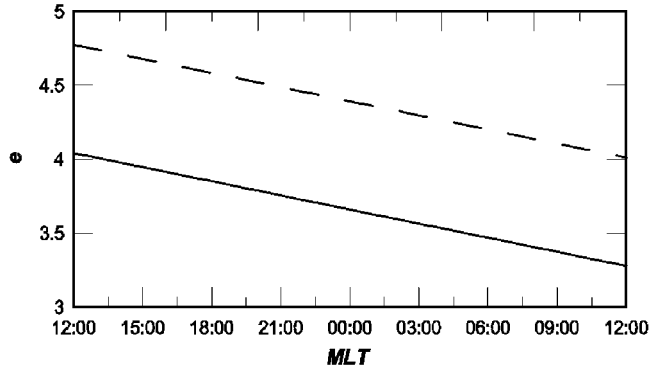

Figure 10. Unmodified factor $COAG2_B$ (solid line) and modified factor with C = 1.2 (dashed line), plotted as a function of *MLT* and *e*.

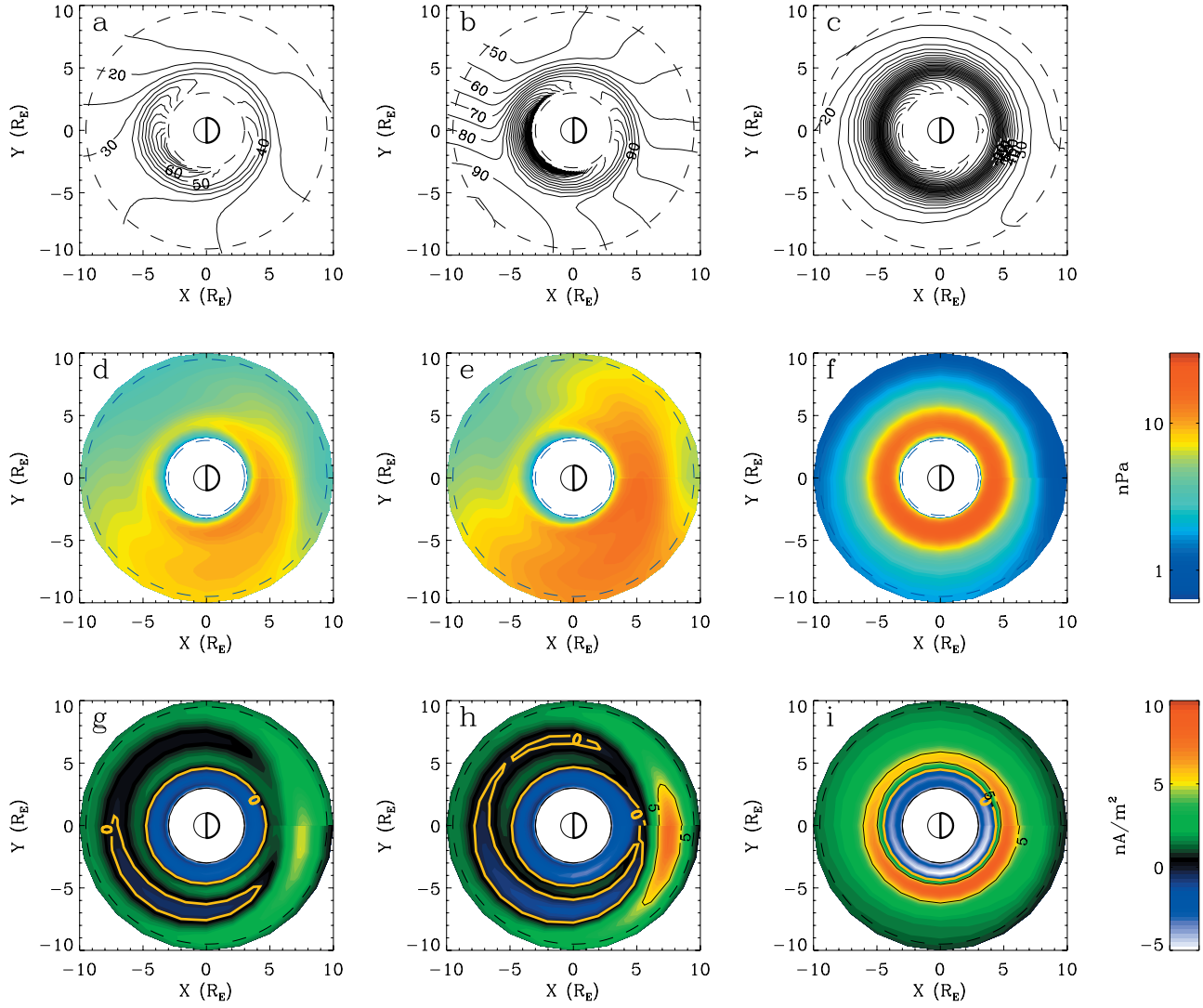

Figure 11. Modified configuration of mean kinetic energy (top panels), perpendicular pressure (middle panels) and ring current (bottom panels). The three columns (from the left) relate to B = 5, C = 1.2, and D = 3, respectively. As in Figure 2, the r = 1, 3, and 9.5 R_E shells are shown.

$r \cong 8$ R_E it becomes 50% of maximum. Conversely, in the other mentioned models the pressure decreases more abruptly so that at the given distance it is reduced by a factor of 10. The perpendicular pressure computed by applying C = 1.2 is shown in Figure 11e. The pressure asymmetry is evident also in this configuration. The magnetospheric pressure increases, and in the dusk-midnight sector it reaches 15 nPa. Anyway, we notice a broad increase of the pressure in the whole inner magnetosphere. The pressure profile shown in Figure 11f, is obtained by assuming D = 3; it grows up to more than 20 nPa in the dusk-midnight sector, and conversely to Figure 11d and 11e, it seems more concentrated in the inner regions below r = 5 R_E, and shows up a relevant decrease of a factor of 10 at r = 8 R_E. This MLT asymmetry is a direct consequence of the asymmetric structure of the high-energy population indicated in the original averaged AMPTE/CCE/CHEM dataset. Generally, this profile is similar to the theoretical pressure profiles derived by *Ebihara and Ejiri* [2000], even if our peak intensity is located closer to the Earth. Since the simulations presented in that paper include only convection without diffusion, it is likely that the G3 population is not only caused by diffusion processes so that the lower energies are partially populated by ions convected inward along open trajectories (as a matter of fact the G3 is superposed to the CO + G2 at lower energies/higher l). This interpretation agrees with the scenario proposed by *Chen et al.* [1993]; according to their studies, for particles at $\mu < .01$ keV/nT ($K < 110$ keV at $l \approx 3$) the inward transport is mainly convective, at $.01 < \mu < .25$ keV/nT (110 keV $< K < 280$ keV at $l \approx 3$) there is a transition between direct convective access and radial diffusion, and at $\mu > .25$ keV/nT ($K > 280$ keV at $l \approx 3$) diffusion becomes predominant.

[50] The equatorial perpendicular current distribution, shown in Figure 11g and 11h, exhibits several asymmetric structures, located at different radial distances. In the outer regions a westward partial ring current peaks in the night sector, reaching in the two panels $\sim$5 and $\sim$8 nA/m^2, respectively. This partial current could be related to the equatorial closure of the Region 2 field-aligned currents

[*Schield et al.*, 1969; *Zmuda and Armstrong*, 1974] that are always present when convection is strong, as seen by polar-orbiting spacecraft [*Blanc et al.*, 1999]. Close to this current, at lower distances, an eastward current, peaking in the dusk sector ($\sim$3 nA/m^2), extends up to 8 R_E. By looking at the panels, especially at Figure 11g, we may notice a sort of vortex in the dusk-noon sector, *L*-shell 5–7. Actually, this kind of vortex could be the product of diamagnetic effects observed especially during perturbed periods [e.g., *Smith et al.*, 1960; *Cahill*, 1966, 1973; *Potemra at al.*, 1985; *Wygant et al.*, 1998; *Terada et al.*, 1998; *Tsyganenko et al.*, 1999] and just theoretically computed by *Ebihara and Ejiri* [2000]. In fact, as stated by *Ebihara and Ejiri* [2000], the magnetospheric currents would produce, in the dusk-noon sector, magnetic depressions and intensifications. These locally induce ion drifting clockwise around the magnetic depressions and vice versa ion drifting anticlockwise around the magnetic "hills."

[51] In the inner regions two other current systems, less intense and more isotropic, can be identified. The external one (more evident in Figure 11g) moves duskward and exhibits a light asymmetry in the dusk sector; while the most internal current turns eastward, again peaking in the dusk sector ($\sim$4 nA/m^2). The two current systems just described are much more enhanced and asymmetric in Figure 11i (from 5 nA/m^2 at 0700 to 9 nA/m^2 at 1900), where the G3-related D parameter is increased. From the previous considerations it follows that this asymmetric partial ring current probably reproduces the current generated by the particles injected from open trajectories directly in the inner regions.

7. Summary and Conclusion

[52] This paper may be considered as the continuation of Paper 1. There, we showed the architecture of an empirical model, developed by best-fitting average in situ proton fluxes observed by AMPTE-CCE/CHEM. Here, we have interpreted the model major outcomes, by computing on a global scale the physical parameters characterizing the inner equatorial magnetosphere.

[53] In the following, the major results are listed.

[54] 1. We have outlined the presence in the model of two main proton populations, related to magnetospheric injection and diffusion, respectively. By assuming that these populations are the major magnetospheric contributors, some relevant magnetospheric parameters have been derived: proton density, mean kinetic energy and magnetic moment, perpendicular pressure and current density. The showed contours generally reproduce the reference behaviors, theoretically predicted during low geomagnetic activity (i.e., end of recovery phases).

[55] 2. A new electric potential model, simply derived from the mean kinetic energy maps, has been proposed. This model evidences the actual dawn-dusk and noon-midnight asymmetry of the electric potential in the inner magnetosphere. The contours, basically comparable to the *McIlwain* [1972] empirical model, are valid down to $l\sim5-6$ and at lower distances can be well matched to the quiet time *McIlwain* [1986] model. This map can be directly traced from the proton energy spectra effectively measured on the equatorial plane, in any configuration.

[56] 3. By mapping the magnetic moment and by tracing the particle drift pattern, we have seen that the model predicts the entrance of particles with $\mu \cong 0.14$ keV/nT. On the contrary, particles with higher magnetic moment have open trajectories so that they are convected duskward and vanish in the duskside magnetopause; and the particles with lower μ should be convected dawnward and lost in the dawnside magnetopause. Nevertheless, such particles may populate the inner regions under different conditions.

[57] 4. We have shown that the analysis of three sensible factors allows speculating on the dominant physical regimes in any specific geomagnetic condition. (1) The intensification of the flux of the convected population, typical in a perturbed magnetosphere, produces additional current systems. In particular, we observe currents related to diamagnetic effects as well as the equatorial closure of the enhanced Region 2 field-aligned currents. (2) The intensification of the diffused high-energy population produces a partial ring current, actually foreseen during storm-time periods. (3) The electric potential intensity is controlled by a third parameter, described in Section 6.

[58] The shown analysis is presently limited to the study of 90° pitch angle proton equatorial distribution; hence the computation of the physical quantities could be affected by other contributions. For instance, since the oxygen ion density is relevant during major storms [*Daglis*, 1997], the previous considerations could be subjected to modifications when the storms are more intense. The extension of the present model to different pitch angles and ion species will be performed in future studies.

[59] In conclusion, we want to remark that this empirical model exhibits an interesting potential capability in describing the ring current dynamics. Hence in a further paper we will apply the model for studying the time development of geomagnetic storms, as traced by in situ satellite data.

[60] **Acknowledgments.** The authors are grateful to Theodore Fritz (who also brought to our attention the paper by *McIlwain* [1972]). We thank Axel Korth and Chris Mouikis for providing the CRRES/MICS data.

[61] Lou-Chuang Lee thanks Masaki Ejiri and another reviewer for their assistance in evaluating this paper.

References

Blanc, M., J. L. Horwitz, J. B. Blake, I. Daglis, J. F. Lemaire, M. B. Moldwin, S. Orsini, R. M. Thorne, and R. A. Wolf, Source and loss processes in the inner magnetosphere, *Space Sci. Rev.*, *88*, 137–206, 1999.

Buzulukova, N. Y., Y. I. Galperin, R. A. Kovrazhkin, A. L. Glazunov, G. A. Vladimirova, H. Stenuit, J. A. Sauvaud, and D. C. Delcourt, Two types of ion spectral gaps in the inner magnetosphere: Interball-2 observations and modeling, *Ann. Geophys.*, *20*, 349–364, 2002.

Cahill, L. J., Jr., Inflation of the inner magnetosphere during a magnetic storm, *J. Geophys. Res.*, *71*, 4505–4519, 1966.

Cahill, L. J., Jr., Magnetic storm inflation in the evening sector, *J. Geophys. Res.*, *78*, 4724–4730, 1973.

Chen, M. W., M. Schulz, L. R. Lyons, and D. J. Gorney, Stormtime transport of ring current and radiation belt ions, *J. Geophys. Res.*, *98*, 3835–3849, 1993.

Chen, M. W., L. R. Lyons, and M. Schulz, Simulations of space distributions of storm time proton ring current, *J. Geophys. Res.*, *99*, 5745–5759, 1994.

C:son Brandt, P., Y. Ebihara, D. G. Mitchell, E. C. Roelof, and R. Demajistre, Global ENA observations of the ring current: Rapid dayside ion drop out, *J. Geophys. Res*, *107*(A11), 1359, doi:10.1029/2001JA000084, 2002.

Daglis, I. A., The role of magnetosphere-ionosphere coupling in magnetic storm dynamics, *Magnetic Storms*, *Geophys. Monogr. Ser.*, vol. 107, edited by B. T. Tsurutani et al., AGU, Washington, D. C., 1997.

Daglis, I. A., R. M. Thorne, W. Baumjohann, and S. Orsini, The terrestrial ring current: origin, formation and decay, *Rev. Geophys.*, *37*, 407–438, 1999.

Delcourt, D. C., T. E. Moore, J. A. Sauvaud, and C. R. Chappell, Non-adiabatic transport features in the outer cusp region, *J. Geophys. Res.*, *97*, 16,833–16,842, 1992.

De Michelis, P., I. A. Daglis, and G. Consolini, An average image of proton plasma pressure and of current systems in the equatorial plane derived from AMPTE/CCE/CHEM measurements, *J. Geophys. Res.*, *104*, 28,615–28,624, 1999.

Ebihara, Y., and M. Ejiri, Modeling of solar wind control of the ring current buildup: A case study of magnetic storms in April 1997, *Geophys. Res. Lett.*, *25*, 3751–3754, 1998.

Ebihara, Y., and M. Ejiri, Simulation study on fundamental properties of the storm-time ring current, *J. Geophys. Res.*, *105*, 15,843–15,859, 2000.

Ebihara, Y., M. Ejiri, and H. Miyaoka, Coulomb lifetime of the ring current ions with time varying plasmasphere, *Earth Planet. Space*, *50*, 371–382, 1998.

Ejiri, M., Trajectory traces of charged particles in the magnetosphere, *J. Geophys. Res.*, *83*, 4798–4810, 1978.

Ejiri, M., R. A. Hoffman, and P. H. Smith, The convection electric field model for the magnetosphere based on Explorer 45 observations, *J. Geophys. Res.*, *83*, 4811–4815, 1978.

Fritz, T. A., J. Chen, and R. B. Sheldon, The role of the cusp as a source for magnetospheric particles: A new paradigm?, *Adv. Space Res.*, *25*, 1445–1457, 2000.

Jordanova, V. K., R. B. Torbert, R. M. Thorne, H. L. Collin, J. L. Roeder, and J. C. Foster, Ring current activity during the early Bz < 0 phase of the January 1997 magnetic cloud, *J. Geophys. Res.*, *104*, 24,895–24,914, 1999.

Jordanova, V. K., C. J. Farrugia, R. M. Thorne, G. V. Khazanov, G. D. Reeves, and M. F. Thomsen, Modelling ring current proton precipitation by electromagnetic ion cyclotron waves during the May 14–16, 1997, storm, *J. Geophys. Res.*, *106*, 7–22, 2001.

Kovrazhkin, R. A., J.-A. Sauvaud, and D. C. Delcourt, INTERBALL-Auroral observations of 0.1–12 keV ion gaps in the diffuse auroral zone, *Ann. Geophys.*, *17*, 734–742, 1999.

Kozyra, J. U., M. W. Liemohn, C. R. Clauer, A. J. Ridley, M. F. Thomsen, J. E. Borovsky, J. L. Roeder, V. K. Jordanova, and W. D. Gonzalez, Multistep Dst development and ring current composition changes during the 4–6 June 1991 magnetic storm, *J. Geophys. Res.*, *107*(A8), 1224, doi:10.1029/2002JA000023, 2002.

Liemohn, M. W., J. U. Kozyra, V. K. Jordanova, G. V. Khazanov, M. F. Thomsen, and T. E. Cayton, Analysis of early phase ring current recovery mechanisms during geomagnetic storms, *Geophys. Res. Lett.*, *26*, 2845–2848, 1999.

Liemohn, M. W., J. U. Kozyra, M. F. Thomsen, A. J. Ridley, G. Lui, J. E. Borovsky, and T. E. Cayton, Dominant Role of the asymmetric ring current in producing the stormtime Dst*, *J. Geophys. Res.*, *106*, 10,883–10,904, 2001.

Lui, A. T. Y., and D. C. Hamilton, Radial profiles of quiet time magnetospheric parameters, *J. Geophys. Res.*, *97*, 19,325–19,332, 1992.

Lui, A. T. Y., R. W. McEntire, and S. M. Krimigis, Evolution of the ring current during two geomagnetic storms, *J. Geophys. Res.*, *92*, 7459–7470, 1987.

McIlwain, C. E., Plasma convection in the vicinity of the geosynchronous orbit, in *Earth's Magnetospheric Process*, edited by B. M. McCormac, D. Reidel, Norwell, Mass., 1972.

McIlwain, C. E., A Kp dependent equatorial electric field model, *Adv. Space Res.*, *6*(3), 187, 1986.

Milillo, A., S. Orsini, I. A. Daglis, and M. Candidi, Ring current ion flows and convection electric field from SAC-B/ISENA, *Geophys. Res. Lett.*, *23*, 3285–3288, 1996.

Milillo, A., S. Orsini, and I. A. Daglis, Empirical model of proton fluxes in the equatorial innermagnetosphere: 1. Development, *J. Geophys. Res.*, *106*, 25,713–25,730, 2001.

Potemra, T. A., L. J. Zanetti, and M. H. Acuna, AMPTE/CCE magnetic field studies of the September 4, 1984 storm, *Geophys. Res. Lett.*, *12*, 313–316, 1985.

Schield, M. A., J. M. Freeman, and A. J. Dessler, A source for field-aligned currents at auroral latitudes, *J. Geophys. Res.*, *74*, 247, 1969.

Sheldon, R. B., Ion transport and loss in the Earth's quiet ring current 2, Diffusion and magnetosphere-ionosphere coupling, *J. Geophys. Res.*, *99*, 5705–5720, 1994.

Sheldon, R. B., and D. C. Hamilton, Ion transport and loss in the Earth's quiet ring current: 1. Data and standard model, *J. Geophys. Res.*, *98*, 13,491–13,508, 1993.

Shirai, H., K. Maezawa, M. Fujimoto, T. Mukai, Y. Saito, and N. Kaya, Monoenergetic ion drop-off in the inner magnetosphere, *J. Geophys. Res.*, *102*, 19,873, 1997.

Smith, E. J., P. J. Coleman, D. L. Judge, and C. P. Sonett, Characteristic of the extraterrestrial current system: Explorer VI and Pioneer V, *J. Geophys. Res.*, *65*, 1958–1961, 1960.

Takahashi, S., and T. Iyemori, Three-dimensional tracing of charged particle trajectories in a realistic magnetospheric model, *J. Geophys. Res.*, *94*, 5505–5509, 1989.

Terada, N., T. Iyemori, M. Nose, T. Nagai, H. Matsumoto, and T. Goka, Storm-time magnetic field variations observed by the ETS-VI satellite, *Earth Planet. Space Sci.*, *50*, 853–864, 1998.

Tsyganenko, N. A., A magnetospheric magnetic field with a warped tail current sheet, *Earth Planet. Space Sci.*, *37*, 5, 1989.

Tsyganenko, N. A., G. Le, C. T. Russel, and T. Iyemori, A study of the inner magnetosphere based on data of Polar, *J. Geophys. Res.*, *104*, 10,275–10,284, 1999.

Volland, H., A model of the magnetospheric electric convection field, *J. Geophys. Res.*, *83*, 2695–2699, 1978.

Wygant, J., D. Rowland, H. J. Singer, M. Temerin, F. Mozer, and M. K. Hudson, Experimental evidence on the role of the large spatial scale electric field in creating the ring current, *J. Geophys. Res.*, *103*, 29,527–29,544, 1998.

Zmuda, A. J., and J. C. Armstrong, The diurnal flow pattern of field-aligned currents, *J. Geophys. Res.*, *79*, 4611, 1974.

E. De Angelis, S. Massetti, A. Mura, A. Milillo, and S. Orsini, Instituto di Fisica dello Spazio Interplanetario, Consiglio Nazionale delle Ricerche, Via del Gosso del Cavaliere 100, I-00133 Roma Italy. (deangelis@ifsi.rm.cnr.it; massetti@ifsi.rm.cnr.it; mura@ifsi.rm.cnr.it; anna.milillo@ifsi.rm.cnr.it; orsini@ifsi.rm.cnr.it)

D. C. Delcourt, Centre d'etude des Environnements Terrestre et Planetaires, CNRS, 4 Avenue de Neptune, F-94107 Saint-Maur des Fosses, France. (Dominique.Delcourt@cetp.ipsl.fr)

Y. Ebihara, National Institute of Polar Research, 1-9-10 Kaga, Itabashi-ku, Tokyo 173-8515, Japan. (ebihara@nipr.ac.jp)

Energetic neutral atoms at Mars
2. Imaging of the solar wind-Phobos interaction

Alessandro Mura, Anna Milillo, and Stefano Orsini
Istituto di Fisica dello Spazio Interplanetario, Consiglio Nazionale delle Ricerche, Rome, Italy

Esa Kallio
Finnish Meteorological Institute, Helsinki, Finland

Stas Barabash
Institutet för Rymdfysik, Kiruna, Sweden

Received 30 September 2001; revised 22 January 2002; accepted 23 January 2002; published 9 October 2002.

[1] The interactions between the solar wind and the neutral gas from Mars' moon Phobos and from the Martian exosphere are examined in order to check the feasibility of the energetic neutral atoms (ENA) remote sensing technique applied to Phobos' environment. Both solar wind and Mars exosphere models, as given in the literature, have been used. The density distribution of an outgassed neutral oxygen population located at Phobos' orbit has been simulated via Monte Carlo integration. Images and energy spectra of ENA, escaping through charge exchange processes, have been reconstructed applying a line of sight integration method. The performed simulation shows that the ENA signal originated from Phobos' environment is faint while observing far from Phobos location; anyway, it could be detected in some particular Mars-Phobos vantage point configurations. The possibility that the neutral oxygen outgassing rate might be estimated through ENA signal deconvolution is briefly discussed. *INDEX TERMS:* 6230 Planetology: Solar System Objects: Martian satellites; 6025 Planetology: Comets and Small Bodies: Interactions with solar wind plasma and fields; 5464 Planetology: Solid Surface Planets: Remote sensing; 5465 Planetology: Solid Surface Planets: Rings and dust; *KEYWORDS:* Phobos-Mars-solar wind interaction, satellite, ENA imaging, remote sensing

Citation: Mura, A., A. Milillo, S. Orsini, E. Kallio, and S. Barabash, Energetic neutral atoms at Mars, 2, Imaging of the solar wind-Phobos interaction, *J. Geophys. Res.*, *107*(A10), 1278, doi:10.1029/2001JA000328, 2002.

1. Introduction

[2] The purpose of this paper is to check the feasibility of imaging the Mars-Phobos ambient by detecting energetic neutral atoms, in the frame of the ASPERA-3 experiment on board of the ESA/Mars Express mission that will be launched in 2003. This instrument includes a neutral particle imager (NPI) with full 3D view and angular resolution of $10^\circ \times 5^\circ$, and a neutral particle detector (NPD) with $30^\circ \times 5^\circ$ angular resolution and 16 energy steps between 100 eV and 10 keV. During its mission, the Mars Express spacecraft will fly close to Phobos at distances down to 200 km for quite a few times. This opens up an exciting possibility to study the interactions of the Phobos' outgassing with the solar wind and prove (or disprove) the earlier finding made by ASPERA on board the PHOBOS-2 mission [*Dubinin et al.*, 1990]. More generally, ASPERA-3 will provide new opportunities for the study of the properties of solar wind protons [*Holmström et al.*, 2002], of the planetary energetic protons [*Lichtenegger et al.*, 2002], and of the planetary oxygen ions [*Barabash et al.*, 2002].

0148-0227/02/2001JA000328

[3] The solar wind interacts with Mars and its natural satellites, mainly through direct impact with the ambient atmospheric/exospheric gas and the solid bodies of the satellites. Recent results of the MAG/GR instrument on board of Mars-Global-Surveyor showed that Mars has a nonhomogeneous and localized magnetic field of crustal origin [*Acuña et al.*, 1998, 1999, 2001]. Anyway, in a first approximation, the magnetic field effects on the global interaction between Mars and the solar wind may be assumed as marginal. Hence in the following we will consider Mars as a nonmagnetized planet.

[4] Given the previous assumptions, specific regions of interaction may be defined [e.g., *Vaisberg et al.*, 1990] as: (1) a bow shock, where the solar wind impacts the planetary environment; (2) a "magnetosheath," where the solar wind particles are deflected and mixed to planetary particles; (3) a "magnetopause," where the plasma speed decreases; (4) a "magnetosphere," where the energies slow down and the density increases; and (5) an obstacle boundary, no plasma or field penetrates it.

[5] Concerning Mars' natural satellites, Phobos and Deimos, we must take into account that a rocky body without a magnetic field and without an atmosphere interacts with the solar wind plasma only with its surface and with the outgassing material surrounding the body. Hence a bow

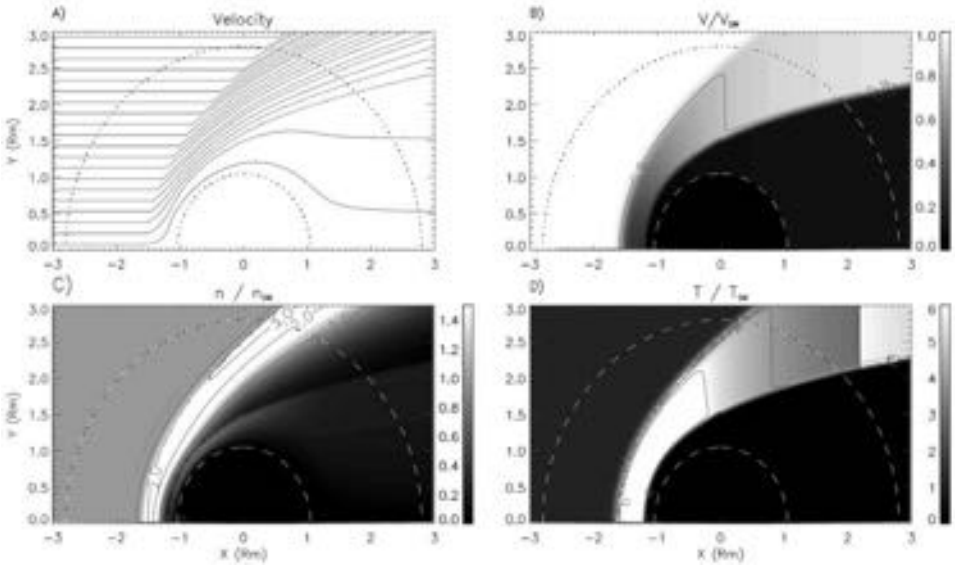

Figure 1. Empirical model of proton flux around Mars: (a) streamlines, (b) protons speed V/V_{SW}, (c) proton density n/n_{SW}, (d) proton temperature T/T_{SW} [from *Kallio*, 1996].

shock able to deflect the solar wind flow does not form around them.

[6] Here we investigate the solar wind interaction with the H, H_2 and O gas components of Mars/Phobos environment. When a H^+ collides with a neutral particle, it may charge exchange and be neutralized, becoming H^-ENA. The charge exchange is a symmetrical resonance process in the case of H target [*Hasted*, 1964], and an accidental resonance process in the cases of O target [*Stebbings et al.*, 1964] and H_2 target [*Hasted*, 1964]. Hence only a few eV are lost in this interaction, and the newly created ENA retains approximately both the energy of the colliding energetic ion and its direction (see section 5.3 for further details).

[7] If its mean free path is long enough, such ENA can transport information out of the generation region, thus allowing remote sensing of the interaction process [e.g., *Roelof et al.*, 1985; *Roelof*, 1987; *Henderson et al.*, 1997; *Orsini and Milillo*, 1999; *Milillo and Orsini*, 2001].

[8] Charge exchange processes are expected to be very effective at Mars, because the solar wind can reach altitudes where the density of the atmospheric neutrals is quite high (up to 10^6 cm^{-3}). Hence ENAs imaging is a potentially useful tool for understanding the geometry, the physics, and the dynamics of the plasma around Mars. [e.g., *Kallio et al.*, 1997].

[9] Mars closest satellite, Phobos, is orbiting nearby the equatorial plane of the planet at a distance of about 2.7 R_M from Mars. Outgassing phenomena may produce a gas torus along its orbit [e.g., *Ip and Banaszkiewicz*, 1990; *Horanyi et al.*, 1990; *Dubinin et al.*, 1990, 1991]. In this paper, we show that a denser neutral population should also be present closer to the satellite. Phobos' orbit is partially embedded in the Martian magnetosheath (in the dusk and dawn sectors) and in the magnetosphere (in the nightside). Hence its outgassing material may interact not only with the undisturbed solar wind, but also with the plasma flowing around Mars [e.g., *Barabash and Lundin*, 1994].

[10] The described interaction can produce a supplementary ENA signal near the satellite as well as along its orbit. This signal could be detected from appropriate vantage points, and discriminated from the background ENA signal of Martian origin. In this way, new information on Phobos environment could be achieved.

[11] In section 2, we discuss the model of plasma distribution in the Martian environment and the characteristics of Mars' atmosphere and exosphere, considered as a basic reference for our analyses. Then, we add the outgassing neutral population coming from Phobos, which generates a torus along its orbit as well as a halo around it. In section 3, we describe the ENA simulation method, and in section 4 we show the resulting simulated ENA images from both Mars and Phobos. In section 5, we discuss the shape of Phobos' torus with the intent to obtain an estimation of the outgassing rate by analyzing the ENA signal. In the end of this section, possible improvements of the described procedures are highlighted. Finally, in section 6 we summarize the main results.

2. Models Description

2.1. Proton Flux Model

[12] The empirical model of the proton flow is based on ASPERA three-dimensional proton velocity measurements, and is ascribed to *Kallio* [1996]. It gives proton velocity, density and temperature in a bidimensional plane, postulating an axial symmetry around Sun-Mars axis. A gas dynamic relationship is used to approximate the proton temperature in the magnetosheath and in the magnetosphere. The model includes a bow shock, a magnetopause and an inner obstacle boundary, which, here, is a sphere of radius equal to 1.05 Mars' radii (R_M). This model involves streamlines that penetrate the magnetopause in the wake as well as on the dayside [*Kallio et al.*, 1997]. The presence of Phobos does not modify the model. In fact, due to its very small dimensions, Phobos is not able to deflect the proton

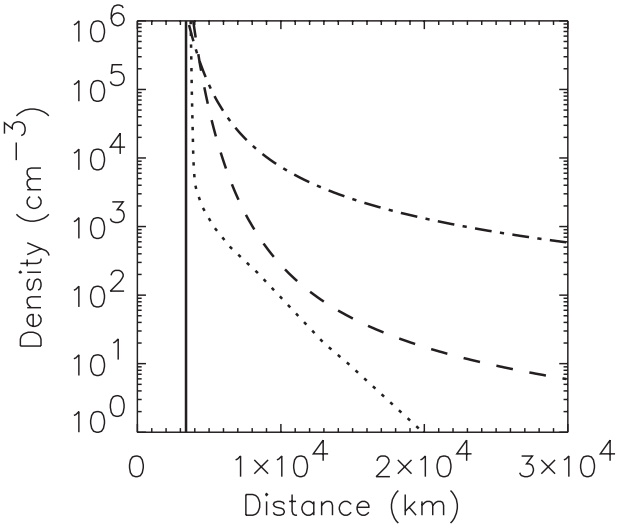

Figure 2. Neutral particle density profiles in the Martian exosphere versus altitude: oxygen (dotted), hydrogen (dash-dotted), and molecular hydrogen (dashed) [from *Krasnopolsky and Gladstone*, 1996]. The solid line indicates the Mars surface.

flux. Figure 1 shows maps of the streamlines, the velocity, the density, and the temperature of the proton flows around Mars, as modeled by *Kallio* [1996]. The inner circumference shows the position of the planetary obstacle boundary, while the outer one shows the position of Phobos orbit. It is worth to notice here that, according to this model, half of Phobos' orbit is inside the bow shock.

2.2. Models of Neutral Atom Distributions

2.2.1. Mars' Atmosphere and Exosphere

[13] Our simplified model considers Mars' atmosphere and exosphere as composed only of oxygen, hydrogen, and molecular hydrogen. It is known that helium is also present in Mars environment [*Krasnopolsky and Gladstone*, 1996], but its presence has not been taken into account, due to its lower charge exchange cross section. The neutral profiles for hydrogen populations are approximated by exponential functions, depending on the exospheric temperature and on the distance from Mars [*Krasnopolsky and Gladstone*, 1996]. The oxygen population is made of a thermal component at low altitude plus a nonthermal corona [*Zhang et al.*, 1993a]. Figure 2 shows the density of those species versus distance from Mars during low solar activity. Since the exospheric temperature depends on solar activity and solar wind conditions, the neutral particle density profiles versus altitude show similar variability. For the same reason also the relative abundances show significant variations: during high activity the main contribution is due to oxygen, while during more quiet periods the hydrogen is the main atmospheric component [*Kallio et al.*, 1997]. In this paper, we concentrate our analysis on the low-activity periods.

2.2.2. Phobos' Gas Torus and Halo

[14] Phobos is the natural satellite closest to the planet. Its orbit, located on the ecliptic plane, is approximately circular, at 9500 km from Mars (R_{MP}); the orbital period is 7 hours. It is an irregular object with an average radius of about 10 km; its mass is only 10^{-8} times the mass of Mars. It has been suggested that Phobos may contain water [e.g., *Fanale and Salvail*, 1989], and that surface-outgassing phenomena may occur. If the escaping velocity of an outgassing particle is small compared to that of Phobos, this particle is trapped in a keplerian orbit around Mars [*Ip and Banaszkiewicz*, 1990]. Hence all of the trapped particles fill a torus, which is, approximately, the envelope of all the permitted trajectories [*Krymskii et al*, 1992]. This torus is positioned on the ecliptic plane, and has an approximately circular cross section. Both the dimension of the torus and the related density of neutrals depend on the velocity distribution of the escaping particles, on the neutrals loss-decay time τ and on the surface outgassing rate $dN/dt = Q$, where N is the number of particles. *Sauer et al.* [1995], when attempting to model the Deimos interaction with solar wind, show that an outgassing rate of 10^{23} s^{-1} would be consistent with PHOBOS-2 IMF and plasma data. Moreover, *Krymskii et al.* [1992] and *Ip and Banaszkiewicz* [1990] show that such a rate could be considered as a basic reference also for Phobos outgassing. With an oxygen outgassing rate $Q = 10^{23}$ s^{-1}, for a lifetime $\tau = 2 \times 10^6$ s (see section 5.1), and for a total volume V of 10^{25} cm^3 [e.g., *Ip and Banaszkiewicz*, 1990; *Krymskii et al*, 1992], the average neutral oxygen density ($\langle n_o \rangle$) inside the torus is:

$$\langle n_o \rangle = \frac{N}{V} = \frac{Q\tau}{V}. \tag{1}$$

By using the given quantities, it follows that $\langle n_o \rangle \sim 10^4$ cm^{-3}.

[15] Close to Phobos, the gas density is higher. In fact, under the hypothesis of a free expansion from Phobos, the oxygen density near the satellite is:

$$n_o = \frac{dN}{dV} = \frac{dN}{4\pi r_P^2 dr_P} = \frac{1}{4\pi r_P^2}\frac{dN}{dt}\frac{dt}{dr_P} = \frac{Q}{4\pi r_P^2 v_n}; \tag{2}$$

where r_P is the distance from Phobos and $v_n = dr_P/dt$ is the mean escape velocity. If $T_P = 250$ K is the surface temperature of Phobos, and m_O is the oxygen mass, $v_n = (2kT_P/m_O)^{1/2} = 500$ m s^{-1} [*Ip and Banaszkiewicz*, 1990; *Krymskii et al*, 1992]. The resulting n_o may be up to 10^6 cm^{-3}.

[16] In order to better estimate the density function inside this torus, we have simulated the trajectories of 10^7 test particles, escaping from Phobos with initial velocity randomly distributed. The lifetime of each test particle has been set equal to τ. At any chosen time t_0, each particle i, actually contributing to the total gas density, may be considered as outgassed at instant $t_0 - T_i$, where T_i is chosen randomly between 0 and τ. Then, each trajectory has been integrated in Phobos noninertial frame, with steps of 0.1 s, from $t_0 - T_i$ to t_0, taking into account Mars gravity, as well as centrifugal and Coriolis force. The gravity of Phobos has not been considered here because, in any point of space, it is less than 1% of that of Mars.

[17] In the model, each test particle starts moving from Phobos along a random direction, and the magnitude of the initial velocity is randomly distributed around its mean value v_n following Maxwell's law. Due to its small dimensions, Phobos may be considered as a point located in the origin of the reference frame. Hence each test particle starts

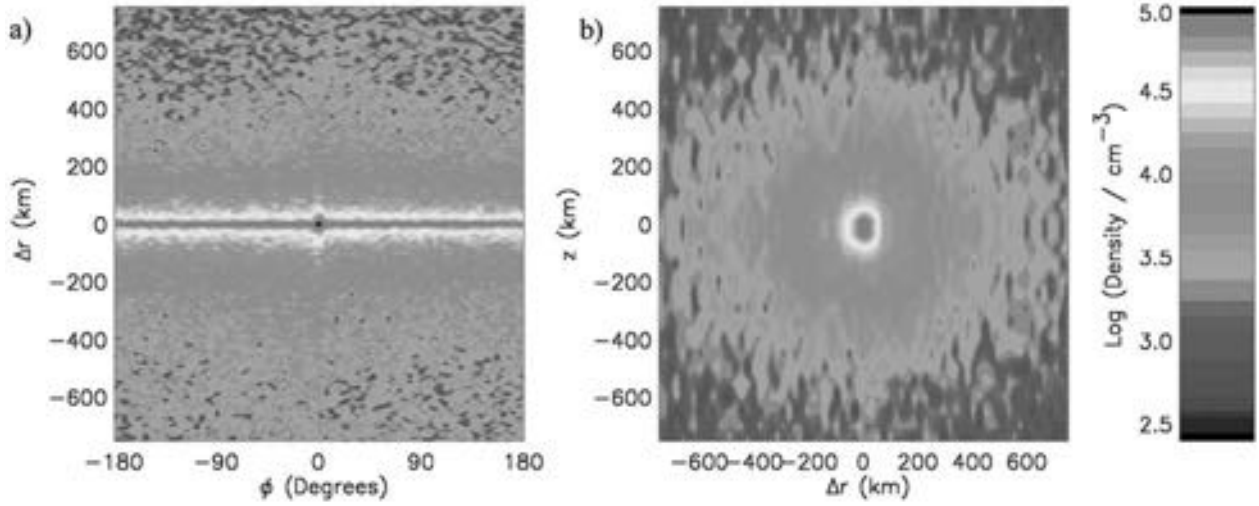

Figure 3. Simulated neutral oxygen density near the orbit of Phobos for different bidimensional sections: (a) ϕ versus r, $z = 0$; (b) Δr versus z, $\phi = 0$; $Q = 10^{23}$ s^{-1}. Phobos' position is at $\Delta r = 0$, $\phi = 0°$, $z = 0$; its velocity is directed toward the increasing ϕ. See color version of this figure at back of this issue.

its motion in the origin, and any subsequent impact between the particle and Phobos is neglected.

[18] Since the integration time T_i of a test particle is often greater than its orbital period around Mars, it is not necessary to numerically integrate the trajectory of a particle over the entire time T_i. In fact, each test particle moves around Mars an integer number of times m_i, plus an extra time ΔT_i equal to:

$$\Delta T_i = T_i - m_i T_i^*, \tag{3}$$

where T_i^* is the period of a full orbit around Mars in its inertial frame. According to Kepler's law, the orbital period can be written:

$$T_i^* = T_P \left(\frac{\eta_i}{R_{MP}} \right)^{3/2}, \tag{4}$$

and where η_i is the main axes of the i-particle elliptical orbit around Mars, in its inertial frame, and T_P is Phobos orbital period. Since we do know the total energy and the momentum at starting time t_0, it is easy to find using energy and momentum conservation laws [e.g., *Hodges*, 1994].

[19] Hence at instant $t_0 - \Delta T_i$, the test particle is in the same position as at instant $t_0 - T_i$, in Mars' inertial frame. It is easy to calculate the position of the particle at instant $t_0 - \Delta T_i$ in Phobos' noninertial frame, and then integrate the motion via numerical computation only on the residual time ΔT_i. The precession of the i-particle orbit due to Mars motion around the Sun has been neglected. The space around Mars has been divided into cells, based on a three-dimensional grid in cylindrical coordinates centered on Mars:

- r, the distance from Mars, with a 20 km resolution;
- z, the altitude above the ecliptic plane, with a 20 km resolution;
- ϕ, the angle between the particle and Phobos, with a resolution of 15°.

[20] The gas density n_{ijk} inside the generic cell of volume V_{ijk} has been assumed proportional to (number of particles)/V_{ijk} at instant t_0. Finally, the density has been normalized in order to have:

$$\sum_i \sum_j \sum_k n_{ijk} V_{ijk} = \tau Q. \tag{5}$$

The two panels of Figure 3 show the derived gas density distribution on two distinct bidimensional sections: ϕ, $r = r - R_{mp}$, $z = 0$. (Panel A), and z, Δr, $\phi = 0$. (Panel B). The halo density profiles, located in a small quasi-circular region surrounding Phobos, reach values up to 2×10^5 cm^{-3}. The torus along the orbit of Phobos exhibits density versus r profiles almost ϕ-independent, with a peak of $\approx 3 \times 10^4$ cm^{-3}.

3. Method for ENA Simulation Through Line of Sight Integration

[21] The differential ENA flux observed, for any energy and line of sight, at a given vantage point S_0, is generated by the interaction of the energetic ion fluxes with the ambient neutral gas. Concerning ion fluxes, only protons, characterized by a Maxwellian velocity distribution function, are considered in the present study. At each point S along the line of sight, the velocity distribution function $f(l, \mathbf{v})$ is:

$$f(l, \mathbf{v}) = \left(\frac{1}{\pi w(l)^2} \right)^{3/2} e^{\left(-\frac{|(\mathbf{v} - \mathbf{u}(l))|^2}{w(l)^2} \right)}; \tag{6}$$

where l is the distance $S - S_0$, $\mathrm{u}(l)$ is the mean proton velocity and w is the thermal velocity defined as:

$$w(l) = \left(\frac{2kT(l)}{m_{H^+}} \right)^{1/2}. \tag{7}$$

[22] Here, T is the solar wind temperature as in the proton flux model shown in section 2.1, k is the Boltzmann constant, and m_{H^+} is the proton mass. So at point S the proton infinitesimal flux dJ_{H^+}, directed toward S_0, is:

$$dJ_{H^+} = n_{H^+}(l) v f(l, \mathbf{v}) d\mathbf{v}, \tag{8}$$

where $n_{H+}(l)$ is the proton density.

[23] By expressing $f(l,\mathbf{v})$ as a function of l, kinetic energy E and direction $\hat{v}$

$$f'(l, E, \hat{v}) dE d\Omega = f(l, \mathbf{v}) d\mathbf{v} \tag{9}$$

where $d\Omega$ is the infinitesimal solid angle, we may estimate the ENA infinitesimal flux $dJ_{ENA}(E, \hat{v})$ and the ENA differential flux integrated along a certain line of sight $\Phi_{ENA}(E, \hat{v})$ as:

$$\begin{aligned} dJ_{ENA}(E,\hat{v}) &= \int_{l=0}^{l=\infty} dJ_{H^+} \sum_k \sigma_k n_k(l) \\ dr &= \int_{l=0}^{l=\infty} \left(\frac{2E}{m_{H^+}}\right)^{1/2} f'(l, E, \hat{v}) \sum_k \sigma_k n_k(l) n_{H^+}(l) dl \; dE \; d\Omega \\ \Phi_{ENA}(E,\hat{v}) &= \frac{dJ_{ENA}(E,\hat{v})}{dE \; d\Omega} \\ &= \int_{l=0}^{l=\infty} \left(\frac{2E}{m_{H^+}}\right)^{1/2} f'(l, E, \hat{v}) \sum_k \sigma_k n_k(l) n_{H^+}(l) dl, \end{aligned} \tag{10}$$

where n_k is the density of any neutral species, σ_k is the charge exchange cross section between protons and the k^{th} neutral species (H, H_2, O), as shown in Figure 4.

4. Hydrogen ENA Images and Spectra Simulation

[24] The hydrogen ENA flux examined here results from charge exchange processes occurring between the solar wind protons and the thermal neutral gas. This flux originates from two different regions: Mars' exosphere and Phobos' halo. However, due to the small dimensions of the Phobos' halo (see Figure 3), only at particular vantage points the related ENA signal (mixed with the stronger signal originating from Mars' exosphere) is sufficiently high to be discriminated. More particularly, the best configuration for detecting such a signal requires a vantage point located on Mars' equatorial plane.

[25] An example of Mars' exospheric ENA image, considered here as the background signal, is shown in Figure 5a. The Mars-Solar-Ecliptic (MSE) coordinates of the chosen vantage point S_0 are $x_{So} = -1.3\ R_M$, $y_{So} = 2.9\ R_M$, $z_{So} = 0\ R_M$, where R_M is Mars' radius (see Figure 5d). The dotted line represents Mars' obstacle boundary. In this case, the numerical integration of equation (10) has been performed with $dl = 0.01\ R_M$. The ENA differential flux with angular resolution $\Delta\theta = 2^\circ$ is integrated over all energies, from 1 eV to 2 keV. The figure shows clearly two different peaks: a narrow one centered on the sunward direction, and a more extended one close to the planet. The first is due to the ENA flux generated directly by the interaction between the solar wind outside the bow shock and the outer exosphere. The second is related to the signal resulting from the interaction between the thermalized solar wind inside the magnetosheath and the inner exosphere. The simultaneous observation of these two separate ENA regions clearly indicates that the vantage point is downstream of the Martian bow shock. It is worth to notice that the obtained ENA fluxes are in good agreement with those calculated by *Kallio et al.* [1997], who used an alternative approach based on a Monte Carlo method.

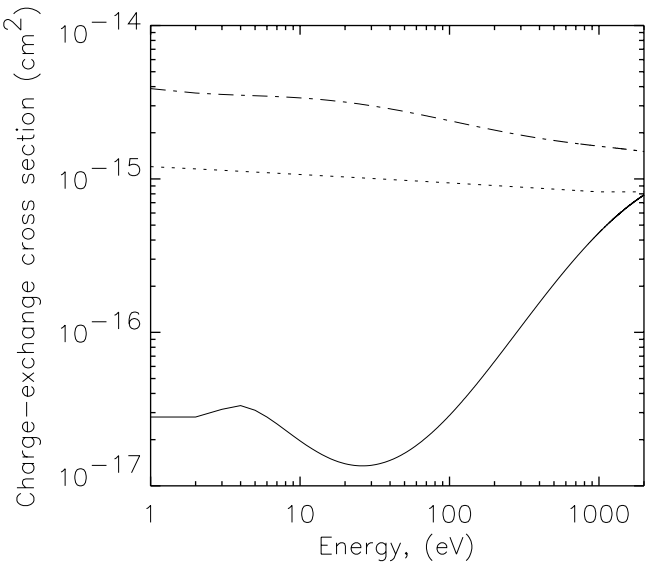

Figure 4. Cross section for charge exchange process between protons and hydrogen (dash-dotted) [*Barnett*, 1990], oxygen (dotted) [*Stebbings et al.*, 1964], and molecular hydrogen (solid) [*Barnett*, 1990] versus energy.

[26] Figure 5b shows the ENA signal generated by Phobos' neutral population (with the exclusion of the background signal reported in Figure 5a), assuming hypothetically that $Q = 10^{23}\ s^{-1}$ (see previous comments in section 2.2.2). The vantage point is the same as in Figure 5a; Phobos' MSE coordinates are: $x_P = -0.9\ R_M$, $y_P = 2.6\ R_M$, $z_P = 0\ R_M$ (see Figure 5d).

[27] The overall ENA image (Figure 5c) would result from the superposition of the two simulated pictures shown in Figures 5a and 5b. For almost all directions, the background from Mars' environment obscures the signal from Phobos. Nonetheless, the Phobos' ENA flux in between 40^0–60^0 on Mars' equatorial plane is higher and detectable.

[28] Figure 6 shows the ENA spectra relative to Figure 5, integrated over all directions in the sky. The spectrum related to Mars' ENA flux (solid line) is the envelope of the fluxes from three different regions. The signal at lower energy (2–6 eV) is generated close to Mars surface, where the energy of the proton flux is low (subsolar point). The signal at higher energy (0.4–2 keV) results from interaction of neutral gas with unperturbed solar wind outside the bow shock (~1–2 keV), as well as deflected solar wind in the magnetosheath.

[29] Phobos' ENA energy spectrum (dashed line) exhibits a trend similar to the previous one. On the other hand, its

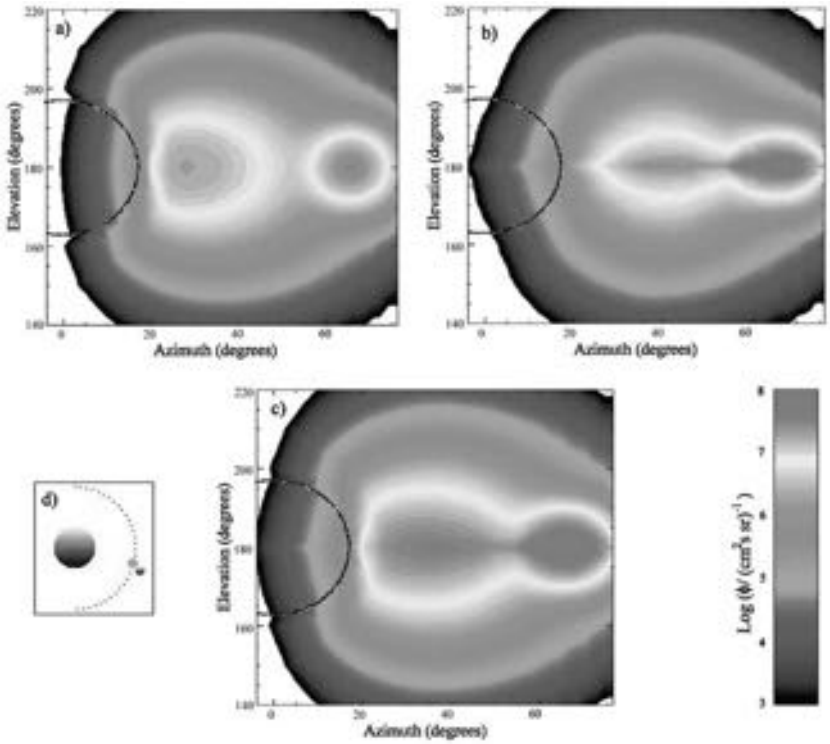

Figure 5. (a) Pseudocolor map of the ENA differential flux, function of the elevation and azimuth angle, if only Mars exosphere was present. The dashed line represents Mars' obstacle boundary. Azimuth angle is measured on the equatorial plane, beginning from Mars' center; elevation angle is measured perpendicular to the equatorial plane, Mars' center is at 180°. (b) Same as Figure 5a, if only Phobos torus-halo was present. (c) Overall ENA image resulting from the superposition of Figures 5a and 5b. The flux is integrated over all energy from 1 eV to 2 keV. (d) The spheres show an equatorial view of the relative positions of Mars (red), Phobos (blue), and the vantage point (gray); the Sun is up. See color version of this figure at back of this issue.

intensity is comparable to Mars' ENA spectrum only in the 0.4–2 keV range. This is due to the position of Phobos' orbit, which allows the halo-torus neutral gas to interact only with the unperturbed or magnetosheath solar wind.

5. Discussion

[30] In our study, we have analyzed the characteristics of the oxygen neutral population, outgassed from Phobos, and distributed along its orbit around Mars. Furthermore, we have attempted to interpret the ENA signal originated through charge exchange between such a neutral gas and the directional proton flux.

5.1. Phobos' Neutral Oxygen Distribution

[31] Phobos' neutral oxygen distribution function has been reconstructed via Monte Carlo simulation. Usually, this approach allows getting information about the density distribution from the entire test particle trajectory [e.g., *Hodges*, 1994], which could be obtained by using numerical or analytical computations. However, in our case this simple method is subjected to two significant limitations: (1) the trajectory of a test atom is too long to allow numerical integration of the motion without large computational errors; (2) the presence of noninertial forces makes the analytical approach difficult to perform. In the case of long

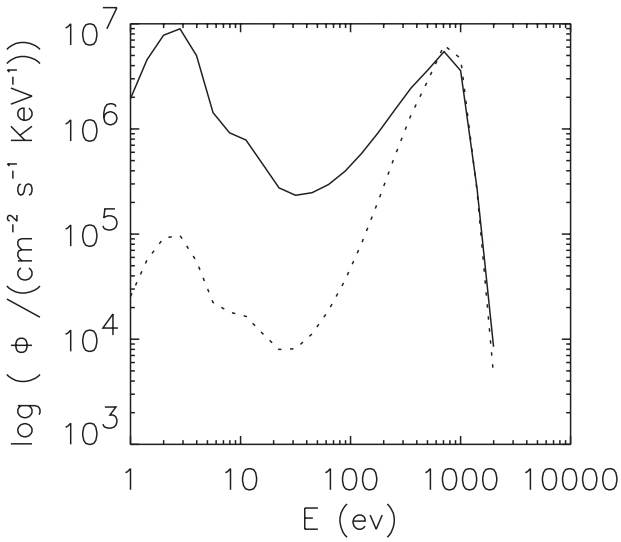

Figure 6. Spectra of the ENA fluxes coming from Mars (solid line) and Phobos (dotted line), integrated over all directions in the sky. Vantage point and Phobos position are the same as in Figure 5.

trajectories in noninertial frames, the only way to solve this problem is to use first analytical and then numerical computations (see section 2.2.2).

[32] It is possible to find an analytical function, which fits the empirical data. With the exclusion of Phobos' halo, the neutral density on the $z = 0$ plane can be estimated by a very simple function with only two free parameters:

$$n(r, \phi) = \frac{A}{B + \mid r - R_{MP} \mid}, \tag{11}$$

where $A = 7.25 \times 10^8 \pm 7.17 \times 10^6$, and $B = 1.20 \times 10^4 \pm 2.30 \times 10^2$, if n is expressed in cm^{-3} and r is expressed in m. The correlation coefficient between this function and the data is 0.996. This function may be easily extended to the whole space around Phobos' orbit, since the cross section of the torus is approximately circular (see Figure 3b).

[33] The discussed distribution is obviously influenced by loss processes. There are three main causes of O atom ionization in Phobos' torus: charge exchange, photoionization and electron impact ionization. All of the mentioned processes do produce significant loss of neutral gas. In fact, after ionization, oxygen is supposed to be removed by Jeans escape and solar wind capture. The detailed estimate of the relative contribution of the mentioned processes would need a careful analysis of the plasma circulation around Phobos. A zero-order estimate could be based on solar wind plasma features, taking into account that Phobos is embedded by solar wind-like plasma for more than half of its period. With this assumption, the proton velocity $V_{SW} = 4 \times 10^7$ cm s^{-1}, and density $n_{SW} = 2.5$ cm^{-3} may be considered. This yields a proton flux of 1×10^8 cm^{-2} s^{-1}. Taking into account the H^+-O charge exchange cross section (see Figure 4), we obtain a charge exchange frequency $f_{CE} = 10^{-7}$ s^{-1}. It is worth noticing that charge exchange effect is comparable to other loss processes. As a matter of fact, at Mars' orbit, during solar minimum, the photoionization frequency is $f_\gamma = 10^{-7}$ s^{-1}, and the electron impact ionization frequency is $f_e = 2 \times 10^{-7}$ s^{-1} [*Zhang et al.*, 1993b]. The total loss frequency f is then the sum of all these frequencies ($f = 4 \times 10^{-7}$ s^{-1}). Hence we have generally considered an oxygen gas lifetime $\tau = f^{-1} = 2 \times 10^6$ s (see section 2.2.2).

5.2. ENA Signal Analysis and Outgassing Rate Estimation

[34] From these simulations, it results that the ENA flux generated close to Phobos is detectable, but only for particular configurations. As an example, in Figure 5 we have analyzed the ENA signal if detected from a vantage point located on Mars' equator. The chosen $80° \times 80°$ field of view is centered on a line of sight parallel to the deflected solar wind direction. The Sun direction is inside the field of view; the Sun is a source of strong background noise, due to both the photon radiation and the unperturbed solar wind ENA signal. Nevertheless, from Figure 5 it appears that most of the incoming signal from Phobos can be discriminated from this background. The signal is, of course, maximum in the equatorial plane. We have simulated ENA images and spectra for many different Mars-Phobos vantage point configurations, and observed that if the vantage point is placed outside from the equatorial plane, the ENA flux from Phobos becomes very weak, and hardly detectable.

[35] The neutral density from Phobos depends on the outgassing rate Q as well as on the mean lifetime τ. The shape of the distribution, however, depends only on τ, which is known with a sufficient accuracy [*Zhang et al.*, 1993b]. Hence the neutral density originated from Phobos, as well as the related ENA signal, are simply proportional to Q (see equations (5) and (9)). From our simulation, it results that the presence of a neutral population originated from Phobos induces an extra ENA signal that is detectable. This potentially allows the estimate of Q by analyzing the ENA signal.

5.3. Model Limits and Future Improvements

[36] In the present study a preliminary analysis of the interaction between the solar wind and the Mars/Phobos system is performed. The properties of the system environment, as well as those of the nearby solar wind are not well known. Therefore the used analytical model of the ion flux includes several free parameters to control the properties of the plasma near the planet, like the height of the obstacle boundary, the magnetopause location and shape, and others. Moreover, we are forced to make some assumptions on the neutral distribution of the system. Further improvements to the present analysis could be better modeling of: (1) the proton flux (including the nonhomogeneous and localized magnetic field effects [*Acuña et al.*, 2001]), (2) the exospheric neutral density (presently approximated by an exponential extrapolation that overstates densities at great distances), (3) the fast-oxygen corona (up to altitudes 7000 km form the surface [e.g., *Hodges*, 2000; *Kim et al.*, 1998])

[37] In the present study, the solar activity is assumed low. However, solar activity fluctuations should be considered, since the exospheric temperature depends on solar activity and solar wind conditions, the neutral particle density profiles versus altitude show similar variability. For the same reason also the relative abundances show significant variations: during high activity the main contribution is due to oxygen, while during more quiet periods the hydrogen is the main atmospheric component [*Kallio et al.*, 1997]. Hence the resulting ENA fluxes could be different during high activities.

[38] Energetic O^+ ions (not considered here) of planetary origin have been detected both in the flanks of the Martian magnetosphere and in the central tail by Phobos/ASPERA instrument [*Kallio et al.*, 1995]. The charge exchange between the neutrals and the oxygen ions could be effective in the Mars environment [*Kallio and Koskinen*, 1998].

[39] The simplified outgassed neutral population considers oxygen as the only constituent. This simplification comes out from the fact that such a population has been effectively hypothesized by *Dubinin et al.* [1990]. A more sophisticated model should eventually include all of the possible components/phenomena.

[40] The ENA imaging technique is based on the assumption that, after charge exchange process, the H-ENA retains the energy and the direction of the incoming proton. In the

case of an asymmetric/accidental resonance process (like H^+-O), the energy variation (a few eV) may be assumed as negligible in our case [*Stebbings et al.*, 1964]. The differential cross section $\frac{d\sigma(\theta)}{d\Omega}$, in the energy range between 500 eV and 5 keV, strongly peaks in the forward direction (within 2.5°), even if large scattering angles may occur [*Lindslay et al.*, 1996]. The presence of a scattering angle in the charge exchange process may result in a blurring of the ENA images. In the present study, such an effect has not been taken into account. In fact, the H-ENA flux originated from H^+-O interaction comes from both Mars' and Phobos' environments. However, the bulk of the H-ENA flux from Mars' environment is originated from H^+-H interactions (exhibiting a very low scattering), due to both the higher hydrogen density and the higher charge exchange cross section (see Figures 2 and 4). Hence the blurring of the total signal due to scattering may be neglected on first approximation. The H-ENA flux from Phobos is supposed to originate only from H^+-O interactions; the peak energy (see Figure 6) falls within the 0.5–5 keV range mentioned before. Generally, the related scattering should not be negligible even if, due to the small distance between the source and the vantage point, it should not strongly affect our results. Further improvements to the present analysis could consider the scattering angle of the charge exchange process, simply by increasing the temperature of the proton fluxes. In fact, we could simulate scattering at charge exchange process by adding to the proton temperature w (a free parameter of our model) a further free parameter Δw, due to scattering.

6. Conclusions

[41] One of the main aspects about Phobos' exosphere composition and outgassing rate is related to the presence of water on this Martian satellite; a definite clarification of such an intriguing issue would be of fundamental interest for determining the time evolution of Phobos [e.g., *Fanale and Salvail*, 1989]. In the present study, we have presented a method able to investigate Phobos' exosphere properties, by simulating the ENA signal generated through interaction between the solar wind and the outgassed neutrals. The simulations show that oxygen outgassing generates an ENA flux, whose signal may be discriminated from the background for particular positions of the vantage point. This technique can provide relevant information, useful for determining the major characteristics of neutral outgassing, whose rate has not been directly measured. This procedure may be improved by considering more neutral species, various solar activity conditions, and by adding a model for the local magnetic field.

[42] The simulated ENA signal will be tested with in situ measures: the ASPERA 3 instrument, on board the next ESA mission Mars Express that will be launched in 2003, will give the scientific community an opportunity to analyze the ENA signal from the Mars/Phobos system, hence procuring an important tool for the future of planetary investigation.

[43] **Acknowledgments.** Janet G. Luhmann thanks the referees for their assistance in evaluating this paper.

References

Acuña, M. H., et al., Magnetic field and plasma observations at Mars: Initial results of the Mars global surveyor mission, *Science*, *279*(5357), 1676, 1998.

Acuña, M. H., et al., Global distribution of crustal magnetism discovered by the Mars global surveyor MAG/ER experiment, *Science*, *284*(5415), 790, 1999.

Acuña, M. H., et al., Magnetic field of Mars: Summary of results from the aerobraking and mapping orbits, *J. Geophys. Res.*, *106*, 23,403, 2001.

Barabash, S., and R. Lundin, On a possible dust-plasma interaction at Mars, *IEEE Trans. Plasma Sci.*, *22*(2), 173, 1994.

Barabash, S., M. Holmström, A. Lukyanov, and E. Kallio, Energetic neutral atoms at Mars, 4, Imaging of the oxygen escape, *J. Geophys. Res.*, *107*, 10.1029/2001JA000326, in press, 2002.

Barnett, C. F., Collisions of H, H_2, He and Li atoms and ions with atoms and molecules, in *Atomic Data for Fusion Ser.*, vol. 1, *Rep. ORNL-6086*, edited by H. T. Hunter et al., Oak Ridge Nat. Lab., Oak Ridge, Tenn., 1990.

Dubinin, E. M., R. Lundin, N. F. Pissarenko, S. V. Barabash, A. Z. Zakharov, H. Koskinen, K. Schwingenschuh, and Y. G. Yeroshenko, Indirect evidences for a gas/dust torus along the Phobos orbit, *Geophys. Res. Lett.*, *17*, 861, 1990.

Dubinin, E. M., N. F. Pissarenko, S. V. Barabash, A. Z. Zakharov, R. Lundin, H. Koskinen, K. Schwingenschuh, and Y. G. Yeroshenko, Tails of Phobos and Deimos in the solar wind and in the Martian magnetosphere, *Planet. Space Sci.*, *39*(1), 123, 1991.

Fanale, F. P., and J. R. Salvail, Loss of water from Phobos, *Geophys. Res. Lett.*, *16*, 287, 1989.

Hasted, G. B., *Physics of Atomic Collisions*, 416 pp., Butterworths, London, 1964.

Henderson, M. G., G. D. Reeves, H. E. Spence, R. B. Sheldon, A. M. Jorgensen, J. B. Blake, and J. F. Fennell, First energetic neutral atom images from polar, *Geophys. Res. Lett.*, *24*, 1167, 1997.

Hodges, R. R., Jr., Monte Carlo simulation of terrestrial hydrogen exosphere, *J. Geophys. Res.*, *99*, 23,229, 1994.

Hodges, R. R., Jr., Distribution of hot oxygen for Venus and Mars, *J. Geophys. Res.*, *105*, 6971, 2000.

Holmström, M., S. Barabash, and E. Kallio, Energetic neutral atoms at Mars, 1, Imaging of solar wind protons, *J. Geophys. Res.*, *107*, 10.1029/2001JA000325, in press, 2002.

Horanyi, M., M. Tatrallyay, and J. G. Luhmann, Simulations of dust particles in the Martian environment, *Geophys. Res. Lett.*, *17*, 857, 1990.

Ip, W.-H., and M. Banaszkiewicz, On the dust/gas tori of Phobos and Deimos, *Geophys. Res. Lett.*, *17*, 857, 1990.

Kallio, E., An empirical model of the solar wind flow around Mars, *J. Geophys. Res.*, *101*, 11,133, 1996.

Kallio, E., and H. Koskinen, Ion acceleration in the Martian plasma environment, *Adv. Space Res.*, *21*, 573, 1998.

Kallio, E., H. Koskinen, S. Barabash, C. M. C. Nairn, and K. Schwingenschuh, Oxygen outflow in the Martian magnetotail, *Geophys. Res. Lett.*, *22*, 2449, 1995.

Kallio, E., J. G. Luhmann, and S. Barabash, Charge exchange near Mars: The solar wind absorption and energetic neutral atom production, *J. Geophys. Res.*, *102*, 22,183, 1997.

Kim, J., A. F. Nagy, J. L. Fox, and T. E. Cravens, Solar cycle variability of hot oxygen atoms at Mars, *J. Geophys. Res.*, *103*, 29,339, 1998.

Krasnopolsky, V. A., and G. R. Gladstone, Helium on Mars: EUVE and PHOBOS data and implications for Mars' evolution, *J. Geophys. Res.*, *101*, 11,765, 1996.

Krymskii, A. M., T. K. Breus, M. K. Dougherty, D. J. Southwood, and W. I. Axford, The electromagnetic effects of the solar wind interaction with the Phobos neutral gas halo and dust torus, *Planet. Space Sci.*, *40*(8), 1033, 1992.

Lichtenegger, H., H. Lammer, and W. Stumptner, Energetic neutral atoms at Mars, 3, Flux and energy distribution of planetary energetic H atoms, *J. Geophys. Res.*, *107*, 10.1029/2001JA000322, in press, 2002.

Lindslay, B. G., D. R. Sieglaff, D. A. Schafer, C. L. Hakes, K. A. Smith, and R. F. Stebbings, Charge transfer of 0.5-, 1.5-, and 5-keV protons with atomic oxygen: Absolute differential and integral cross sections, *Phys. Rev. A*, *53*, 212, 1996.

Milillo, A., and S. Orsini, Energetic neutral atoms: Potential merits and first observations, *Recent Res. Devel. Geophys. Res.*, *3*, 153, 2001.

Orsini, S., and A. Milillo, Magnetospheric plasma loss processes and energetic neutral atoms, *Nuovo Cimento C*, *22*(5), 633, 1999.

Roelof, E. C., Energetic neutral atom image of a storm-time ring current, *Geophys. Res. Lett.*, *14*, 652, 1987.

Roelof, E. C., D. G. Mitchell, and D. J. Williams, Energetic neutral atoms E 50 keV from the ring current: IMP 7/8 and ISEE 1, *J. Geophys. Res.*, *90*, 10,991, 1985.

Sauer, K., E. Dubinin, K. Baumgartel, and A. Bogdanov, Deimos: An obstacle to the solar wind, *Science*, *269*, 1075, 1995.

Stebbings, R. F., C. H. Smith, and H. Ehrahardt, Charge transfer between oxygen atoms and O^+ and H^+ ions, *J. Geophys. Res.*, *69*, 2349, 1964.

Vaisberg, O. L., J. G. Luhmann, and C. T. Russell, Plasma observations of the solar wind interaction with Mars, *J. Geophys. Res.*, *95*, 14,841, 1990.

Zhang, M. H. G., J. G. Luhmann, S. W. Bougher, and A. F. Nagy, The ancient oxygen exosphere of Mars: Implication for atmosphere evolution, *J. Geophys. Res.*, *98*, 10,915, 1993a.

Zhang, M. H. G., J. G. Luhmann, A. F. Nagy, J. R. Spreiter, and S. S. Stahara, Oxygen ionization rates at Mars and Venus: Relative contribution of impact ionization and charge exchange, *J. Geophys. Res.*, *98*, 3311, 1993b.

S. Barabash, Swedish Institute of Space Physics, P.O. Box 812, SE-98128 Kiruna, Sweden. (stas@irf.se)

E. Kallio, Finnish Meteorological Institute, Vuorikatu 15 A, P.O. Box 503, FIN-00101 Helsinki, Finland. (Esa.Kallio@fmi.fi)

A. Milillo, A. Mura, and S. Orsini, Istituto di Fisica dello Spazio Interplanetario, CNR, via del Fosso del Cavaliere 100, I-00133 Roma, Italia. (anna.milillo@ifsi.rm.cnr.it; mura@ifsi.rm.cnr.it; stefano.orsini@ifsi.rm.cnr.it)

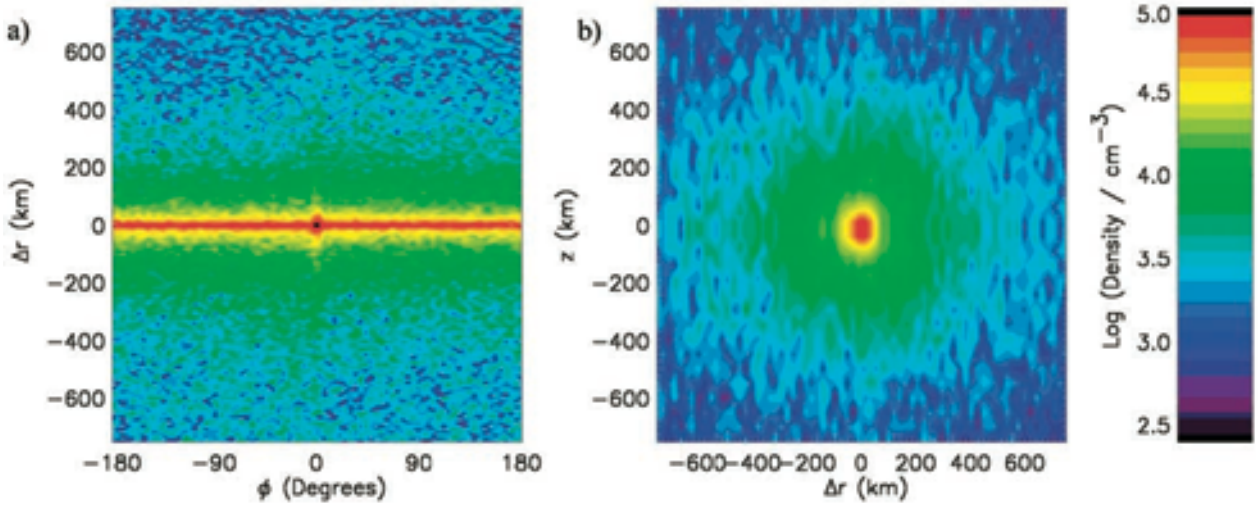

Figure 3. Simulated neutral oxygen density near the orbit of Phobos for different bidimensional sections: (a) ϕ versus r, $z = 0$; (b) Δr versus z, $\phi = 0$; $Q = 10^{23}$ s^{-1}. Phobos' position is at $\Delta r = 0$, $\phi = 0°$, $z = 0$; its velocity is directed toward the increasing ϕ.

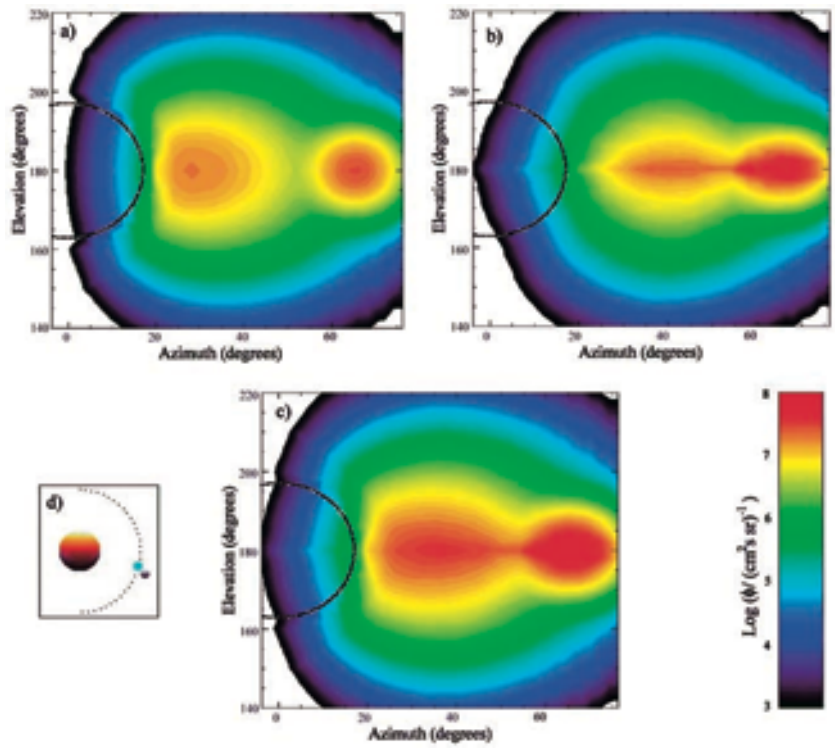

Figure 5. (a) Pseudocolor map of the ENA differential flux, function of the elevation and azimuth angle, if only Mars exosphere was present. The dashed line represents Mars' obstacle boundary. Azimuth angle is measured on the equatorial plane, beginning from Mars' center; elevation angle is measured perpendicular to the equatorial plane, Mars' center is at 180°. (b) Same as Figure 5a, if only Phobos torus-halo was present. (c) Overall ENA image resulting from the superposition of Figures 5a and 5b. The flux is integrated over all energy from 1 eV to 2 keV. (d) The spheres show an equatorial view of the relative positions of Mars (red), Phobos (blue), and the vantage point (gray); the Sun is up.

Available online at www.sciencedirect.com
SCIENCE DIRECT®
ELSEVIER
Icarus 166 (2003) 229–237
ICARUS
www.elsevier.com/locate/icarus

Mapping of the cusp plasma precipitation on the surface of Mercury

S. Massetti,[a,*] S. Orsini,[a] A. Milillo,[a] A. Mura,[a] E. De Angelis,[a] H. Lammer,[b] and P. Wurz[c]

[a] *Istituto di Fisica dello Spazio Interplanetario, Consiglio Nazionale delle Ricerche, via Fosso del Cavaliere 100, I-00133 Roma, Italy*
[b] *Space Research Institute, Department of Extraterrestrial Physics, Austrian Academy of Sciences, Schmiedlstr. 6, A-8042 Graz, Austria*
[c] *Physikalisches Institut, University of Bern, Sidlerstr. 5, CH-3012 Bern, Switzerland*

Received 15 November 2002; revised 21 August 2003

Abstract

The presence of a magnetosphere around Mercury plays a fundamental role on the way the solar wind plasma interacts with the planet. Since the observations suggest that Mercury should occupy a large fraction of its magnetosphere and because of lack of an atmosphere, significant differences in solar wind-magnetosphere coupling are expected to exist with respect to the Earth case. On the basis of a modified Tsyganenko T96 model we describe the geometry of the magnetic field that could characterize Mercury, and its response to the variations of the impinging solar wind and of the interplanetary magnetic field. The investigation is focused on the shape and dimension of the open magnetic field regions (cusps) that allow the direct penetration of magnetosheath plasma through the exosphere of Mercury, down to its surface. The precipitating particle flux and energy are evaluated as a function of the open field line position, according to different solar wind conditions. A target of this study is the evaluation of the sputtered particles from the crust of the planet, and their contribution to the exospheric neutral particle populations. Such estimates are valuable in the frame of a neutral particle analyser to be proposed on board of the ESA/BepiColombo mission.

Keywords: Mercury; Magnetosphere; Solar wind; Magnetic field

1. Introduction

The presence of a magnetosphere around Mercury plays a fundamental role on the way the solar wind plasma interacts with the planet (e.g., Ness et al., 1976). On the other hand, the existence of a weak intrinsic magnetic field together with the absence of an atmosphere, leads to important differences between the magnetospheric phenomena acting on Earth and Mercury. The magnetosphere of Mercury has been the object of various studies (e.g., Goldstein et al., 1981; Slavin et al., 1997; Luhmann et al., 1998; Killen et al., 2001), and some of them discussed the interaction of the solar wind plasma with the planetary surface. Nevertheless, because of the small amount of data available (Mariner 10 flybys, see Ness et al., 1976), modelling the magnetic field of Mercury involves some uncertainty. The relevant amount of crucial physical issues related to Mercury's environment induced the international space agencies (NASA, ESA, and ISAS) to plan important space missions devoted to the exploration of this planet (Messenger and BepiColombo). The scientific community is now facing the challenge to design instruments and improve data processing according to the present knowledge and theoretical expectations.

The present work aims to realize a *tool of analysis* to be used for determining the different configurations that could occur on the basis of the variation of the input parameters within a range of realistic values, without pretending to depict an "exact" model of the magnetosphere of Mercury. The uncertainties arising from many factors (e.g.: the density of the exosphere, magnetic field strength and geometry, surface conductivity, and others) force us to focus on qualitative more than on quantitative aspects. On the basis of a modified Tsyganenko T96 model (Tsyganenko, 1996), we establish the geometry of the magnetic field that could characterize Mercury, and its response to the variations of the impinging solar wind. The investigation is focused on the shape and dimension of the regions characterized by open magnetic field (magnetospheric cusps) that allow the direct penetration of magnetosheath plasma through the exosphere of Mercury, down to its surface. Section 2 is focused on the solar wind condition at Mercury's orbit, the model of Mercury's mag-

* Corresponding author.
E-mail address: stefano.massetti@ifsi.rm.cnr.it (S. Massetti).

0019-1035/$ – see front matter
doi:10.1016/j.icarus.2003.08.005

netosphere and the magnetosheath properties. Section 3 describes the acceleration mechanism associated with the magnetic reconnection on the dayside magnetopause. Section 4 shows the characteristics of the open field related area on Mercury, and Section 5 illustrates the sputtering generated by the magnetosheath plasma interaction with Mercury's surface. Summary and discussion are given in Section 6.

2. Sun–Mercury relationship and input parameters

2.1. The solar wind at Mercury

The solar wind at Mercury's orbit (0.29–0.44 AU) differs substantially from the average condition present at 1 AU. The Parker's spiral forms an angle of about 20° with the solar wind direction, less than half of the value at the Earth's orbit ($\sim 45°$), which implies a change of the relative weight of the interplanetary magnetic field (IMF) components with respect to the near Earth conditions, thus modifying the solar wind—magnetosphere interaction. Burlaga (2001) reported the IMF at Mercury to be 3–6 times the average strength at 1 AU ($B(E) \sim 5$ nT); by assuming a mean value of 4.5 we have $B(M) = 4.5B(E) \sim 23$ nT, and by taking into account the direction of the Parker's spiral we can estimate the IMF tangential component at Mercury to be roughly $B_t(M) \sim \sin 20° B(M) \sim 8$ nT. In the case of Mercury, the contribution of the IMF B_y component is less relevant than at the Earth, so that the magnetic reconnection at the dayside magnetopause is essentially driven by the IMF B_z component. Moreover, the increasing weight of the IMF B_x component might play a role in the way the Mercury's magnetosphere links with the solar wind (e.g., Kabin et al., 2000; Sarantos et al., 2001). Nevertheless, we expect the IMF at the orbit of Mercury to be characterised by strong deviation from the nominal Parker spiral, especially during periods of high solar activity. In the present study we focused on the effects associated with the IMF tangential component and the B_x contribution is not taken into account. The average solar wind density is about a factor of ten higher than at the Earth's orbit, even if this value varies considerably due to the high eccentricity of the planetary orbit (Burlaga, 2001): in fact, using the formula derived from the data of *Helios* spacecraft between 0.3–1.0 AU (Bougeret et al., 1984):

$$N = 6.4 \times R^{-2.1}\ \mathrm{cm}^{-3} \quad (1)$$

we obtain $N_{\min} = 34\ \mathrm{cm}^{-3}$ at aphelion ($R = 0.44$ AU), $N_{\max} = 83\ \mathrm{cm}^{-3}$ at perihelion ($R = 0.29$ AU), and average value $N_{\mathrm{ave}} = 52\ \mathrm{cm}^{-3}$ ($R = 0.36$ AU), compared to $N \sim 6\ \mathrm{cm}^{-3}$ at 1 AU. Table 1 reports some important average values evaluated for $R = 0.36$ AU (e.g., Kabin et al., 2000; Burlaga, 2001).

Table 1
Average solar wind parameters at Mercury

Solar wind speed	$430\ \mathrm{km\,s}^{-1}$
Solar wind density	$52\ \mathrm{cm}^{-3}$
Solar wind ion temperature	$\sim 2 \times 10^5$ K
Dynamic pressure	16 nPa
Ion sound speed	$74\ \mathrm{km\,s}^{-1}$
Alfvén speed	$120\ \mathrm{km\,s}^{-1}$
Specific heat ratio (γ)	5/3
Mach number (M_∞)	5.8
Alfvénic Mach number ($M_{\mathrm{A}\infty}$)	3.6

2.2. Modeling the magnetosphere of Mercury

In the present work, we approximate the magnetosphere of Mercury by means of a modified Tsyganenko T96 model (Tsyganenko, 1996). This magnetospheric model version includes an explicitly defined realistic magnetopause, large-scale Region 1 and 2 Birkeland current systems, the IMF penetration across the magnetospheric boundary, and accepts both IMF B_y and B_z components as independent input parameters. We removed the contribution of the ring current, since Mercury's magnetic field seems to be not able to trap particles into closed drift paths around the planet, although the injection of plasma into the magnetosphere during magnetic substroms could generate at least a transient partial-ring current (e.g., Orsini et al., 2001; Lukyanov et al., 2001). Due to the expected lack of a conducting ionosphere on Mercury there is still a wide debate regarding the existence of field-aligned currents, together with the existence of mechanisms capable to allow the closure of the magnetospheric current systems. In the present work, our choice is to assume a 50% contribution of the Birkeland currents in the T96 model, that is an halfway position between the Earth's case and a null contribution. In addition, to address the differences of both the intensity of the magnetic field and the radius of Mercury with respect to the Earth, we have scaled the T96 model by a factor 6.9, like in previous analyses based on the *Mariner* 10 data (e.g., Luhmann et al., 1998). To find the open magnetic field lines (the field lines that cross the magnetopause and merge with the IMF), we used the subroutine *Locate* (Tsyganenko, 1996) that approximates the dayside magnetopause with an ellipsoid, as in the T96 model. In this context, it must be noted that, as well as other magnetospheric models, the T96 model does not describe the field depression caused by the diamagnetic effect of the plasma engulfing the magnetospheric cusps (Tsyganenko and Russell, 1999). To some extent, this lack causes a misrepresentation of the Mercury's magnetosphere/magnetopause on the dayside, which must be kept in mind when dealing with the cusp-related regions (low latitude boundary layer, cusp proper and mantle), since these areas are much wider on Mercury than on Earth.

2.3. The magnetosheath of Mercury

The magnetosheath is the region localized between the bow shock and the magnetopause (the thin current layer enveloping the magnetosphere), and it is populated by thermalised solar wind plasma that flows anti-sunward along the

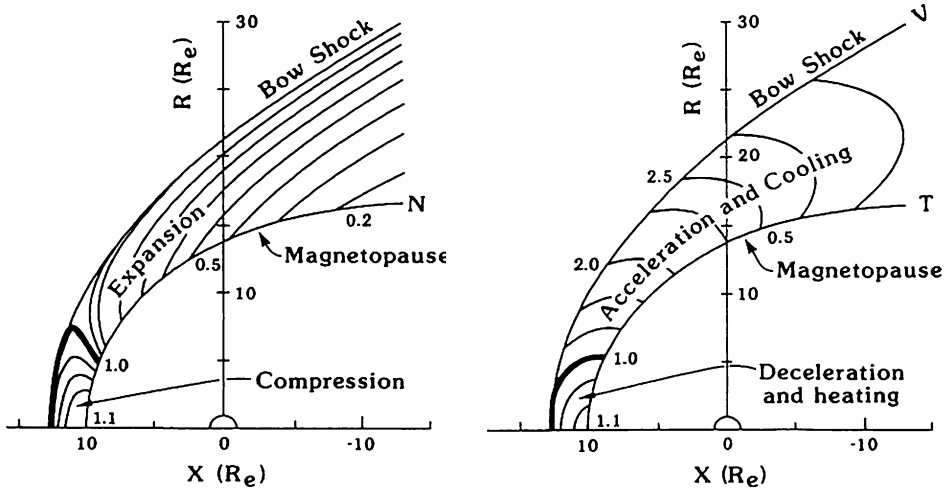

Fig. 1. Overall properties of the magnetosheath plasma parameters, density (N, left panel), velocity (V, right panel, upper values) and temperature (T, right panel, lower values), as a function of the position along the magnetosheath (after Song et al., 1999), and normalized to the unperturbed solar wind values.

flanks of the magnetosphere: the plasma is decelerated, compressed and heated in the subsolar region, then its speed increases progressively as the plasma moves tailward, with density and temperature gradually decreasing. In addition, on the dayside magnetosheath the frozen-in IMF dragged by the shocked solar wind plasma undergoes intensification, resulting from the compression of the plasma on the subsolar region. The parameters needed for defining the magnetosheath plasma environment were derived from the work of Spreiter et al. (1966), where the ratio of the local velocity (V), density (N), and temperature (T) with respect to the unperturbed upstream values (V_∞, N_∞, and T_∞), were calculated for an hydromagnetic flow around a magnetosphere (see Fig. 1).

In the Spreiter et al. (1966) work, most of the calculations were done for a gasdynamic free-stream Mach number ~ 8, which in the case of a magnetosphere should be more properly identified by a free-stream pseudo Mach number (Spreiter et al., 1966):

$$M^*_\infty = M_\infty M_{A_\infty} / \left(M^2_\infty + M^2_{A_\infty} - 1\right)^{1/2} \quad (2)$$

where M_∞ and M_{A_∞} are the free-stream Mach number and Alfvén Mach number, respectively, of the solar wind. We have extrapolated the V/V_∞, N/N_∞, and T/T_∞ variation along the magnetopause assuming that in the case of Mercury $M^*_\infty \sim 3$ (using data of Table 1), although the V/V_∞ ratio is roughly independent from M^*_∞. Then, these three parameters were fitted as a function of the distance from the subsolar point "d" along the GSM X-axis, as follow:

$$V/V_\infty = -0.249d + 0.953d^{1/2}, \quad (3)$$

$$N/N_\infty = 3.300 - 3.220d + 1.400d^{1.5}, \quad (4)$$

$$T/T_\infty = 1 + 3.000\left(1 - (V/V_\infty)^2\right). \quad (5)$$

Figure 2 shows V/V_∞ (solid line, right scale) and N/N_∞ (dashed line, left scale) in the upper panel, and T/T_∞ in the lower panel.

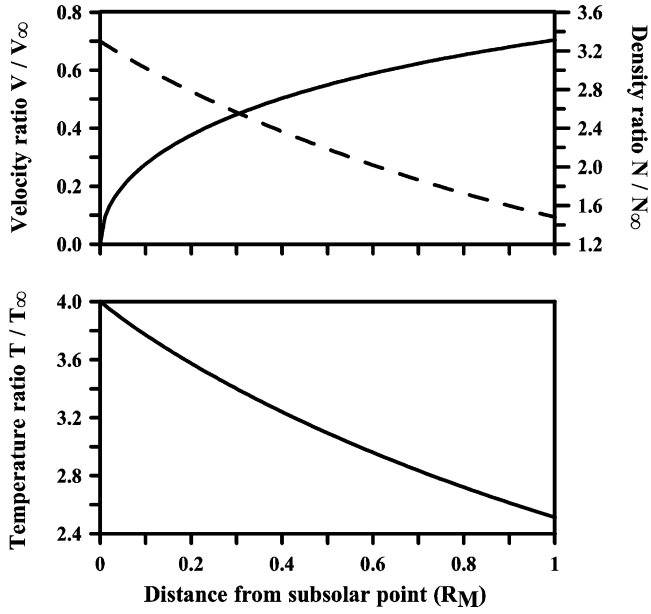

Fig. 2. Magnetosheath parameters variation along the magnetopause, as a function of the distance from the subsolar point, scaled to Mercury: T/T_∞ (lower panel), V/V_∞ (solid line, upper panel) and N/N_∞ (dashed line, upper panel).

3. A tool of analysis for the plasma precipitation at Mercury

3.1. Properties of the Earth's magnetospheric cusp regions

Before investigating the direct solar wind plasma entry into the magnetosphere of Mercury, we briefly describe in the following the configuration of the regions where this process takes place on the Earth's magnetosphere. Actually, the geomagnetic regions generally referred as *cusps* (one for each hemisphere) exhibit a complex structure. The cusp regions are usually divided into three sub-regions: the low latitude boundary layer (LLBL), the cusp proper (cusp)

and the mantle. The relative position and size of these sub-regions depend on the IMF B_y and B_z component, and when magnetic merging occurs at the dayside magnetopause with $B_z < 0$, the LLBL lies equatorward the cusp proper and the mantle poleward of it (e.g., Newell and Meng, 1992). The three regions are divided according to the energy and flux of the precipitating particles along those magnetic field lines that are connected to the IMF: the particle energy is at maximum in the LLBL and decreases when moving through the cusp and the mantle, while the particle flux has a maximum in the cusp proper.

The differentiation between the cusp sub-regions is also affected by a velocity filter effect, due to the fact that the higher the particle energy is (and speed), the less is the time it takes to flow along the field line: as a result, the lower energy particles are dragged at higher latitude as the open field line convects poleward. On the Earth, there is a step in the flux distribution between the LLBL and the cusp proper due to the existence of two distinct plasma populations in the magnetosheath: a lower energy component ($E < 1.3$ keV) with $\sim 80\%$ of the density, and a higher energy one ($E > 1.3$ keV) with the remaining 20% of the density (Fuselier et al., 1999). The hotter population is thought to be constituted by solar wind ions that, after being reflected back at the bow shock, perform a partial gyration into the upstream region before crossing the shock to enter the magnetopause (Fuselier et al., 1999, and references therein). This fact, associated with the velocity filter effect, causes the LLBL particles to be more energetic than expected on a basis of a single magnetosheath population.

3.2. Dayside magnetic reconnection and plasma entry

When the interplanetary magnetic field (which is compressed inside the magnetosheath) has a component that is antiparallel to the magnetospheric field near the magnetopause, a magnetic reconnection occurs between the two fields, and the magnetosheath plasma can cross the magnetopause and precipitate toward the planet. The reconnected fields generate a *rotational discontinuity* that moves away from the merging site, along the magnetopause itself. If the magnetopause is approximated as a one-dimensional discontinuity we can define a reference frame located on the discontinuity, called *de Hoffmann–Teller* frame (HT), where the reconnected field line is at rest. With respect to the planet, the HT frame moves along the magnetopause with velocity V_{HT}, which depends both on the flow velocity in the magnetosheath and on the magnetic tension due to the geometry of the reconnected field line. In the HT reference frame the energy and pitch angle are conserved, and the bulk flow on either side of the discontinuity is field-aligned and moving at the local Alfvén speed: in fact, by applying the tangential stress balance condition, one finds that the change in the momentum of the plasma must balance the magnetic field tension, and that the field-aligned speed of the plasma in the HT frame must be equal to the Alfvén speed in both the magnetosheath and the magnetosphere (Cowley and Owen, 1989; Cowley, 1995).

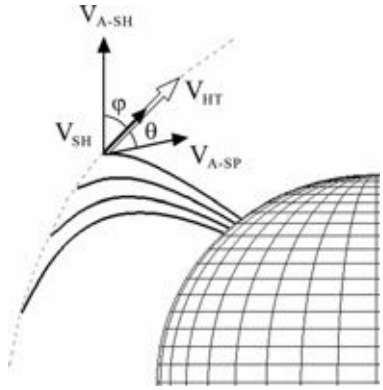

Fig. 3. Sketch of a reconnected field line on the dayside magnetopause, illustrating the parameters associated with the *de Hoffman–Teller* reference frame: $V_{\text{A-SH}}$ and $V_{\text{A-SP}}$ are the Alfvén speed on the magnetosheath and on the magnetosphere side, which are tangent to the local magnetic field; φ and θ are the angles formed by $V_{\text{A-SH}}$ and $V_{\text{A-SP}}$ with the magnetopause (dashed gray line); V_{SH} is the flow velocity in the magnetosheath (black arrow tangent to magnetopause); and V_{HT} is the HT reference frame velocity (white arrow).

Figure 3 depicts the geometry of a reconnected field line on the GSM XZ-plane (dayside, i.e., $X > 0$), assuming IMF pointing southward ($B_z < 0$): $V_{\text{A-SH}}$ and $V_{\text{A-SP}}$ are the Alfvén speed on the magnetosheath and on the magnetosphere side, which are tangent to the local magnetic field; φ and θ are the angles formed by $V_{\text{A-SH}}$ and $V_{\text{A-SP}}$ with the magnetopause (dashed gray line); V_{SH} is the flow velocity in the magnetosheath (black arrow tangent to magnetopause); and V_{HT} is the HT reference frame velocity (white arrow). In general, the aforementioned vectors do not lie on the same plane, and the stress balance condition in the HT frame can be written as (e.g.: Cowley and Owen, 1989; Lockwood and Smith, 1994; Cowley, 1995; Lockwood, 1995):

$$\overline{V}'_{\mathrm{SH}} = \pm(V_{\text{A-SH}}\cos\varphi)\hat{b}_{\text{SH-MP}} \tag{6}$$

the upper (lower) sign refers to the Northern (Southern) hemisphere, where $V_{\text{A-SH}}$ is antiparallel (parallel) to the field line, and $\cos\varphi = \hat{b}_{\mathrm{SH}} \cdot \hat{b}_{\text{SH-MP}}$, being $\hat{b}_{\mathrm{SH}}$ and $\hat{b}_{\text{SH-MP}}$ the unit vector along the magnetosheath field line and its projection on the magnetopause, respectively. In the planet reference frame this translates to

$$\overline{V}_{\mathrm{HT}} = \overline{V}_{\mathrm{SH}} \mp (V_{\text{A-SH}}\cos\varphi)\hat{b}_{\text{SH-MP}}. \tag{7}$$

Since the minimum field-aligned velocity of the injected magnetosheath plasma is zero in the HT frame, in the planet frame we have:

$$\overline{V}_{\min} = (\overline{V}_{\mathrm{HT}} \cdot \hat{b}_{\mathrm{SP}})\hat{b}_{\mathrm{SP}} \rightarrow V_{\min} = V_{\mathrm{HT}}\cos\theta, \tag{8}$$

where $\hat{b}_{\mathrm{SP}}$ is the unit vector along the magnetospheric field line. For the resulting peak and maximum field-aligned velocity of the magnetosheath distribution in the planet frame, we have:

$$\overline{V}_{\mathrm{p}} = \overline{V}_{\min} + V_{\text{A-SP}}\hat{b}_{\mathrm{SP}} \rightarrow V_{\mathrm{p}} = V_{\mathrm{HT}}\cos\theta + V_{\text{A-SP}}, \tag{9}$$

$$\overline{V}_{\max} = \overline{V}_{\rm p} + V_{\rm th}\hat{b}_{\rm SP} \rightarrow V_{\max} = V_{\rm HT}\cos\theta + V_{\rm A\text{-}SP} + V_{\rm th}, \quad (10)$$

where $V_{\rm th}$ is the plasma thermal speed. From Eqs. (8)–(10) the corresponding energies $E_{\min}$, $E_{\rm p}$, and $E_{\max}$ can be calculated. In the present study the HT concept is applied to the dayside magnetopause of Mercury, assuming the magnetic field to be approximated by the modified T96 model described in Section 2.2.

4. LLBL, cusp, and Mantle precipitations on Mercury's surface

By applying of the above-described *tool of analysis*, we can outline the plasma entry through open field lines on the dayside surface of Mercury. In the following, the results of a preliminary analysis are shown, obtained by varying the input parameters within realistic ranges. We assume a 50% of the magnetosheath plasma on reconnected field lines to actually cross the magnetopause (the remaining 50% is reflected by the boundary) by applying a reflection factor of 0.5, which is a typical value in the case of the Earth (e.g., Lockwood, 1997). In addition, we estimated the fraction of the precipitating ions reaching the planet surface along reconnected field lines to be limited to particles with a pitch-angle smaller than 35° (loss cone angle), being the remaining ones reflected back due to the intensification of the magnetic field toward the planet. The pitch angle (α) limit is derived from the relation:

$$\sin^2\alpha = B_{\rm SS}/B_{\rm SURF}, \quad (11)$$

where the magnetic field strength at the subsolar point ($B_{\rm SS}$) and at the planet surface ($B_{\rm SURF}$) are about 100 and 300 nT, respectively. By combining the two aforementioned estimations we get an overall factor equal to 0.1, which means that only 10% of the nominal flux precipitates onto the planet.

To reduce the number of variables involved in the calculations, we consider the Alfvén speed in the magnetosheath to be constant and equal to $V_{\rm A\text{-}SH} = 120$ km s^{-1} (Table 1), while the magnetospheric Alfvén speed is tentatively set to be $V_{\rm A\text{-}SP} = 6V_{\rm A\text{-}SH}$ (owing to the lower plasma density in the magnetosphere), because of the large uncertainties on the exospheric density distribution around Mercury (Lammer and Bauer, 1997; Lammer et al., 2003, *companion paper*; Wurz and Lammer, 2003). These values are in line with typical Alfvénic speeds at both outer and inner side of the Earth's magnetopause (e.g., Lockwood, 1997). The plasma thermal speed $V_{\rm th}$ affecting $V_{\max}$ (Eq. 10) and $E_{\max}$, is derived from the magnetosheath plasma temperature calculated by means of Eq. (5). For a 2×10^5 K solar wind, from Eq. (5) we get $T \sim 0.8 \times 10^6$ K at the subsolar point of the Mercury's magnetopause, to be compared with $T \sim 4.4 \times 10^6$ K in the case of the Earth, with a ratio of about 1/5. Finally, all the calculations were performed for the case of a zero tilt angle for the magnetic dipole of Mercury, which is a likely situation (Ness et al., 1976).

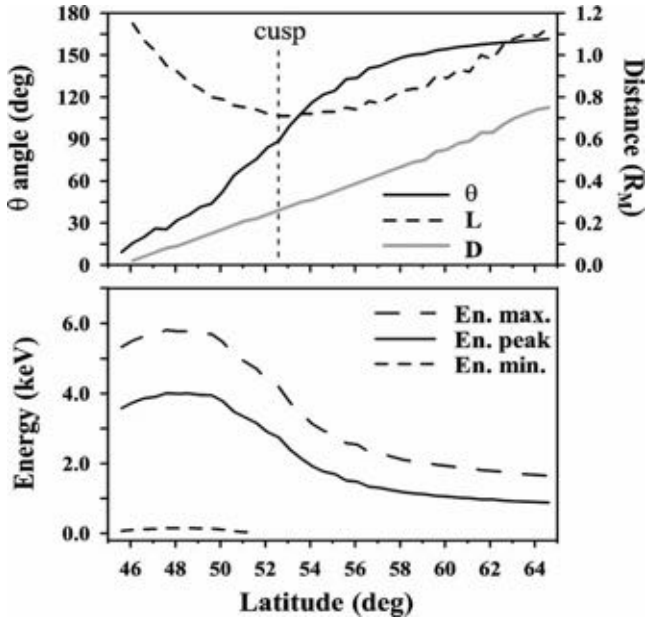

Fig. 4. Results obtained for an open field line moving on the XZ-plane (IMF $B_Z = -10$ nT). Upper panel: θ angle, open field line length (L) from planet surface to the magnetopause, and HT frame distance from the subsolar point (D) measured along the magnetopause. Lower panel: particle energy minimum, peak and maximum $E_{\min}$, $E_{\rm p}$, and $E_{\max}$. The vertical dotted line marks the nominal cusp location ($\theta = 90°$ and minimum of L).

Figure 4 shows typical parameters plotted as a function of latitude, characterizing the time evolution of a reconnected field line that moves from low to high latitudes along the meridian on the GSM XZ-plane (as depicted in Fig. 3), and calculated with a solar wind pressure $P_{\rm dyn} = 16$ nPa, IMF $B_y = 0$ nT, and IMF $B_z = -10$ nT. In the upper panel: θ angle, open field line length (L) from planet surface to the magnetopause, and distance (D) of the HT frame from the subsolar point measured along the magnetopause, the vertical dotted line marks the nominal cusp location, where $\theta = 90°$ and L is minimum. In the lower panel: particle distribution energies $E_{\min}$, $E_{\rm p}$, and $E_{\max}$. By comparing the two panels of Fig. 4, we can see that the injected particle energies: (a) initially increase as the field line straightens (LLBL, $\theta < 90°$, Lat $\sim 45°$–$49°$); (b) subsequently decrease to magnetosheath values in the cusp (no energy gain, $\theta \sim 90°$, Lat $\sim 53°$); (c) finally reach lower and lower values when the field line moves through the mantle ($\theta > 90°$, Lat $> 53°$). To minimize arbitrary hypotheses, in this preliminary study we neglected the *velocity filter effect*, and assumed the magnetosheath filled by just one plasma population (defined by the Eqs. (3)–(5)). In fact, part of the solar wind plasma impinging on the bow-shock of Mercury could be energised, giving rise to a second (hotter) magnetosheath plasma population, as happens at the Earth (Section 3.1). In this case, thanks to the *velocity filter effect*, the Mercury's LLBL will be more energetic than shown here, and there will be also a step in the energy between the LLBL itself and the cusp proper. However, the shape and size of the open field area, together with

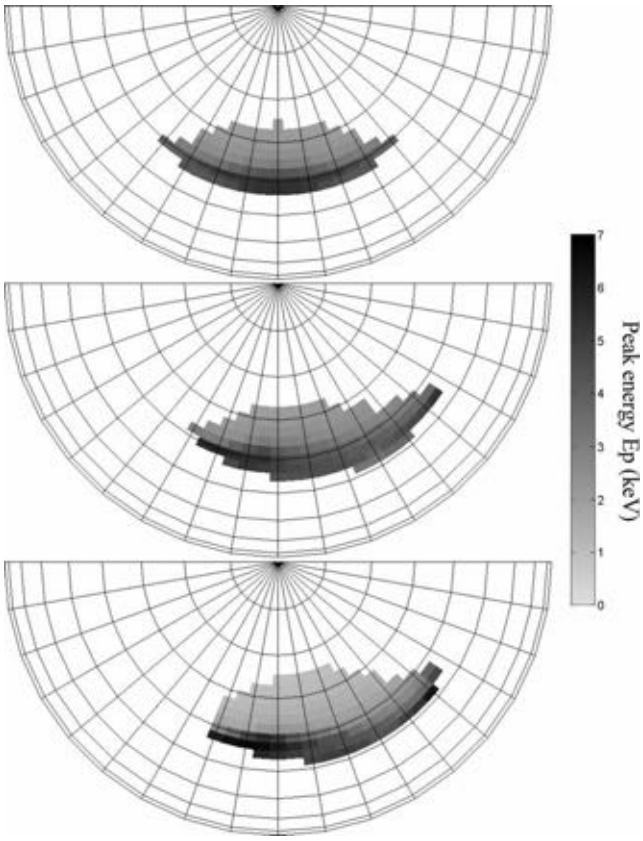

Fig. 5. Mapping of the open field area as a function of the incident peak energy (keV, left scale) on the northern dayside surface of Mercury (only the field lines crossing the magnetopause within $2R_M$ from the planet are considered). The three panels show the both area position and dimension according to different solar wind conditions: (top) $P_{dyn} = 16$ nPa, $B_y = 0$ nT, and $B_z = -10$ nT; (middle) $P_{dyn} = 16$ nPa, $B_y = -5$ nT, and $B_z = -10$ nT; (bottom) $P_{dyn} = 60$ nPa, $B_y = -5$ nT, and $B_z = -10$ nT.

the mean flux of the precipitating particles, are not affected by these choices, as most of the results derived here.

The three panels of Fig. 5 show both position and extension of the surface area with open field lines (AO), mapped on the northern dayside surface of Mercury in response to different solar wind conditions. The area is gray-coded according to the energy E_p of the particle distribution. We mapped only the open field lines that cross the magnetopause within $2R_M$ (the field lines at higher latitudes are open indeed, but the rate of solar wind plasma entry is low, since they map far in the magnetic tail), by using a 5° longitude per 2.5° latitude grid. The three configurations were calculated for: $P_{dyn} = 16$ nPa ($V_{sw} = 400$ km s^{-1}, $N_{sw} = 60$ cm^{-3}), $B_y = 0$ nT, and $B_z = -10$ nT (top panel), $P_{dyn} = 16$ nPa, $B_y = -5$ nT, and $B_z = -10$ nT (middle panel), $P_{dyn} = 60$ nPa ($V_{sw} = 600$ km s^{-1} and $N_{sw} = 100$ cm^{-3}), $B_y = -5$ nT, and $B_z = -10$ nT (bottom panel). By comparing Figs. 4 and 5, we notice that most of the energy (and flux) of the precipitating magnetosheath particles is deposited on a region that is narrow in latitude, but conversely extended in longitude. This region can be identified as low latitude boundary layer (LLBL, $\theta < 90°$), while the remaining area is characterized by a monotonous decrease of both energy and flux of the precipitating particles. In the upper panel of Fig. 5 we can observe what should be a typical configuration of the open field area of Mercury's cusps during moderate southward pointing IMF, under the assumption of a typical solar wind pressure at 0.36 AU (16 nPa): the open area ranges between about 45° and 65° in latitude, and about −40° and 40° in longitude. In the middle panel we see the effect associated with a negative IMF B_y (causing the shift of cusp proper toward dawn) that drags the whole open area eastward. In this case, the open area expands equatorward to about 40° latitude, and the most intense precipitation occurs on the South–West edge of the open area itself. Finally, the effect associated by a strengthening of the solar wind pressure up to 60 nPa is shown in the lower panel of Fig. 5. The open area shifts slightly eastward and expands poleward, mostly on the North–East edge. The ramming of the solar wind over the Mercury's magnetosphere causes a strong tailward bending of the magnetic field lines, and inhibits the particle precipitation at high latitudes, focusing the plasma entry on the equatorial edge of the open area. This effect is associated with an increase of both particle flux and energy, due to the rise of V_{sw} and/or D_{sw} that causes the P_{dyn} intensification. It must be stressed that all the above considerations apply also to the southern magnetic cusp, apart the fact that the IMF B_y effect reverses in this hemisphere.

When comparing the results of Fig. 5 with those of Sarantos et al. (2001) (Figs. 2 and 4), derived on the basis of the TH93 magnetospheric model (Toffoletto and Hill, 1993) with the explicit contribution of the IMF B_x component, we note a substantial match of the longitudinal extent of the open field area (about 80°–90°) and its displacement in response of IMF B_y variations. Nevertheless, a difference exists about the open area latitudinal width: their interval ranges between 60° to 10°–20° (IMF $B_z = -5$ nT and −20 nT, respectively) in latitude, to be compared with our range of about 65°–45°. In the TH93 model, the main effects of a strong IMF B_x are a North–South asymmetry and an equatorward expansion of the cusp region. The Sarantos et al. (2001) analysis was performed with a rather low solar wind pressure $P_{dyn} = 3.4$ nPa (four times smaller than the mean values at Mercury), and by assuming the penetration fraction of the IMF through the magnetopause (which is a free parameter of the TH93 model) to be as high as 40%, twice the Earth's case. Since both values affect the geometry of the magnetic field lines, the above comparison should be considered as only indicative.

The size of the open field associated area is an important parameter for characterizing the plasma precipitation on the planet, and we derived the dependence of the area size with respect to the IMF B_z (Fig. 6, upper panel) and to the solar wind pressure P_{dyn} (Fig. 6, lower panel). In the upper panel the open area is calculated with constant $P_{dyn} = 20$ nPa ($V_{sw} = 450$ km s^{-1}, $N_{sw} = 60$ cm^{-3}), while in the lower one with a constant IMF $B_z = -10$ nT, and by assuming IMF $B_y = 0$ nT in both cases. We see that the open field area is

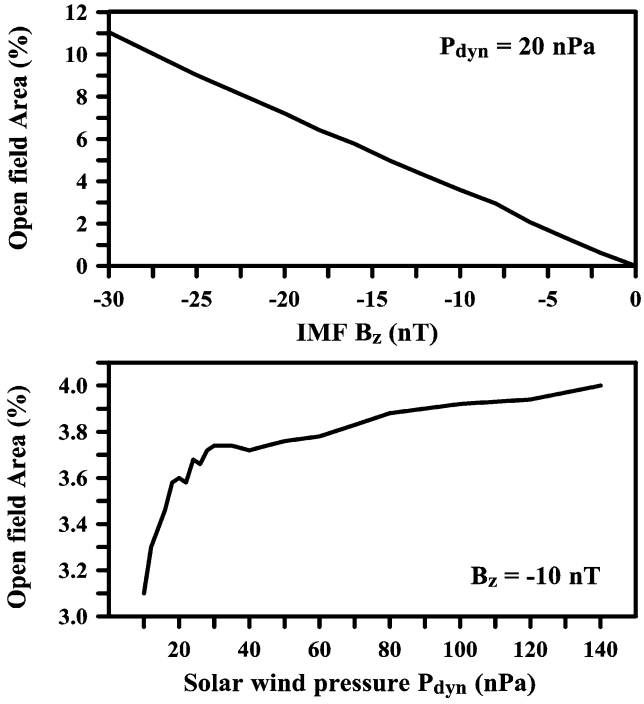

Fig. 6. Open field area (AO) of Mercury's cusps as a function of the IMF B_z component (upper panel), and of the solar wind pressure $P_{\rm dyn}$ (lower panel). The two sets of data were derived with IMF $B_y = 0$, together with the IMF B_z and $P_{\rm dyn}$ values indicated in the legends.

Table 2
Mean values of particle flux and open field area at Mercury ($P_{\rm dyn} = 20$ nPa)

IMF B_z (nT)	Open field area (cm^2)	Particle flux (cm^{-2} s^{-1})	Open field area rate (s^{-1})
−10	2.8×10^{16}	4.1×10^{8}	1.1×10^{25}
−20	5.4×10^{16}	3.8×10^{8}	2.1×10^{25}
−30	8.3×10^{16}	3.7×10^{8}	3.0×10^{25}

more modulated by IMF B_z than by $P_{\rm dyn}$ variations. The dependence on IMF B_z is nearly linear and can be expressed as:

$$\mathrm{AO}(\%) \sim -0.36 B_z \ (\mathrm{nT}). \tag{12}$$

The dependence on $P_{\rm dyn}$ is weak and exhibits a kink at about 30 nPa (in the present case where IMF $B_z = -10$ nT); two linear relations can tentatively approximate the trend:

$$\mathrm{AO}(\%) \sim 2.962 + 0.028 P_{\rm dyn} \ (\mathrm{nPa}), \quad P_{\rm dyn} < 30 \ \mathrm{nPa}, \tag{13a}$$

$$\mathrm{AO}(\%) \sim 3.624 + 0.003 P_{\rm dyn} \ (\mathrm{nPa}), \quad P_{\rm dyn} > 40 \ \mathrm{nPa}. \tag{13b}$$

In a first approximation, and within the assumptions considered, the effect of the solar wind pressure on the open field related area can be assumed to be negligible. As reference, Table 2 shows three mean values of the open field area and particle flux at Mercury, computed for IMF $B_z = -10, -20, -30$ nT, and $P_{\rm dyn} = 20$ nPa. The mean particle flux through the open field area (last column) increases by a factor proportional to |IMF $B_z/10$ nT|, while the mean particle flux itself decreases slightly due to the increase of the relative weight of the low flux regions (cusp proper and mantle). As a realistic upper limit for the particle flux precipitation we get the value of about 2×10^9 cm^{-2} s^{-1}, obtained with $P_{\rm dyn} = 164$ nPa ($V_{\rm sw} = 700$ km s^{-1}, $N_{\rm sw} = 200$ cm^{-3}), $V_{\text{A-SH}} = 180$ km s^{-1}, and $V_{\text{A-SP}}/V_{\text{A-SH}} = 8$, which leads to a mean particle flux across the Mercury's cusps of $\sim 10^{26}$ s^{-1}.

5. Discussion: surface sputtering and ENA production from cusp-mapped surface of Mercury

Where the open field lines intersect the planetary surface, the soil becomes directly linked to the magnetosheath plasma population, and then exposed to ion precipitation. The ion impact on the soil leads to a particle release process called "ion-sputtering" (e.g., Lammer and Bauer, 1997; Killen et al., 2001; Lammer et al., 2003; Wurz and Lammer, 2003). The sputtered particles follow ballistic trajectories, before falling back to the surface or escaping from the planet, depending on their initial energy and direction. The energy distribution for sputtered particles, $F(E_{\rm e})$, with ejection energy $E_{\rm e}$, can be expressed as (Sieveka and Johnson, 1984):

$$F(E_{\rm e}) \sim \frac{E_{\rm e}}{(E_{\rm e} + E_{\rm b})^3} \left[1 - \sqrt{\frac{E_{\rm e} + E_{\rm b}}{E_{\rm i}}} \right], \tag{14}$$

where $E_{\rm i}$ is the energy of the incident particle and $E_{\rm b}$ is the surface binding energy of the sputtered particle. The products arising from this particle bombardment depend both on the composition and chemical structure of the planet surface. In the case of Mercury, the small amount of data does not allow any precise estimate of the surface composition. However, the presence of H, He, O, Na, K, and Ca in the exosphere of the planet was established by both space and ground-based observations (Broadfoot et al., 1976; Potter and Morgan, 1986; Bida et al., 2000). Because the sodium spatial and temporal distribution was found to be compatible with solar activity variations (Killen et al., 2001), sputtering may be an important process. Since sodium is likely bound to oxygen (oxide composites), the binding energy could be assumed to be 2 eV (McGrath et al., 1986). Figure 7 shows the normalized integral of $F(E_{\rm e})$, from $E_{\rm e}$ to infinity, as a function of ejected particle energy $E_{\rm e}$, in the case of $E_{\rm i} = 1$ keV solar wind protons (assuming an overall binding energy for oxygen equal to 4 eV, Lammer and Bauer, 1997).

If we derive $F(E_{\rm e})$ from Eq. (14) and then apply the estimated precipitating ion fluxes as obtained in the analysis performed in the previous paragraph, we can estimate the neutral atom (ENA) fluxes extracted by the soil of Mercury. Figure 8 shows an estimation of the sputtered Na-ENA (right scale) and O-ENA (left scale) fluxes, induced by the magnetosheath plasma precipitating throughout the Mercury's northern cusp. The fluxes are calculated by using the surface sputter yield derived in our companion paper (Lammer

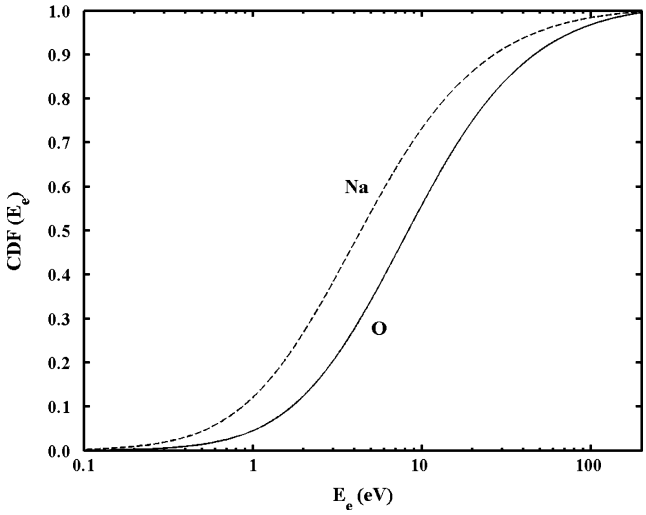

Fig. 7. Normalized integral (from E_e to infinity) of the energy distribution of Na and O sputtered particles, as a function of their ejection energy E_e, in the case of $E_i = 1$ keV solar wind protons.

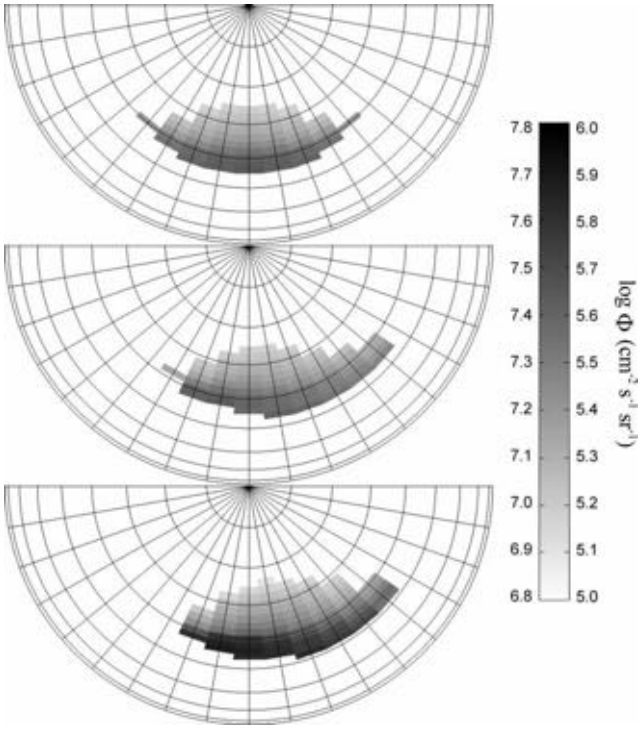

Fig. 8. Gray-coded Na-ENA (right scale) and O-ENA (left scale) flux spatial distribution (calculated assuming an energy E_p for all precipitating particles) generated by ion-sputtering from the open field area, on the northern dayside surface of Mercury. As in Fig. 5, the three panels refer to different solar wind conditions: (top) $P_{dyn} = 16$ nPa, $B_y = 0$ nT, and $B_z = -10$ nT; (middle) $P_{dyn} = 16$ nPa, $B_y = -5$ nT, and $B_z = -10$ nT; (bottom) $P_{dyn} = 60$ nPa, $B_y = -5$ nT, and $B_z = -10$ nT.

et al., 2003), 0.07 for sodium and 0.03 for oxygen in the case of 1 keV proton impacts, and by assuming a relative abundance of 0.0053 for sodium and 0.8 for oxygen in the soil of Mercury. Moreover, we consider that all precipitating ions have the same energy E_p (corresponding to the magnetosheath distribution peak as derived from Eq. (9)), and that the energy distribution of the sputtered particles is integrated above the energy corresponding to the escape velocity from the planet (4.3 km s^{-1} $\sim$ 2 eV for Na).

Using the same input values of Fig. 5 we derived the three patterns illustrated in Fig. 8. According to the patterns depicted in Fig. 5, the ENA induced by ion-sputtering have a distribution peaked in a narrow band on the equatorward edge of the open field area (upper panel). The ENA distribution is stretched in longitude, with a East–West displacement controlled by the IMF B_y (middle panel). An increasing solar wind pressure P_{dyn} (due to an increase of V_{sw} and/or N_{sw}) causes the widening of the sputtered area and an intensification of the signal (lower panel). Within the ion-sputtering context, the solar wind plasma precipitating through cusp regions can be seen as a beam that probes the planet surface, and induces a signal whose geographical extension and intensity depend on the incoming solar wind conditions, whereas its mass spectrum is strongly related to the atomic composition of the soil.

6. Summary

We modelled the solar wind interaction with the magnetosphere of the planet Mercury by means of a numerical *tool of analysis*. Our study is focused on the direct solar wind plasma entry through the magnetic cusps of Mercury. In particular, details on the size and shape of the regions where the open magnetic field lines map, as well as on the particles acceleration generated by the magnetic reconnection with the interplanetary magnetic field are given. For IMF $B_z = -10$ nT, we found a mean open field area of 2.8×10^{16} cm^2, a mean proton flux of 4.1×10^8 cm^{-2} s^{-1}, and a proton precipitation rate via open field area of 1.1×10^{25} s^{-1}. We evaluated also the upper limit of the mean proton flux precipitating along open field lines, under *non-extreme* solar wind conditions, to be of the order of 2×10^9 cm^{-2} s^{-1}. For the first time, a pattern of the plasma precipitation through the open dayside magnetosphere of Mercury as a function of the particle energy is given. The acceleration produced by the magnetic reconnection on the dayside magnetopause seems to be able to increase the solar wind plasma energy up to several keV, while the reconnection mechanism itself causes the most energized particles to fall within a narrow band on the equatorward edge of the open field area, while the rest of the open field area is populated by particles with monotonously decreasing energy. In addition, we simulated the ENA signal produced by Na sputtered atoms, under different solar wind conditions, according to the sputtering yield calculated in our companion paper (Lammer et al., 2003). The ENA signal derived reveals to be a proxy of the solar wind plasma precipitation pattern through the open field lines.

The determination of the energy and flux precipitation pattern is useful for the analysis of the phenomena related to the direct solar wind plasma interaction with the surface

of Mercury, as particle release by ion-sputtering, resulting in thermal and non-thermal atom emission. The ENA signal is triggered by the state of the impinging solar wind, and its mass spectrum is expected to reflect the surface atomic composition, possibly giving information on the elemental composition of the Mercury surface.

A Neutral Particle Analyser (NPA-SERENA) is proposed for the ESA BepiColombo mission to Mercury. This detector consists of three spectrometers, capable to detect neutral atoms from thermal energies up to tens of keV, with high time and space resolution. NPA-SERENA will be able to monitor the sputtering-induced refilling of the exosphere, as well as the high-energy part of the non-thermal (directional) neutrals. Such measurements will allow the investigation of the solar wind interaction with the surface, providing new insights on the exosphere together with surface composition and erosion processes.

Acknowledgments

Authors thank N. Tsyganenko and the NASA/Goddard Space Flight Center for making magnetospheric models available to the scientific community. Referees are acknowledged for useful comments.

References

Bida, T.A., Killen, R.M., Morgan, T.H., 2000. Discovery of calcium in Mercury's atmosphere. Nature 404, 159–161.

Broadfoot, A.L., Shemansky, D.E., Kumar, S., 1976. Mariner 10: Mercury atmosphere. Geophys. Res. Lett. 3, 557–580.

Bougeret, J.L., King, J.H., Schwenn, R., 1984. Solar radio burst and in situ determination of interplanetary electron density. Solar Phys. 90, 401–412.

Burlaga, L.F., 2001. Magnetic fields and plasma in the inner heliosphere: helios results. Planet. Space Sci. 49, 1619–1627.

Cowley, S.W.H., 1995. Theoretical perspectives of the magnetopause: a tutorial review. In: Physics of the Magnetopause. In: AGU Geophysical Monograph, Vol. 90, pp. 29–43.

Cowley, S.W.H., Owen, C.J., 1989. A simple illustrative model of open flux tube motion over the dayside magnetopause. Planet. Space Sci. 37, 1461–1475.

Fuselier, S.A., Lookwood, M., Onsager, T.G., Peterson, W.K., 1999. The source population for the cusp and cleft/LLBL for southward IMF. Geophys. Res. Lett. 26, 1665–1668.

Goldstein, B.E., Suess, S.T., Walker, R.J., 1981. Mercury: magnetospheric processes and the atmospheric supply and loss rates. J. Geophys. Res. 86, 5485–5499.

Kabin, K., Gombosi, T.I., DeZeeuw, D.L., Powell, K.G., 2000. Interaction of Mercury with the solar wind. Icarus 143, 397–406.

Killen, R.M., Potter, A.E., Reiff, P., Sarantos, M., Jackson, B.V., Hick, P., Giles, B., 2001. Evidence for space weather at Mercury. J. Geophys. Res. 106, 20509–20525.

Lammer, H., Bauer, S.J., 1997. Mercury's exosphere: origin of surface sputtering and implications. Planet. Space Sci. 45, 73–79.

Lammer, H., Wurz, P., Patel, M.R., Killen, R., Kolb, C., Massetti, S., Orsini, S., Milillo, A., 2003. The variability of Mercury's exosphere by particle and radiation induced surface release processes. Icarus 166, 238–247.

Lockwood, M., 1995. Location and characteristics of the reconnection X line deduced from low-altitude satellite and ground-based observations. 1. Theory. J. Geophys. Res. 100, 21791–21802.

Lockwood, M., 1997. Energy and pitch-angle dispersion of LLBL/cusp ions seen at middle altitudes: prediction by the open magnetosphere model. Ann. Geophys. 15, 1501–1514.

Lockwood, M., Smith, M.F., 1994. Low and middle altitude cusp particle signatures for general magnetopause reconnections. 1. Theory. J. Geophys. Res. 99, 8531–8553.

Luhmann, J.G., Russell, C.T., Tsyganenko, N.A., 1998. Disturbances in Mercury's magnetosphere: are the Mariner 10 "substorms" simply driven? J. Geophys. Res. 103, 9113–9119.

Lukyanov, A.V., Barabash, S., Lundin, R., Brandt Jr., P.C., 2001. Energetic neutral atom imaging of Mercury's magnetosphere. 2. Distribution of energetic charged particles in a compact magnetosphere. Planet. Space Sci. 49, 1677–1684.

McGrath, M.A., Johnson, R.E., Lanzerotti, L.J., 1986. Sputtering of sodium on the planet Mercury. Nature 323, 694–696.

Ness, N.F., Behannon, K.W., Lepping, R.P., Whang, Y.C., 1976. Observations of Mercury's magnetic field. Icarus 28, 479–488.

Newell, P.T., Meng, C.-I., 1992. Mapping the dayside ionosphere to the magnetosphere according to particle precipitation characteristics. Geophys. Res. Lett. 19, 609–612.

Orsini, S., Milillo, A., De Angelis, E., Di Lellis, A.M., Zanza, V., Livi, S., 2001. Remote sensing of Mercury's magnetospheric plasma environment via energetic neutral atoms imaging. Planet. Space Sci. 49, 1659–1668.

Potter, A.E., Morgan, T.H., 1986. Potassium in the atmosphere of Mercury. Icarus 67, 336–340.

Sarantos, M., Reiff, P.H., Hill, T.H., Killen, R.M., Urquhart, A.L., 2001. A B_x-interconnected magnetosphere model for Mercury. Planet. Space Sci. 49, 1629–1635.

Sieveka, E.M., Johnson, R.E., 1984. Ejection of atoms and molecules from Io by plasma-ion impact. Astrophys. J. 287, 418–426.

Slavin, J.A., Owen, J.C.J., Connerney, J.E.P., Christon, S.P., 1997. Mariner 10 observations of field-aligned currents at Mercury. Planet. Space Sci. 45, 133–141.

Song, P., Russell, C.T., Gombosi, T.I., Spreiter, J.R., Stahara, S.S., Zhang, X.X., 1999. On the processes in the terrestrial magnetosheath. 1. Scheme development. J. Geophys. Res. 104, 22345–22355.

Spreiter, J.R., Summers, A.L., Alksne, A.Y., 1966. Hydromagnetic flow around the magnetosphere. Planet. Space Sci. 14, 223–253.

Toffoletto, F.R., Hill, T.W., 1993. A nonsingular model of the open magnetosphere. J. Geophys. Res. 98, 1339–1344.

Tsyganenko, N.A., 1996. Effects of the solar wind conditions on the global magnetospheric configuration as deduced from data-based field models. In: Proc. of 3rd International Conference on Substorms (ICS-3). In: ESA SP, Vol. 389, pp. 181–185.

Tsyganenko, N.A., Russell, C.T., 1999. Magnetic signatures of the distant polar cusp: observations by polar and quantitative modelling. J. Geophys. Res. 104, 24939–24956.

Wurz, P., Lammer, H., 2003. Monte Carlo simulation of Mercury's exosphere. Icarus 164, 1–13.

Available online at www.sciencedirect.com
SCIENCE DIRECT
ELSEVIER
Icarus 175 (2005) 305–319
ICARUS
www.elsevier.com/locate/icarus

Dayside H^+ circulation at Mercury and neutral particle emission

A. Mura [a,*], S. Orsini [a], A. Milillo [a], D. Delcourt [b], S. Massetti [a], E. De Angelis [a]

[a] *Istituto di Fisica dello Spazio Interplanetario, Via del Fosso del Cavaliere 100, 00133 Roma, Italy*
[b] *CETP-CNRS, Saint Maurice des Fossés, France*

Received 20 February 2004; revised 2 December 2004

Available online 3 March 2005

Abstract

In this study we discuss the proton circulation and the neutral atom emission at Mercury. The H^+ distribution in space, energy and pitch angle has been simulated by means of a single-particle Monte Carlo model. The applied electric and magnetic field model has been parameterized to take into account different boundary conditions such as interplanetary magnetic field and cross-tail potential drop. Particular attention has been paid to the estimation of the surface-sputtered neutral atoms and the energetic neutral atoms generated via charge-exchange process. The peculiar configuration of the hermean magnetosphere, as it is expected after the Mariner-10 observation of a weak magnetic field, allows a significant part of the incoming solar wind to enter Mercury's environment. For the $B_z < -10$ nT conditions, intense ion fluxes are expected in the cusp regions, which are extremely large when compared to the Earth's ones. The solar wind particles are likely to rapidly leave the hermean magnetosphere or precipitate onto the planetary surface, thus originating neutral particle emission via ion-sputtering. Two instruments, proposed to fly on board ESA mission BepiColombo (namely: the NPA-IS SERENA suite on the MPO segment and the ENA instrument on the MMO segment) will monitor the neutral signal as well as the precipitating ion particles. The modeled distribution presented here may be considered as a reference tool for the future observations.

Keywords: Mercury; Plasma; Magnetosphere

1. Introduction

Since Mariner-10 observations of Mercury revealed an intrinsic magnetic field (Ness et al., 1976), several studies have been focused on the solar wind/magnetosphere/exosphere/surface interaction at Mercury (Goldstein et al., 1981; Slavin et al., 1997; Killen et al., 2001). The weakness of the intrinsic magnetic field and the absence of an atmosphere make the magnetospheric phenomena on Mercury extremely peculiar. In fact, numerical simulations (e.g., Kallio and Janhunen, 2003) and theoretical studies (e.g., Massetti et al., 2003) suggest that the solar wind may directly access to the inner magnetosphere and reach the surface of Mercury. The interaction between solar wind/magnetospheric ions with the surface results in ion-sputtering process, which is one of the sources of the exospheric populations; the role of ion-sputtering among other exospheric-feeding surface processes, such as thermal desorption and photon-stimulated desorption, is still disputed (Sprague et al., 1998; Killen and Ip, 1999; Wurz and Lammer, 2003; Leblanc and Johnson, 2003).

The purposes of the present study are: (i) to investigate the circulation of protons of solar wind origin in the dayside of the planet; (ii) to obtain a first-order quantitative estimation of their contribution to Mercury's magnetosphere; (iii) to estimate the neutral flux generated by ion-sputtering process in different external configurations; (iv) to discuss the feasibility of the neutral-particle imaging of the plasma circulation and the surface. In fact, important information about surface and plasma circulation properties could be obtained by means of the detection of the directional emitted neutrals. For this reason, we focus our attention to ion-sputtering and CE (charge exchange) processes only, since other surface source of neutrals (for example, thermal and

* Corresponding author. Fax: +39-064993-4383.
E-mail address: mura@ifsi.rm.cnr.it (A. Mura).

0019-1035/$ – see front matter
doi:10.1016/j.icarus.2004.12.010

photon-stimulated desorption) could not provide energetic (i.e., suitable for imaging) particles (Lammer et al., 2003). Even if we do not discuss explicitly other release process, this study could be also a useful tool for the evaluation of the relative importance of the exospheric sources.

We have used a three-dimensional, single-particle Monte Carlo model to reconstruct the trajectories, the spatial distribution and the energy spectrum of H^+ ions, following the study by Delcourt et al. (2003). The investigation is focused on the regions characterized by open magnetic field (magnetospheric cusp), where magnetosheath plasma can directly penetrate through the exosphere of Mercury down to its surface. Within the limits of the model, we show that this plasma is able to generate a noticeable amount of neutral particles, both via charge-exchange with the neutral exosphere of Mercury and via ion-sputtering processes on its surface. Moreover, we show that the neutral flux coming from both those processes is extremely sensible to the external conditions (i.e., the interplanetary magnetic field and the cross-tail potential drop), thus leading to a "neutral imaging" investigation technique for Mercury's magnetosphere and surface, through directional neutral atoms detection.

While the scientific community is waiting for future Mercury exploration missions (BepiColombo and Messenger), uncertainties persist about most of Mercury's magnetospheric features (density of the exosphere, surface conductivity, magnetic field strength and geometry), and it is difficult to develop an "exact" model of the magnetosphere of Mercury. Hence, the model introduced in this paper should be compared with others (for instance, Kallio and Janhunen, 2003), in order to come to a most-probable configuration. To this purpose, we explore the different configurations that could occur by varying the input parameters within a range of realistic values.

The boundary conditions of the simulation, in terms of electric and magnetic field, is illustrated in Section 2; the source of test particles will be discussed in Section 3. In Section 4 we present the 3D Monte Carlo model, including ion-sputtering and charge-exchange. In Sections from 5 to 7 we present the results in terms of (i) proton circulation; (ii) neutral particles emission via ion-sputtering and charge exchange; (iii) estimated exospheric vertical profiles. Summary and conclusions are given in Section 8. In Appendix A we discuss a very simple ring-current model, used to evaluate: (i) the possible H^+ nightside-to-dayside equatorial convection; (ii) the error made by considering only the cusp-precipitating protons as plasma source; (iii) the error made by neglecting the ring-current contribution in the Tsyganenko model.

2. Boundary conditions

2.1. Solar wind at Mercury

The magnetic and the electric field models developed in this study originate respectively from Tsyganenko T96 (Tsyganenko, 1996) and Volland (Volland, 1978) models, which refer to the Earth. They have been modified considering the different intrinsic magnetic field of Mercury and the different properties of the solar wind at the orbit of Mercury (0.36 ± 0.08 AU). At these distances from the Sun, Parker's spiral forms an angle of about 20° with the solar wind direction, thus changing the relative weight of the interplanetary magnetic field (IMF) components with respect to the Earth conditions. The IMF strength at Mercury is from 3 to 6 times the average strength at 1 AU (5 nT) (Burlaga, 2001), which leads to a mean value of about 20 nT. At Mercury, the solar wind proton density N^+ is highly variable, due to the high eccentricity of the planetary orbit. Here we have assumed a mean value of about 10 times the solar wind density at the Earth, which leads to $N^+ = 60$ cm^{-3}; the unperturbed solar wind velocity and dynamical pressure adopted here are, respectively, 450 km s^{-1} and 20 nPa (Massetti et al., 2003).

2.2. Magnetic field model

Once assumed these solar wind conditions, we have reconstructed the magnetic field around Mercury by means of a modified T96 Tsyganenko model (Luhmann et al., 1998; Massetti et al., 2003). Its main features are: (i) defined realistic magnetopause; (ii) large-scale Region 1 and 2 Birkeland current systems; (iii) IMF penetration across the magnetospheric boundary (Tsyganenko, 1996). It accepts both IMF B_y and B_z as independent input parameters.

First of all, to take into account the differences between both the intensities of the magnetic fields and the radii of Mercury and the Earth, we have divided every space constants in the T96 model by a factor of 7, like in previous analyses based on the Mariner 10 data (Siscoe et al., 1975; Luhmann et al., 1998). Then, we have removed from the model the contribution of the ring current, because the presence of this structure in the magnetosphere of Mercury is uncertain; a more detailed discussion of this feature is reported in Appendix A. We have also assumed a 50% contribution of Birkeland currents in the T96 model, which is a halfway position between the Earth's case and a null contribution. In fact, due to the expected lack of a conducting ionosphere on Mercury, there is still a wide debate regarding the existence of field-aligned currents (Slavin et al., 1997). Moreover, this assumption is consistent with the electric field model (see next section).

Finally, it must be noted that: (i) this model does not describe the field depression caused by the diamagnetic effect of the plasma engulfing the magnetospheric cusps; (ii) it is not possible to introduce a non-zero x component of IMF magnetic field; (iii) the model is stationary and hence it cannot take into account particle acceleration due to magnetic field line drag. Even if the magnetic reconnection at the dayside magnetopause is essentially driven by the IMF B_z component (Massetti et al., 2003), the B_x component should play a role in the magnetosphere solar wind coupling (e.g., Kabin et al., 2000; Sarantos et al., 2001), because of the

different orientation of the Parker's spiral at Mercury with respect to the Earth's case. In principle, one could expect to have more proton penetration with a B_x-interconnected magnetosphere (Kallio and Janhunen, 2004). Unfortunately, as stated above the present magnetic field model does not allow us to explore such configurations; As a *reference* configuration, here we assume $\mathbf{B}_{\mathrm{IMF}} = (0, 0, -20)$ nT, which may be considered as reasonable values (Massetti et al., 2003), if we discard the B_x component. Other configurations of the magnetosphere have been considered by changing $\mathbf{B}_{\mathrm{IMF}}$ components ($B_y = \pm 5$ nT and $B_z = -10$ nT), in order to study the dependence from the parameters of the plasma circulation. Northward IMF configurations are not discussed here, since we have observed no significant proton circulation if $B_z > -10$ nT.

2.3. Electric field model

The electric field in any point of the space is obtained from the electric potential $V(\mathbf{r})$. With the assumption: $\mathbf{E} \cdot \mathbf{B} = 0$, $V(\mathbf{r})$ in an arbitrary point of the space can be calculated following the $\mathbf{B}$ field line as far as it reaches any region where $V(\mathbf{r})$ is well known. As a zero order hypothesis, here we have assumed that the potential at the surface of Mercury is similar to Volland potential. The first Volland analytical formula for the potential Φ was (Volland, 1975):

$$\Phi = -i A_i \left(\frac{L}{L_i}\right)^{\frac{p_i}{2}} e^{i\tau}, \tag{1}$$

where L is the shell parameter of a coaxial dipole field ($L = rR^{-1}\sin^{-2}\theta$), τ is the local time, A_i, L_i, and p_i are parameters to be given separately in two different zones: polar cap ($p_i = -1$) and mid/low latitudes ($p_i = 4$). In our work, however, we have adopted a second version of this formula (Volland, 1978). In this case, between the two above-mentioned regions a third region is defined (mid latitudes). The application of such a model to Mercury's case has been already discussed by Delcourt et al. (2003).

The absence of an ionosphere at Mercury may make it difficult to comprehend whether and how the field-aligned currents, if present, can close the electric circuit between the planet and the cross-tail potential drop. The argument is still widely debated, even if some evidences of the presence of field-aligned current at Mercury exist (Slavin et al., 1997). Using the given solar wind parameters, and taking into account the different size of Mercury's magnetospheric cavity with respect to the Earth's one, we can estimate a cross-polar cap potential drop (PD) between 10 and 100 kV (Delcourt et al., 2003). To explore the behavior of the model under different external conditions, here we use PD = 10 kV as "*reference*" condition (Ogilvie et al., 1977; Ip, 1987), PD = 100 kV as "*high PD*" condition and PD = 1 kV as "*extremely low PD*" condition. This last value intentionally depletes the influence of $\mathbf{E}$, and can be also used to evaluate the importance of $\mathbf{E}$ in the reconstruction of the proton circulation.

The mean electric field in the central magnetotail is, in these three cases, equal to 1, 10, and 0.1 mV m^{-1}, respectively.

3. Proton source

In our simulation we start tracking the protons as they cross the magnetopause (MP), entering the magnetosphere from the magnetosheath. In agreement with the T96 model, we have approximated the dayside magnetopause by means of an ellipsoid, and all test particle trajectories start from this surface. According to this model, the distance between the surface of Mercury and the magnetopause at the subsolar point is approximately 0.5 Mercury radii (R_M).

Proton mean energy and density functions over this surface have been derived from the work of Spreiter et al. (1966), and adapted to the case of Mercury by Massetti et al. (2003). Figure 1 shows contours of H^+ density and mean-energy on the MP surface, in a MLT vs. geographic latitude plane, obtained by using the unperturbed solar wind density, velocity and dynamical pressure discussed in Section 2.1. For simplicity, we have assumed the proton flux, in a given point of the magnetopause, as mono-energetic (with energy equal to the local mean energy), and the pitch angle (PA) distribution as flat.

It should be noted that the mean proton energy peaks near the subsolar point, whereas the proton bulk velocity increases while they move away from it, as they are dragged together with the frozen-in IMF. Here we consider the energy of those protons in the reference system of the magnetic field lines, since the magnetic field is steady in our model. Hence, the energy we use as initial condition for our test particle reaches its maximum near the subsolar point, where the proton acceleration due to magnetic reconnection is higher (stress balance condition in de Hoffmann–Teller reference frame; for more details see, for example, Massetti et al. (2003)).

It may be useful to estimate the total H^+ flux impacting the MP of Mercury, as predicted by our model, in order to have a reference value when discussing the proton precipitation on the planetary surface. A very rough calculation, made by using the planetary cross-section, the unperturbed solar wind velocity and density, gives a number between 10^{26} and 10^{27} s^{-1}. It is worth noting that this value, as well as the distribution of protons over the MP and the shape of the MP itself, depends on the external conditions, such as the SW pressure. However, in our model we use a source with fixed parameters: a change in the unperturbed SW density results in a linear variation of the proton magnetospheric density; the change of the MP shape after pressure modification has been neglected for simplicity. This model gives proton distribution over all the MP. In principle, test particles could be generated all over this surface, and then let be free to possibly enter the magnetosphere. However, since they approximately follow the magnetic field lines, only the part of

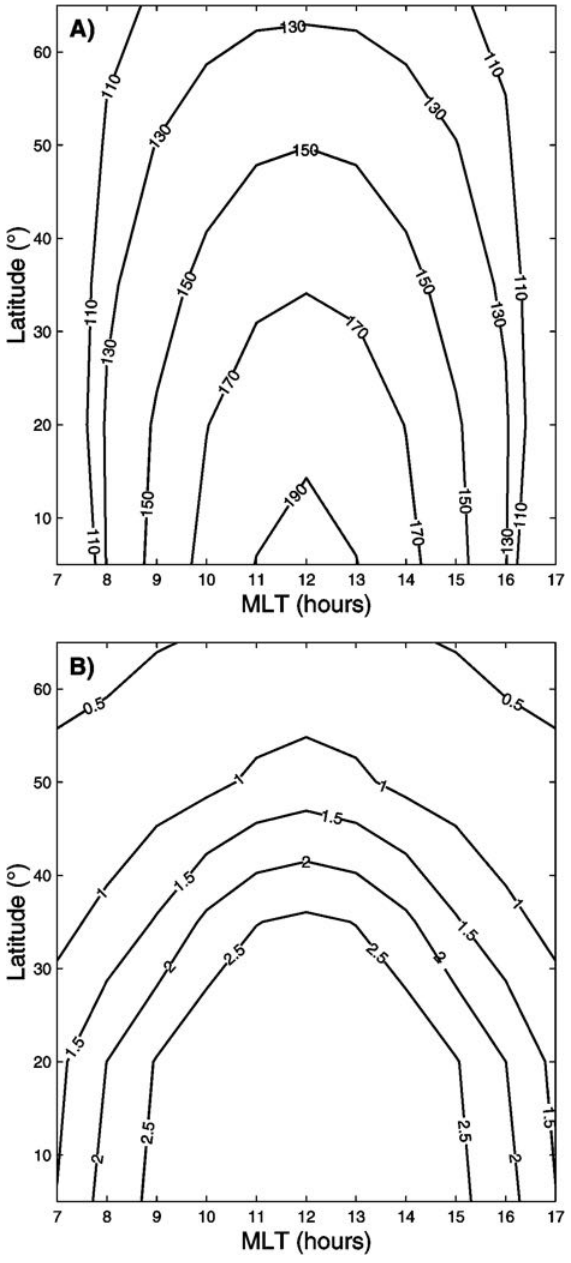

Fig. 1. Panel (A): Lines of equal H^+ density at the magnetopause, in the MLT versus Latitude plane, in cm^{-3}. Panel (B): same as (A), with lines of equal H^+ mean energy at the magnetopause, in keV.

the MP that, according to the T96 model, is magnetically connected with the surface is actually a source for magnetospheric protons.

4. Simulation concepts

4.1. Simulation of H^+

To obtain the proton distribution in the magnetosphere of Mercury we have used a Monte Carlo (MC) single-particle model. We have simulated the trajectories of about $N_{\text{tp}} = 2 \times 10^6$ protons (hereafter called "test particles") by solving the full equation of motion (including electromagnetic and gravitational forces). In fact, non-adiabatic effects may become of crucial importance for most of the ion magnetospheric transport (Delcourt et al., 2003), and the use of an adiabatic treatment based on the guiding center approximation will lead to non-negligible errors when reconstructing H^+ paths in full 3D space around Mercury.

Each test particle trajectory begins at the magnetopause of Mercury (see Section 3) and finishes if either:

(i) the test particle hits the surface of the planet; or
(ii) the test particle reaches a IMF field line not connected with Mercury's surface; or
(iii) the test particle gets too far from Mercury in the nightside ($r > 10R_M$).

The H^+ distribution function in space, energy and pitch angle has been reconstructed over a 5-dimensional grid, associated to a matrix N_{jklmn}. The grid extends from 1 to $2R_M$ in radius (r), 0 to 24 h in magnetic local time (MLT), $-90°$ to $90°$ in latitude (φ), $0°$ to $180°$in pitch angle (α) and 100 eV to 10 keV in energy (E); the number of bins for each dimension is respectively $8 \times 48 \times 24 \times 4 \times 4$.

We have divided the MP into a number of N_{tp} elementary surfaces ΔS_i. Each test particle starts from one ΔS_i and, in our simulation, represents a certain number of real protons. We can assume that all those protons are "born" (i.e., they enter the simulation region) within ΔS_i, and with fixed initial energy (see Section 3). Since the number N_{tp} is relatively high, we can assume that ΔS is infinitesimal, and all protons generated there have the same trajectory. We can also imagine that those protons are "born" from ΔS_i with a fixed frequency $1/\Delta T$. If the H^+ flux at ΔS_i is Φ_i, the time interval between these protons is:

$$\Delta T = \frac{1}{\Phi_i \Delta S_i}. \tag{2}$$

Since they are equally spaced in time along the trajectory (forming a sort of "train"), the number of protons N^* within an arbitrary cell $jklmn$ is simply $T/\Delta T$, where T is the time a proton stays within that cell. Since this time is the same for both protons and the associated test particle, we have:

$$T = N^* \Delta T = n\,dt, \tag{3}$$

where dt is the time integration step for the trajectory and n is the number of times that, during this trajectory, the associated test particle is inside that cell. It follows that:

$$N^* = \frac{n\,dt}{\Delta T} = n(dt\,\Phi_i \Delta S_i). \tag{4}$$

Hence, after every integration step dt, we just have to increase the value of the bin corresponding to its position (N_{jklmn}) of a value w:

$$w = dt\,\Phi_i \Delta S_i. \tag{5}$$

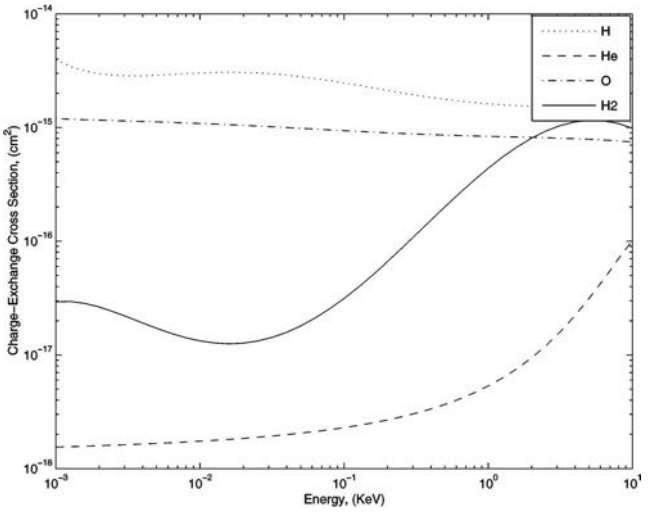

Fig. 2. Cross section for charge-exchange between H^+ and various neutral species: H (dotted line), He (dashed line), O (dash-dotted line), and H_2 (solid line). Data from Barnett et al. (1977), Stebbings et al. (1964), Barnett (1990).

A coefficient f_{CE} has been multiplied to w to take into account the losses due to charge-exchange with the neutral exosphere of Mercury. This coefficient is function of the time elapsed since the test particle generation, and has been calculated solving numerically the following differential equation:

$$\begin{cases} f_{CE}(0) = 1, \\ \frac{df_{CE}}{dt} = f_{CE}|\mathbf{v}| \sum_i \sigma_i n_i, \end{cases} \tag{6}$$

where σ_i and n_i are the charge-exchange cross-section (see Fig. 2) and the local number density of the ith neutral species. The neutral species included in this simulation are H, H_2, He, and O; their vertical density profiles have been given by Wurz and Lammer (2003). It is worth noting that the H_2 density has been depleted as suggested by authors. The depletion coefficient here is 0.01, in order to be conservative with the estimation of ENA fluxes.

The quantity $(dn_{H^+}/dE\,d\alpha)$ in any point of the grid is obtained by dividing the bin value N_{jklmn} by the relative 5D-volume, while the proton flux (Φ_H) is obtained by knowing the density, the velocity $v(E)$ and the PA distribution.

In principle, to perform an accurate numerical integration of the motion, it should be necessary to calculate the electric field in a very large number of points along each trajectory. This procedure, in general, is very expensive in terms of machine-time, because at each point it is necessary to trace the magnetic field line up to the planetary surface (see Section 2.3). To permit the simulation of a large number of test particles, we have preliminarily estimated the electric potential V on the vertexes of a three-dimensional cubic grid. The potential in any other point can be calculated via 3-linear interpolation using the eight nearest vertexes. The bin size is 500 km, which leads to an error on the potential, which has been empirically found to be less than 5‰. This error may be neglected when compared to other uncertainties in the model.

4.2. Simulation of neutral particles

In our model, neutral particle emission is related to ion circulation through two processes: ion-sputtering and charge exchange. In fact, such processes are included in our proton model as proton losses, and both of them may produce neutral particles. In Sections 6 and 7 we will present simulated neutral signal coming from both processes.

4.2.1. Sputtering

This process is the result of the impinging of a H^+ on the surface of Mercury; if the impact energy (E_i) is sufficient, a particle, in most cases neutral, may be extracted from the surface. The energy distribution of the sputtered particles, $f_S(E_e, E_i)$, can be expressed as:

$$f_S\left(E_e, E_i'\right) \propto \begin{cases} \frac{E_e}{(E_e+E_b)^3}\left[1 - \left(\frac{E_e+E_b}{E_i'}\right)^{1/2}\right] & E_e \leqslant E_i - E_b, \\ 0 & E_e > E_i - E_b, \end{cases}$$

$$E_i' = E_i \frac{4m_1m_2}{(m_1+m_2)^2} \tag{7}$$

(Sigmund, 1969; Sieveka and Johnson, 1984; Betz and Wien, 1994), where E_e is the ejection energy, E_b^k is the surface binding energy of the atomic kth species extracted, m_1 and m_2 are the masses of the projectile and the target atom. For simplicity, in our calculations we have assumed $E_i' = E_i$, since this approximation leads to an error on the energy spectrum that is below 2% for the oxygen and below 4% for the sodium. The consequent neutral flux is hence:

$$\frac{d\Phi_k}{dE_e} = Y_k R_k \int_{E_{min}}^{E_{max}} \frac{d\Phi_{H^+}}{dE_i} f_S(E_e, E_i)\, dE_i, \tag{8}$$

where Y_k and R_k are the yield and the relative abundance of the kth species respectively. In our MC simulation, this equation is solved numerically. Every time a test-particle hits the surface, it is converted to a test-neutral or a test-ion, with random initial direction. The energy is chosen randomly according to energy distribution in Eq. (7); the species of the sputtered particle is chosen randomly according to different relative abundances R_k; the weight w in Eq. (5) is multiplied by a factor Y_k. This new test-particle may, of course, hit the surface again: the procedure exposed here is then performed again, as far as its weight is grater then one and its energy is able to produce sputtering ($E_i' > E_b$).

In this study we have concentrated our attention to oxygen and sodium only. In fact, both O and Na have been observed in the exosphere of Mercury (Broadfoot et al., 1976; Potter and Morgan, 1985, 1997). The overall fraction of oxygen (R_O) in the surface minerals, if we consider all molecules containing O, may be up to 50% (Wurz and Lammer, 2003). The sodium content of the surface (R_{Na}) has been estimated to be within 0 and 1.4% (Goettel, 1988); here we

have chosen a halfway value, i.e., 0.5%. Yields for those species strongly depend on the molecular structure of the surface; here we have adopted a rough value of 0.1 for both O and Na, since the uncertainty on the surface abundance probably overcomes the error on the yield. Moreover, the yield also depends on the ion energy and direction; a complete description can be found in (Lammer et al., 2003). It is worth noting that a bad estimation of either Y or R does not affect the estimated vertical profile of the neutral emitted population, but it can be considered as a scale factor for the whole density distribution function of neutrals. More particularly, an overestimation of the O sputtering flux may come from considering the same yield for all surface constituents containing oxygen.

The surface binding energy, conversely, has a deep impact on the shape of the energy spectrum of the particles emitted. If $E_i \gg E_b$, in fact, it may be shown that $f_S(E_e, E_i)$ peaks approximately at $E_b/2$. Surface binding energies are, generally, of the order of some eV; here we have adopted, respectively, 3.5 and 2 eV for O and Na. Some studies (Weins et al., 1997) indicate lower values (∼0.5 eV) for the Na binding energy. Considering that the lower is E_b the less is the function F at energies well above E_b, if this estimation is found correct, the Na flux from ion-sputtering calculated in the following should be reduced by a factor of 10 approximately.

4.2.2. Charge exchange

This process may occur when an energetic H^+ hits an exospheric neutral; the result is a hydrogen *energetic neutral atom* (ENA), retaining both energy and direction of the incoming H^+ (for a complete discussion see, for example, Hasted (1964)). Since ENAs travel on straight lines just as photons, ENA imaging is a common way to indicate the ENA flux detected at some vantage point Q, while looking at different directions. ENA imaging is a powerful tool to obtain information about both plasma and exospheric properties (see, for example, Roelof et al. (1985)).

We want to compute the total ENA flux detected in point Q integrated over a given energy range. The ENA production rate for unitary length $d\Phi_{\mathrm{ENA}}/ds$ for any point of the grid may be calculated as:

$$\frac{d\Phi_{\mathrm{ENA}}}{ds} = n_{\mathrm{H}^+} \frac{df_{\mathrm{CE}}}{dt}, \tag{9}$$

where f_{CE} is the function defined in Eq. (6), and n_{H^+} is the proton number density obtained by integrating $dn_{\mathrm{H}^+}/(dE\,d\alpha)$ over all pitch angles and over the given energy range. The total flux escaping from a cell located in P_{jkl} and detected in Q is:

$$\Phi_{\mathrm{ENA}}(Q)_{jkl} = \frac{d\Phi_{\mathrm{ENA}}(P_{jkl})}{ds} \Delta V f_\alpha(\hat{v}) \frac{1}{|\overline{QP}|^2}, \tag{10}$$

where ΔV is the volume of the jklth cell; $f_\alpha(\hat{v})$ is the 3D angular distribution function, $\hat{v}$ is the direction from P to Q. The function f_α can be obtained from the PA distribution function (included in the 5D model of protons), with the hypothesis that the distribution does not depend on gyroangle. It is then sufficient to integrate over all jkl cells to obtain the ENA image at Q.

5. Proton dayside circulation

Here we present our results in terms of H^+ circulation. Six different sets of boundary conditions have been used, and about 3×10^5 test-particles have been tracked for each set. A particular set of boundary conditions, called "*reference*" conditions, is: $\mathbf{B}_{\mathrm{IMF}} = (0, 0, 20)$ nT, PD = 10 kV. Then we have changed PD (1 kV and 100 V), $B_y(\pm 5$ nT) and $B_z(-10$ nT). To reduce the amount of runs, we have not explored all combinations of these values, but just all variations of a single parameter from the "*reference*" one. This must be taken into account in general, since variations of potential drop and $\mathbf{B}_{\mathrm{IMF}}$ often occur simultaneously.

To obtain the H^+ number density n_{H^+}, the differential number density $(dn_{\mathrm{H}^+}/(dE\,d\alpha))$ has been integrated over all pitch angles and over two different energy ranges: 0.1–1 and 1–10 keV. Particles outside these two ranges have been discarded.

To help the discussion, we present an overall summary of results (Table 1), sections of H^+ density (Fig. 3) and maps of H^+ flux on the surface (Fig. 4). Table 1 shows four parameters that synthesize some features of the H^+ flux impacting the surface, i.e., the total flux (F_T), the mean MLT ($\overline{\mathrm{MLT}_S}$) and the mean latitude ($\bar{\varphi}_S$). Those parameters have been calculated for different boundary conditions and energy ranges. In particular, the mean position of the H^+ spot on the surface corresponds roughly to the bulk of the emission of the sputtered neutrals, which will be monitored by the NPA-SERENA orbiting sensor; the total flux of H^+ impacting the surface has important implications on the exospheric refilling.

Panels in Fig. 3 show color-coded sections of the H^+ density distribution. Each panel shows n_{H^+} over the superposition of two different surfaces: the one outside the red circle is the x–z plane; the one inside the red circle is a hemisphere just above Mercury's surface, in the dawn side. The Sun is on the right. Different panels refer to different external conditions and energy ranges. It is worth noting that panels in Fig. 3 do not show the protons that cross the magnetopause (thus becoming elements of the simulation) in the south hemisphere. In this way, the protons that are found in the southern hemisphere can be immediately identified as "bouncing protons." To obtain the complete distribution it is sufficient to superimpose this H^+ distribution to another one, which is symmetric to the first respect to the equatorial plane.

Panels in Fig. 4 show polar-stereographic projections of the H^+ flux on the northern surface of Mercury, color-coded according to the $\log_{10}$ of the intensity. This flux has been obtained using the estimated H^+ 5D distribution function in

Table 1

Energy range (keV)	B_y (nT)	B_z (nT)	P. drop (V)	Total flux (s^{-1})	Mean MLT (hh:mm)	Mean lat (°)	Area (m^2)
Total:	−5	−20	10^4	4.4×10^{25}	11:28	42	1.9×10^{13}
0.1–10	0	−10	10^4	3.7×10^{25}	11:54	47	1.4×10^{13}
	0	−20	10^3	6.0×10^{25}	10:40	36	3.0×10^{13}
	0	−20	10^4	4.1×10^{25}	11:41	43	1.8×10^{13}
	0	−20	10^5	1.1×10^{25}	11:23	57	1.6×10^{13}
	5	−20	10^4	4.4×10^{25}	11:27	42	1.9×10^{13}
Low energy:	−5	−20	10^4	6.8×10^{24}	11:44	58	9.3×10^{12}
0.1–1	0	−10	10^4	9.4×10^{24}	11:52	60	8.3×10^{12}
	0	−20	10^3	9.4×10^{24}	11:43	53	9.8×10^{12}
	0	−20	10^4	7.2×10^{24}	11:42	58	9.5×10^{12}
	0	−20	10^5	1.6×10^{24}	11:09	67	1.1×10^{13}
	5	−20	10^4	7.4×10^{24}	11:37	57	9.6×10^{12}
High energy:	−5	−20	10^4	3.6×10^{25}	11:25	38	1.6×10^{13}
1–10	0	−10	10^4	3.2×10^{25}	11:54	43	1.1×10^{13}
	0	−20	10^3	5.0×10^{25}	10:33	32	2.4×10^{13}
	0	−20	10^4	3.4×10^{25}	11:40	40	1.4×10^{13}
	0	−20	10^5	9.8×10^{24}	11:24	56	1.4×10^{13}
	5	−20	10^4	3.6×10^{25}	11:25	39	1.5×10^{13}

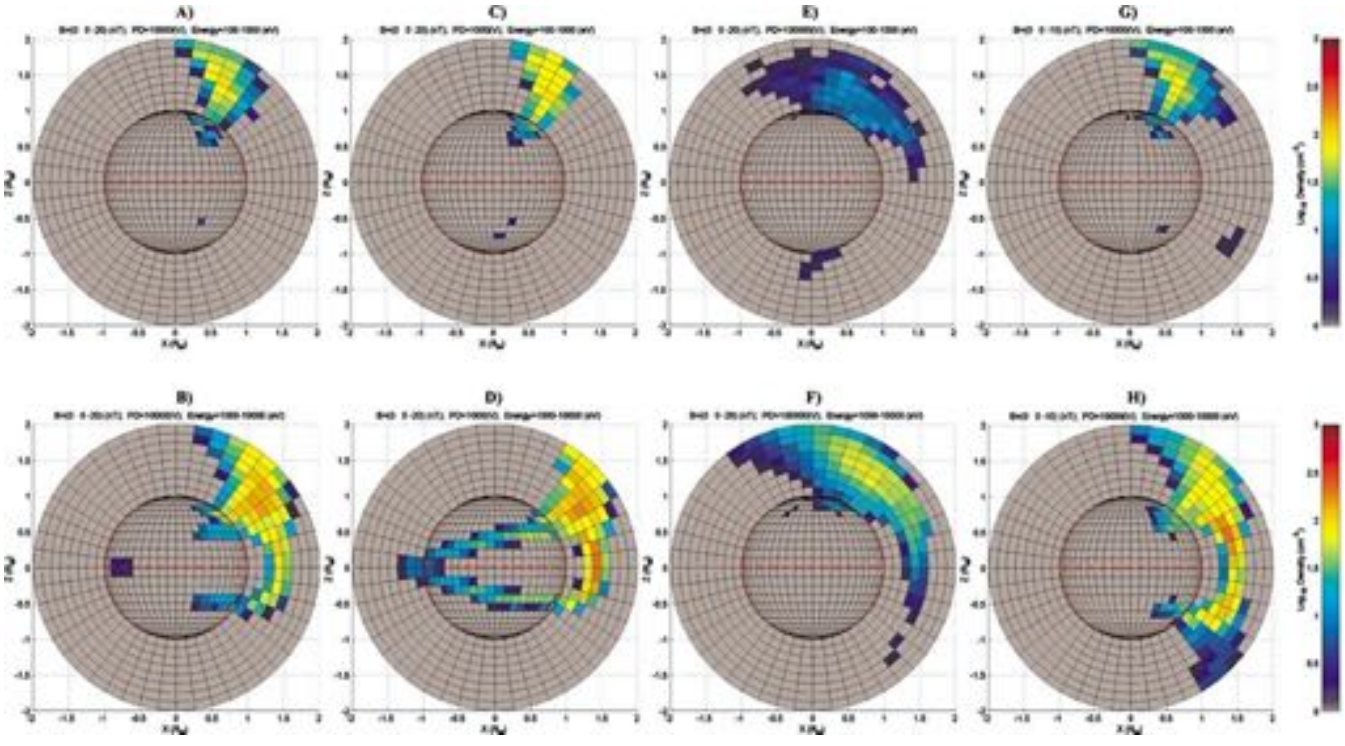

Fig. 3. Color-coded maps of H^+ density over two different surfaces: x–z plane (outside the red circle) and Mercury surface (inside red circle). Panels (A), (C), (E), (G): low proton energy (100 eV–1 keV). Panels (B), (D), (F), (H): high proton energy (1–10 keV). Panels (A), (B): *reference* condition. Panels (C), (D): same as (A), (B), but low potential drop (PD = 1 kV). Panels (E), (F): same as (A), (B), but high potential drop (PD = 100 kV). Panels (G), (H): same as (A), (B), but low $\mathbf{B}_{\rm IMF}(B_z = -10$ nT).

the cells just above the surface. However, a small error will arise from this procedure. In fact, those cells have a height of about 300 km, and even if the **B** field lines can be considered more or less parallel over this short scale, some protons may bounce inside this cell. The flux obtained in this way is hence an upper limit for the real flux at the surface. Different panels refer to different external conditions and energy ranges.

5.1. General features

In a typical H^+ simulated distribution it is possible to recognize three different and peculiar populations, whose relative intensity is a matter of interest of the present study. The first one (α), present in all external conditions, is the population precipitating towards the planet along the mag-

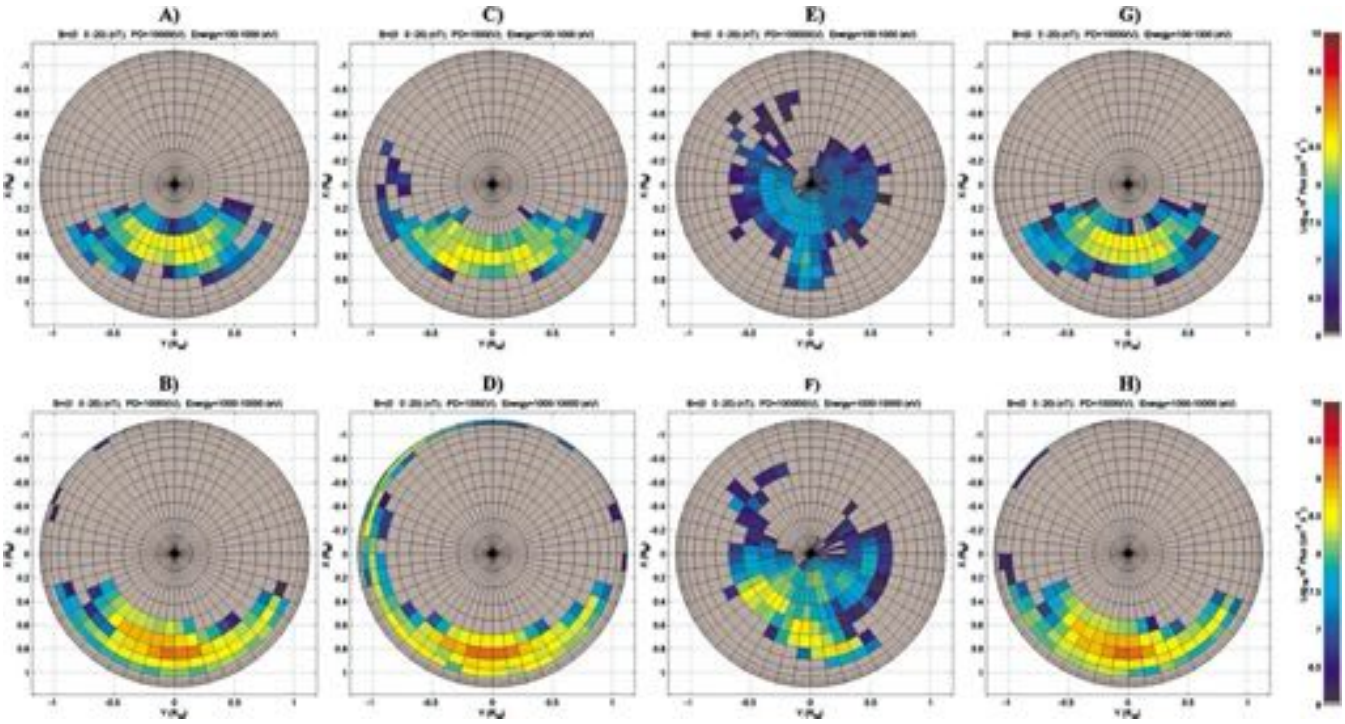

Fig. 4. Color-coded maps of H^+ flux over Mercury's surface. Panels (A), (C), (E), (G): low proton energy (100 eV–1 keV). Panels (B), (D), (F), (H): high proton energy (1–10 keV). Panels (A), (B): *reference* condition. Panels (C), (D): same as (A), (B), but low potential drop (PD = 1 kV). Panels (E), (F): same as (A), (B), but high potential drop (PD = 100 kV). Panels (G), (H): same as (A), (B), but different $\mathbf{B}_{\mathrm{IMF}}(B_y = -5\ \mathrm{nT})$.

netic field lines. Some of them are bounced by the increasing magnetic field; the others reach the planetary surface. During this motion, particles are drifted northward by the $\mathbf{E} \times \mathbf{B}$ drift and westward by the grad-$\mathbf{B}$ drift. The former is energy-independent; the latter is more efficient for the highest energies. The proton source is symmetric around noon, and any longitudinal shift in the surface precipitation (evidenced by the parameter $\overline{\mathrm{MLT}_S}$) is due to $\mathbf{B}$-grad drift.

The second population (β) is made by protons that are bouncing in the dayside, and is concentrated between the subsolar point and the surface. The third population (γ) is made by protons that move westward and eventually hit the surface in the nightside.

5.2. Reference conditions

Figures 3A and 3B show the precipitating H^+ in the "*reference* conditions" for different energy ranges. In both cases the α population extends down to the surface, but high energy protons (1–10 keV, Fig. 3B) impact Mercury at lower latitudes with respect to low energy ones (100 eV–1 keV, Fig. 3A). In fact, the mean energy of the H^+ at the magnetopause is higher when close to the sub-solar point (see Fig. 1). The population close to the Low Latitude Boundary Layer (Massetti et al., 2003) is able to move towards lower latitudes and to start bouncing, raising the β population. The low energy protons are injected at higher latitude and cannot experience any bouncing. No β population is, in fact, recognizable in Fig. 3A.

The H^+ flux impacting the surface (see Figs. 4A, 4B) is up to $5 \times 10^8\ \mathrm{cm^{-2}\,s^{-1}}$ for low-energy protons and may exceed $10^9\ \mathrm{cm^{-2}\,s^{-1}}$ in the case of high-energy protons. The mean flux intensity in the open field line area is approximately $10^8\ \mathrm{cm^{-2}\,s^{-1}}$ for both energy ranges, which is in agreement with previous studies (McGrath et al., 1986). The difference of the distribution for the two energy ranges is more evident if we look at the mean position of the precipitating protons (see Table 1 and Figs. 4A, 4B), which is (11:40 MLT, 40° N) for protons above 1 keV, and (11:42 MLT, 58°) for protons below 1 keV.

5.3. Electric field variation

In this analysis we have used two extreme values for the potential drop (1 and 100 kV) in order to have two extreme conditions for the electric field. The mean $|\mathbf{E}|$ in each case is respectively 0.1 and 10 $\mathrm{mV\,m^{-1}}$ (see Section 2.3). The first, clear effect of the increasing/decreasing $\mathbf{E}$ is the increasing/decreasing of the northward shift of the surface footprint due to the $\mathbf{E} \times \mathbf{B}$ drift. This effect is energy-independent, and actually is clearly recognizable by comparing Fig. 3C with Fig. 3E (low energy), and Fig. 3D with Fig. 3F (high energy). The same comparison may be done, with identical results, on Fig. 4 (panels (C), (E), (D), and (F)), using the H^+ flux at the surface instead of the density.

Another evident effect, originated from the same cause, is the modulation of β and γ population magnitude. With the

increasing of the **E** field, in fact, protons are drifted northward and no β population is able to form. Conversely, if the potential drop is low, the **B**-grad drift becomes predominant for high and low energy protons, and the γ population is drifted more westward, while β population does not change significantly. In this case, high-energy protons may reach the nightside. Figure 3D clearly indicates that γ particles are bouncing during their drift, and they are gradually getting closer to the planet. Hence, a sort of small "partial ring current" is able to form; an important consequence of this drift is the possibility of proton precipitation in the nightside and the subsequent emission of sputtered particles from that region (Fig. 4D). As far as it concerns low energy protons (Figs. 3C and 4C), some of them are drifted westward, but the bulk precipitates directly onto the surface with a small spread.

According to Table 1, intense electric fields cause less surface precipitation. The protons are supposed to be deflected northward and to be lost in the nightside.

In order to evaluate the effect of the $\mathbf{E} \times \mathbf{B}$ drift on the H^+ precipitation in the *reference* conditions, we may assume that PD = 1 kV depletes the influence of the electric field, so that it roughly corresponds to a "*zero electric field*" condition. By comparing total precipitating flux as reported in Table 1, in the cases of PD = 10 kV (4.1×10^{25} s^{-1}) and PD = 1 kV (6×10^{25} s^{-1}), we conclude that at least one third of the protons that could precipitate onto the planetary surface are removed by $\mathbf{E} \times \mathbf{B}$ drift.

5.4. Magnetic field variation

The efficiency of the reconnection process is roughly proportional to the negative z component of the $\mathbf{B}_{\mathrm{IMF}}$ field. This phenomenon has been studied here by comparing the "*reference*" case with the case of $\mathbf{B}_{\mathrm{IMF}} = (0, 0, -10)$ nT. The total precipitating flux, in this latter case, is lower (3.7×10^{25} cm^{-2} instead of 4.1×10^{26} cm^{-2}). Moreover, protons impact at higher latitudes on the average (see Table 1). There is no other evident modulation on the density distribution shape (see Figs. 3G and 3H); the β population is slightly more evident, and there is less nightside precipitation. In conclusion, the influence of B_z parameter is more on the intensity rather than on the shape of the n_{H^+} distribution function.

There is no evidence of an influence of the B_y component on the general shape of the H^+ distribution (see Figs. 4G and 4H for example).

It is worth noting that, in terms of influence on the proton distribution, the $\mathbf{B}_{\mathrm{IMF}}$ variation seems to be less relevant than PD because in the first case we have chosen a more conservative range of values. Actually, more extreme conditions can be expected at Mercury; the B_z component, for example, may range between −30 and 30 nT, to say nothing of the B_x component disregarding.

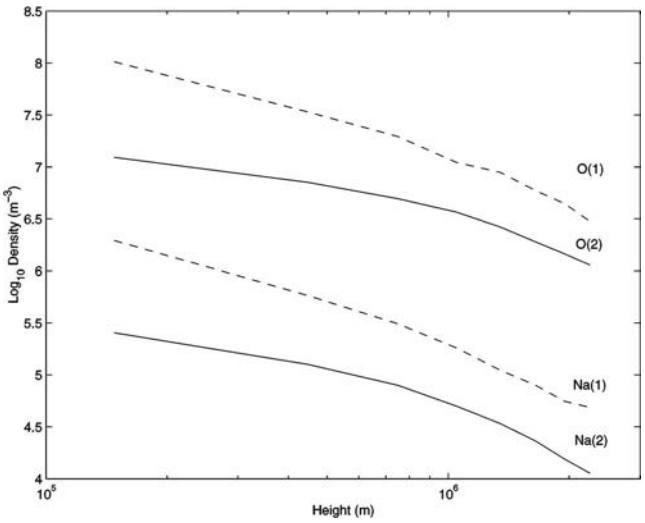

Fig. 5. Exospheric density for O and Na, function of altitude from planetary surface, calculated considering sputtering as the only release process (solid lines, (2)). Dashed lines (1) still consider only sputtering, but refer to the vertical profile over the point of maximum proton precipitation.

6. Sputtering emissions

In this study we concentrate on the sputtering of oxygen and sodium. Both of them have been proved to exist in Mercury's exosphere: the first has been observed by Mariner 10 UVS (Broadfoot et al., 1976); the second has been detected by ground-based observations (Potter and Morgan, 1985). We will first discuss the simulated vertical profiles for these species, as they are a general matter of interest; then we will concentrate on the feasibility of monitoring the cusp proton precipitation by means of a neutral particle imager.

Figure 5 shows the estimated mean vertical profile for these species in the dayside exosphere (solid lines), obtained by averaging the neutral density at a given height in the dayside hemisphere. These densities have been calculated considering sputtering as the only source; other important processes, such as photon-stimulated and thermal desorption, must be considered separately. Moreover, we do not take into account the "ambient atoms" (Killen and Ip, 1999), i.e., atoms that are not at their first ballistic orbit. Dashed lines represent the vertical profiles over the point of maximum proton precipitation, and can be considered as an upper limit for sputtering-generated exosphere. These values have been obtained using the "*reference*" conditions, and the vertical profile density in other cases can be estimated just applying a simple proportion, using total flux in Table 1. Sputtering emission, in fact, is roughly proportional to precipitating flux (E_i does not modify much the emission spectrum, except for very high E_i). Hence, densities may be up to 50% higher (for example in the minimum potential drop conditions), or down to 80% lower (in maximum potential drop conditions).

As far as it concerns oxygen, the estimated total column density is between 5×10^8 and 5×10^9 cm^{-2}, the surface density is between 20 and 200 cm^{-3} and the scale-height es-

timation is between 500 and 1000 km. The first measure of the oxygen exospheric content made by Mariner UV camera indicates 7×10^3 cm^{-3} as an upper limit, even if the scale-eight estimation was doubtful. As far as it concerns Na, it has been noted (Killen et al., 2001) that its temporal variability was found to be compatible with solar activity, which is in turn related to sputtering. On the other hand, our estimated total column density is up to 10^8 cm^{-2}, whereas the measured value is considerably higher (between 1 and 3×10^{11} cm^{-2}, Killen et al., 1990). This fact may be explained if sputtering were not the first source for exospheric sodium, as suggested by Leblanc and Johnson (2003). Another reason, which must be taken into account while discussing the results, is that we have intentionally discarded the ambient atoms (i.e., neutral scattering on the surface plus accommodation/release), which have lower energy and reside in the lower part of the exosphere. Their inclusion in our model will be a further step, and will lead to a modeled sodium exosphere more concentrated in the lower altitudes. Scale-height analysis seems to confirm this last hypothesis. For example, simulated scale-height for Na is about 500 km, and a factor 10 greater than that observed (50 km) (Killen et al., 1990; Wurz and Lammer, 2003). Another effect that is not taken into account in our simulation is the possible high spatial and temporal variability of sodium content in the hermean surface, which has been suggested by observations (Sprague et al., 1998) and theoretical studies (e.g., Leblanc and Johnson, 2003).

We now want to speculate on the possibility of remote sensing the plasma–surface interaction, as suggested by Grande (1997). The estimated total proton flux on Mercury surface is between 10^{25} and 10^{26} s^{-1}, depending on external conditions. For comparison, we can obtain the amount of protons removed in one second by the charge-exchange process by integrating the charge-exchange loss function (Eq. (6)) in all the 5D space. This value is between 10^{22} and 10^{24} s^{-1}, depending on the boundary conditions and exospheric models. We can conclude that surface impact is the first cause of loss, in terms of magnitude, for proton plasma circulation. Consequently, sputtering process is an important source for the refilling of the exosphere, and since both sputtering and CE result in neutral atoms production, neutral atom imaging of the sputtering process is probably the best way to make remote-sensing of the plasma circulation. The ENA instrumentation on board BepiColombo will be able to detect the high-energy tail of the neutral sputtering emission, approximately above 10 eV. These particles travel more or less along straight lines (escape energy is 1.4 eV for O and 2 eV for Na) and their detection at MPO orbit (height: 1500 km at epicenter, 400 km at pericenter) would give an image of the sputtering release at the surface.

Figure 6 shows the simulated intensity of sputtered O flux at the surface, integrated over all energies above 10 eV and over all directions, in the "*reference conditions*"; in the same configuration, the Na flux is similar in shape and approximately 1% of the O flux. In both cases, the intensity is high enough to be detected by ENA instruments; provided that the angular resolution of the instrument results in a surface resolution down to tens of km, it will be possible to monitor the variations in shape and intensity of the H^+ precipitation on the surface. Also, in the case that the ENA sensor can discriminate masses, the observation of differences in the surface local composition will be possible. Last but not least, the global analysis of the sputtering erosion of the surface would give unique information about the present and the past of Mercury's surface, revealing if (and how) the so-

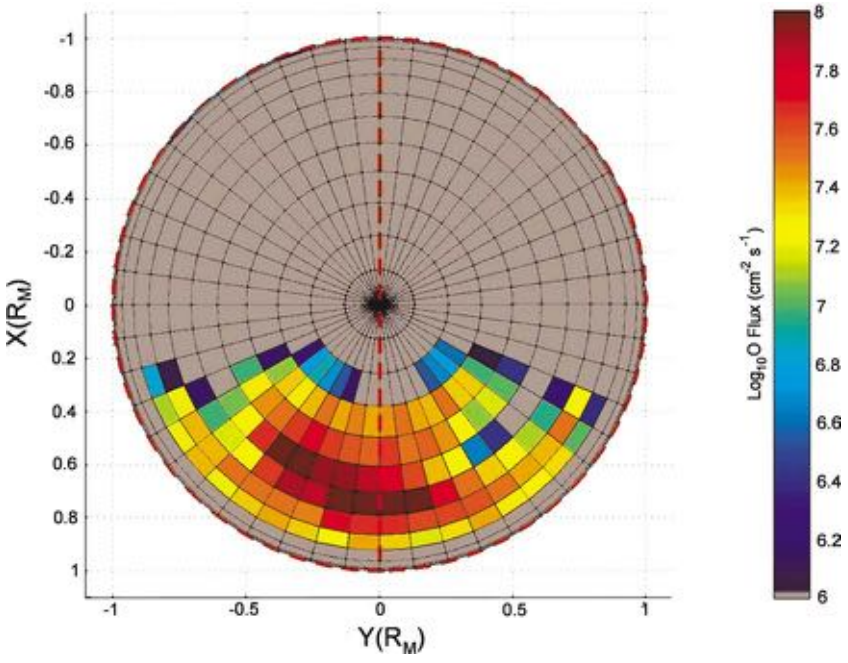

Fig. 6. Color-coded O-ENA flux generated by ion-sputtering on the northern surface of Mercury.

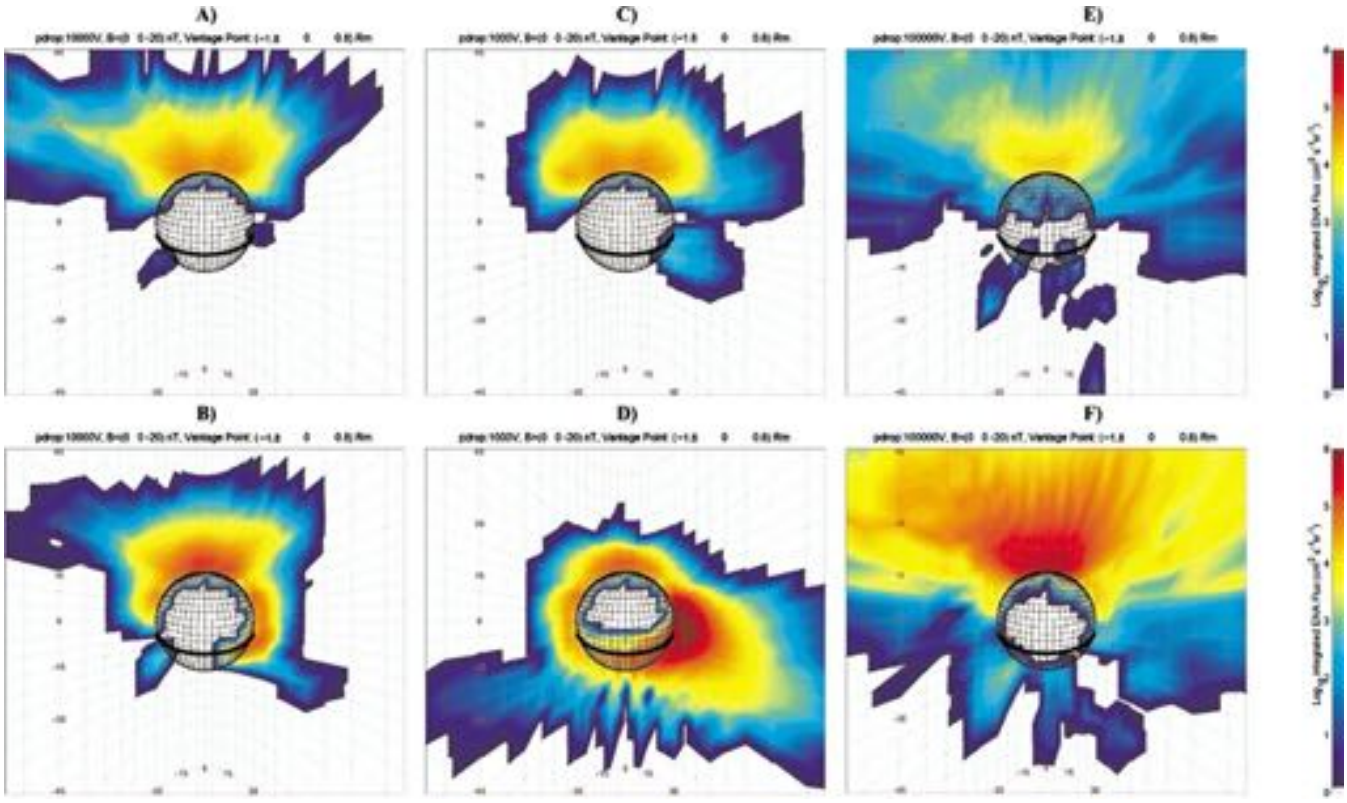

Fig. 7. Simulated ENA images, from a vantage point in the nightside ($P_1 = (1.8, 0, 0.8)\,R_M$). Color is coded according to ENA flux, integrated over two energy ranges: 100 eV–1 keV (panels (A), (C), and (E)) and 1–10 keV (panels (B), (D), and (F)). The boundary conditions are: $\mathbf{B}_{\mathrm{IMF}} = (0, 0, -20)$ nT; PD = 10 kV (panels (A) and (B)), PD = 1 kV (panels (C) and (D)), PD = 100 kV (panels (E) and (F)).

lar wind/surface interaction, in the past millions of years, has influenced the present surface composition.

7. ENA emissions

Even if charge-exchange is not the main loss mechanism for magnetospheric protons, monitoring the product of such an interaction allows having important information about the magnetospheric and exospheric properties (Barabash et al., 2001). In this frame, we will first discuss the general feasibility of ENA imaging and then its implications for a generic neutral particle sensor on board BepiColombo.

ENA images have been simulated, for different vantage points, by applying the procedure described in Section 4.2 to the simulated H^+ density shown in Fig. 3. After a preliminary study, we have focused on two different positions for the vantage point. The first one is in the tail region, outside the equatorial plane but still in the shadow of the planet; as an example, we have chosen the point P_1: $(-1.8, 0, 0.8)\,R_M$. From this point, by looking sunward, it is possible to monitor simultaneously the plasma precipitating into the cusp, and that circulating in the dawn region. The second point P_2, which can be located in the dawn hemisphere, approximately on the y axis and with $r < 2$, is a good point to look at the γ population that drifts from dayside to nightside. In our study we have located P_2 at $(0, -2, 0)\,R_M$.

Figure 7 shows simulated ENA images, as seen from P_1 in a "fish-eye" projection, for different PD values and integrated over two different energy ranges: 100 eV–1 keV, and 1–10 keV. As for Fig. 3, protons that enter the simulation area in the southern hemisphere are not shown. Generally, in these images it is possible to observe ENA coming from two different H^+ populations. The first one is α, made by protons that are precipitating into the cusp regions or that are passing above the North Pole before escaping in the nightside, and that get close enough to experience charge-exchange with the hermean exosphere. This process results in an intense signal in the upper part of the ENA image. The second population (γ), which is clearly evident especially for low PD and in the higher energy range, is made of protons that are drifting westward and are bouncing during their motion. These protons reach low altitude at their mirroring points, and even if their flux is generally lower than the flux of the precipitating ones, they may produce an intense ENA signal, distinguishable in the right side of ENA images.

The westward proton circulation is generated by **B**-grad drift, the intensity of which is proportional to proton energy. Hence, the second ENA signal is present only at energies above 1 keV; moreover, the **B**-grad drift dominates the $\mathbf{E} \times \mathbf{B}$ drift if the PD is low. Hence, the second ENA peak is more evident for low values of PD.

Similar considerations apply to ENA images simulated from point P_2 (Fig. 8). In this case the ENA signal has

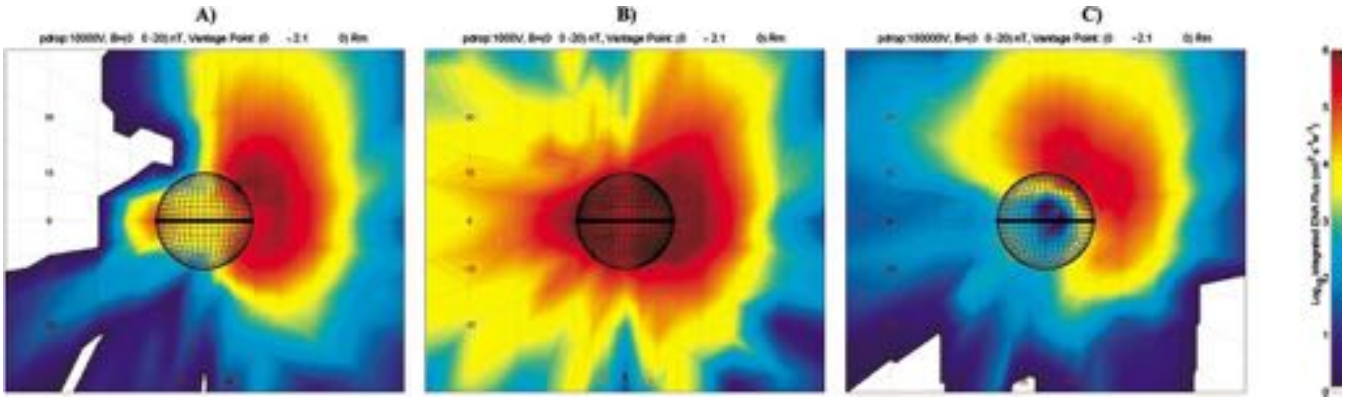

Fig. 8. Simulated ENA images, from a vantage point in the dawn sector ($P_2 = (0, 2.1, 0)R_M$). Color is coded according to ENA flux, integrated over all energies (100 eV–10 keV). The boundary conditions are: $\mathbf{B}_{\mathrm{IMF}} = (0, 0, -20)$ nT; PD = 10 kV (panel (A)), PD = 1 kV (panel (B)), PD = 100 kV (panel (C)).

been integrated over all energies from 100 eV to 10 keV. In addition to α and γ populations, which are clearly distinguishable, those protons that are mirroring in the dayside (β) generate a clear ENA signal as well. The ENA signal in the center of the image comes from the γ population, and hence increases as the PD decreases.

Generally, the information carried by ENA images need to be unfolded, applying a model of plasma and exosphere. However, our simulations show that ENA imaging at Mercury, alone, is able to give some useful information. This happens, for example, if the vantage point is in P_1. There, the proton precipitation into the cusp can be directly monitored: any increase is immediately reflected in an increase of the ENA flux, since no other sources contribute. Moreover, in the case of a vantage point located in position similar to P_2, it is also possible to instantaneously monitor the open field line area on the surface. The chosen position for the vantage point is suitable for the MPO, and hence for NPA-IS SERENA; the detection of the α and β populations in the dayside will be possible by means of H-ENA imaging. At the same time, it will be possible to detect the γ population that is drifting in the space between the sensor and the surface (through H-ENA imaging), as well as the γ population that is precipitating onto the surface of Mercury (through the imaging of the directional neutral atoms coming from ion-sputtering).

8. Summary and conclusions

In this study we have presented model of the proton circulation around Mercury, and we have used it as an input for the simulation of neutral particle emission from both the surface (via ion-sputtering) and the exosphere (via charge-exchange).

In order to properly simulate the particle flow patterns, we have used a modified a T96 magnetic field model together with a Volland model of the ionospheric potential. Then, the H^+ distribution on the magnetopause has been reconstructed, and used as a source for the model. Any possible proton source in the nightside has been neglected, after having proved the absence of trapped trajectories. Incidentally, this last estimation proves the non-existence of any ring-current in the equatorial plane of Mercury.

The magnetic field model has been developed from an Earth-based model, so that it does not include a non-zero IMF B_x component: this missing contribution could have some impact in our predictions, so that it will be considered in a further study. Moreover, the shape of the magnetopause surface is fixed, i.e., not sensitive to solar wind actual conditions, which are, indeed, highly variable and may alter the magnetopause structure and particle access.

Photon stimulated desorption, thermal desorption processes, as well as particle accommodation/release processes on the surface have not been taken into account in our model. Anyway, such a disregard does not affect the estimation of the neutral atom fluxes as detected by any ENA imager on board BepiColombo, which deals only with "directional" particles (i.e., above escape energy).

The assumed exosphere composition, as derived by Wurz and Lammer (2003), includes H, H_2, He, and O. In particular, H_2 gives the most significant contribution to ENA generation. Since H_2 has not been directly observed, its exospheric vertical profile has been intentionally depleted (in accordance with authors' suggestions); the factor adopted here (0.01) is intentionally very low, to avoid any possible overestimation of ENA fluxes.

The major outcomes from our study may be summarized as follows:

- The presented model reconstructs the circulation of protons in the dayside hemisphere of Mercury; so far, it does not foresee any intense H^+ circulation in the nightside. Three major H^+ populations have been identified, respectively made by protons precipitating towards the planet along the magnetic field lines, protons bouncing in the dayside, and protons drifting westward.
- We have estimated the total flux on the planetary surface in different external conditions. In the *reference* case, the proton precipitation rate is about 4×10^{25} s^{-1}, over an

area of about 2×10^{13} m^2. If we compare this rate to the total H^+ flux crossing the MP (10^{26}–10^{27} s^{-1}, see Section 4.1), we can conclude that about one tenth of it is able to precipitate onto the planetary surface, depending on the external conditions. In our simulation, proton precipitation is possible only in southward IMF conditions; moreover, in the presence of a strong potential drop, the proton precipitation onto the surface could be reduced considerably.

- The model includes charge-exchange as a loss mechanism. Under our assumptions, this process is able to remove approximately 4×10^{24} protons in one second, i.e., 1% of the incoming solar wind protons. We have simulated the H-ENA signal that could be detected from different vantage points. In an optimal vantage point configuration, the integrated H-ENA flux can be up to 10^6 cm^{-2} s^{-1} sr^{-1}; the H-ENA images seem to be very sensitive to the external conditions. In this frame, we have studied the feasibility of neutral atom remote sensing made by a generic ENA instrumentation on board BepiColombo. As a matter of fact, such an instrument should be able to address all the scientific issues discussed in this paper.

Appendix A. Ring current at Mercury?

It has been widely debated about the existence of a ring current at Mercury, and about the lifetime of the plasma in the equatorial regions. The weak magnetic field seems to be not able to trap particles into closed drift paths around the planet, although the injection of plasma into the magnetosphere during magnetic substorms could generate at least a transient partial ring current (Orsini et al., 2001; Lukyanov et al., 2001).

Our assumption that such a ring current does not exist has two implications: we discard nightside to dayside protons transport, and we remove the ring current contribution in the T96 model. To be confident in this hypothesis, we have preliminary performed an extremely simple simulation of the ring current at Mercury. The simulation is based on both the continuity equation and the guiding center (GC) approximation. Such an approximation may be assumed to be reasonable on the equatorial plane, at short distance from the planetary surfaces (Delcourt, private communication). This model considers only the protons circulating in the nightside equatorial plane of Mercury with a 90° pitch angle. In fact, to demonstrate the absence of a stable ring current there is no need of a whole 3D simulation. Particles at 90° PA populating the equator have, indeed, a longer lifetime with respect to those that are more field-aligned. These latter particles, getting closer to the planet at mirroring points, experience more CE and surface-impact losses.

As these protons are treated as a fluid, for the Liouville theorem:

$$\frac{dn_{H^+}}{dt} + \nabla(n_{H^+}\mathbf{u}) = F - S, \tag{A.1}$$

where n_{H^+} and $\mathbf{u}$ are respectively the proton density and velocity, while F and S are two functions for the proton sources and sinks. In our case, this equation must be applied on a 3D space (r, φ, K): r and φ are the polar coordinates of the protons GC in the equatorial plane; K is introduced as the third dimension in the phase-space, being the kinetic energy of the protons. The first two components (u_r and u_φ) of the velocity $\mathbf{u}$ are given by the $\mathbf{E} \times \mathbf{B}$ plus the $\mathbf{B}$-gradient drift, by using electric and magnetic models described in Sections 2.2 and 2.3. The third component of the velocity (u_k) can be estimated considering that, as a zero order hypothesis, only the electric field is able to change the kinetic energy of the particle. Hence, we have:

$$u_k = \frac{dK}{dt} = \frac{dK}{dx}\frac{dx}{dt} + \frac{dK}{dy}\frac{dy}{dt} = E_x u_x + E_y u_y. \tag{A.2}$$

In our case, the function F for the sources is assumed to be zero everywhere. In fact, since we want to demonstrate the impossibility of a stable circulation in the equatorial regions of Mercury, it is sufficient to suppose some a-priori extended distribution in the tail and see how fast it decays, in the absence of a steady source. The $n_{H^+}(0)$ function used here is a simple Gaussian function in the three dimensions r, φ, K, and is shown in Figs. 9A and 9D.

The function S for the sinks is calculated taking into account charge exchange and collisions with the planet. Charge-exchange losses have been estimated using neutral density of O, H_2, and H given by Wurz and Lammer (2003), and relative cross-sections (Fig. 2). As far as it concerns the planetary collisions, we have adopted an ad-hoc function dp representing the dt-probability for a proton to hit the surface. In fact, GC method approximates the trajectory of a particle with a drifting circle of radius equal to Larmor radius (R_L). Hence, a particle close to the planetary surface may have part of this circle inside the planet. Function dp is proportional to the particle velocity v and inversely proportional to R_L:

$$dp = \begin{cases} 0 & r > (R_M + R_L), \\ \frac{v\,dt}{2\pi R_L} & R_M < r < (R_M + R_L), \\ 1 & r < R_M. \end{cases} \tag{A.3}$$

Equation (A.2) has been solved numerically using a grid of $50 \times 50 \times 50$ bins. After having defined the grid, we have preliminary estimated the error we make using GC approximation: the discrepancy between the GC path and the real path, inside one grid cell, is in any case less than 10% of the path length. For the purpose of this preliminary study, this approximation is hence acceptable.

Figure 9 shows an example of the evolution of the H^+ population, in the case of the *reference* conditions. Protons move sunward under the $\mathbf{E} \times \mathbf{B}$ drift and then clockwise around the planet under the $\mathbf{B}$-grad drift, depending on their energy. In fact, the latter drift is energy-dependent, causing the higher energy protons to concentrate in the dusk side.

It is worth noting that the time evolutions of the protons, as simulated in all possible external configurations (see

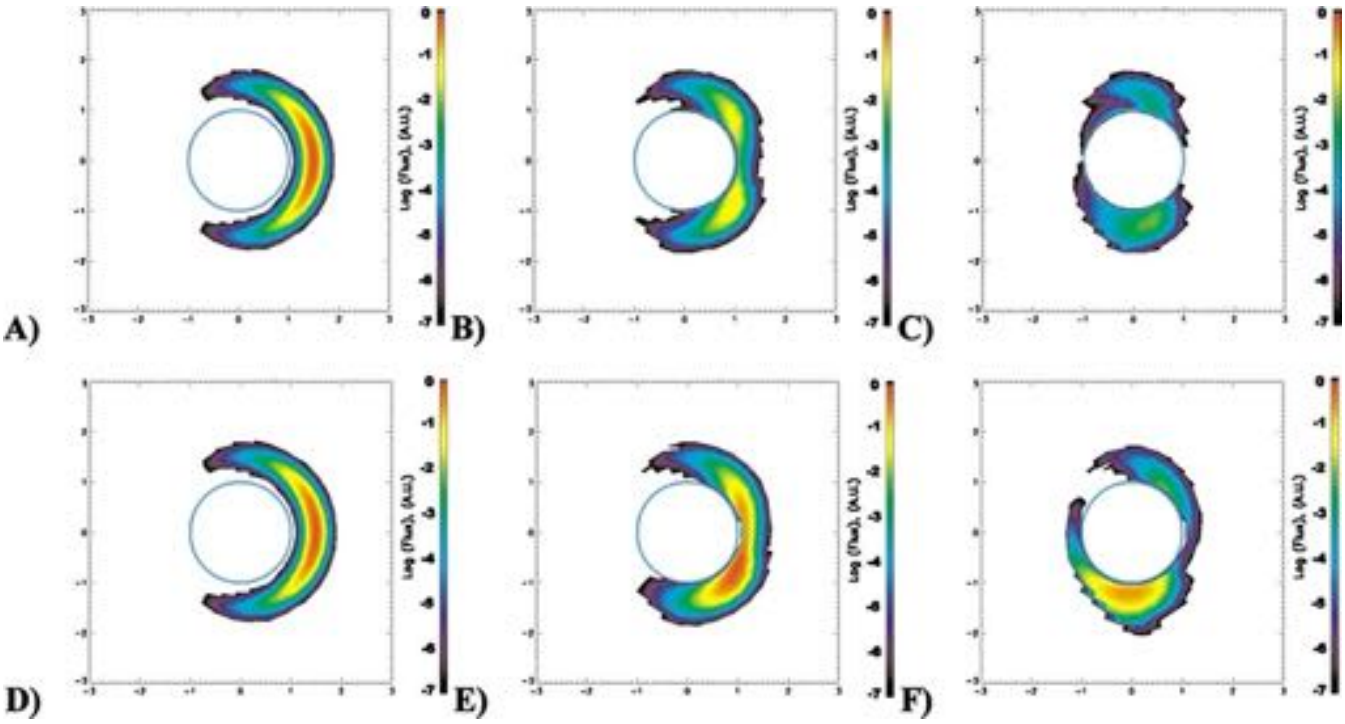

Fig. 9. Equatorial H^+ flux as simulated using the continuity equation and guiding center approximation and an arbitrary source. Panels (A), (B), (C): H^+ flux @ 1 keV, respectively after 0, 20, 100 s from the injection; panels (D), (E), (F): H^+ flux @ 5 keV, after 0, 20, 100 s from injection. Color is coded according to H^+ flux using a logarithmic scale, normalized to the maximum of the initial flux.

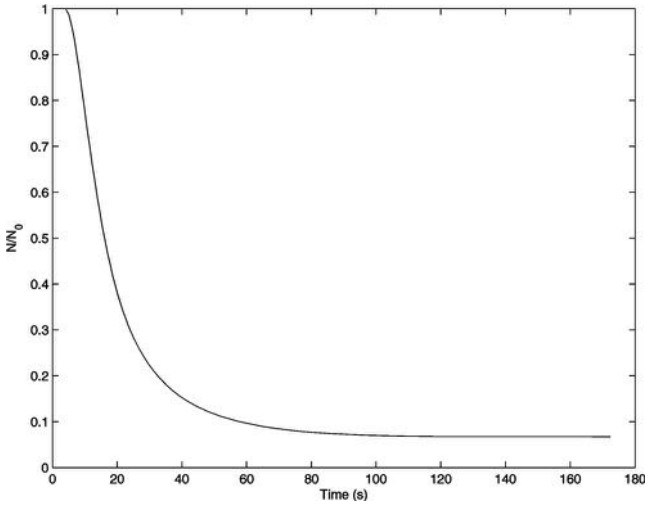

Fig. 10. Relative abundance of protons in the equatorial plane of Mercury, as a function of time elapsed since injection, with respect to proton abundance at $t = 0$. The H^+ distribution at is arbitrary.

Sections 2.2, 2.3), are very similar to that shown in Fig. 9. Hence, the results of our simulations show that, in all cases, it is difficult for protons to reach the dayside, since charge-exchange and planetary collisions rapidly remove the protons from the magnetosphere.

In Fig. 10 we show the relative intensity of the proton flux versus the elapsed time, in the same configuration as in Fig. 9. About 50% of the protons are lost in the first 20 s, and only 20% are still circulating after 40 s.

As a matter of fact, we conclude that, even if some short-time proton circulation is possible in the night side, it will hardly extend to the dayside. A stable circulation of protons around Mercury is extremely improbable, and no ring current is able to form. This latter consideration is important also while reconstructing the **B** field with a Tsyganenko modified model (see Section 2.2).

References

Barabash, S., Lukyanov, A.V., C:son Brandt, P., Lundin, R., 2001. Energetic neutral atom imaging of Mercury's magnetosphere. 3. Simulated images and instrument requirements. Planet. Space Sci. 49, 1685–1692.

Barnett, C.F., 1990. Collisions of H, H_2, He and Li atoms and ions with atoms and molecules. In: Hunter, H.T., Kirkpatrick, M.I. (Eds.), Atomic Data for Fusion Ser., vol. 1. Oak Ridge Nat. Laboratory, Oak Ridge, TN. Rep. ORNL-6086.

Barnett, C.F., Ray, J.A., Ricci, E., Wilker, M.I., McDaniel, E.W., Thomas, E.W., Gilbody, H.B., 1977. Physics Division: Atomic Data for Controlled Fusion. Oak Ridge Nat. Laboratory, Oak Ridge, TN.

Betz, G., Wien, K., 1994. Energy and angular distributions of spattered particles. Int. J. Mass Spectrom. 140, 1–110.

Broadfoot, A.L., Shemanky, D.E., Kumar, S., 1976. Mariner 10: Mercury atmosphere. Geophys. Res. Lett. 3, 577–580.

Burlaga, L.F., 2001. Magnetic fields and plasma in the inner heliosphere: Helios results. Planet. Space Sci. 49, 1619–1627.

Delcourt, D.C., Grimald, S., Leblanc, F., Berthelier, J.-J., Millilo, A., Mura, A., Orsini, S., 2003. A quantitative model of planetary Na^+ contribution to Mercury's magnetosphere. Ann. Geophys. 21, 1723–1736.

Goettel, K.A., 1988. Present bounds on the bulk composition of Mercury: implications for planetary formation processes. In: Vilas, F., Chapman,

C.R., Matthews, M.S. (Eds.), Mercury. Univ. of Arizona Press, Tucson, pp. 613–621.

Goldstein, B.E., Suess, S.T., Walker, R.J., 1981. Mercury: magnetospheric processes and the atmospheric supply and loss rates. J. Geophys. Res. 86, 5485–5499.

Grande, M., 1997. Investigation of magnetospheric interactions with the hermean surface. Adv. Space Res. 19 (10), 1609–1614.

Hasted, G.B., 1964. Physics of Atomic Collisions. Butterworths, London. 416 p.

Ip, W.-H., 1987. Dynamics of electrons and heavy ions in Mercury's magnetosphere. Icarus 71, 441–447.

Kabin, K., Gombosi, T.I., DeZeeuw, D.L., Powell, K.G., 2000. Interaction of Mercury with the solar wind. Icarus 143, 397–406.

Kallio, E., Janhunen, P., 2003. Modelling the solar wind interaction with Mercury by a quasineutral hybrid model. Ann. Geophys. 21, 2133–2145.

Kallio, E., Janhunen, P., 2004. The response of the hermean magnetosphere to the interplanetary magnetic field. Adv. Space Res. 33, 2176–2181.

Killen, R.M., Ip, W.-H., 1999. The surface-bounded atmosphere of Mercury and the Moon. Rev. Geophys. 37 (3), 361–406.

Killen, R.M., Potter, A.E., Morgan, T.H., 1990. Spatial distribution of sodium vapor in the atmosphere of Mercury. Icarus 85, 145–167.

Killen, R.M., Potter, A.E., Reiff, P., Sarantos, M., Jackson, B.V., Hick, P., Giles, B., 2001. Evidence for space weather at Mercury. J. Geophys. Res. Planets 106, 20509–20525.

Lammer, H., Wurz, P., Patel, M.R., Killen, R., Kolb, C., Massetti, S., Orsini, S., Milillo, A., 2003. The variability of Mercury's exosphere by particle and radiation induced surface release process. Icarus 166, 238–247.

Leblanc, F., Johnson, R.E., 2003. Mercury's sodium exosphere. Icarus 164, 261–281.

Luhmann, J.G., Russell, C.T., Tsyganenko, N.A., 1998. Disturbances in Mercury's magnetosphere: are the Mariner 10 'Substorms' simply driven? J. Geophys. Res. 103, 9113–9119.

Lukyanov, A.V., Barabash, S., Lundin, R., C:son Brandt, P., 2001. Energetic neutral atom imaging of Mercury's magnetosphere. 2. Distribution of energetic charged particles in a compact magnetosphere. Planet. Space Sci. 49, 1677–1684.

Massetti, S., Orsini, S., Milillo, A., Mura, A., De Angelis, E., Lammer, H., Wurz, P., 2003. Mapping of the cusp plasma precipitation on the surface of Mercury. Icarus 166 (2), 229–237.

McGrath, M.A., Johnson, R.E., Lanzerotti, L.J., 1986. Sputtering of sodium on the planet Mercury. Nature 323, 694–696.

Ness, N.F., Behannon, K.W., Lepping, R.P., Whang, Y.C., 1976. Observations of Mercury's magnetic field. Icarus 28, 479–488.

Ogilvie, K.W., Scudder, J.D., Vasyliunas, V.M., Hartle, R.E., Siscoe, G.L., 1977. Observations at the planet Mercury by the plasma electron experiment: Mariner 10. J. Geophys. Res. 83, 1807–1824.

Orsini, S., Milillo, A., De Angelis, E., Di Lellis, A.M., Zanza, V., Livi, S., 2001. Remote sensing of Mercury's magnetospheric plasma via energetic neutral atoms imaging. Planet. Space Sci. 49, 1659–1668.

Potter, A.E., Morgan, T.H., 1985. Discovery of Na in the atmosphere of Mercury. Science 229, 651–653.

Potter, A.E., Morgan, T.H., 1997. Sodium and potassium atmospheres of Mercury. Planet. Space Sci. 45, 95–100.

Roelof, E.C., Mitchell, D.G., Williams, D.J., 1985. Energetic neutral atoms ($E \sim 50$ keV) from the ring current, IMP 7/8 and ISEE 1. J. Geophys. Res. 90, 10991–11008.

Sarantos, M., Reiff, P.H., Hill, T.W., Killen, R., Urquhart, A.L., 2001. A B_x-interconnected magnetosphere model for Mercury. Planet. Space Sci. 49, 1629–1635.

Sigmund, P., 1969. Theory of sputtering. I. Sputtering yield of amorphous and polycrystalline targets. Phys. Rev. 184, 383–416.

Sieveka, E.M., Johnson, R.E., 1984. Ejection of atoms and molecules from Io by plasma–ion impact. Astrophys. J. 287, 418–426.

Siscoe, G.L., Ness, N.F., Yeates, C.M., 1975. Substorms on Mercury? J. Geophys. Res. 80, 4359–4363.

Slavin, J.A., Owen, J.C.J., Connerney, J.E.P., Christon, S.P., 1997. Mariner 10 observations of field-aligned currents at Mercury. Planet. Space Sci. 45, 133–141.

Sprague, A.L., Schmitt, W.J., Hill, R.E., 1998. Mercury: sodium atmospheric enhancements, radar bright spots and visible surface features. Icarus 136, 60–68.

Spreiter, J.R., Summers, A.L., Alksne, A.Y., 1966. Hydromagnetic flow around the magnetosphere. Planet. Space Sci. 14, 223–253.

Stebbings, R.F., Smith, C.H., Ehrahardt, H., 1964. Charge transfer between oxygen atoms and O^+ and H^+ ions. J. Geophys. Res. 69, 2349–2355.

Tsyganenko, N.A., 1996. Effects of the solar wind conditions on the global magnetospheric configuration as deduced from data-based field models. In: Proc. of 3rd International Conference on Substorms (ICS-3), Versailles, France. ESA SP, vol. 389, pp. 181–185.

Volland, H.A., 1975. Models of global electric fields within the magnetosphere. Ann. Geophys. 31, 159–173.

Volland, H., 1978. A model of the magnetospheric convection electric field. J. Geophys. Res. 83, 2695–2699.

Weins, R.C., Burnett, D.S., Calaway, W.F., Hansen, C.S., Lykkem, K.R., Pellin, M.L., 1997. Sputtering products of sodium sulphate: implications for Io's surface and for sodium bearing molecules in the Io's torus. Icarus 128, 386–397.

Wurz, P., Lammer, H., 2003. Monte Carlo simulation of Mercury's exosphere. Icarus 164 (1), 1–13.